Quark and Gluon Jet Response from Dijet and Z + Jet Events at ATLAS

by

Alexander Taras Bunka

B.Sc., University of British Columbia, 2019

Thesis Submitted in Partial Fulfillment of the
Requirements for the Degree of
Master of Science

in the
Department of Physics
Faculty of Science

SIMON FRASER UNIVERSITY
Spring 2024

Declaration of Committee

Name:	**Alexander Taras Bunka**
Degree:	**Master of Science**
Thesis title:	**Quark and Gluon Jet Response from Dijet and Z + Jet Events at ATLAS**
Committee:	**Chair: David Sivak** Associate Professor, Physics
	Michel Vetterli Supervisor Professor, Physics
	Matthias Danninger Committee Member Assistant Professor, Physics
	Sarah Johnson Examiner University Lecturer, Physics

Abstract

The most commonly produced objects in proton-proton collisions at the Large Hadron Collider (LHC) are jets, collimated sprays of particles representing an initial quark or gluon from the collision. Jet response is the fraction of jet energy measured by the detector, determined through jet calibration. Jets initiated by quarks and gluons develop differently and thus have different responses. This thesis determines the responses of quark and gluon initiated jets by comparing two different event types, two back-to-back jets (dijet) and Z-boson plus one jet (Z + jet). A method is developed to calibrate dijet events using the same technique as Z + jet events, and is shown to be successful. The responses of quark and gluon jets are calculated, and while the quark jet response behaves as expected, the gluon jet response does not. Additional examination reveals why the gluon response may be flawed and how it can be improved in future research.

Keywords: ATLAS; Large Hadron Collider; Jets; Quarks; Gluons; MPF

Acknowledgements

Plenty of people help when you complete a Master's degree, especially when you take a little longer than usual. I'll start by thanking Javier and Sahil, who greatly eased the experience of starting grad school and learning the different software tools. Many other people from both the SFU HEP group and ATLAS experiment helped as well. I also want to thank Max for his help during my program and the opportunities afterwards, and Matthias for his work on my committee. Additionally, I must thank my parents, siblings, other family and friends for their constant support throughout this process. Lastly, I wish to thank my supervisor Mike, who provided a wealth of physics insight and encouragement throughout my degree.

Table of Contents

List of Tables

List of Figures

Chapter 1

Introduction

1.1 The Standard Model of Particle Physics

The Standard Model of particle physics is among the most successful scientific theories developed. The model effectively describes the structure and behaviour of the known subatomic particles as well as three of the four fundamental forces. It has achieved remarkable experimental success; time and again theory and experiment have converged to produce astonishing results.

Under the Standard Model, elementary particles are classified as *bosons* (integer spin, follow Bose-Einstein statistics) and *fermions* (half-integer spin, follow Fermi-Dirac statistics). There are 12 elementary fermions; six leptons and six quarks (six *flavours* of each), each with its own antiparticle [1]. Antiparticles have the same mass as their counterparts, but with reversed quantum numbers (such as electrical charge). The leptons include the electron, muon, and tau as well as a corresponding neutrino for each, which makes for three generations of particles. The quarks also fall into three generations, as shown in figure 1.1. Fermions are matter particles; combinations of quarks form protons and neutrons, which with electrons make up all the atoms in the universe. Particles that are made up of quarks and gluons and interact by the strong force are called hadrons. The quarks and gluons are collectively known as partons. The elementary gauge (vector) bosons are responsible for interactions and are often referred to as mediators. Each of the fundamental forces described by the Standard Model has its own mediating particle, and a corresponding theory to describe the interaction. The electromagnetic force is described by quantum electrodynamics (QED) and is mediated by the photon. Quantum chromodynamics (QCD) describes the strong force which is mediated by gluons. The weak force is mediated by charged W and neutral Z bosons. The fundamental forces are summarized in table 1.1, while the mediators are shown in figure 1.1. The interaction vertices of the Standard Model, the building blocks of all known particle interactions, are pictured in figure 1.2.

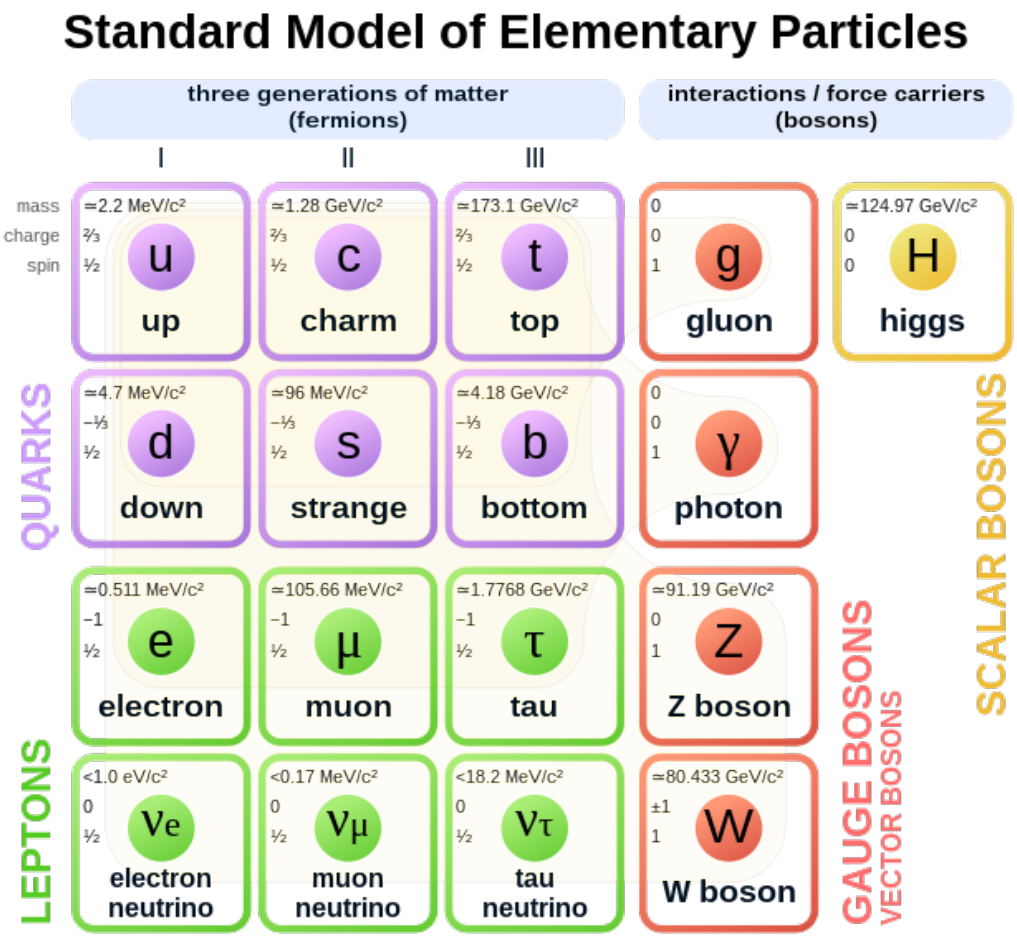

Figure 1.1: The Standard Model effectively classifies all the elementary particles, including quarks, leptons, force mediators, and the Higgs boson [2].

Force	Strength	Theory	Mediator	Acts On
Strong	10	Chromodynamics	Gluons	Quarks and Gluons
Electromagnetic	10^{-2}	Electrodynamics	Photon	Charged Particles
Weak	10^{-13}	Flavourdynamics/ Electroweak	Z and W Bosons	Quarks and Leptons
Gravitational	10^{-42}	Geometrodynamics	Graviton	All massive particles

Table 1.1: The fundamental forces describe all interactions of elementary particles in nature. The strong force binds together quarks into protons and neutrons, which are further bound by the residual strong force. The weak force accounts for nuclear decay, and electromagnetism binds electrons to nuclei to produce atoms. Additionally, the physical effects people experience in day-to-day life such as heat, light, and sound result from the electromagnetic force. Gravity is not yet described by the Standard Model, and no mediator has been found [3].

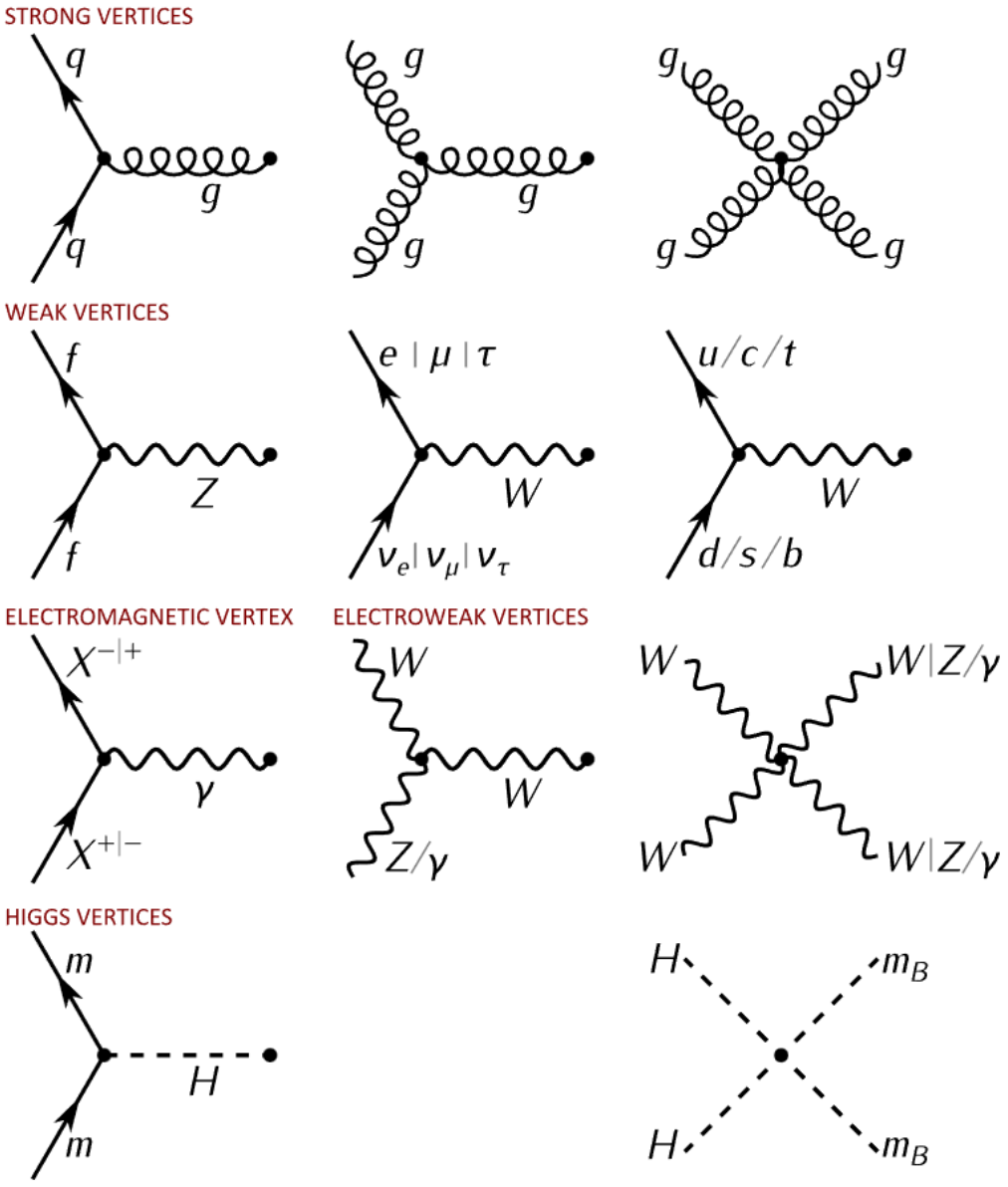

Figure 1.2: The interactions of the Standard Model are described by these vertices. The electromagnetic vertex corresponds to the interactions of photons (γ) with electrically charged particles ($X^{\pm}$). The weak vertex with the Z boson represents weak neutral currents, while the W boson represents weak charged current interactions. The QCD interactions occur between particles with colour charge, quark-gluon or gluon self-interactions. There are also interactions between the mediators of the combined electroweak interaction, as well as interactions between the higgs boson and any massive particle (m) or massive boson (m_B) [4].

The Dirac equation for free particles (1.1) describes all spin-$\frac{1}{2}$ particles consistently with both quantum mechanics and special relativity (m is the particle mass, ψ is a Dirac spinor, and γ are the four Dirac matrices).

$$i\gamma^{\mu}\partial\psi - m\psi = 0 \tag{1.1}$$

Under the local phase transformation

$$\psi \to \psi' = \psi e^{iq\chi(x)}, \tag{1.2}$$

the Dirac equation becomes:

$$i\gamma(\partial_{\mu} + iq\partial_{\mu}\chi)\psi - m\psi = 0 \tag{1.3}$$

For physics to remain invariant under this transformation, i.e. maintaining $\mathrm{U}(1)_Q$ symmetry, the term iqA_{μ} must be added to the Dirac equation:

$$i\gamma^{m}u(\partial_{\mu} + iqA_{\mu})\psi - m\psi = 0 \tag{1.4}$$

The field A_{μ} represents a massless gauge boson, and the new modified Dirac equation is invariant if this term transforms as $A_{\mu} \to A'_{\mu} = A_{\mu} - \partial_{\mu}\chi$.

This implies two important facts: Firstly, the Dirac equation requires the addition of an interaction term for physics to remain invariant under the $\mathrm{U}(1)_Q$ transformation. The gauge transformation of this field is identical to how electromagnetic fields transform in classical electromagnetism. Secondly, all of QED, interactions between spin-$\frac{1}{2}$ charged particles and a massless, neutral gauge boson, follows from this requirement [1].

This method of requiring invariance across a transformation can be applied to different symmetries to produce different interactions. The rest of the Standard Model can be derived in a similar, albeit more complicated manner.

The Standard Model is a Quantum Field Theory (QFT); a combination of special relativity, field theories, and quantum mechanics. The theory satisfies a number of symmetries, including translational and rotational symmetries, as well as Lorentz Invariance. Additionally, the interactions of the Standard Model arise from the requirement of a combination of three local gauge symmetries, SU(3)× SU(2) × U(1), which represent different transformations.

Note that earlier (when discussing the Dirac equation and QED) the symmetry in play was $\mathrm{U}(1)_Q$, yet here the "Q" is dropped. Indeed, the three gauge symmetries of the Standard Model do not all map one-to-one with the three interactions. While the SU(3) interaction pairs off with QCD (discussed further in the following section), it is not so simple for the SU(2)× U(1) component, and the U(1) here is not the same as before. The SU(2)× U(1) symmetry is better known as $\mathrm{SU}(2)_L\times \mathrm{U}(1)_Y$, where the L represents the fact that

the SU(2) interaction only applies to left-handed particles and right-handed antiparticles. At high energy, a particle's "handedness" refers to its helicity state[1]; right-handed if the particle's spin and direction of motion are aligned and left-handed if they are opposite.

$SU(2)_L \times U(1)_Y$ corresponds to the combined electroweak interaction, with three fields for the $SU(2)_L$ component ($W_{1,2,3}$) and a fourth for $U(1)_Y$ (B), just as $U(1)_Q$ generated the A_μ field. These four fields do not directly represent the known mediators of the weak and electromagnetic interactions, but instead correspond to non-physical massless bosons. Electroweak mixing, driven by the Higgs mechanism, results in the known neutral Z boson and the photon as a mixture of the B and W_3 fields:

$$\begin{pmatrix} \gamma \\ Z^0 \end{pmatrix} = \begin{pmatrix} cos\theta_W & sin\theta_W \\ -sin\theta_W & cos\theta_W \end{pmatrix} \begin{pmatrix} B \\ W_3 \end{pmatrix} \tag{1.5}$$

where θ_W is the weak mixing angle, determined by measurements to be $sin^2\theta_W = 0.23121$ [5]. Additionally, the charged W bosons are combinations of the $W_{1,2}$ fields:

$$W^\pm = \frac{1}{\sqrt{2}}(W_1 \mp iW_2) \tag{1.6}$$

The breaking of electroweak symmetry also produces the more familiar $U(1)_Q$ theory of electromagnetism, with regular electric charge

$$Q = I_3 + \frac{1}{2}Y_W \tag{1.7}$$

where I_3 is the third component of weak isospin and Y_W is weak hypercharge, the generators (charges) of the $SU(2)_L \times U(1)_Y$ symmetries.

Electroweak theory is often known as Glashow-Weinberg-Salam theory for the three primary physicists who developed it. Electroweak Unification and GSW theory have been thoroughly proven by experiment [6]. In fact, numerous experiments predated the theory and inspired its development [7].

In addition to the mediators, there is a Higgs boson (a *scalar* boson), named for one of the physicists who predicted its existence. The Higgs particle has been shown to be responsible for the masses of the gauge bosons [8, 9] by way of spontaneous symmetry breaking in complex scalar fields, and the fermion masses through Yukawa couplings to the Higgs boson [10]. The Higgs boson was discovered at the Large Hadron Collider in 2012 [11, 12].

[1]In general, the weak interaction acts on left-*chiral* particles. Chiral states are the eigenstates of the γ^5 matrix (the product of the four Dirac matrices, $\gamma^5 = i\gamma^0\gamma^1\gamma^2\gamma^3$), and only in the limit of $E >> m$ are the chiral and helicity states equivalent. For more information, see Thompson [1], chapters 6 and 15.

1.1.1 Quantum Chromodynamics

Just as electroweak theory has a "charge" for each symmetry, so too does QCD. Indeed, the name chromodynamics comes from the name for a property carried by all strongly interacting particles, colour charge. Unlike electric charge, there are three different colour charges known as red, green, and blue, and three anti-colours. The requirement of SU(3) symmetry generates eight different massless gauge bosons, the gluons, each in a mixed colour-anticolour state such as $(r\bar{b} + b\bar{r})/\sqrt{2}$. Since gluons carry colour charge, they are capable of self-interaction, unlike the electrically neutral photon of QED.

After electroweak symmetry breaking QED is obtained from $U(1)_Q$ symmetry, and QCD can be derived the same way. Now however, the SU(3) local phase transformation applied to the Dirac equation (1.1) is:

$$\psi \rightarrow \psi' = \psi e^{ig\vec{\lambda}\cdot\vec{\theta}(x)} \tag{1.8}$$

While this is similar in form to 1.2, $\vec{\lambda}$ are eight 3×3 Gell-Mann matrices and $\vec{\theta}(x)$ are eight functions in space-time. This means that to maintain invariance across such a transformation, eight fields (G_μ) are required, corresponding to eight gluons. The Gell-Mann matrices have three degrees of freedom, thus the generator of QCD requires three components; the colour charge.

The SU(3) transformation remains invariant if the eight fields transform as:

$$G^k_\mu \rightarrow G^{k'}_\mu = G^k_\mu - \partial_\mu\theta_k - gf_{ijk}\theta_i G^j_\mu \tag{1.9}$$

Where $[\lambda_i, \lambda_j] = 2if_{ijk}\lambda_k$ are the commutation relations of the Gell-Mann matrices. All but eight of these relations are zero, and the final term of 1.9 implies gluon self-interaction [1].

Gluon self-interactions give rise to perhaps the most important properties of QCD: colour confinement and the running coupling constant. In both QCD and QED, the strength of the interactions is quantified by a coupling constant, α for QED (also known as the fine structure constant) and α_s for QCD. α is generally taken as 1/137, but is in fact not constant. While the simplest QED interactions are described by the standard photon-electron-electron vertex, higher-order interactions also exist and are infinite in number, as seen in the loop diagrams of figure 1.3. The loops create a screening effect that increases with distance/decreases with energy; at low energy/large distance, the previous value is accurate. At approximately 90 GeV, α increases to about 1/127. The total effect of the loops is, after renormalization [13];

$$\alpha(|q^2|) = \frac{\alpha(0)}{1 - [\alpha(0)/3\pi]ln[|q^2|/(mc)^2]} \tag{1.10}$$

q^2 is the momentum transferred in the interaction. While this would become infinite, such an effect would not occur until energies of $\mathcal{O}(10^{280})$ MeV [3]. Thus, the effects of higher-

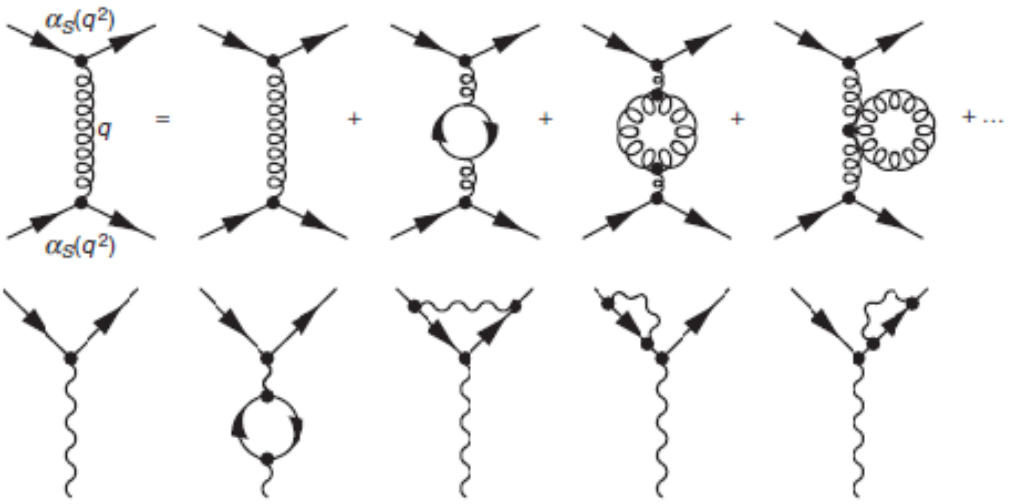

Figure 1.3: A simple QCD (or QED) interaction is in fact a combination of higher-order corrections. The lower diagrams show modifications to the standard QED vertex to produce second-order terms. All these terms exist in QCD as well if gluons and quarks are swapped for photons and leptons. The upper diagrams show that in QCD, there are still more terms to be considered due to gluon self-interaction. From Thomson [1].

order terms in QED can be well accounted for. However, in QCD there are not only loops caused by quark-gluon interactions, but additional loops caused by gluon self-interactions. The cumulative effect on α_s is anti-screening, and the strength of the interaction *increases* with distance:

$$\alpha_s(|q^2|) = \frac{\alpha_s(\mu^2)}{1 + [\alpha_s(\mu^2)/12\pi](11n - 2f)ln(|q^2|/\mu^2)} \tag{1.11}$$

$|q^2| >> \mu^2$, and n and f are the numbers of colours and flavours, respectively. With three colours and six flavours, the effect is that α_s increases uncontrollably with decreasing energy. Figure 1.4 shows α_s as a function of energy.

The behaviour of α_s means that QCD must be handled differently for different energies. At high energy ($\mathcal{O}(100)GeV$, within the range of most high energy accelerators/colliders) the coupling constant is sufficiently small that QCD may be treated perturbatively, albeit with the added work of higher order calculations. At lower energies, α_s becomes too large and alternative methods are needed to properly characterize QCD [1]. Both forms of QCD are important to collider physics, as lower energy interactions occur after the initial particle collision (in the formation of jets, for example. See chapter 3).

Colour confinement, though not analytically proven, can be well described by considering gluon self-interactions and the nature of α_s. If two quarks are separated, the mediating gluons between them experience attractive self-interactions, thus the gluon field between the quarks is squeezed into a thin flux-tube. As the quarks are pulled apart, the tube

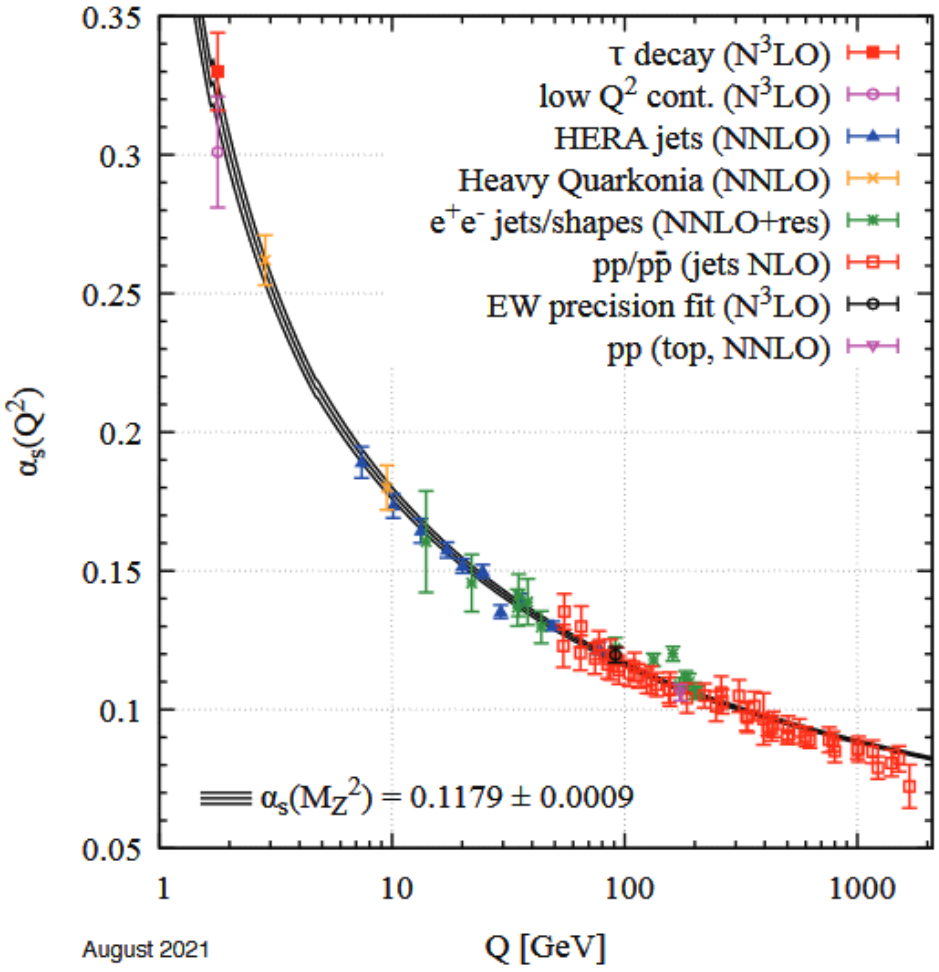

Figure 1.4: The strong coupling constant as a function of energy, from numerous different measurements. NLO means "Next to Leading Order", NNLO means "Next to Next..." and so on. At higher energy, the coupling constant is smaller such that quarks only interact weakly. This leads to asymptotic freedom and QCD can be treated perturbatively in this regime [5].

narrows, the energy density increases, and the total energy required to separate the particles increases. It would require infinite energy to separate the quarks entirely, so it is energetically favourable for new quarks to be created from the gluon field, and each quark is again part of a bound colour-neutral state.

This hypothesis makes it impossible to observe free quarks, or any particle that is not colour neutral. Only combinations of colour and anticolour or three colours (three anti-colours) can be observed. These are the mesons and baryons, respectively.

To study coloured objects, scientists must look at the colour-neutral signature left behind by a quark or gluon, a jet. Jets are discussed in detail in chapter 3.

1.2 Calorimetry

Energy measurement is essential to particle physics research. To understand how physicists determine the energy of a particle, it is important to understand how particles interact with matter. Generally, calorimeters work by interacting with particles and absorbing all of their energy, converting it to an electronic signal. In this way, calorimeters provide an additional service in many experiments as radiation shielding. Since theirs is a destructive measurement, calorimeters must be positioned outside of other detectors (though there are exceptions in special cases, such as muon detection). There are two main kinds of calorimeters, sampling and homogeneous. Sampling calorimeters generally use two separate materials, one to produce a particle shower and one to measure the energy, while homogeneous calorimeters use a single material for both purposes. Typically, in sampling calorimeters, a significant portion of the energy will be lost within the absorber material which can make for lower resolution than in homogeneous calorimeters. However, homogeneous calorimeters are less efficient in absorbing particles and must be built much larger and at greater cost.

The process by which particles traverse a calorimeter is known as *showering*. A particle shower is a multi-stage process wherein an initial particle radiates other particles with fractions of the initial energy and/or decays into two or more particles with the initial energy divided amongst them. The properties of a shower depend on the characteristics of the initiating particle; type, energy... Most importantly showering can be divided into two forms, hadronic and electromagnetic, depending on the interactions the particles undergo in the detector. Photons and electrons generate electromagnetic showers since they interact via the electromagnetic force, while hadrons such as protons and pions interact primarily via the strong force.

In the following sections, the development of electromagnetic and hadronic showers is discussed. Also, a description of the interactions that lead to measurable energy and electronic signals in the detector, as well as how shower properties influence calorimeter design, is provided.

1.2.1 Electromagnetic Showers

Photons, electrons, and positrons can undergo many different interactions in matter depending on the materials involved and the particles' initial energy. Understanding these interactions and how they impact the development of electromagnetic showers is essential to the design of any calorimeter. Photons interact mainly through the following mechanisms:

1. Pair Production: For photons with $E > 2m_e$ ($m_e = 0.511$ MeV) pair production becomes possible. In this process, an initial photon in the presence of a nuclear electromagnetic field decays into an electron-positron pair. The process can also occur around the field of an atomic electron, albeit much more rarely [14]. Depending on the material, pair production begins to dominate the other interactions at energies of $\mathcal{O}(10)$ MeV.

2. Compton Scattering: The Compton effect is the scattering of an incident photon off of an atomic electron. The photon will have its energy reduced and be deflected by some angle, while the recoil electron will become unbound from the atom. This effect dominates over a range from hundreds of keV to several MeV, depending on the material[2].

3. Photoelectric Effect: Low energy photons can eject an electron from an atom while themselves being absorbed. If the electron is ejected from an inner orbital, it is replaced by another from a higher energy outer orbital. This excess energy is carried off by an Auger electron or X-rays [15]. The photoelectric cross section shows marked discontinuities at the various atomic shell binding energies and depends on the material as Z^5, where Z is the atomic number of the material. This effect dominates in the low energy region and is typically how most photons are finally absorbed in an electromagnetic calorimeter.

The photon interaction cross sections are plotted as a function of photon energy in figure 1.5.

Electrons (and positrons) typically interact through either ionization or bremsstrahlung. Charged particles such as electrons/positrons will kick electrons out of atoms as they traverse matter, leaving negative and positive ions behind. The ions and/or electrons can be gathered in an electric field to provide a signal. Ionization is among the main detection and signalling techniques in not only calorimeters but also tracking detectors.

Bremsstrahlung occurs for high-energy electrons interacting with the electromagnetic field of an atomic nucleus. As the electron is deflected in the field it emits photons with

[2] An additional process, Rayleigh scattering, can occur at lower energies. In Rayleigh scattering the photon does not lose energy, so this only affects the spatial development of the shower. This process never has a larger cross-section than the effects mentioned above for photons.

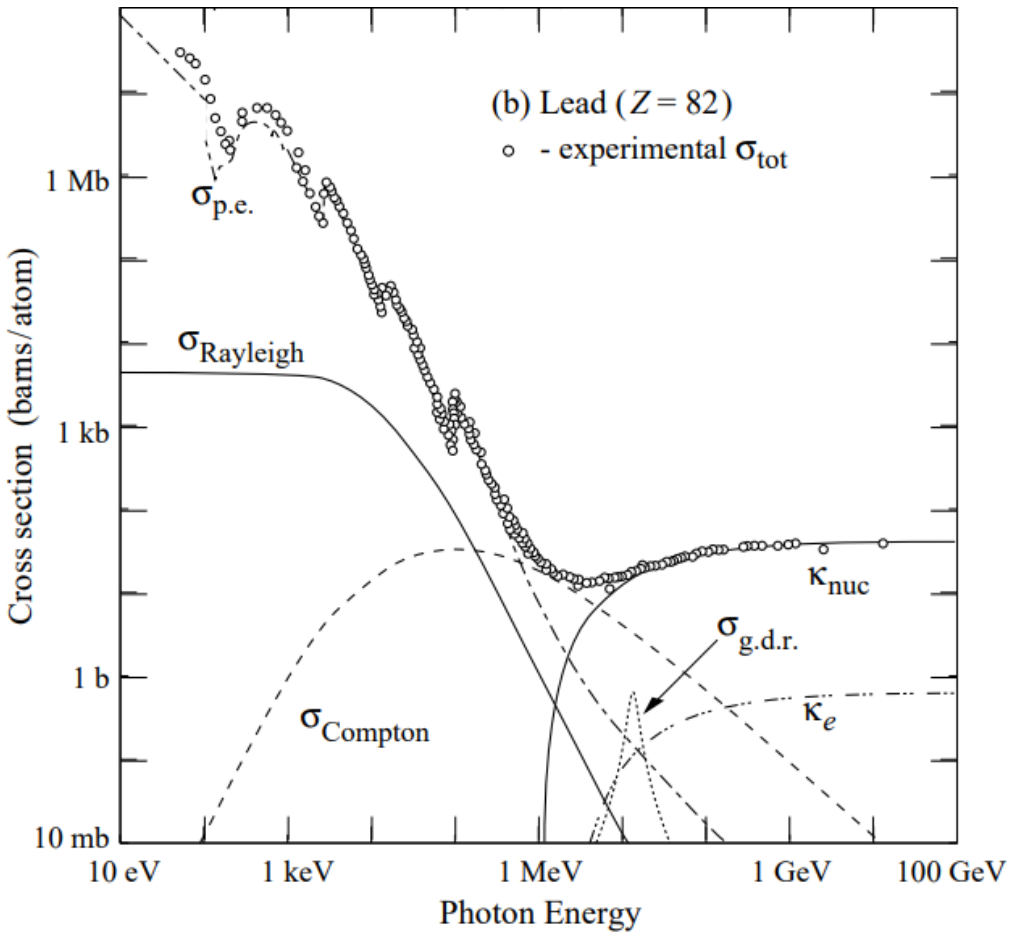

Figure 1.5: Cross section versus energy for photon interactions. At low energy the photoelectric effect $\sigma_{p.e.}$ dominates, and pair production κ_{nuc}, κ_e takes over at high energy. Compton scattering $\sigma_{Compton}$ bridges the gap, and several other processes play smaller roles [16].

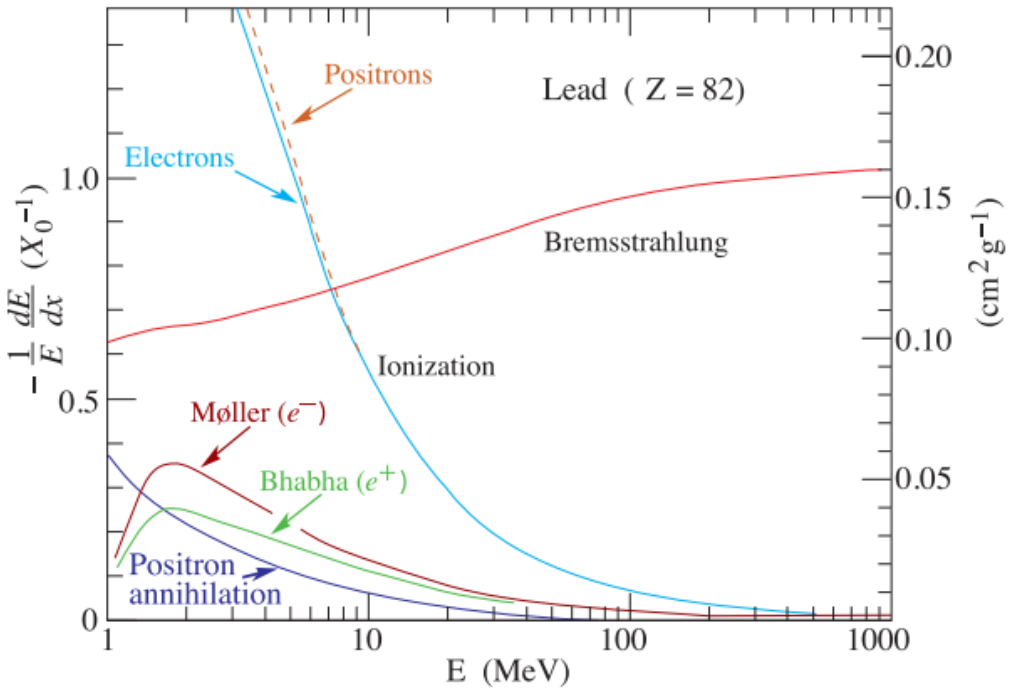

Figure 1.6: Fractional energy loss per radiation length (see equation 1.16) for electrons in lead. While ionization and bremsstrahlung are the main contributors, scattering and annihilation play a small role at low energy [16].

a small fraction of its energy. An electron of only a few GeV will emit thousands of photons in just a single centimetre of lead, most in the keV to MeV range [14]. The rate of bremsstrahlung is inversely proportional to the square of a particle mass, and thus while it is a very common process for electrons, it is substantially suppressed for heavier particles by a factor of $(m_e/m)^2$ [1]. For this reason, hadrons interact with the calorimeter primarily through the strong interaction rather than electromagnetically (charged hadrons do still experience ionization, primarily at lower energies). Even muons see a 40,000 times reduction in bremsstrahlung, and are largely undetected by calorimeters as they also do not interact through the strong interaction. Muons require dedicated detectors to be measured. The energy loss of these electromagnetic mechanisms is shown in figure 1.6 as a function of electron energy.

At particle energies in excess of about 100 MeV [17] electromagnetic showers are primarily driven by pair production and bremsstrahlung. These two processes iterate, increasing the number of particles in the shower until the energy of the particles is low enough for other processes to take over. The lower energy processes result in the absorption of the

particles and electronic signal generation. The majority of the shower energy is deposited in the detector by these soft[3] particles, even more so for higher Z materials [14].

As the goal of calorimetry is to precisely measure the energy of the particle that initiates the shower, it is essential that the detector collects as many of the particles developed in the shower as possible. Thus the size of the shower, namely the width and depth, is of utmost importance in the design of the detector. The width of the shower is important in designing the granularity (the size of the calorimeter cells). Accounting for the shower depth necessitates building the detector thick enough to absorb all of the particles. Knowing the necessary thickness requires some further discussion on showering characteristics.

In a given material, an electron will lose $1 - e^{-1}$ of its energy through bremsstrahlung over a distance X_0, the radiation length. Additionally, the mean free path for a photon to undergo pair production is given by $\frac{9}{7}\ X_0$. The energy at which the main driving interactions of the shower give way to the low energy absorption processes is known as the critical energy, given by

$$E_c = \frac{610}{Z + 1.24}\ [\text{MeV}] \tag{1.12}$$

in solids and liquids, and by

$$E_c = \frac{710}{Z + 0.92}\ [\text{MeV}] \tag{1.13}$$

for gasses. The exact definition of the critical energy varies [16]; typically it is either the energy at which losses to bremsstrahlung and ionization are equal or the energy where ionization loss over one X_0 is equal to the electron energy [14]. Electrons below the critical energy will be absorbed within the next radiation length, while photons require more material [17]. Figure 1.7 shows the average energy contained within the calorimeter for different initial energies and detector materials.

The point at which the average particle in the shower reaches the critical energy is known as the shower maximum. Here the shower has its greatest number of particles and is at its broadest. Thus, to ensure the majority of energy is deposited in the calorimeter, it should be designed approximately 10 X_0 thicker than the shower maximum of the highest energy particles expected.

Consider a simplified model [17] where the number of particles doubles after each radiation length and the energy is shared evenly among particles. The shower maximum is reached when the particle energy is equal to the critical energy,

$$E_c = E_0 \cdot 2^{-t_{max}} \tag{1.14}$$

[3] "Hard" and "soft" are used to describe high and low energy particles, respectively.

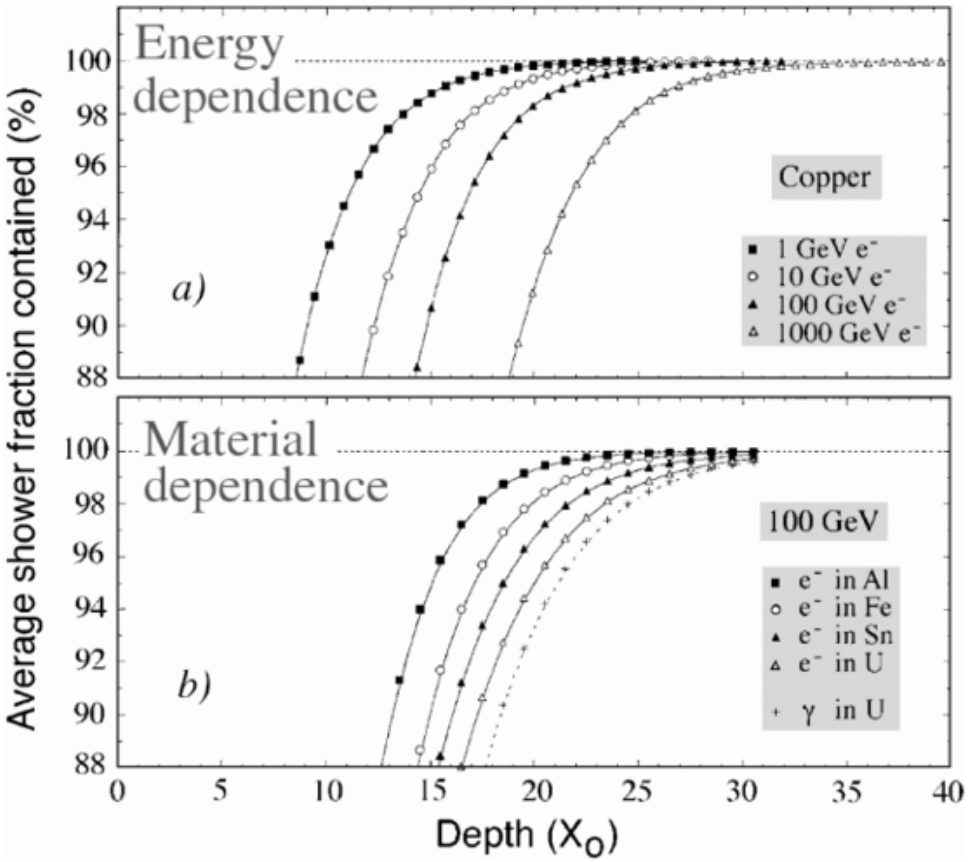

Figure 1.7: EGS4 Monte Carlo simulations showing the approximate containment achieved at subsequent radiation lengths for different energy electrons and materials. 100 GeV photons in uranium are included [14].

where t is the distance in units of radiation lengths. The position of the shower maximum, in radiation lengths, is then given by:

$$t_{max} = \frac{ln(E_0/E_c)}{ln2} \tag{1.15}$$

While the radiation length of a particular material is:

$$X_0 = 1433 \text{ gcm}^{-2} \frac{A}{Z(Z+1)(11.319 - lnZ)} \tag{1.16}$$

Thus the depth of the shower maximum scales with $ln(E_0/E_c)$. This, combined with the earlier expression for the critical energy and the knowledge of extra material needed for photon containment, gives a good estimate of the material thickness required for effective electromagnetic shower containment.

Another important design consideration is hermiticity, ensuring that the calorimeter detects not just the entirety of individual showers, but as large a portion of the entire initial collision products as possible. Complete coverage is impossible, as there must be some opening for the particle beam (two openings in a collider), but detectors can be designed to minimize the area through which particles can escape. These detectors are known as "4π" devices, for the full solid angle of a sphere. Capturing the maximum possible amount of the collision is essential for determining the missing transverse energy in an event, an important value in searches for new physics and detector calibration/performance (see chapter 2.2.2).

The most important aspect of calorimetry is response. Calorimeter response is the ratio of measured energy to the actual energy of a particle, so if the calorimeter detects 9.5 GeV for a particle with 10 GeV of initial energy, the response is 0.95. Calorimeter response differs for sampling versus homogeneous calorimeters as well as electromagnetic versus hadronic calorimeters. Calorimeters generally have very efficient energy absorption for particles that interact electromagnetically and thus a high response to EM showers.

Homogeneous calorimeters have a linear response with respect to energy for electromagnetic particles, with a single material for shower development/detection throughout. These calorimeters maintain excellent electromagnetic energy resolution at high energy. One of the largest homogeneous calorimeters in the world is used by the CMS collaboration at CERN. Made of lead-tungstate crystals and measuring energy through scintillation, the electromagnetic component has an energy resolution on the order of just a few percent [18].

Sampling calorimeters are more complicated as particles are lost to the absorber material, and thus their contribution to the energy measurement is lost. Large amounts of soft (< 1 MeV) photons are produced by bremsstrahlung in the absorber, and through Compton scattering and the photoelectric effect are converted to electrons. These electrons are very low energy and can be absorbed within distances much smaller than the usual thickness of absorber material. As such, they are lost within the absorber, and will only contribute to the energy measurement if they are produced very close to the boundary of the absorber

and sampling material [19]. Despite these effects, the measured energy is proportional to the total deposited energy, and the total energy can be calibrated. The ATLAS electromagnetic sampling calorimeter is the largest in the world, and it has energy resolutions that are comparable to that of the CMS homogeneous calorimeter, ranging from 8% to less than 1% [20].

1.2.2 Hadronic Showers

Particles that interact exclusively through the electromagnetic force are very well measured, but they do not give the whole picture. High energy collisions also produce hadrons that interact through the strong force such as protons, neutrons, and pions. The charged hadrons still lose a portion of their energy through ionization, but none of the hadrons produce bremsstrahlung as they are far too massive. The hadronic showers initiated by such particles develop very differently from the electromagnetic kind, which fundamentally impacts the measurement of their energy.

Instead of the radiation length used in the previous section, the longitudinal development of hadronic showers is measured by the nuclear interaction length,

$$\lambda_I \approx 35 \text{ gcm}^{-2} A^{1/3}, \tag{1.17}$$

the average quantity of material traversed by a particle before undergoing a nuclear interaction. This is much larger than the radiation length for most calorimeter materials (10 times larger for copper, 33 times for lead...), so hadronic calorimeters must be significantly larger than electromagnetic ones [17].

Among the different particles of a hadronic shower are neutral mesons, like the π^0, that decay into photon pairs. This means that some part of the hadronic shower will become electromagnetic, as the photons will begin the processes outlined in the previous section. Neutral pi mesons provide a useful measure of how large a portion of the shower will develop electromagnetically [17]:

$$f_{em} = 1 - (1 - f_{\pi^0})^n \tag{1.18}$$

Here f_{π^0} is the fraction of neutral pions in an interaction, and n is the number of interactions, increasing with energy. Roughly one-third of the mesons produced are π^0's, as the three types of pions ($\pi^\pm$ & π^0) are produced equally on average due to isospin symmetry. Pions are also by far the most commonly produced meson, as they are the lightest and thus energetically favourable. However, particles other than mesons are also produced, so f_{π^0} will be less than 1/3. For higher initial energy, more generations of neutral pions are produced and a larger total fraction of the shower proceeds electromagnetically. Figure 1.8 shows what the first interaction could look like (simplified of course). The initial hadron interacts

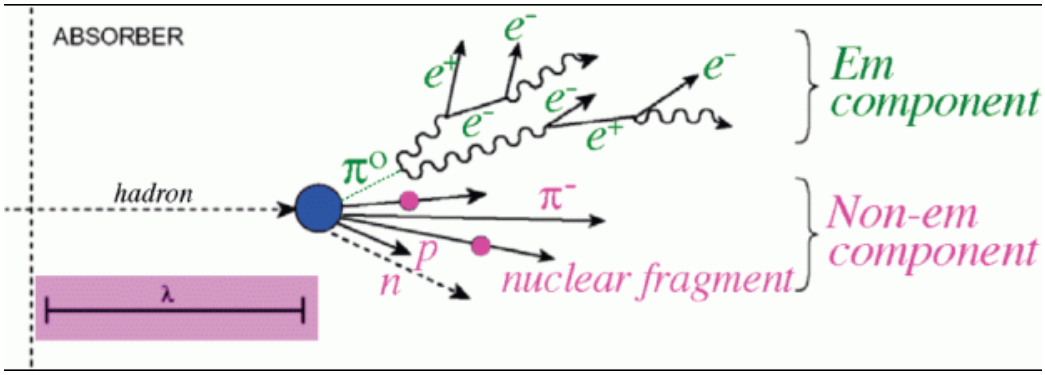

Figure 1.8: This schematic of part of a hadronic shower shows the electromagnetic and hadronic components. While the two components appear to have the same geometric size here, the hadronic component would be much larger than the electromagnetic in a real shower [14].

with an atomic nucleus, and the resulting hadrons follow both nuclear and electromagnetic processes.

Since the electromagnetic component has a high response, better measurement can be performed on hadronic showers with a larger f_{em}.

This portion of the hadronic shower is not much more complicated than the electromagnetic type. Furthermore, the charged hadrons will constantly lose energy through ionization, another relatively simple process. The remaining interactions, between hadrons and atomic nuclei, are what make hadronic showers distinct.

The most frequent result of a collision between a high-energy hadron and a nucleus is spallation, wherein the incident hadron impacts protons and neutrons within the nucleus. The struck nucleons then move through the nucleus, themselves colliding with more nucleons. Spallation is a two-stage process [21], beginning with a nuclear cascade and ending with the slow evaporation of nucleons and, depending on the energy, heavier nucleon combinations. The evaporation continues until the excitation energy is less than the nuclear binding energy, and the remaining energy is carried off by gamma rays.

Within the spallation process rests perhaps the most important difference between hadronic and electromagnetic showers; invisible energy. The energy used to overcome the nuclear binding energy of freed nucleons is fundamentally undetectable and therefore does not contribute to the calorimeter signal. This is not a small effect, and a significant portion of the energy (see table 1.2) from a hadronic shower may be lost this way, and the fluctuations event-by-event are large [22].

Another (much smaller) contribution to the invisible energy is the recoil of the struck nucleus. This net kinetic energy arises from the cascade particles being primarily in the direction of the initiating particle while the evaporation particles are ejected isotropically [23].

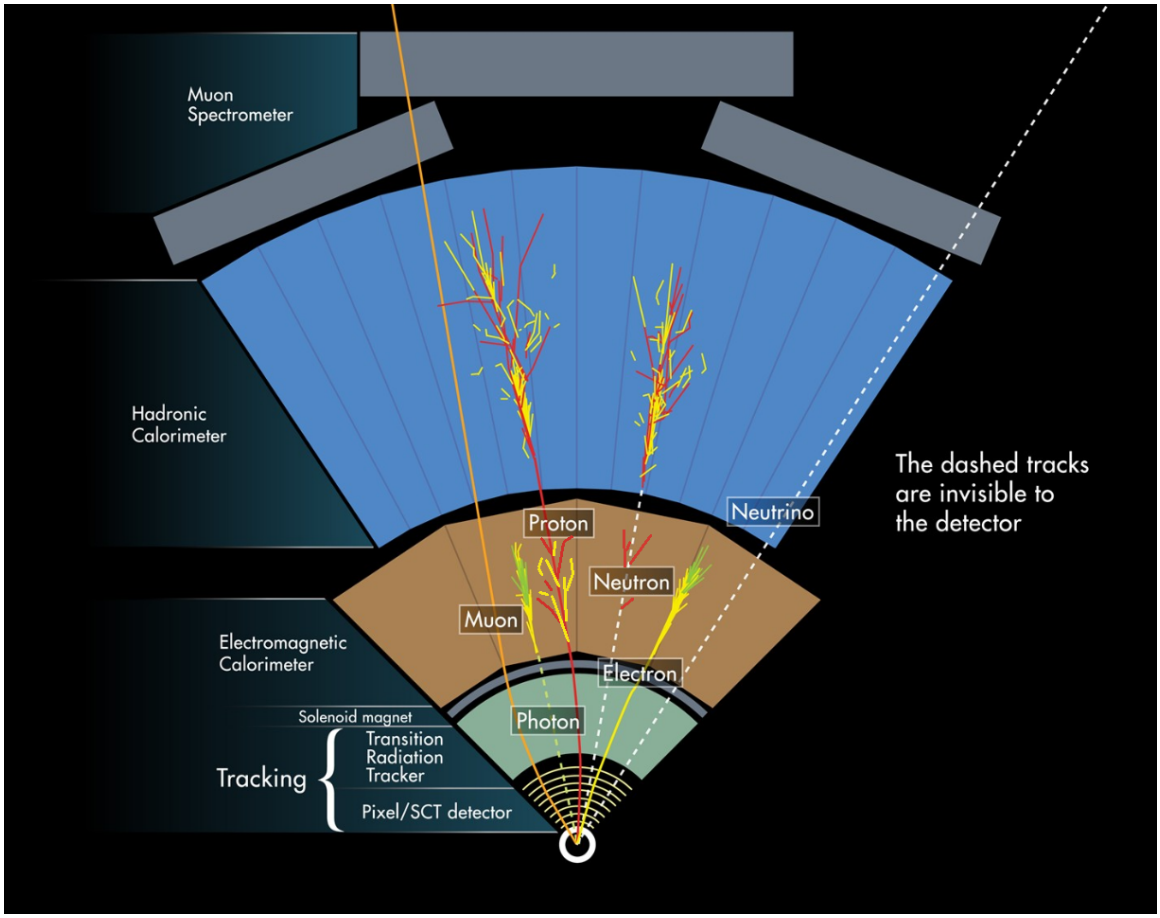

Figure 1.9: This cross-sectional diagram provides a useful visual of the differences between hadronic and electromagnetic showers. The hadronic shower is both broader and longer, and has more particle tracks, than the electromagnetic shower. This figure also gives an introduction to the layout of the ATLAS detector, detailed further in 2.2. [24]. Courtesy of the ATLAS Collaboration

The struck nucleus will undergo further interactions, the specifics of which are determined by its energy.

The particles emitted from a spallation reaction depend on both the energy of the initial particle and the detector material. If the initial energy is below a certain threshold, only nucleons that are "knocked out" in the fast cascade or ejected in the evaporation will appear. At higher energies, such as those experienced by ATLAS at CERN, new hadrons can form. The primary particles produced this way are pions, as they are the lightest hadrons. In the low-energy evaporation step, a material dependence arises through the nuclear Coulomb barrier. More energy, on the order of several MeV, is needed to pry protons from the nucleus due to their electric charge compared to neutrons. This is a larger effect for larger Z materials; a 750 MeV pion in iron will produce roughly 1.3 neutrons per proton, while for a 1300 MeV pion in lead the ratio is greater than 10/1 (see table 1.2).

Mechanism/Particle	Lead	Iron
Ionization by pions	23%(0.77)	35%(1.4)
Ionization by protons	35%(3.4)	37%(8)
Nuclear binding energy	30%	16%
Target recoil	3%	7%
Evaporation Neutrons	9%(31)	5%(5)

Table 1.2: Fractional energy loss due to different mechanisms in the non-em portion of a hadronic shower, and estimates of produced particle multiplicities per GeV (in brackets). This example is built around a 1300 MeV pion in lead and a 750 MeV pion in iron, and the pion ionization occurs before the spallation. Note that in addition to evaporation neutrons, approximately five cascade neutrons are produced in both materials [14]. Thus, the ratio of neutrons/protons is 10.6/1 (1.3/1) in lead (iron).

Knowing the different particles produced is essential as they can interact in different ways. Hard (high energy) particles from the cascade can trigger secondary spallations, while soft (low energy) charged particles will be absorbed through ionization. Soft neutrons can be absorbed in a variety of processes. In the eV to low MeV range the energy loss of neutrons is mainly due to scattering, and absorption occurs through neutron capture, where the particle excites a nucleus that in turn emits photons.

Table 1.2 provides an example of how energy is deposited in a hadronic shower. A distinction between the model used for table 1.2 and a more realistic shower is an overestimation of the contribution from ionization by pions. There are several pion-nucleon resonance production interactions, $\pi + N \to \pi + N$, that significantly decrease the mean free path of low energy pions [14], thereby reducing the energy loss by ionization.

Altogether, these nuclear interactions have two major effects on hadronic calorimetry. Firstly, the missing energy brings about a low response. Also, the fluctuations between events make for a very broad response (figure 1.10), which in turn means lower energy resolution. Secondly, λ_I being much larger than X_0 means that hadronic showers travel much further before complete absorption. The isotropic emission of evaporation products[4] and varied momentum transfers in the fast cascade make hadronic showers far broader as well, as seen in figure 1.9.

It should be noted that these hadronic effects are not the only contributions to missing energy. A small portion of the hadrons in these interactions decay weakly into muons and neutrinos. Muons are not well measured in the calorimeter, and their contributions must be accounted for by separate muon detectors. Meanwhile, neutrinos interact only very weakly and thus their energy is also not accounted for. Neutrino detection/measurement requires very large, specific detectors. Super Kamiokande, in Japan, has 55 kt of ultra-pure water

[4]Isotropic in the centre-of-mass frame of the nucleus. The evaporation particles are overall boosted in the direction of the initiating particle.

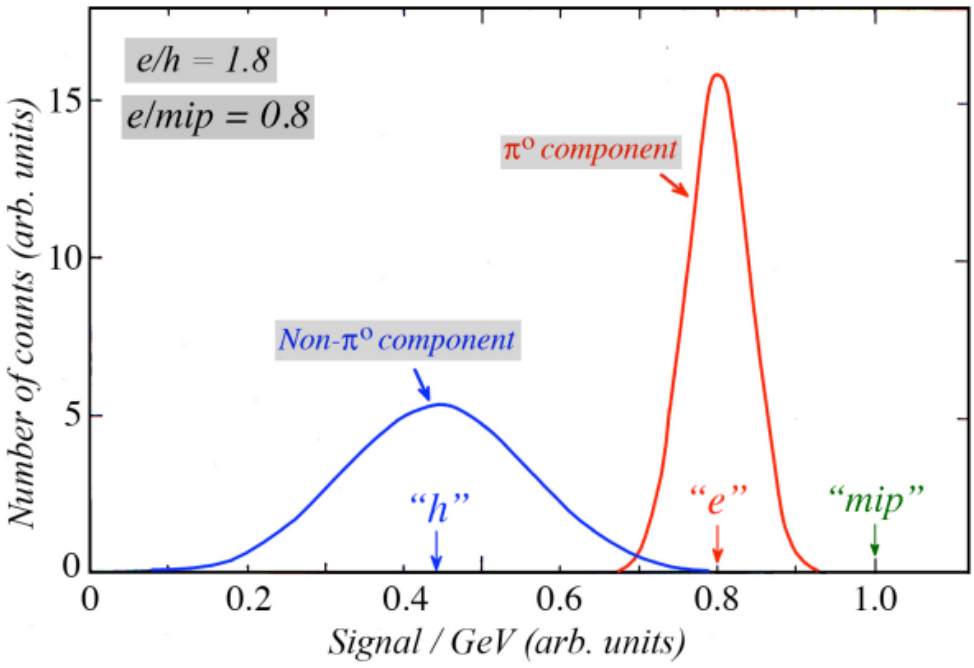

Figure 1.10: An illustration of the calorimeter response for different kinds of particles in a hadronic shower [22]. "mip" is a minimum ionizing particle, with the lowest possible energy loss per unit distance.

and uses phototubes to detect Cerenkov radiation from neutrino interactions [25]. Cerenkov radiation comes from the electrons produced in a neutrino-electron interaction. Detectors of this size are not feasible to use on top of already large accelerator/collider experiments such as ATLAS at CERN. Though not directly detected, neutrinos can be investigated at ATLAS through the missing transverse energy. Since the initial colliding particles have no net momentum transverse to the beamline, conservation of energy dictates that any offset from zero in the transverse energy measured by the detector must indicate invisible energy, such as from hadronic interactions or neutrinos.

To compare the difference in hadronic and electromagnetic responses, the response ratio e/h is used. This ratio is not directly measured and instead comes from the response of pions and the electromagnetic fraction as [19]:

$$\frac{e}{\pi} = \frac{e/h}{1 - \langle f_{em} \rangle (1 - e/h)} \tag{1.19}$$

For most calorimeters, the response ratio ranges from 1.5 to 2. However, in some specialized cases, hadronic calorimeters are designed in such a way that $e/h \approx 1$. These calorimeters are known as compensating, while the more common ones are under-compensating (calorimeters with a response ratio less than one would be overcompensating). Compensation can be achieved in sampling calorimeters through the use of hydrogenous sampling

material and a high Z absorber, with a precise sampling fraction [22]. This design boosts the signal collected from neutrons, as they deposit energy very efficiently by scattering off hydrogen nuclei.

The ATLAS calorimeters used in this thesis are all of the sampling type, and are described in detail in the next chapter. The hadronic calorimeter is non-compensating with a response ratio of $e/h = 1.36$.

Chapter 2

The LHC and ATLAS

2.1 The Large Hadron Collider

The Large Hadron Collider (LHC) is a pair of proton synchrotrons located in Switzerland and France. Using the tunnel of the earlier Large Electron-Positron collider, the LHC is the largest particle accelerator in the world. The LHC began operation in 2008 and recorded world-record 8 TeV collisions in 2010 before ramping up to 13 TeV in 2015. The LHC has the largest collision rate, or luminosity, of any collider experiment. Luminosity is the ratio of events detected per unit time to the cross section (the likelihood of a specific collision or event), and the integrated luminosity is simply the time integral of this. Femtobarnes (fb) are a measure of area equivalent to 10^{-43} m^2, thus fb^{-1} represents the number of collisions per fb. At 7 & 8 TeV in data collection Run 1 (2011,12), the LHC delivered 5.46 and 22.8 fb^{-1} of integrated luminosity [26]. During the 13 TeV Run 2 (2015-18), the total integrated luminosity delivered was 156 fb^{-1} [27]. Each fb^{-1} corresponds to about 100 trillion collisions, thus the LHC is delivering truly immense quantities of data.

A simple diagram of the LHC is provided in figure 2.1. Indeed, the LHC is just the last in a series of accelerators that take protons to record-breaking energies. The protons start in a linear accelerator before moving up through three smaller synchrotrons and finally enter the LHC. These smaller accelerators have two important roles: Supplying lower-energy particles to other experiments, and preparing bunches of protons and injecting them into the LHC. This second job involves focusing the proton beam and timing the injection to match the frequency of the LHC accelerating cavities.

Proton bunches are accelerated around the ring in two counter-rotating beamlines by electric fields, steered by giant dipole magnets, and focused by quadrupole magnets as well as sextupole, octupole and even decapoles. At different points along the ring, the two beamlines converge to collide the protons, and this is where the detectors are situated. Several experiments are working with LHC data, but the four main ones are ATLAS, CMS, ALICE, and LHCb. The ATLAS and CMS experiments are general-purpose, while ALICE focuses on heavy ion collisions (lead on lead and lead on proton, producing very high

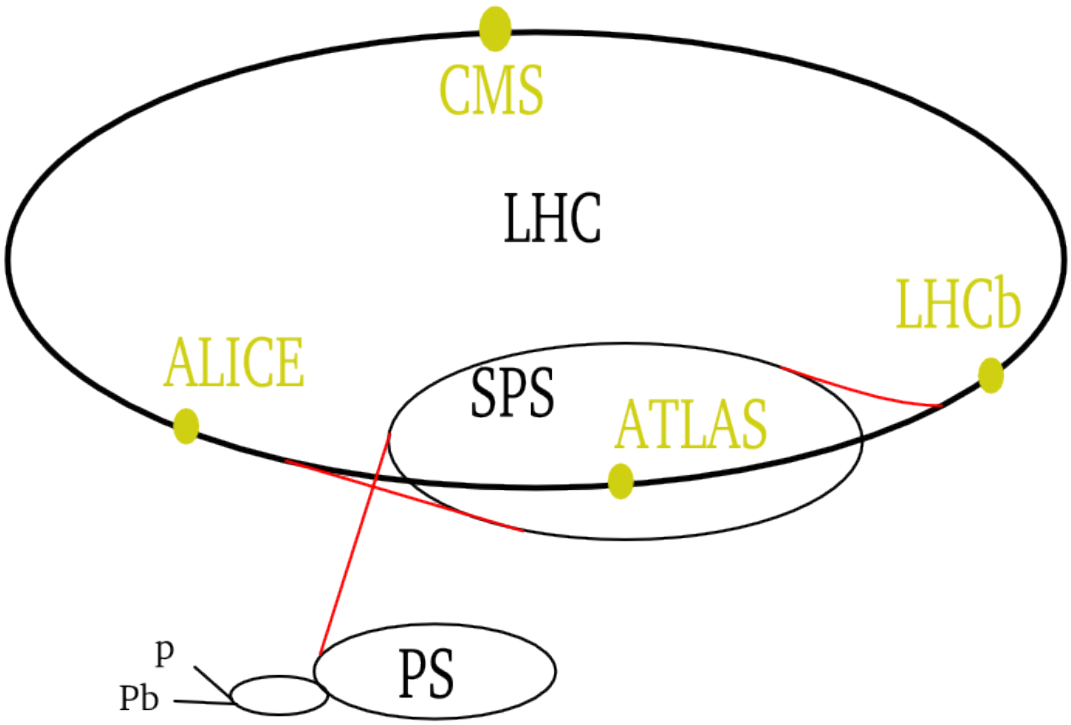

Figure 2.1: A simple view of the CERN accelerator complex, showing the major experiments at LHC crossing points. PS and SPS are the Proton Synchrotron and Super Proton Synchrotron, and the p/Pb labels indicate protons and lead ions, the two objects used in LHC collisions [28].

multiplicity final states) and LHCb targets B-hadron physics. In this thesis, the analyses are conducted using data from the ATLAS detector, which will be described in greater detail shortly. One of the main objectives of the LHC is to investigate the Higgs boson, and in 2012 both ATLAS [11] and CMS [12] reported the discovery of a new boson with a mass of 125 GeV that fits the properties of the Higgs particle. Subsequent measurements with improved precision have confirmed this identification. The LHC continues to serve on the cutting edge of particle physics.

2.2 ATLAS

The largest high energy physics experiment/detector at the LHC, and in the world, is ATLAS (**A** **T**oroidal **L**HC **A**pparatu**S**). ATLAS is the name of both the detector itself and the international collaboration of scientists conducting research with it. It consists of three main layers: Tracking detectors closest to the beamline, followed by calorimeters, and then the muon spectrometer on the outside. Each of these sections comprises numerous different detectors and focuses on specific measurements. Two large systems of magnets, solenoids and toroids, sit between the trackers and calorimeters and within the muon spectrometer, respectively. All these detector components are shown in figure 2.2.

Overall, the tracking detectors measure momentum and participate in the identification of charged particles. The calorimeters measure energy and assist with the identification of particle type, including neutral particles, which are not measured by the trackers. The outer spectrometer is specially focused on muon measurements. The following sections describe the functions of the detector systems in greater detail. In this thesis, the calorimeters are the most important, though the trackers and muon spectrometer play a valuable role as well.

It is important to discuss the ATLAS coordinate system before moving on. A right-handed system is defined with the x-axis pointing toward the center of the LHC ring, the y-axis pointing vertically upward, and the z-axis in the direction of the beam. ϕ is the azimuthal angle, measured around the beamline, and θ is the polar angle from the beamline (see figure 2.3). However, θ is not Lorentz invariant, and for this reason rapidity is defined as:

$$y = \frac{1}{2} ln \left(\frac{E + p_z}{E - p_z} \right) \tag{2.1}$$

Differences in rapidity are Lorentz invariant [1]. At high energies like those of the LHC, this can be reduced to the pseudorapidity, η, where

$$\eta = -ln \left(tan \left(\frac{\theta}{2} \right) \right) \tag{2.2}$$

and thus a Lorentz invariant angular distance between particles is described by ΔR:

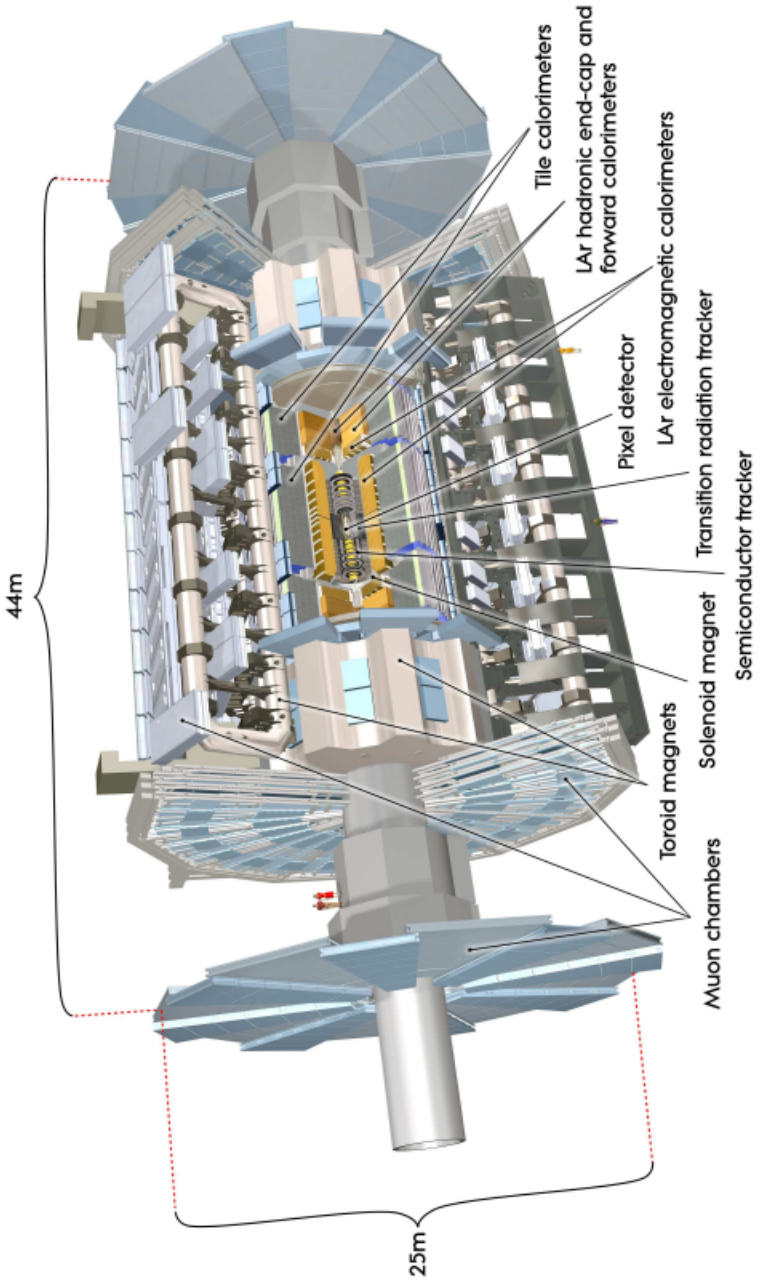

Figure 2.2: The ATLAS detector is the largest general-purpose particle detector ever built. The detector is 44m long, 25m in diameter, and weighs over 7000 tonnes [29]. Courtesy of the ATLAS Collaboration.

$$\Delta R = \sqrt{\Delta\eta^2 + \Delta\phi^2} \tag{2.3}$$

ΔR, η, and ϕ appear regularly in the following chapters. Additionally, the *transverse* momentum (p_T) is frequently discussed. This is the component of an object's (particle, jet) momentum in the x/y plane. This value is highly important as the sum of all transverse momentum before the collision is effectively zero, and thus it should remain zero after the collision. Any net transverse momentum recorded after the collision indicates something that was not measured, either a mismeasurement of known objects, an indication of neutrinos, or a sign of new physics.

2.2.1 Inner detector

Located inside a 2 T field created by the large solenoid magnet, the inner detector (ID) performs a number of critical functions in a tremendously high-density environment. Some 1000 particles must be tracked from the collision point every 25 ns [29], and this requires exceptional precision and granularity. The general measurement principle relies on the relationship between momentum, magnetic field, charge, and radius of curvature.

$$r = \frac{\gamma p}{qB} \tag{2.4}$$

γ is the Lorentz factor[1], as the particles are moving at relativistic speeds. In a controlled magnetic field, measuring the track of a particle can give momentum based on how tightly the track curves and the sign of its charge from the direction of the curve (via the right-hand rule).

There are three primary detectors used for the ID:

1. Pixel Detector: The closest section to the beamline, the Pixel Detector consists of four layers of extremely fine, doped silicon pixels. There are two major geometries in play, cylindrical and planar for the barrels and end-caps respectively[2], which ensure that charged particles within $|\eta| = 2.5$ are detected by at least three segments (Fig. 2.4). Before the start of Run 2, an additional pixel detector was added just 3 cm from the beam, known as the Insertable B-Layer (IBL). The IBL provides improved tracking and vertex (collision point) determination and also helps to protect the older pixel layers from radiation damage [31].

   The three original layers and the end-cap disks have a granularity of $50\times400\,\mu m^2$, while the IBL is even finer at $50\times250\,\mu m^2$. This allows for resolution on the order of

[1] $\gamma = \frac{1}{\sqrt{1-\beta^2}}$, where $\beta = v/c$.

[2] This is common to many detector components.

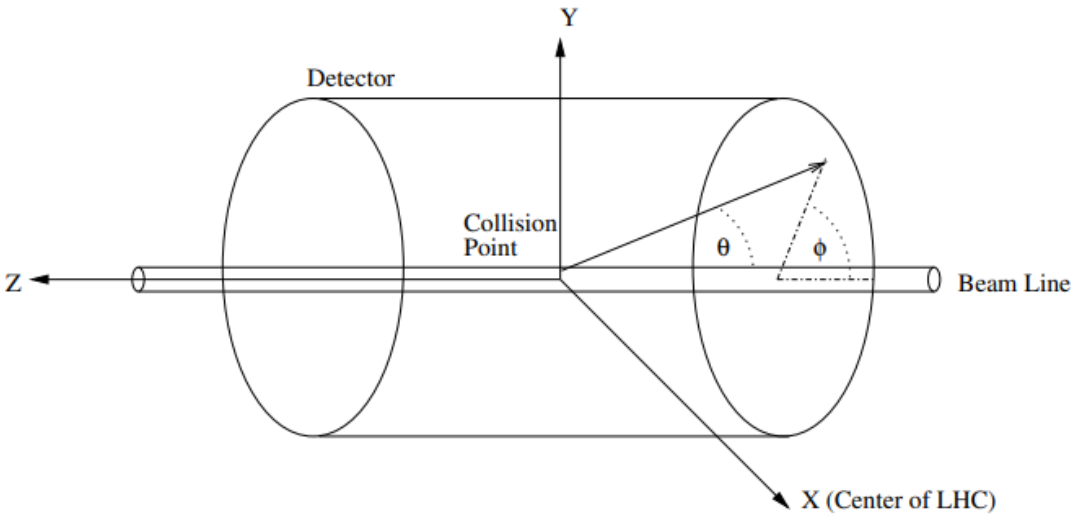

(a) ATLAS coordinates [30].

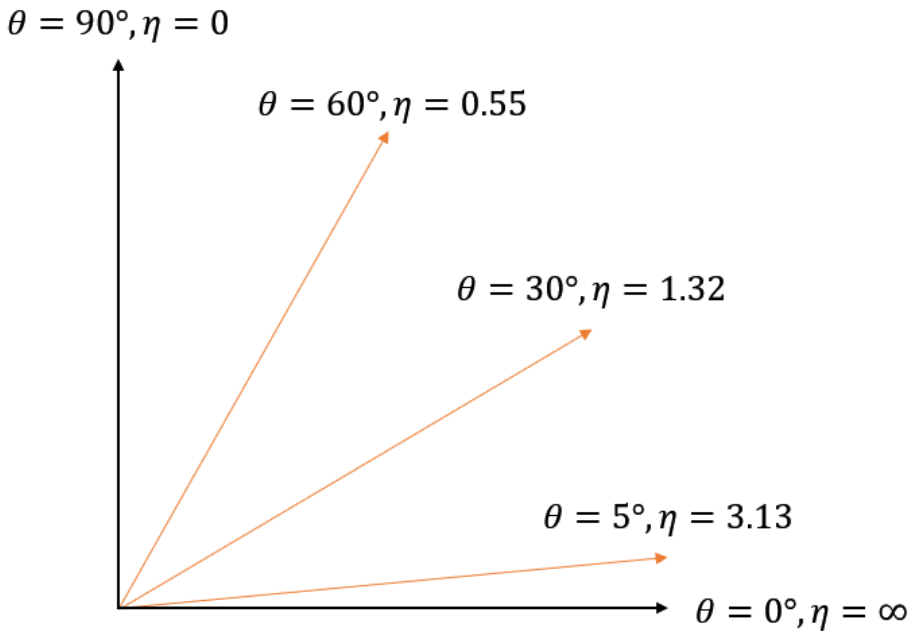

(b) Pseudorapidity

Figure 2.3: On top, an outline of the coordinate system of the ATLAS detector. The polar angle θ is replaced by the pseudorapidity, and the relationship between the two is displayed on the bottom.

10 µm (100 µm) in the $R-\phi$ (z) direction for the outer layers [29], and even better resolution for the IBL (table 2.1).

Charged particles traversing these silicon pixels create electron-hole pairs within the material. An electric potential is applied to the detector, which causes the charges to move towards p-n junctions for collection. In an average crossing, a charged particle will liberate $\mathcal{O}(10,000)$ electrons, and the electronic signal from the collected charge can be further amplified.

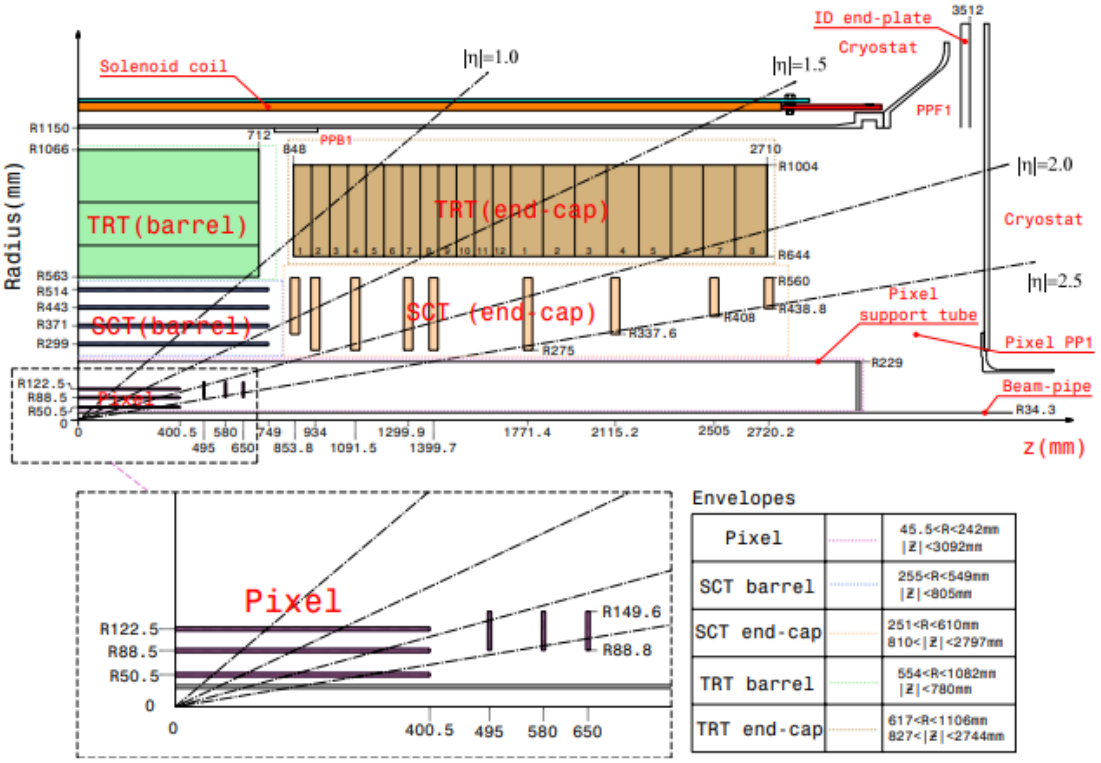

Figure 2.4: The geometry of the inner detector, before the addition of the IBL [29]. Courtesy of the ATLAS Collaboration.

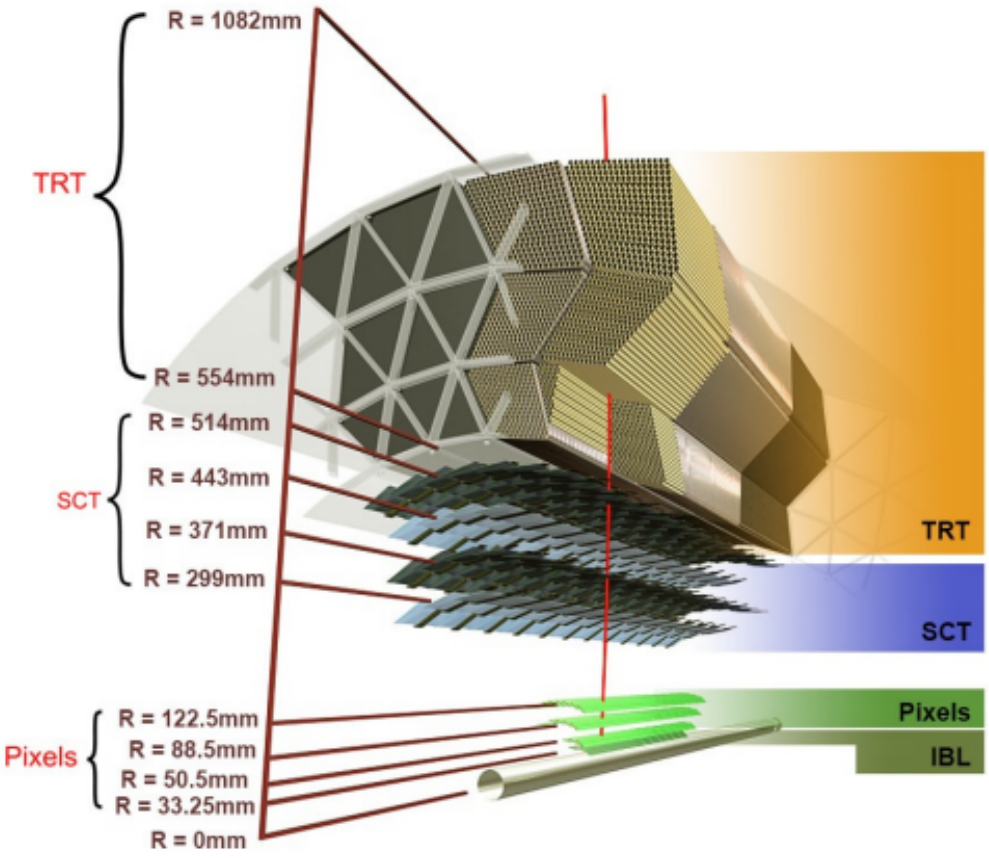

Figure 2.5: Cross section of the inner detector with the IBL included [31]. Courtesy of the ATLAS Collaboration.

2. Semiconductor Tracker (SCT): Following the Pixel Detector is another silicon-based instrument, the SCT. The SCT uses long strips of silicon in 4 barrels and 18 end-caps. The strips have an 80 µm pitch and run in the direction of the beamline. In both the barrels and end-caps, each layer has two sets of strips; one parallel to the beamline, and another at a 40 mrad stereo angle. This allows for the measurement of both $R - \phi$ and z coordinates. The resolution for $R - \phi$ is still very good here, while the z resolution is about five times worse than the Pixel Detector. The resolution and pseudorapidity coverage for the inner detector components are summarized in table 2.1. As another silicon detector, the signal development process of the SCT is similar to that of the Pixel Detector.

3. Transition Radiation Tracker (TRT): The TRT is the largest and outermost module of the tracking detectors. Here, due to cost reasons and silicon's inefficiency in detecting X-rays, the silicon technology of the other inner detector systems is replaced by drift-

System	Geometry	Resolution ($R-\phi \times z$)	Channels (10^6)	$\lvert\eta\rvert$ Coverage
Pixels	IBL	8×40 µm	12	2.5
	Barrels	10×115 µm	97	1.7
	End-Caps	10×115 µm	43	1.7-2.5
SCT	Barrels	17×570 µm	3.2	1.4
	End-Caps	17×570 µm	3.0	1.4-2.5
TRT	Barrels	130 µm	0.1	0.7
	End-Caps	130 µm	0.32	0.7-2.5

Table 2.1: The inner detector provides excellent spatial resolution, allowing for precise momentum calculation and vertexing [33, 34].

tube straws. The straws are 4 mm in diameter with 35 µm walls made principally of polyimide acting as a cathode. The anode is a tungsten wire with gold plating running down the center of each tube, and the tubes are filled with a gas mixture of 70% Xe, 27% CO_2 and 3% O_2. Some 50,000 straws are aligned in the direction of the beam in the barrel segment, and 250,000 sit perpendicular to the beam in the end-caps [32]. This layout allows for fairly precise $R-\phi$ resolution (table 2.1), and each particle passes through at least 35 straws, providing for excellent tracking. However, the TRT does not measure in the z-direction.

Particles ionize the gas while passing through the tubes, and the resulting electrons and ions will drift to the anode (wire) and cathode (walls) under an applied potential (as exists in the detector). The drift time of the electrons/ions provides a spatial measurement when combined with the drift velocity, a known property of the gas mixture. In addition to tracking, the TRT assists in particle identification by way of its namesake, transition radiation. The electric field of a charged particle is altered by moving between materials with different dielectric constants, and the changing field produces electromagnetic radiation [15]. Transition radiation is typically emitted as X-rays, and is proportional to the Lorentz factor γ: highly relativistic particles produce more transition radiation. This allows for discrimination between lighter and heavier particles, particularly electrons versus hadrons [32].

2.2.2 Calorimeters

The ATLAS calorimeters provide nearly hermetic (4π) coverage around the interaction point and perform a destructive energy measurement. That is, the vast majority of particles resulting from a proton-proton collision are absorbed in this detector. The calorimeter setup is shown in figure 2.6, where five primary systems are seen: Electromagnetic and hadronic barrels and end-caps as well as the forward calorimeter. All of these detectors are *sampling* calorimeters, meaning that shower development and energy measurement are conducted by different materials/layers. The electromagnetic calorimeters use liquid argon (LAr) for

measurement, with lead for the passive layers of the barrel and end-caps. The hadronic end-caps and forward calorimeter also use LAr for measurement, but with copper and copper-tungsten for the passive materials, respectively. The hadronic barrel has plastic scintillator tiles for energy sampling and iron for shower development [35].

The LAr calorimeters are situated in three cryostats which maintain a temperature of 87K [36]; one for the barrel and two on the ends for the hadronic and electromagnetic end-caps as well as the forward calorimeters. Liquid argon was selected as the sampling material for its resiliency (it has high radiation hardness and maintains a steady response) and cost effectiveness [36, 29].

Essential to the design of the LAr calorimeters is the aforementioned 4π coverage, part of which is provided by an accordion geometry in the electromagnetic barrel and end-caps [29]. Layers of absorbing lead are nested in a zig-zag pattern with Kapton-gold electrodes, all of which are immersed in the liquid argon. This design allows for perfect azimuthal coverage, and no gaps exist in the electromagnetic LAr calorimeters around the $|\phi|$ direction. The different calorimeter components also cover all the way to $|\eta| = 4.9$, less than a degree from the beamline.

Hermiticity is important in obtaining the best measure of the *missing transverse energy*, or MET. Earlier in this chapter the coordinates and units of the ATLAS detector were discussed, including the transverse momentum, which should sum to zero if all the particles from the proton-proton collision are accounted for. The offset of this sum from zero is the MET, which can be caused by several processes including the invisible energy in hadronic showers and undetected particles such as neutrinos. MET beyond these causes can be indicative of new physics, thus it is essential that the calorimeter provide an accurate measure of this quantity.

In addition to the components already mentioned, there is a presampler layer positioned between the LAr barrel and the preceding materials. The goal of this layer is to adjust for the energy losses of particles in the inner detector and cryostat walls [35].

The different calorimeter components have multiple layers, segmented by changes in granularity. The granularity, layers, and η coverage of the different calorimeters are presented in table 2.2. In this thesis, the data used are restricted to the barrel, and figure 2.7 displays many of the features of the LAr electromagnetic calorimeter in this region. The fine strips of the first layer (denoted layer 1, layer 0 is the presampler) provide an accurate η measurement and valuable particle identification information [35], while the thick middle layer performs the bulk of the absorption and the third layer tempers the leakage of energy (punch-through).

Angular coverage is one of two major aspects of ensuring total absorption, the other being thickness. The interactions of particles in a calorimeter were discussed in section 1.2, and it was shown that depending on the properties of the material and the energy/type of the particles certain thicknesses of material are required to contain the showers. The ATLAS

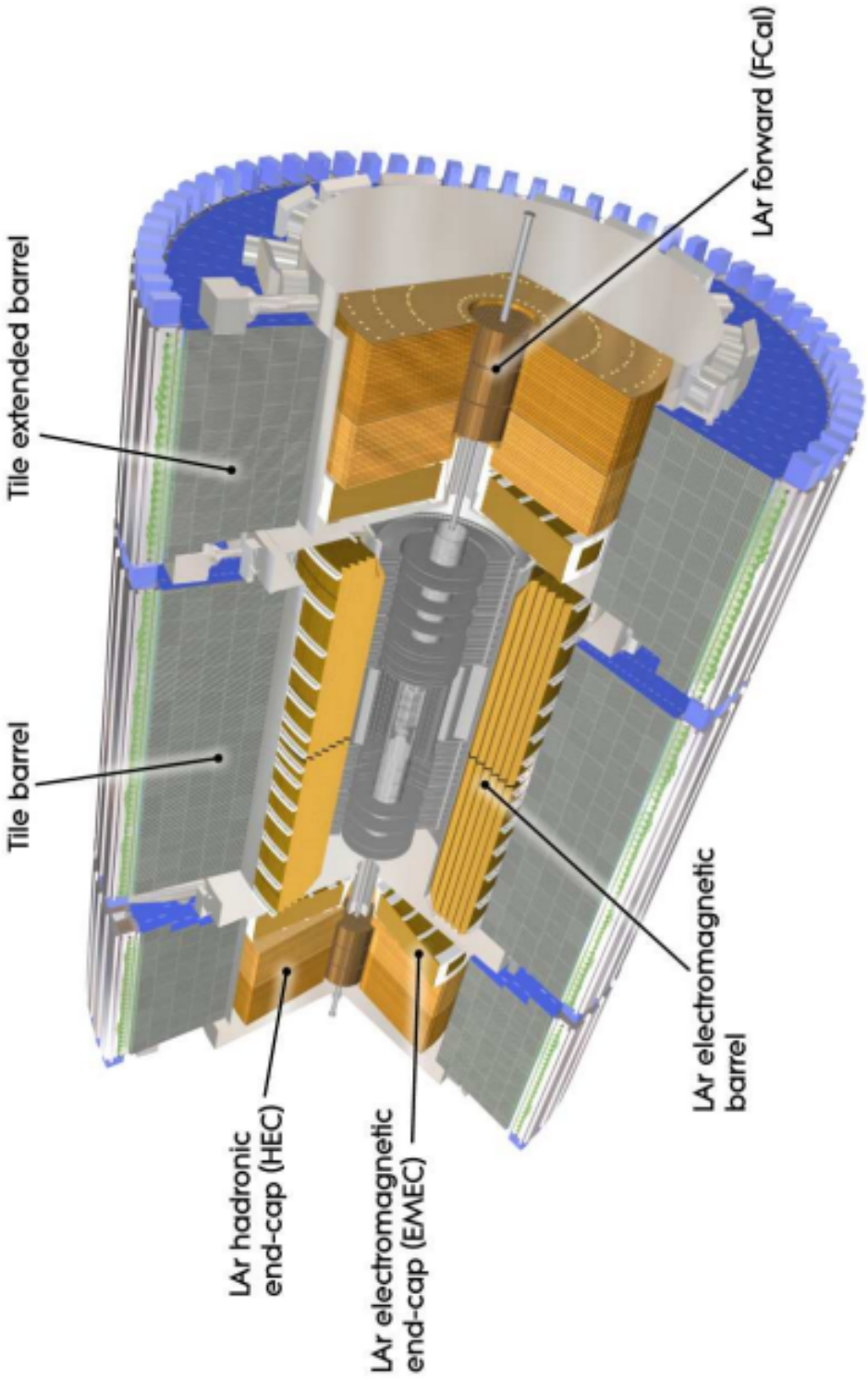

Figure 2.6: Layout of the ATLAS calorimeters [29]. Courtesy of the ATLAS Collaboration.

calorimeters are highly effective in absorbing the showers from high energy particles [29, 35]. The LAr barrel is over 22 radiation lengths thick, and the end-caps are more than 24. In the tile calorimeter, where it is more appropriate to discuss interaction lengths, the thickness exceeds 10 λ. These massive quantities of material ensure nearly complete absorption, which provides a high-resolution energy measurement, important for studies of jets and missing transverse energy.

In the LAr calorimeters, signals are produced through the ionization of Argon. The charges are collected on electrodes (gathered there by a potential difference applied over the calorimeter), similar to the various signal collection processes in the inner detector. In the tile calorimeter, the process is different. Here, plastic tiles produce scintillation light that is later converted to an electric signal by photomultiplier tubes. Charged particles passing through the scintillator tiles excite atoms, which in turn emit photons when returning to their ground state [15]. This radiation is transported by wavelength-shifting fibers to photomultipliers where it is changed into a readable signal.

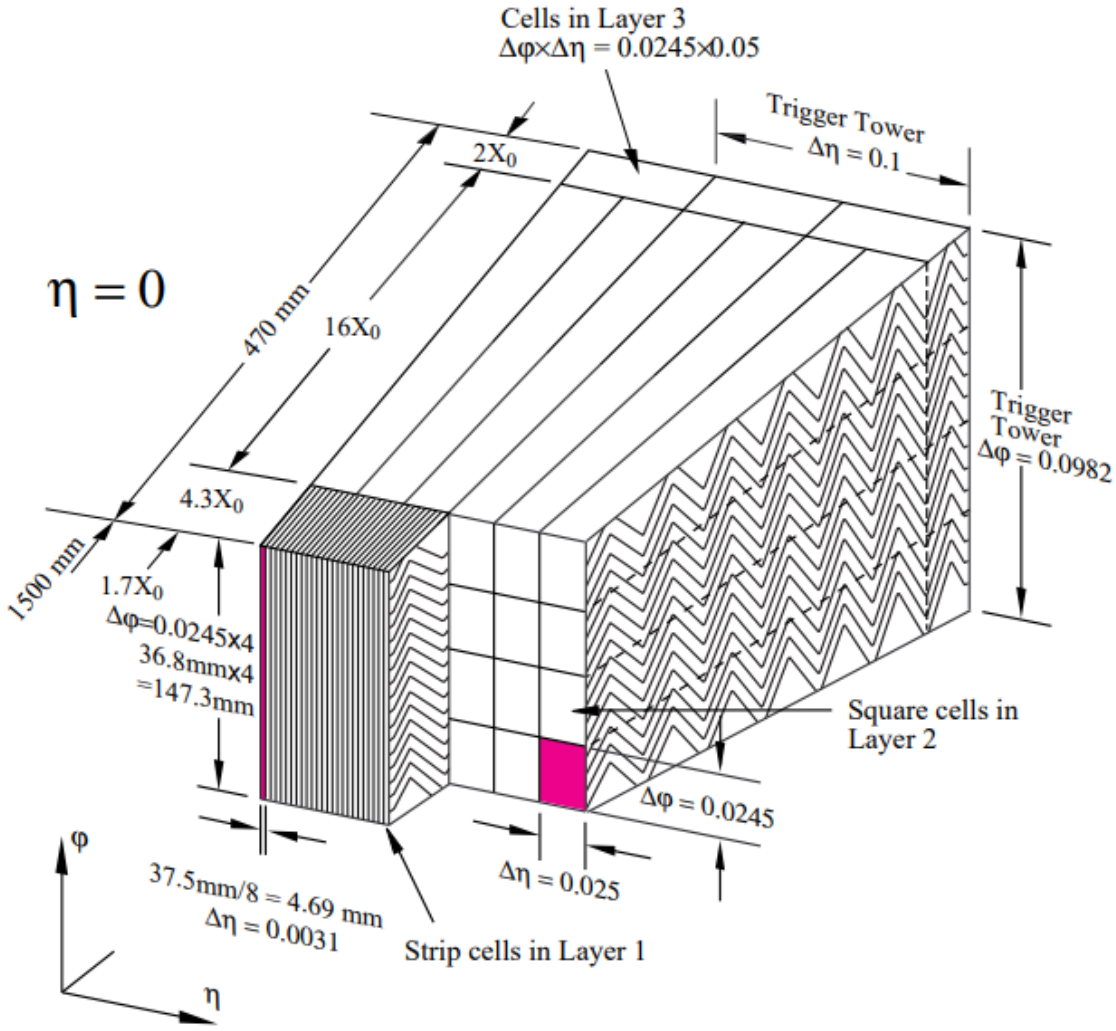

Figure 2.7: A cutout of the LAr barrel, displaying the accordion geometry, layers, and granularity [29]. Courtesy of the ATLAS Collaboration.

	Barrel		End-cap	
EM calorimeter				
Number of layers and $\|\eta\|$ coverage				
Presampler	1	$\|\eta\| < 1.52$	1	$1.5 < \|\eta\| < 1.8$
Calorimeter	3	$\|\eta\| < 1.35$	2	$1.375 < \|\eta\| < 1.5$
	2	$1.35 < \|\eta\| < 1.475$	3	$1.5 < \|\eta\| < 2.5$
			2	$2.5 < \|\eta\| < 3.2$
Granularity $\Delta\eta \times \Delta\phi$ versus $\|\eta\|$				
Presampler	0.025×0.1	$\|\eta\| < 1.52$	0.025×0.1	$1.5 < \|\eta\| < 1.8$
Calorimeter 1st layer	$0.025/8 \times 0.1$	$\|\eta\| < 1.40$	0.050×0.1	$1.375 < \|\eta\| < 1.425$
	0.025×0.025	$1.40 < \|\eta\| < 1.475$	0.025×0.1	$1.425 < \|\eta\| < 1.5$
			$0.025/8 \times 0.1$	$1.5 < \|\eta\| < 1.8$
			$0.025/6 \times 0.1$	$1.8 < \|\eta\| < 2.0$
			$0.025/4 \times 0.1$	$2.0 < \|\eta\| < 2.4$
			0.025×0.1	$2.4 < \|\eta\| < 2.5$
			0.1×0.1	$2.5 < \|\eta\| < 3.2$
Calorimeter 2nd layer	0.025×0.025	$\|\eta\| < 1.40$	0.050×0.025	$1.375 < \|\eta\| < 1.425$
	0.075×0.025	$1.40 < \|\eta\| < 1.475$	0.025×0.025	$1.425 < \|\eta\| < 2.5$
			0.1×0.1	$2.5 < \|\eta\| < 3.2$
Calorimeter 3rd layer	0.050×0.025	$\|\eta\| < 1.35$	0.050×0.025	$1.5 < \|\eta\| < 2.5$
Number of readout channels				
Presampler	7808		1536 (both sides)	
Calorimeter	101760		62208 (both sides)	
LAr hadronic end-cap				
$\|\eta\|$ coverage			$1.5 < \|\eta\| < 3.2$	
Number of layers			4	
Granularity $\Delta\eta \times \Delta\phi$			0.1×0.1	$1.5 < \|\eta\| < 2.5$
			0.2×0.2	$2.5 < \|\eta\| < 3.2$
Readout channels			5632 (both sides)	
LAr forward calorimeter				
$\|\eta\|$ coverage			$3.1 < \|\eta\| < 4.9$	
Number of layers			3	
Granularity $\Delta x \times \Delta y$ (cm)			FCal1: 3.0×2.6	$3.15 < \|\eta\| < 4.30$
			FCal1: $\sim$ four times finer	$3.10 < \|\eta\| < 3.15$,
				$4.30 < \|\eta\| < 4.83$
			FCal2: 3.3×4.2	$3.24 < \|\eta\| < 4.50$
			FCal2: $\sim$ four times finer	$3.20 < \|\eta\| < 3.24$,
				$4.50 < \|\eta\| < 4.81$
			FCal3: 5.4×4.7	$3.32 < \|\eta\| < 4.60$
			FCal3: $\sim$ four times finer	$3.29 < \|\eta\| < 3.32$,
				$4.60 < \|\eta\| < 4.75$
Readout channels			3524 (both sides)	
Scintillator tile calorimeter				
	Barrel		Extended barrel	
$\|\eta\|$ coverage	$\|\eta\| < 1.0$		$0.8 < \|\eta\| < 1.7$	
Number of layers	3		3	
Granularity $\Delta\eta \times \Delta\phi$	0.1×0.1		0.1×0.1	
Last layer	0.2×0.1		0.2×0.1	
Readout channels	5760		4092 (both sides)	

Table 2.2: Properties of the ATLAS calorimeter systems [29]. Courtesy of the ATLAS Collaboration.

2.2.3 Muon Spectrometer

At the high energies of the ATLAS experiment, muons behave as minimum ionizing particles. This means that muons lose only a small fraction of their energy through electromagnetic processes, and travel largely unperturbed through the calorimeters. Thus, a dedicated detection system is required to perform momentum measurements on muons.

Overall, the muon spectrometer is similar to the inner detector in that it is a tracking detector conducting non-destructive measurements. While the inner detector curved particle tracks with solenoid magnets, the muon spectrometer uses massive air-core toroids, in a barrel/end-cap layout. The barrel toroid covers $0 < |\eta| < 1.4$, and the end-caps cover $1.6 < |\eta| < 2.7$. The gap between the magnets is covered by overlap from both, albeit with a lower magnetic field [29]. The muon spectrometer also requires an independent trigger system.

Four detector systems are used in the muon spectrometer, two of which are focused on tracking while the others are mainly for triggering. The resolutions and layouts of these components are shown in table 2.3. For tracking, most of the detection is handled by monitored drift tubes (MDT), in the range of $|\eta| < 2.7$ for the outer regions. Tracking in the inner end-cap region ($2.0 < |\eta| < 2.7$) is conducted by cathode strip chambers (CSC), as they are better suited for the higher particle flux closer to the beamline. The p_T resolution is better than 4% for most momentum ranges, climbing to 11% at 1 TeV [37].

Resistive plate chambers (RPC) and thin gap chambers (TGC) perform the triggering function in the barrel region ($|\eta| < 1.05$) and end-caps ($1.05 < |\eta| < 2.4$)[3], respectively. Subsequent hits on multiple layers of these systems provide the first-level trigger. Additionally, these chambers assist in tracking by providing a measurement in the non-bending direction of the magnet [37]. For these detectors, speed is more important than resolution, as triggering is completed in time frames on the order of microseconds.

Signal generation in the muon spectrometer follows the same process, ionization and charge collection, as the LAr calorimeters and the inner detector. In the monitored drift tubes, electrons from the ionization of gas are collected on a positively charged central wire. The CSCs are multi-wire proportional chambers [15], similar to the MDTs but with multiple wires in each chamber, perpendicular to cathode strips. One set of cathode strips is oriented in the ϕ direction and another in the η direction to allow for determination of the muons' $\eta - \phi$ position. Charge is collected on cathode readout strips for electronic signal generation.

The RPCs do not have wires, instead using two parallel charged plates surrounding an active gas. The signalling is again a product of ionization, with electrons collected on the charged plates. The TGCs have wires between the plates, much like the CSCs, and collect both electrons and ions to produce a signal.

[3]The triggering extends to $|\eta| = 2.4$, but the tracking aspect of the TGC continues out to 2.7

		Chamber resolution (RMS) in			Measurements/track		Number of	
Type	**Function**	z/R	ϕ	time	barrel	end-cap	chambers	channels
MDT	tracking	35 μm (z)	—	—	20	20	1088 (1150)	339k (354k)
CSC	tracking	40 μm (R)	5 mm	7 ns	—	4	32	30.7k
RPC	trigger	10 mm (z)	10 mm	1.5 ns	6	—	544 (606)	359k (373k)
TGC	trigger	2–6 mm (R)	3–7 mm	4 ns	—	9	3588	318k

Table 2.3: Coverages, channel counts, and functions of the four types of detectors in the Muon Spectrometer [29]. Courtesy of the ATLAS Collaboration.

2.2.4 Triggering and Data

Triggers

In Run 2, proton bunches in the LHC were separated by 25 ns, resulting in a beam-crossing rate of 40 MHz at ATLAS with roughly 20 events per crossing. Even after inactive portions of the detector are removed (where no particles travelled during a given event), each event takes up roughly 1.6 MB of digital storage. Altogether, the total data output in the detector is more than 60 TB each second [38]. This would be a major issue if all the data were of equal importance, but the majority of these events are not interesting in a high energy physics experiment. For example, many of the events are elastic proton collisions with no interaction between the constituent quarks and gluons.

The ATLAS triggering system provides high-speed event filtering, significantly reducing the amount of data to be processed and stored while recording rare events with interesting properties, such as high MET. There are two sequential triggers, Level 1 (L1) and the High-Level Trigger (HLT). The L1 trigger uses custom electronic hardware to reduce the data rate to 100 kHz, deciding to keep or discard each event in just 2.5 µs [29]. The HLT is implemented through software, using some 40,000 dedicated computer cores located near the experiment to reduce the data rate further to roughly 1 kHz.

L1 uses three trigger sub-systems: Two of the sub-systems process signals from the calorimeter (L1Calo) and muon spectrometer (L1Muon) with a coarser granularity than the full event reconstruction. The third sub-system (L1Topo) uses the previous two to analyze the overall event topology. L1Calo looks for events with large MET or high jet multiplicities, or specific energy deposits in the electromagnetic versus hadronic calorimeter, to trigger certain events. Meanwhile, L1Muon looks for high energy muons or high muon multiplicities. L1Topo calculates properties such as the angular separation or invariant mass of objects from L1Calo and L1Muon [39]. The outputs of these are combined in the central trigger processor (CTP) which makes the final decision. The CTP selects events by comparing the results of the L1 triggers to a trigger menu, a list of event properties that are of interest to physicists. Different trigger menus are used to select events based on jets, electrons, and other objects.

The L1 trigger also uses this information to define regions of interest, areas in the detector where important physics phenomena occur for a given collision event. These regions of interest are passed to the HLT for further inspection [29].

The HLT is a software trigger, which selects or rejects events in a time of 200 µs. The HLT only looks at the regions of interest passed on from L1, but it does so at full granularity and with tracking information from the inner detector. Specific trigger options can be implemented by data analyzers, to check events for certain properties. For example, this thesis makes use of HLT_jX triggers, which pass events with jets above some X= p_T threshold. Similar triggers exist for other particles as well, and provide event rejection/acceptance for the analysis of electrons, photons, and muons. Events that pass the HLT are recorded on magnetic tape at the CERN data centre, with a second copy distributed worldwide on the computing grid (see below).

The Grid

Lastly, a word on the distributed grid computing system used by CERN experiments. Despite the triggers' effectiveness in reducing the number of events stored, the ATLAS datasets from Run 2 of the LHC remain very large. Running analysis code locally over such a dataset, even with a very powerful machine, would be inefficient.

The grid computing system stores and analyses data from the ATLAS experiment in three tiers. The CERN data centre, known as tier-0, stores the raw data from the detector and trigger system and performs initial analysis and reconstruction [40]. A second copy of the data is split up and sent via high bandwidth fibre-optic cable to 10 tier-1 computing centres spread around the world, which provide a backup of the data stored at CERN. The tier-1 centres also reprocess the data, with improvements regarding detector performance/properties, and produce simulated data. Finally, there are more than 160 tier-2 centres worldwide, typically at universities and other large research facilities (the tier-2 centres are not used exclusively by CERN). These provide much of the computing power of the grid for data analyzers, and each conducts a proportional share of user analysis and data simulation. The tier-1 centres also store simulated data from the tier-2 sites.

A user need only submit their analysis code to the grid, which will locate the requested datasets and allocate available computing resources. The grid has access to roughly 1.4 million computing cores in more than 40 countries, a testament to the international nature of the ATLAS collaboration.

Chapter 3

Jet Physics

Jets are the most commonly produced physics objects in proton-proton collisions, and because of this it is essential that they are well understood. In section 1.1 the idea of colour confinement was introduced; that all naturally existing/observable particles must be colour neutral. This means that particles with net colour charge such as quarks and gluons cannot be studied directly, and instead physicists must use the remnants of these particles that are seen in the detector. The quarks and gluons produced in a proton-proton collision are nearly instantly transformed into jets, collimated sprays of particles that represent the properties of the initiating parton due to conservation of 4-momentum.

The process by which a parton becomes a jet is known as fragmentation, which has two steps. First is the parton shower, where high energy quarks and gluons iteratively separate into more, lower energy partons. Quarks radiate gluons, and gluons split into $q\bar{q}$ pairs. These processes continue until the energy of the partons is low enough that they can recombine to form heavier, colour-neutral particles. This is the second half of fragmentation, known as hadronization. These hadrons are then measured in the detector, giving a representation of the individual initial parton.

Due to the nature of α_s, the parton shower can be treated perturbatively and calculated accurately. The lower energy hadronization process however is non-perturbative and must be handled by models. Monte Carlo simulations (MC) have both a perturbative parton shower component and a hadronization model.

3.1 Reconstruction

Jets [41] can be reconstructed using the calorimeter alone or with additional inputs from the tracking detectors. Jets that include the tracking detectors are known as PFlow jets (particle flow), while those with only calorimeter inputs are known as EMTopo, for topological clusters. This thesis makes use of EMTopo jets.

Topological clusters are constructed from groups of cells in the calorimeter, using the 4/2/0 algorithm [42]. For this technique, the ratio of signal collected to the background

noise of a cell is used to determine signal significance. The background is a combination of electronic noise and pileup, additional interactions that occur within the time the detector is measuring an event of interest. If a cell is determined to have at least a 4σ signal-to-noise ratio, it is used as the seed of a proto-cluster. Then, any adjacent cells with greater than 2σ signal are added to the proto-cluster. This repeats iteratively until there are no further 2σ cells in contact with what has thus far been used. Finally, a layer around the 2σ cells is made from any cells with greater than 0σ. The name, of course, represents the signal-to-noise ratios used: 4/2/0.

This algorithm is utilized at the electromagnetic scale, and thus the clusters are known as EMTopo clusters. Another clustering technique known as LCTopo (Local Calibration) compensates for the energy loss of hadrons. LCTopo is no longer used at ATLAS for primary jet reconstruction.

The proto-clusters built thus far may represent multiple particles, and to remedy this a system of cluster splitting is used. Cluster splitting looks for proto-clusters with two or more local maxima, defined as cells with energy greater than 500 MeV and at least four neighbours with lower energy. Within a proto-cluster, the splitting algorithm builds sub-clusters surrounding the signal maxima. Cells that lie on the border between two of these new clusters have their energy divided up, with portions going to each new cluster depending on the clusters' relative energy and position. The splitting algorithm ensures that each reconstructed cluster represents just a single particle, which allows for a better reconstruction of the energy flow from a collision event. This is important for accurate calculation of the MET and jet finding.

Jets are constructed using these clusters, and the algorithm used to combine the clusters must meet several important conditions [43]. Among these requirements is infrared and collinear safety; that is, soft and collinear radiation must not impact the jet reconstruction (figure 3.1). The number of jets reconstructed, and their respective topology, should not depend on soft particles radiated by the candidate particles (used to build clusters) or any splitting of the candidate particles.

Additional requirements include invariance under Lorentz boosts, boundary stability (the kinematic variables describing the jet must be insensitive to the final state), and order independence: The same jet must be reconstructed at particle and calorimeter levels (see below). There are further practical requirements regarding ease of implementation and computational intensity of the algorithm.

Particle level means the jet is reconstructed using the particles emerging from the collision as inputs, without the effects of the detector. Calorimeter level includes the detector effects, such as missing transverse energy, electronic noise, and the particles' propagation through the spectrometer. Particle level is inherently unreachable in data, but can be modeled well in MC. Before particle level is parton level, where the original quarks and gluons

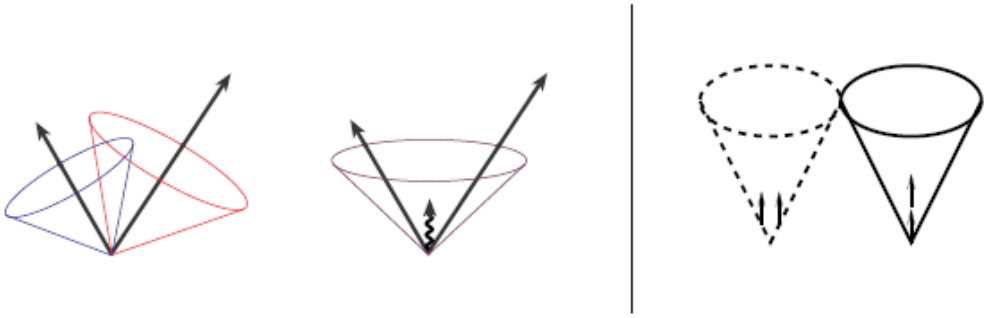

Figure 3.1: Left: A soft particle emitted between two candidate jets causes them to be combined in an algorithm that is not infrared safe. Right: Without collinear safety, a jet algorithm could fail to construct a jet when the energy is split among multiple sources [43].

that become jets are considered. Parton level is also unavailable in data and must be studied in simulations.

Cone algorithms were historically a popular method of jet reconstruction. These work by selecting a seed, such as a topo cluster, and building a jet from all inputs that lie within a specific ΔR in $\eta - \phi$ space [43]. However, cone algorithms are often collinear or infrared unsafe, so ATLAS uses a more advanced algorithm known as Anti-k_t [44].

The Anti-k_t algorithm is a recursive recombination algorithm that depends primarily on two parameters:

$$d_{ij} = min(k_{ti}^{2p}, k_{tj}^{2p}) \frac{\Delta_{ij}^2}{R^2}, \tag{3.1}$$

$$d_{iB} = k_{ti}^{2p} \tag{3.2}$$

Where d_{ij} and d_{iB} are the distances between proto-jets i and j (the inputs to the jet algorithm, e.g. EMTopo clusters) and between i and the beam, $\Delta_{ij}^2 = (y_i - y_j)^2 + (\phi_i - \phi_j)^2$, k_t is the transverse momentum, and y and ϕ are the rapidity and azimuthal angle.

For the anti-k_t algorithm, $p = -1$. $p = 1$ and $p = 0$ are two additional algorithms, k_t and Cambridge/Aachen, respectively.

The anti-k_t algorithm begins by making a list of all proto-jets and calculates the distance between each pair of proto-jets, as well as the distance between each proto-jet and the beamline. The algorithm looks for the smallest distance parameter; if it is a d_{iB}, then proto-jet i is defined as a jet, and it is removed from the list of all proto-jets. If the smallest distance parameter is between two proto-jets, d_{ij}, then i and j are combined, by adding their four-momenta, as a single proto-jet. Since the two-proto-jet distance parameters depend on the *inverse* of the transverse momentum, the algorithm starts by combining hard clusters rather than soft ones. The result of this is often jets that appear highly conical, albeit from a theoretically more robust algorithm.

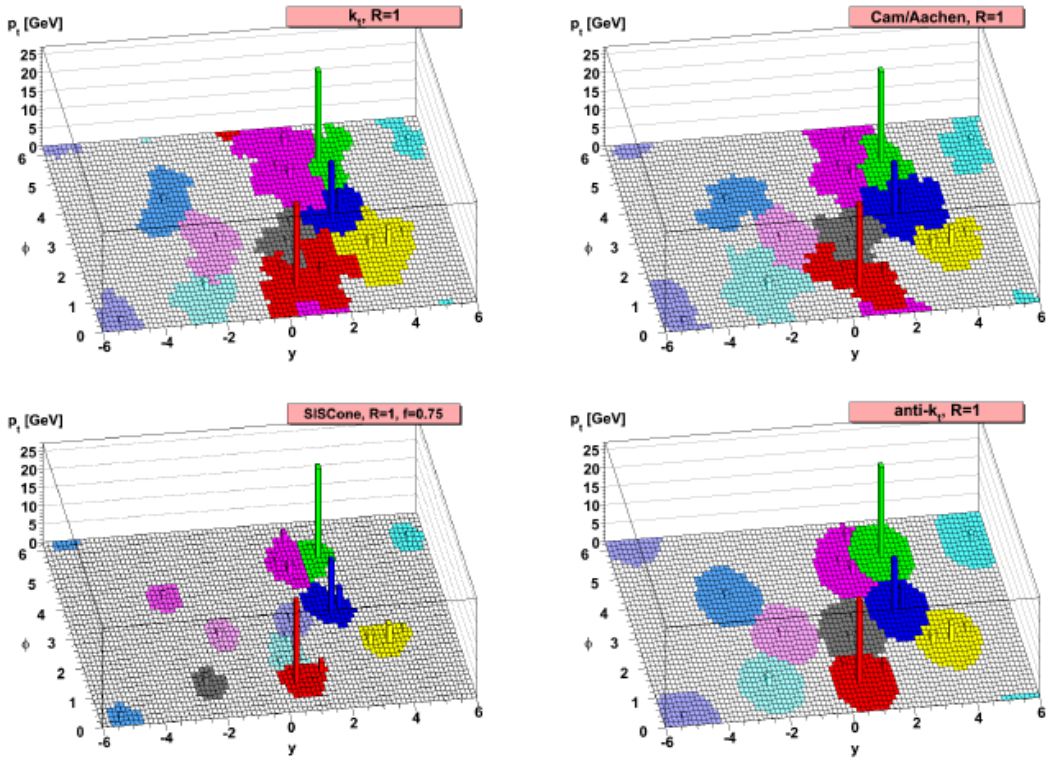

Figure 3.2: Comparison of different jet finding algorithms. The anti-kt algorithm, at the bottom right, creates the most uniform jet shapes. This example was produced with HERWIG and represents a single parton-level event [45, 44]. Only SISCone, at bottom left, is not a recursive recombination algorithm. SISCone is a seedless algorithm and is infrared safe [46].

Similarly to the construction of clusters, there is a method for splitting the jets, determined by the parameter R. R defines the radius of the jet, and if there is only one hard proto-jet within a distance of $2R$, a single jet is built. If there is another hard proto-jet within $2R$ but outside R, the proto-jet with significantly higher transverse momentum will be built as the first jet, and a second jet will be built with some overlapping section cut out. In the case where the two proto-jets have similar transverse momenta, they are divided almost equally. Finally, if the proto-jets are within R, they are combined into a single object. These properties can be seen in figure 3.2, where the anti-k_t algorithm is compared to other jet finding methods.

Since soft inputs will be included in a jet built around a hard input without altering its shape, the algorithm is infrared safe. Additionally, the splitting/sharing/combining determined by R makes the algorithm collinear safe. The anti-k_t algorithm meets all the requirements desired of a jet algorithm and is the primary jet reconstruction method used

by ATLAS. The k_t and Cambridge/Aachen algorithms are also used by ATLAS, in studies of jet sub-structure or large-radius jets [45, 47].

This thesis makes use of anti-k_t jets with $R = 0.4$, constructed from topological clusters.

3.2 Calibration/Jet Energy Scale

In accelerator/collider experiments, the accelerated objects will in general possess momentum along only a single axis, in line with the particle beam[1]. Therefore, after a collision has occurred, the vector sum of all p_T in the event should equal zero, due to momentum conservation. In the previous sections the MET was introduced; the offset from zero of the measured p_T. Several factors contribute to the missing energy, including the production of neutrinos or non-interacting new particles. The most common cause though is the invisible energy of hadronic showers (section 1.2.2), fundamentally undetectable energy lost to the nuclear interactions of hadrons in the calorimeter.

Jets produced in the ATLAS experiment result in large numbers of hadrons, and this means that a portion of the jet's particle level energy is not measured. While this effect is largest for low-energy jets, and the jet response is quite high at high energy, it still must be accounted for. Jet calibration is the process of correcting the measured jet energy to the particle level energy. This correction is also known as the jet energy scale, or JES.

3.2.1 The Calibration Chain

There are numerous steps to jet calibration in the ATLAS detector, accounting for different effects such as pileup and forward vs. central (barrel) jets. Additionally, there are calibration steps to account for differences between simulated and real data, since ATLAS uses a MC-based calibration [48, 49]. The different aspects of jet calibration at ATLAS are outlined in figure 3.3. The first step is jet reconstruction, discussed in the previous section. The next steps are pileup corrections, so some discussion of pileup is necessary.

Pileup is the presence of excess energy in the event, caused by additional interactions within a bunch crossing as well as interactions in other bunches that occur within the detector response window for a given event of interest. The interactions from other bunches are known as out-of-time pileup, while those within the same bunch crossing are in-time pileup. Out-of-time pileup affects the calorimeters as the bunch spacing of 25 ns is significantly less than the calorimeter response time, on the order of hundreds of nanoseconds. In-time pileup affects all detector components, and should not be confused with the underlying event; particles from the colliding protons that are not involved in the hard scatter. In time pileup can be attenuated by accepting only particles that come from the primary vertex.

[1] If the particle in question is composite, the constituent parts may have some small momentum off the beam axis. This is generally negligible.

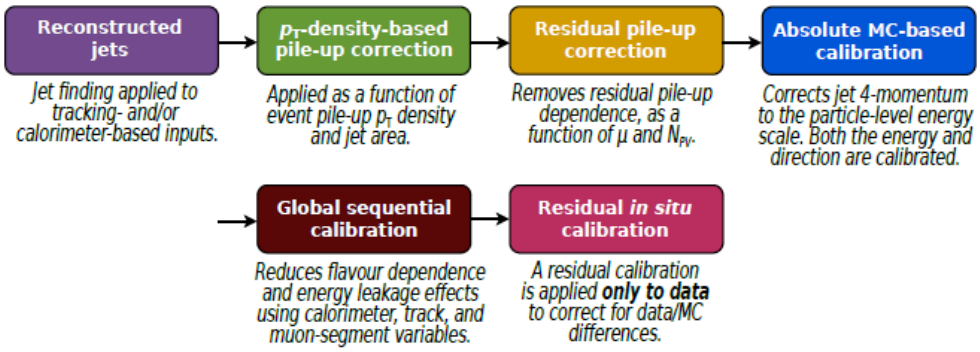

Figure 3.3: The calibration steps for jets in the ATLAS detector. This thesis focuses on modifications to the techniques used in the MC-based and in-situ calibrations [48]. Courtesy of the ATLAS Collaboration.

In-time pileup is characterized by the number of primary vertices, N_{PV}, while out-of-time pileup is represented by $\langle\mu\rangle$, the average interactions per bunch crossing. These properties are used together to correct for pileup in jet events. The first pileup correction depends on the jet area, determined by adding large numbers of ghost particles (virtual particles with very low momentum) to the event offline. For an even distribution of ghost particles in $\eta - \phi$ space, the number of ghost particles that lie within the reconstructed jet is representative of the jet area, A. This area is multiplied by the pileup energy density ρ, determined by observing low occupancy regions of the detector (areas where there are no reconstructed objects, such as jets or leptons) [50]. After this, a residual pileup correction is applied to account for problems in the jet-area pileup correction, such as differences in the pileup energy density between the forward and central regions of the detector or the high energy density of jets. This correction uses N_{PV} and $\langle\mu\rangle$ and compares reconstructed jets to truth level, i.e. particle level, jets in simulated data. Altogether, the pileup correction is

$$p_T^{corr} = p_T^{reco} - \rho \times A - \alpha \times (N_{PV} - 1) - \beta \times \mu, \tag{3.3}$$

where the p_T terms are the reconstructed and pileup corrected momentum. The α and β coefficients are calculated in bins of p_T and η, and depend logarithmically on p_T [51]. The combined pileup corrections are known as pileup subtraction.

After the pileup corrections come the absolute jet energy scale (MCJES, as this calibration is based on Monte Carlo) and η calibrations, which correct reconstructed, pileup subtracted jets to a point where they agree with the truth level energy and η. This correction measures in simulations the ratio of reconstructed energy to true energy (the jet response) in bins of energy[2] and η. The variation in the response with increasing energy is due to a

[2]In a 2020 summary of the jet energy scale, [48], the response was binned by E^{reco}. More recently in 2023 [49], the binning was done in E^{true}.

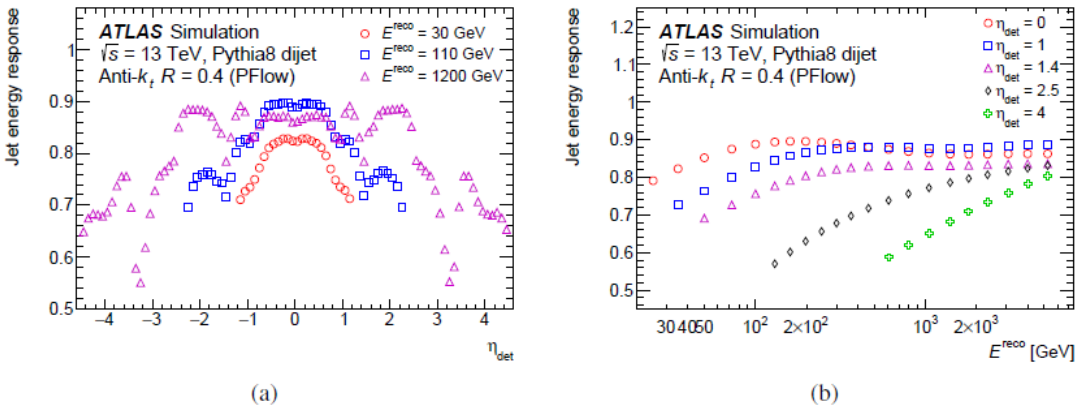

Figure 3.4: The η dependence at fixed energies, (a), and energy dependence at fixed η, (b), of the jet response. The jet response was calculated in Pythia8 MC, with jets above 20 GeV [48]. Courtesy of the ATLAS Collaboration.

larger portion of particles interacting with the calorimeter electromagnetically. Variations over the pseudorapidity are the result of different calorimeter technologies and changes in granularity. The η and E^{reco} dependence of the jet response at ATLAS are shown in figure 3.4.

The final MC calibration is the Global Sequential Calibration (GSC). The GSC is a multi-stage calibration to account for different kinds of jets. Jets initiated by different particles, gluons and different flavours of quarks, have different properties in the calorimeter. The differences between quark vs. gluon initiated jets are explored in greater detail in section 3.3. Suffice it to say that gluon jets generally have more, lower energy particles than quark jets. The GSC also accounts for jet fluctuations such as differing electromagnetic and hadronic fractions. The GSC looks at the energy deposited in the last layer of the electromagnetic calorimeter and the first layer of the hadronic, as well as the number of tracks, track width, and muon tracks associated with jets. The GSC uses these properties to empirically improve the jet energy calibration and resolution.

Thus far, the primary jet energy calibration has been completed in MC, where access to truth/particle level information exists. However, the MC is not perfect, and to correct simulation errors the final step of the chain is the residual in-situ calibration. This step is performed only on data, and accounts for inconsistencies in the JES determined from MC. The detector materials and physical processes, such as pileup and fragmentation, are imperfectly reconstructed in MC. In-situ techniques ensure the data are calibrated correctly.

There are several different in-situ calibration techniques used by ATLAS [49, 48]. First, the η-intercalibration is conducted to correct the response of jets in the forward detector regions to that of jets in the central region. After this, the response of jets is determined by comparing a jet to a well-measured reference object, such as a Z boson or a γ. In events where a jet and a reference object are produced back-to-back, the transverse momentum

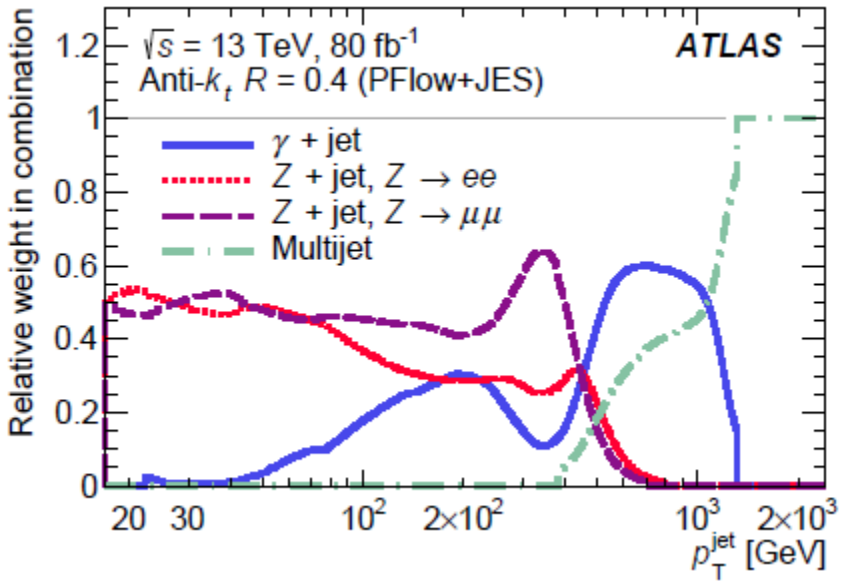

Figure 3.5: The relative weight of different in-situ techniques within the full in-situ calibration. Z+jet, with two decay channels (electrons and muons), is the primary calibration from 20-400 GeV, and multijet balance takes over at about 1000 GeV. γ+jet bridges the gap; though the calibration techniques for Z and γ+jet events are very similar [48]. Courtesy of the ATLAS Collaboration.

of the two objects should balance. Thus, measurement of the reference p_T can provide the true p_T of the probe jet. The response of the jet in this case is $p_T^{jet,measured}/p_T^{ref}$.

Different event topologies are more common at different energies. At lower energies, below roughly 1 TeV, Z+jet and γ+jet events are common, so calibration with these objects is typically conducted between 50-1000 GeV. At higher energies the production of dijet/multijet events dominates, so another technique known as multijet balance is used. In this method a high energy jet is balanced against multiple lower energy jets, which have already been calibrated using the Z/γ + jet technique. Figure 3.5 shows the energy ranges where different events/calibration techniques are most prominent.

This thesis focuses on the method used to calibrate Z and γ+jet events, the missing E_T projection fraction (MPF). In the next section the use of MPF in Z/γ+jet events is detailed, and over the next chapters a technique is outlined for using the MPF in dijet events.

3.2.2 Missing Transverse Energy Projection Fraction

The MPF method is the primary in-situ jet calibration technique used by the ATLAS collaboration [48, 49]. The technique was first developed by the major experiments at Fermilab's Tevatron [52].

The reconstructed jet does not inherently include all the energy from the original parton, as some particles may fall outside the region defined by the reconstruction algorithm.

Additionally, particles from other objects will be included within this region and can be erroneously counted towards the jet energy. A calibration of the reconstructed jet against a reference object therefore does not account for the entire hadronic recoil, which is what actually balances the p_T of the reference object. This method is called direct balance, and accounting for the particles that enter and exit the defined jet is known as the out-of-cone correction, which can be as high as 10%.

The MPF calibration balances the entire *recoiling* system with the reference object. A Z+jet event (or γ + jet, see figure 3.6) begins as a Z+parton event, and the energy of the parton fundamentally balances the p_T of the Z. At the particle level:

$$\vec{p}_T^{\,ref} + \vec{p}_T^{\,parton} = 0 \tag{3.4}$$

At the calorimeter level, where there is missing energy due to the calorimeter response being less than 1, this balance becomes:

$$\vec{p}_T^{\,ref} + R_{MPF} \cdot \vec{p}_T^{\,recoil} = -\vec{E}_T^{\,miss} \tag{3.5}$$

where R_{MPF} is the response, the ratio of measured to true energy, of the recoiling system. *parton* is replaced with *recoil* here; they represent the same object, but it makes more sense to describe the parton as the resulting recoil system at calorimeter level, and $\vec{E}_T^{\,miss}$ is the missing transverse energy. The response of the reference object is 1, so it is not included. The goal is to find R_{MPF};

$$R_{MPF} = -\frac{\vec{p}_T^{\,ref} + \vec{E}_T^{\,miss}}{\vec{p}_T^{\,recoil}} \tag{3.6}$$

Substituting in 3.4 and projecting in the direction of the reference object gives:

$$R_{MPF} = 1 + \frac{\vec{E}_T^{\,miss} \cdot \hat{p}_T^{\,ref}}{\vec{p}_T^{\,ref}} \tag{3.7}$$

Thus, the response of the recoiling system can be determined using only the missing transverse energy and the reference object. This is not the response of the jet, for as mentioned the jet is not the same as the whole recoil, so corrections are needed. These are known as the showering and topology corrections. The defined jet encompasses the high energy density centre of the recoil, and will have a higher response than the lower energy density outer portion of the recoil. The topology correction accounts for these differences. Meanwhile, the showering correction accounts for particles that moved in or out of the defined jet while developing through the calorimeter. These corrections largely cancel out, and the combined showering and topology corrections are only a few percent.

The missing transverse energy here depends on more than just the jet generated by the parton. The underlying event, pileup, and initial and final state radiation (ISR/FSR,

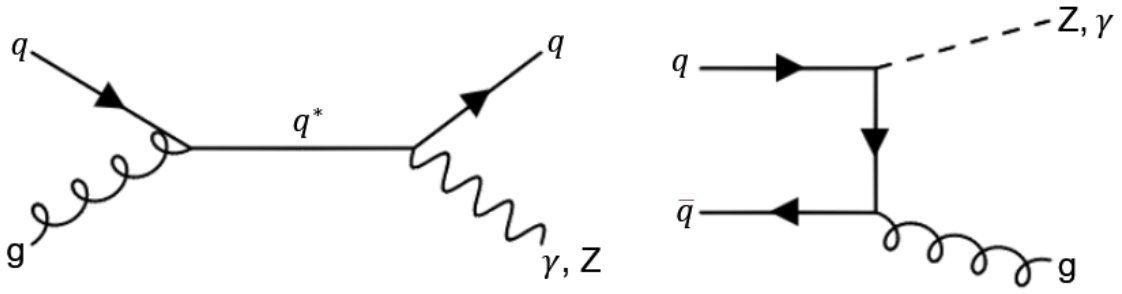

Figure 3.6: Feynman diagrams for the s- and t-channel production of a Z/γ + jet event. The s-channel, seen on the left, generates a quark jet, while the t-channel has a gluon jet [53].

particles radiated by the particles involved in the hard scatter before/after the interaction) all make additional contributions. This gives the MET as:

$$\vec{E}_T^{\,miss} = -\vec{E}_T^{\,ref} - \sum \vec{E}_T^{\,n} \tag{3.8}$$

n represents all the energy deposits in the calorimeter (other than those related to the reference object). 3.7 becomes

$$R_{MPF} = -\frac{\sum \vec{E}_T^{\,n} \cdot \hat{p}_T^{\,ref}}{\vec{p}_T^{\,ref}}, \tag{3.9}$$

Where $\vec{E}_T^{\,ref} = \vec{p}_T^{\,ref}$. This shows how the net energy of an event is balanced against the reference. Since the total energy includes contributions outside of the hard scatter this may seem problematic. However, over many events the effects of pileup and the underlying event average to zero, and the MPF technique becomes very robust against these, showing little dependence on N_{PV} and $\langle\mu\rangle$ [49]. Direct balance on the other hand has pileup dependence through the definition of the jet. For this reason, as well as the much smaller uncertainty in the showering and topology corrections versus out-of-cone corrections, MPF is the main in-situ calibration at ATLAS.

3.3 Quark and Gluon Jets

There are three single-gluon exchange interactions that partons undergo during fragmentation. These are: gluon radiates gluon, quark radiates gluon, and gluon splits to quark/anti-quark. The relative likelihood of each of these processes is dictated by averaged colour factors [1], resulting from the different colour states possible for quarks and gluons (8 for gluons, 3 for quarks). The processes of $q \to gq$ and $g \to gg$ have colour factors of 4/3 and 3, respectively, denoted by C_F and C_A. The colour factor for gluon splitting to quarks is only

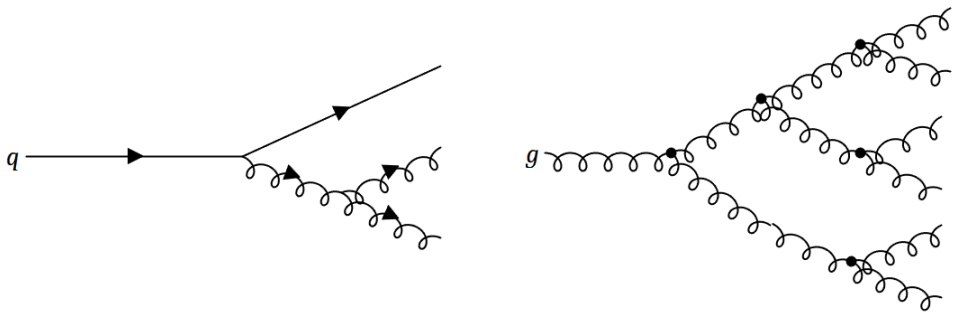

Figure 3.7: A display of how a gluon jet (right) develops more particles than a quark jet (left). $g \to gg$ is the most probable single gluon radiation process, and if the initiating partons have the same energy, the energy will be more spread out in the gluon jet.

$T_F = 1/2$, much lower than the others. The ratio $C_A/C_F = 9/4$ shows that gluon-gluon radiation is much more likely than quark-gluon, and the particle multiplicities in jets initiated by gluons will be larger by this ratio [54]. This is shown in figure 3.7.

Gluon jets having more particles leads to several other differences between quark and gluon jets. The average energy of the particles in gluon jets is lower than that of quark jets, and the large number of lower energy particles results in a lower response. With higher energy per particle, quark initiated jets penetrate further into the calorimeter. Quark jets are contained in a relatively narrower region than gluon jets, as the low energy particles in a gluon jet have a larger portion of their momentum transverse to the direction of the jet, a result of the repeated $g \to gg$ splitting. The lower energy per particle in a gluon jet also causes the particles to bend more in the magnetic field of the detector. Increased bending can have a small, lowering effect on the response, though the main cause for the lower response of gluon jets is the low energy per particle.

The different properties of quark and gluon jets allow for some level of discrimination between the two, though it is challenging because of the large fluctuations in the processes that generate jets. While gluon jets generally have more, lower energy particles and are shorter/broader than quark jets, the distributions of these properties are very broad, and there is significant overlap in the appearance of quark and gluon jets in the detector.

While there are efforts to tag individual jets as gluon or quark [54, 55], the specific response of each jet type is not typically measured. For any event type, the response can be treated as a combination of the responses of different jet types and the fraction of each jet type present in the event or collection of events. For Z+jet this is

$$R_{ZJ} = R^g f^g_{ZJ} + R^q f^q_{ZJ} + R^c f^c_{ZJ}, \tag{3.10}$$

while for dijets it is

$$R_{DJ} = R^g f^g_{DJ} + R^q f^q_{DJ} + R^c f^c_{DJ} \tag{3.11}$$

Here g denotes gluon jets, q represents light quark jets; up, down, and strange, and c is for charm quark jets. c quark jets are produced much less than gluon/light quark jets, and for this thesis the corresponding R^c terms are estimated in MC. The particle fractions are also determined in MC, where the truth-level information allows for the exact flavour of each jet to be known. While jets can be initiated by bottom quarks, it is very rare due to the b-quark mass (more than triple the c-quark), so b-quark jets are not considered.

Solving for the light quark and gluon responses gives:

$$R^g = \frac{f^q_{ZJ}(R_{DJ} - R^c f^c_{DJ}) + f^q_{DJ}(R^c f^c_{ZJ} - R_{ZJ})}{f^q_{ZJ} f^g_{DJ} - f^g_{ZJ} f^q_{DJ}}, \tag{3.12}$$

$$R^q = \frac{f^g_{DJ}(R_{ZJ} - R^c f^c_{ZJ}) + f^g_{ZJ}(R^c f^c_{DJ} - R_{DJ})}{f^q_{ZJ} f^g_{DJ} - f^g_{ZJ} f^q_{DJ}}, \tag{3.13}$$

With the jet-type fractions and charm jet response determined from MC, all that is needed to determine the responses of light quark and gluon jets is R_{ZJ} and R_{DJ}. R_{ZJ} is the standard result of the MPF calibration outlined in the previous section, and the following chapter will detail how a study of jet properties can allow for the MPF technique to be used in dijet events, giving R_{DJ}.

Chapter 4

Jet Properties Study

The research conducted here is a follow-up to a similar study from 2016 by James Walter Beare [56]. The overall objective is to determine the response of jets originating from gluons versus the response of jets generated by quarks. Before the quark and gluon level responses can be calculated, the MPF response of jets from two different event topologies must be known. Then, using equations 3.12 and 3.13, along with jet flavour fractions and charm quark jet responses from simulations, the quark and gluon-generated jet responses can be determined in both data and MC.

The problem then is calculating the MPF response in a dijet event, where there is no well-defined reference object. In this thesis, a technique is examined using the various properties of jets to correct jets to their truth level energy. The corrected jets can then be used as reference objects in the MPF calculation.

In MC simulation, truth level information of the jets is known, and the response for any jet can be calculated as

$$R_{MC} = p_T^{PileCorr}/p_T^{True} \tag{4.1}$$

where "PileCorr" denotes the pileup-corrected reconstructed momentum, and "True" designates the real, particle level momentum of the jet, unobscured by detector effects.

The response of a jet is influenced strongly by its π^0 content. The vast majority of π^0's decay electromagnetically into two photons, so jets with a large fraction of π^0's will thus have a larger electromagnetic showering portion in the calorimeter. Thus a jet that fluctuates to have a larger portion of π^0's will have a better response. Section 1.2 discussed how, in the calorimeter, electromagnetically interacting particles produce geometrically smaller showers, with fewer particles and higher energy density. Altogether, this means that high response jets in the calorimeter will more closely resemble electromagnetic showers. Due to the differences between the types of showering, high and low response jets can be discriminated between to some extent using their properties in the calorimeter.

Jet Property	Description
NumTrkPtX	Number of charged tracks within the jet with at least X = 500, 1000 MeV of transverse momentum.
TrackPtXFrac	The fraction of the total jet transverse momentum carried by charged tracks with more than X = 500, 1000 MeV p_T.
AvgTrackPtXFrac	The fraction of jet p_T carried by charged tracks with more than X = 500, 1000 MeV p_T divided by the number of tracks with at least that much p_T (TrackPtFrac/NumTrackPt).
TrackWidthX	The width of a jet using tracks with at least X = 500, 1000 MeV p_T.
Width	The jet width determined as $\frac{\sum(\Delta R_{jet,constit} P_{T,constit})}{\sum P_{T,constit}}$
PREBFrac	The fraction of the jet energy deposited in the barrel presampler layer.
EMBFrac	The fraction of the jet energy deposited in the electromagnetic barrel (EMB) calorimeter.
EMBXFrac	The fraction of jet energy deposited in the X = 1,2,3 layer of the EMB calorimeter.
EMBXOverEMB	The jet energy absorbed in the X = 1,2,3 layer of the EMB calorimeter divided by the total energy absorbed in the EMB calorimeter.
Mass	The jet mass is calculated by summing the four-vectors of the constituents.
TILEBXFrac	The fraction of jet energy absorbed in the X = 1,2,3 layer of the hadronic barrel calorimeter (TILEB).
TILEBXOverTILE	The energy deposited in the X = 1,2,3 layer of the TILEB calorimeter divided by the total energy in the TILEB calorimeter.
MostELayer	The calorimeter layer that absorbed the most energy.
EndLayer	The calorimeter layer by which 95% of the jet energy is absorbed.

Table 4.1: The jet properties used to create a dijet correction factor. See the text for more details.

4.1 Jet Properties

The jet variable study was conducted using Pythia8 MC, with roughly 2.3 billion simulated events. The jet properties used fall primarily into two groups: Track variables, describing reconstructed particle paths through the detector, and energy per sampling layer, representing the portion of a jet's energy deposited in each layer of the calorimeter. The jet properties used in the study can be seen in table 4.1, along with a short description of what they measure and how they are calculated.

Each jet property was calculated in multiple bins of $p_T^{PileCorr}$ over a range of 25-1100 GeV, with lower bin edges at 25, 45, 65, 85, 105, 125, 160, 210, 260, 310, 400, 500, 600, and 800 GeV. The bins 105-125 GeV and 500-600 GeV are used for most of the figures in this section, while the rest of the plots are available in the appendices.

Jets were divided into two groups based on response. For the primary analysis, jets with a response greater than 0.9 were considered high response, while jets with a response less than 0.7 were considered low response. Alternative response cuts of (high/low) 0.9/0.5 and 0.8/0.7 were used to determine the uncertainty associated with this response classification. By recording the jet properties for both high and low response jets, the variables that discriminate between high and low response can be determined. Before moving on to the statistical methods used to select key jet properties, it is useful to examine the properties themselves.

For the track variables, the results for the 500 and 1000 MeV versions are generally similar, so only the 1000 MeV plots are shown here. In all of the following plots, the nominal 0.9/07 response cut is used. High response jets are labelled as signal and low response jets are labelled as background in the variable plots. The count for each variable is normalized to the total number of events in the plot, emphasizing the shape of the distributions; if the real count were used, the low response background would appear far larger than the signal, as the background cut allows a much larger response range.

Figure 4.1 shows the NumTrkPt1000 property for jets in select transverse momentum bins, at pileup subtracted scale. Visually, NumTrkPt1000 is effective in discriminating signal (high response) and background (low response) jets. The signal jets in both momentum bins have fewer tracks than the background, as the high response jets fluctuate towards a higher π^0 fraction. π^0 decay into pairs of electrically neutral photons that do not leave charged tracks. A larger portion of the energy of these jets is deposited through electromagnetic showers, giving a higher response. Additionally, it can be seen that the mean of both distributions increases in the larger p_T bin; jets with a higher momentum will have more tracks with greater than 1000 MeV.

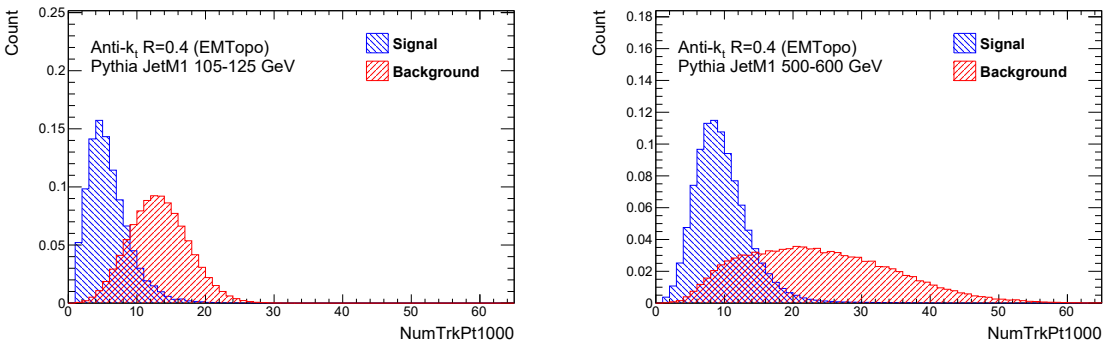

(a) (b)

Figure 4.1: The number of tracks within each jet with greater than 1000 MeV p_T, for jet energies of 105-125 and 500-600 GeV. The spectra are normalized to unit integral to emphasize the shapes of the distributions.

The fraction of the total jet p_T carried by these 1000 MeV tracks is shown in figure 4.2. This variable also shows reasonably good separation between signal and background jets, for the same reasons as the previous property. Signal jets have less of their p_T carried by charged particles, as much of it is carried by neutral pions.

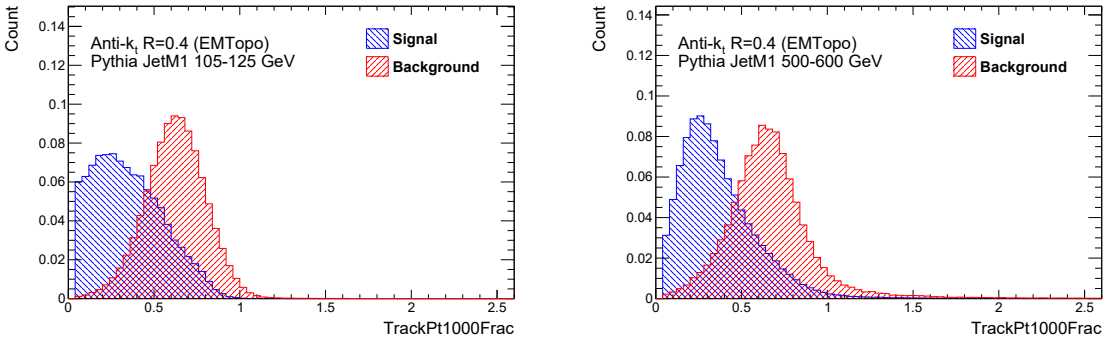

(a) (b)

Figure 4.2: The fraction of jet p_T carried by tracks with greater than 1000 MeV p_T. The spectra are normalized to unit integral to emphasize the shapes of the distributions.

The ratio of these variables, AvgTrackPt1000Frac (figure 4.3), is not a good discriminator. The number of charged tracks and the fraction of total jet momentum carried by those tracks are closely correlated. More tracks will carry a higher total fraction of the jet momentum. Thus, the ratio of the p_T fraction to the number of the tracks is similar for both signal and background jets.

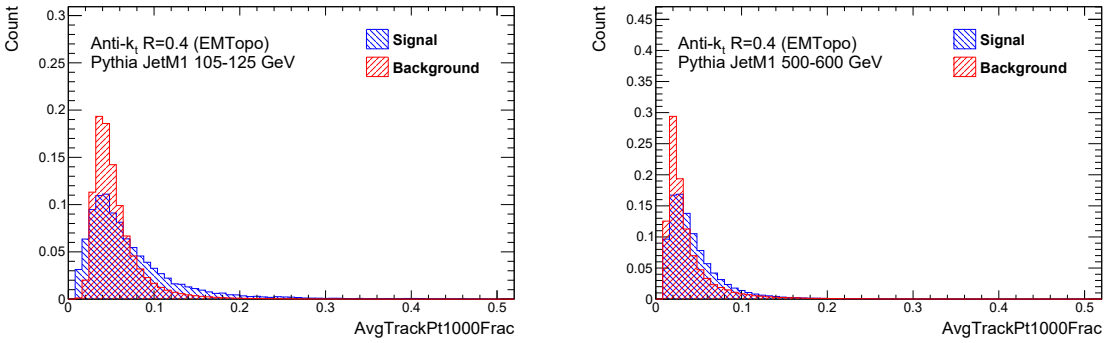

(a) (b)

Figure 4.3: The ratio of jet p_T carried by charged tracks to the number of tracks, for charged tracks with greater than 1000 MeV p_T. The spectra are normalized to unit integral to emphasize the shapes of the distributions.

The two different measurements of lateral jet size, TrackWidthX (determined through ghost association) in figure 4.4 and Width (determined using clusters) in figure 4.5 give slightly different results. Neither shows a substantial separation between high and low response, but the separation appears better in the Width. In all cases, the calculated width of the jet is smaller for signal jets, as they have fewer charged tracks and have a large electromagnetic component, depositing their energy in a smaller area.

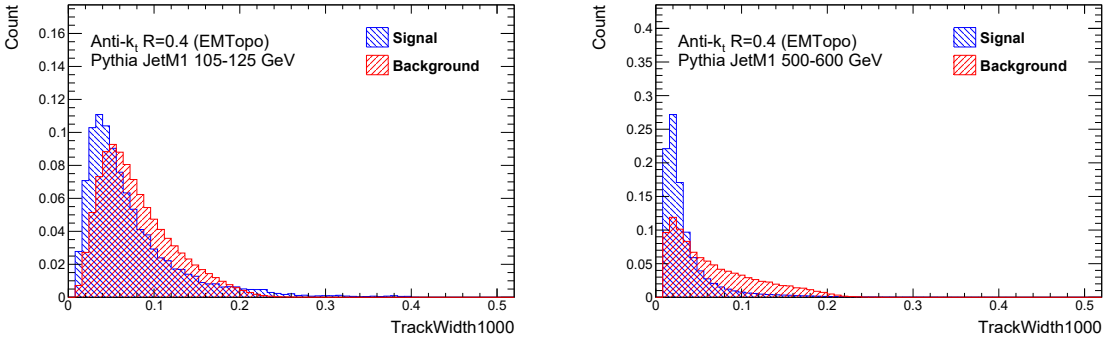

(a) (b)

Figure 4.4: The width of the jets calculated using tracks with greater than 1000 MeV p_T. The spectra are normalized to unit integral to emphasize the shapes of the distributions.

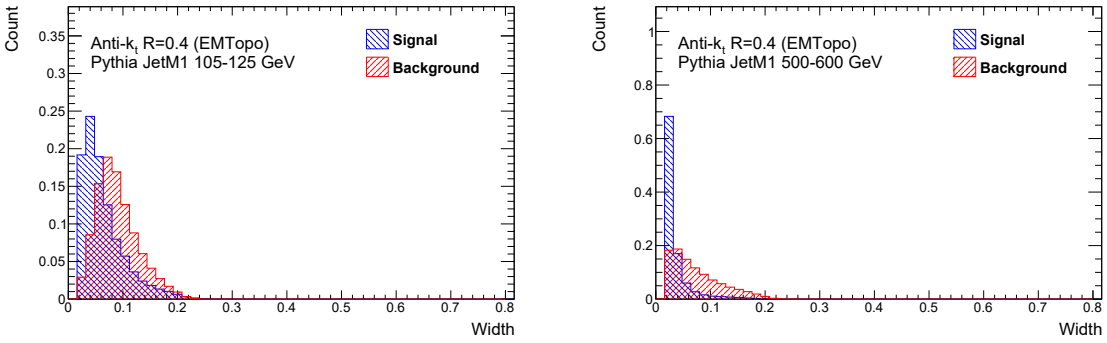

(a) (b)

Figure 4.5: The width of the jets calculated using the ΔR and p_T of the jet constituents. The spectra are normalized to unit integral to emphasize the shapes of the distributions.

Moving on to the energy deposit variables, the total EMBFrac is a good discriminator, as expected. The signal jets have a larger electromagnetic portion, which is primarily absorbed in the EMB.

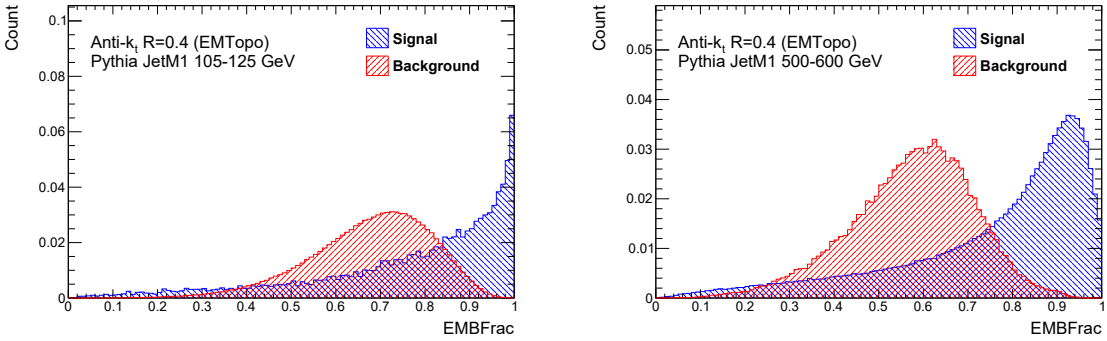

(a) (b)

Figure 4.6: The fraction of the jet energy deposited in the electromagnetic barrel. The spectra are normalized to unit integral to emphasize the shapes of the distributions.

Most of the energy deposited in the EMB goes to the second layer, EMB2, as it is far thicker than the other layers. As it makes up the majority of the EMB, the EMB2 signal/background distributions appear fairly similar to figure 4.6. EMB1 and EMB3 are shown in figures 4.7 and 4.8, respectively. The first layer provides moderate discrimination between signal and background jets. The first layer of the calorimeter is more sensitive to the parton shower, part of the jet formation, than the calorimeter shower which is just starting. Later calorimeter layers are dominated by the effects of the calorimeter shower. While signal jets have more energy absorbed due to their larger portion of electromagnetic showering, it is not especially different for high and low response jets. Nonetheless, the expected effect is present.

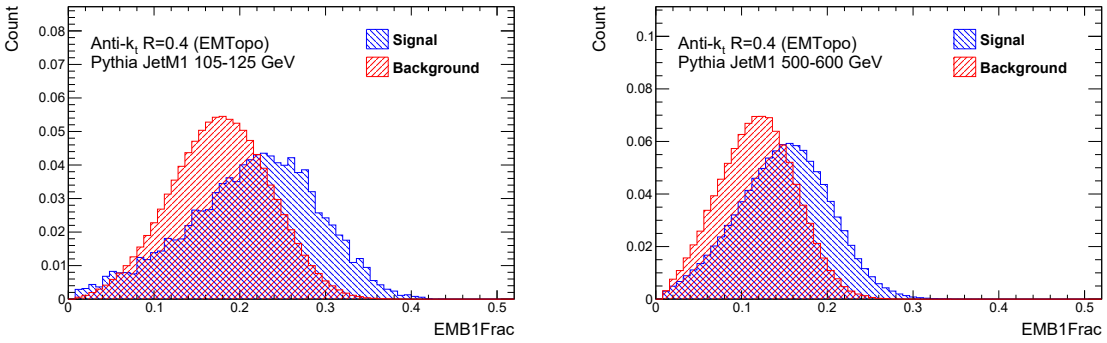

(a) (b)

Figure 4.7: The fraction of the jet energy deposited in the first layer of the electromagnetic barrel. The spectra are normalized to unit integral to emphasize the shapes of the distributions.

The third layer is in some ways the opposite of the first. Most of the signal jet energy is absorbed by the end of EMB2, thus only a small portion is deposited in EMB3. The energy in the third electromagnetic barrel layer rarely exceeds 10% of the total, but there is a marked difference between signal and background jets, the latter depositing significantly more energy.

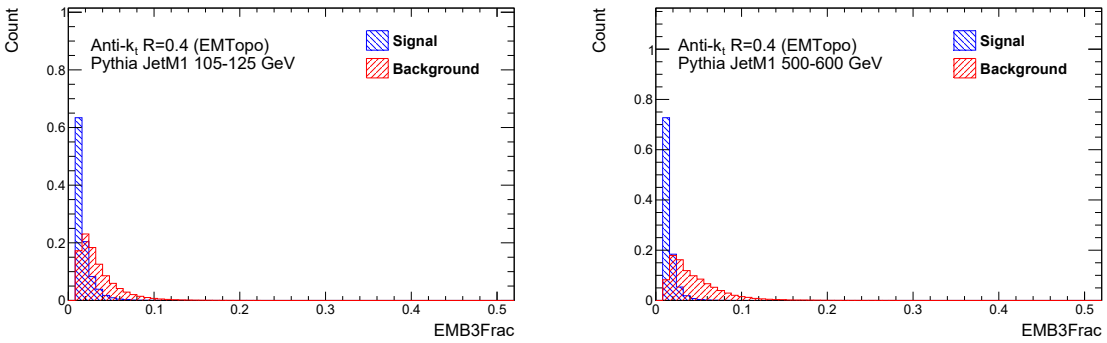

(a) (b)

Figure 4.8: The fraction of the jet energy deposited in the third layer of the electromagnetic barrel. The spectra are normalized to unit integral to emphasize the shapes of the distributions.

Signal jets often are completely absorbed in the electromagnetic calorimeter, so there is a large portion of these jets that leave no energy in the tile hadronic calorimeter. The first two tile barrel layers show good separation between signal and background jets; while the signal jets have very low fractions of deposited energy in this region, the more hadronic background jets have far more energy remaining after the EMB and deposit it in the TILEB. Figure 4.9 shows the first layer of the TILEB, while figure 4.10 shows the third layer. The

third layer has similar, very low, energy deposits for both high and low response jets. By the time a jet has reached the last layer of the calorimeter, it will have lost the vast majority of its energy to the EMB and/or the earlier tile layers. The distributions for TILEB2Frac are similar to TILEB1 but with lower average energy deposited.

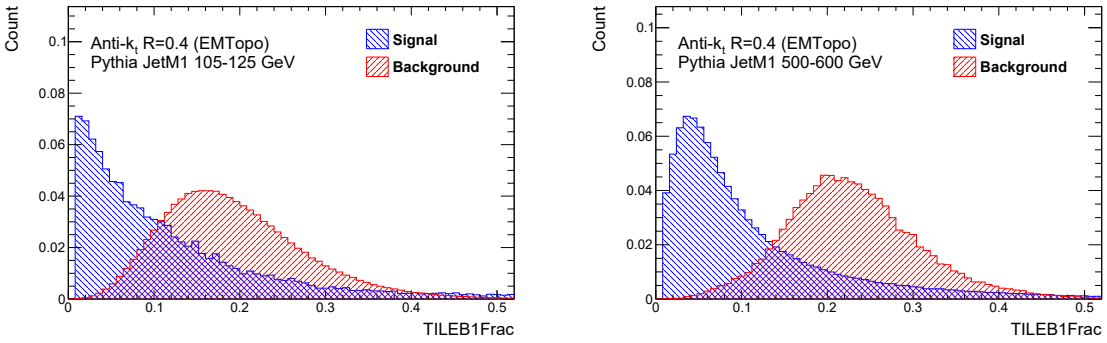

(a) (b)

Figure 4.9: The fraction of the jet energy deposited in the first layer of the tile barrel. The spectra are normalized to unit integral to emphasize the shapes of the distributions.

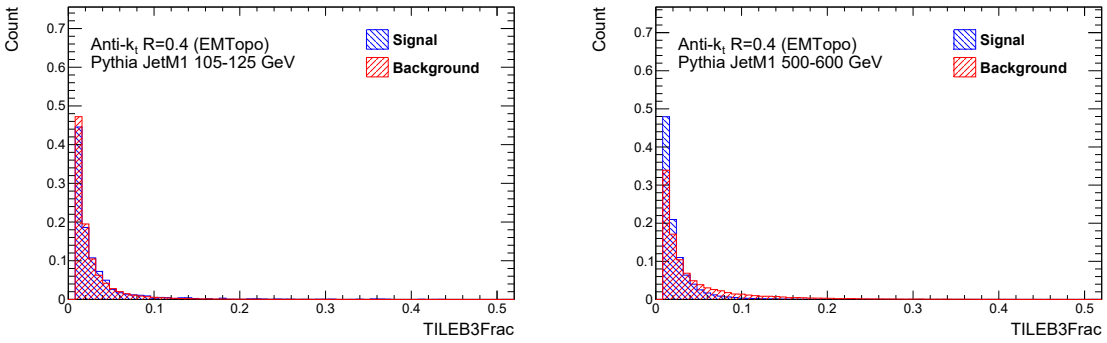

(a) (b)

Figure 4.10: The fraction of the jet energy deposited in the third layer of the tile barrel. The spectra are normalized to unit integral to emphasize the shapes of the distributions.

The other jet properties related to energy depositions are the ratios of energy deposited in each barrel layer to the total energy in the electromagnetic and tile barrels. In both the EMB and TILEB calorimeters, the first two layers are highly anti-correlated (see figures 4.17 and 4.18); a large deposit of energy in one corresponds to a smaller deposit in the other, which is of course expected. The third and second layers of both calorimeters are neither correlated nor anti-correlated strongly. If little energy is deposited in the first layer, then the second and third layers would appear anti-correlated, but if the first layer absorbs a large portion of the energy, then both the second and third layers will be low, and will

appear correlated. This largely cancels out, and over many jets the second and third layers appear less related than the others.

As discussed, signal jets deposit most of their energy in EMB1 and 2, and the majority of that is in the second layer. EMB2OverEMB is shown in figure 4.11, and the signal jets have a higher fraction than the background jets, as expected. The separation of signal and background jets is shown to increase with jet p_T, as expected. EMB1OverEMB provides similar separation, albeit with smaller deposited energy fractions overall. EMB3OverEMB is very similar to the regular EMB3Frac variable in figure 4.8, with both signal and background jets depositing only small fractions of their total EMB energy, but noticeably less deposited by the signal jets.

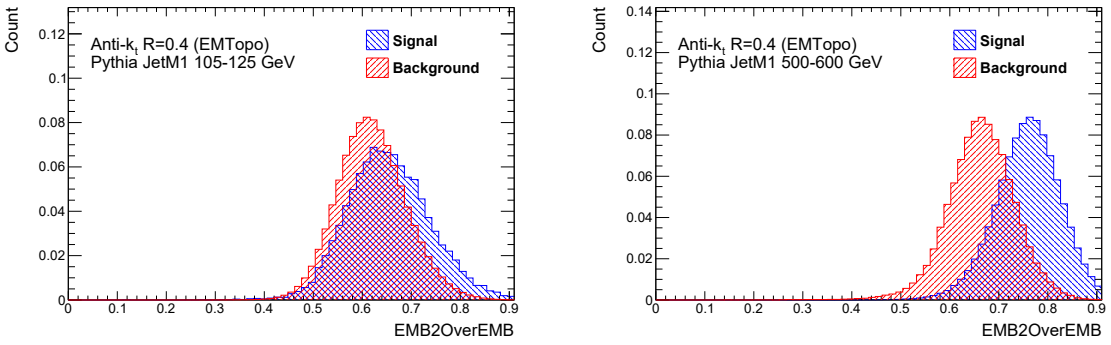

(a) (b)

Figure 4.11: The fraction of the total EMB energy deposited in EMB2. The spectra are normalized to unit integral to emphasize the shapes of the distributions.

The TILEB1OverTile distributions are seen in figure 4.12. The separation here is useful, due to the larger hadronic portion in background jets.

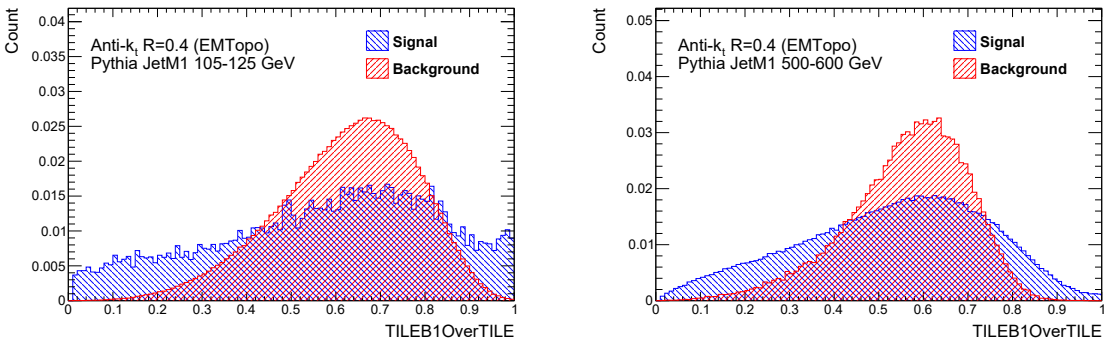

(a) (b)

Figure 4.12: The fraction of the total TILEB energy deposited in TILEB1. The spectra are normalized to unit integral to emphasize the shapes of the distributions.

Figures 4.13 and 4.14 show MostELayer and EndLayer, respectively. Only the electromagnetic and tile barrels are used in this study, so only certain values in the plots have events. The values 1-3 correspond to EMB1-3, while values 12-14 represent the TILEB layers. Overwhelmingly, jets deposit most of their energy in EMB2, regardless of whether they are high or low response. At higher p_T there is some discrimination as background jets sometimes deposit the most energy in the first or second TILEB layers.

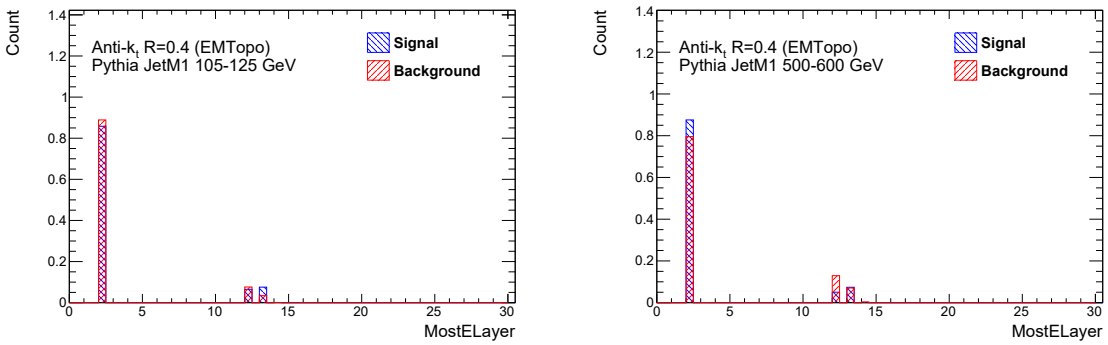

(a) (b)

Figure 4.13: The calorimeter layer that absorbed the most energy. The spectra are normalized to unit integral to emphasize the shapes of the distributions.

The EndLayer is most often TILEB2, especially for background jets. Signal jets sometimes end in the EMB, but are more likely to also reach the TILEB.

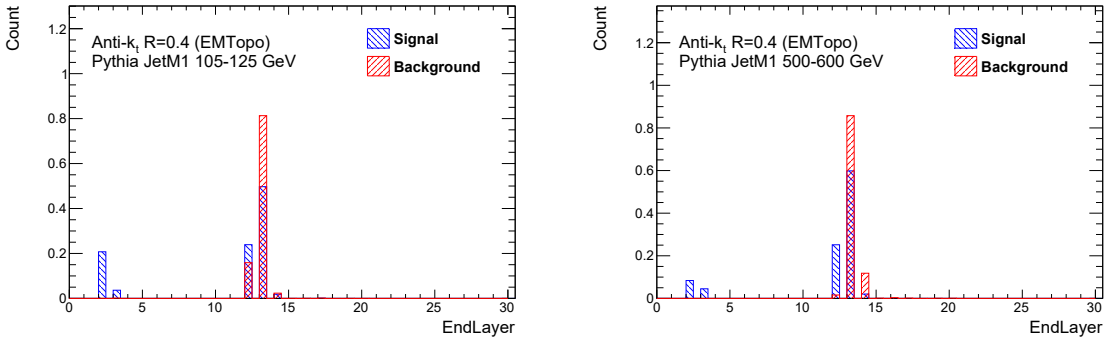

(a) (b)

Figure 4.14: The Calorimeter layer by which point 95% of the jet energy is absorbed.

The last variable investigated was the jet mass, shown in figure 4.15.

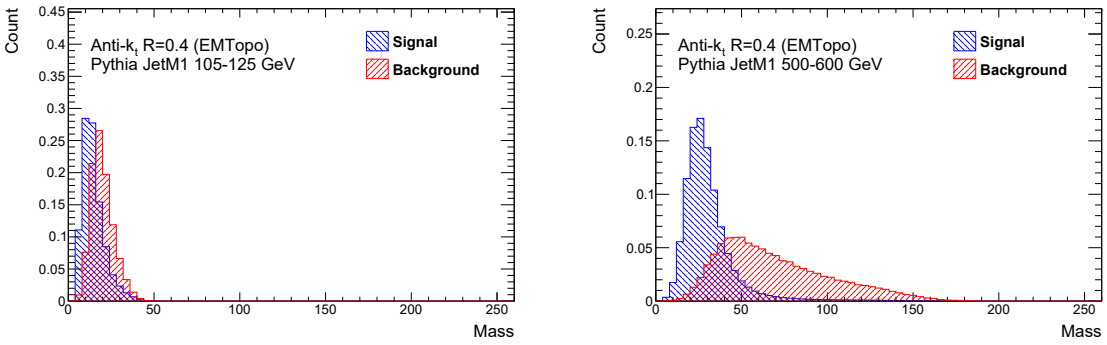

(a) (b)

Figure 4.15: Signal and background distributions of the jet mass. The spectra are normalized to unit integral to emphasize the shapes of the distributions.

Jet mass provides strong discrimination at higher p_T, though at low p_T the high and low response distributions are fairly similar. The mass is defined as $m^2 = E^2 - P^2$, where the energy and momentum are from the four-vector sum of all the constituents within the jet. Factors of the speed of light, c, are suppressed in the equation. This means that the possible values for the jet mass are limited by its energy; low-energy jets can only have a small range of mass values, as shown in the lower p_T bin in figure 4.15. With increasing jet energy, the mass distribution becomes broader, especially for background jets.

Higher mass particles receive less of a Lorentz boost in the hard scatter direction, and this carries over to their decay products. This results in greater lateral spreading of the particles within the detector. It has been shown that jets with greater width are more likely to be background jets, and thus the same can be said for those with high mass. Mass and the width/Track variables are highly correlated, as seen in figures 4.17 and 4.18.

To properly rank the variables based on the separation of signal and background jets, several benchmarks are used. First is the integrated probability,

$$P = \int \frac{S}{S+B}, \tag{4.2}$$

which provides a simple measure of the probability of a high response jet. In each p_T bin of the variable histogram being considered, S is the signal distribution and B is the background.

Next is the signal-weighted integrated probability,

$$SWP = \int \frac{S^2}{S+B}, \tag{4.3}$$

which helps to account for bins in the histogram with low statistics. If a given bin has only a handful of signal events and no background, it will have a large contribution to the

simple integrated probability. Weighting by the signal mitigates this effect. Additionally, the integrated event-weighted signal-to-background ratio is used:

$$EWSB = \int \frac{(S+B) \times S}{B} \tag{4.4}$$

P gives a measure of the separation of signal and background jets, but it can be skewed to regions of a variable with fewer events. The SWP and EWSB account for this by considering the number of events in each bin.

The mean asymmetry is a simple measure of the difference in the mean of the signal and background distributions, given by

$$M_A = \frac{M_S - M_B}{M_S + M_B} \tag{4.5}$$

M_A provides a good measure of separation, but only for the average values of the distributions. For broad distributions with a greater deviation, it is less useful.

Lastly, a Chi2 test is used. The Chi2 test is a strong determinant of separation, but it struggles with variables that have fewer bins.

To account for the various strengths and weaknesses of each measure, the jet properties are ranked based on each of the five statistical methods. These ranks are then combined, giving a balanced list of which variables provide the best discrimination between high and low response. The pre-integrated probability measures for EMBFrac are shown in figure 4.16 for the momentum bin 105-125 GeV, where the problems with a simple probability calculation are apparent. The standard probability measures a large separation between signal and background jets at low EMBFrac, but in figure 4.6 it is clear this is the result of a low relative event count. The SWP and EWSB measures show that the true separation occurs at high EMBFrac, as expected.

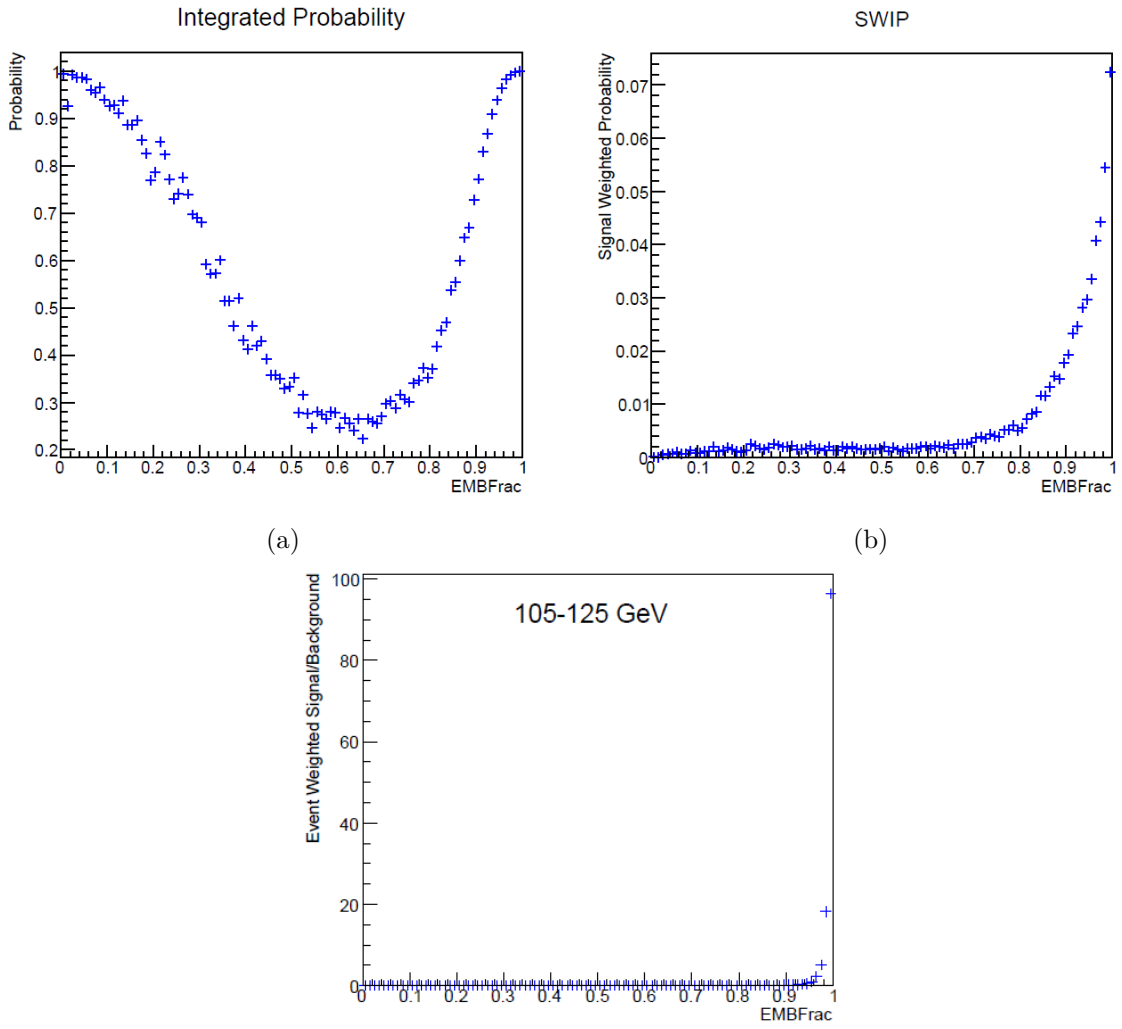

Figure 4.16: The probability, signal-weighted probability, and event-weighted signal-to-background ratio of EMBFrac at 105-135 GeV.

Certain jet properties are highly correlated (or anti-correlated) with one another. Variables that are related in this way provide little new information, so a cut is applied to the variable list to eliminate the lower ranked variables within a correlation score of ± 0.4 with respect to higher ranked variables. The correlation cut is varied to provide an uncertainty, with additional cuts of ± 0.6 and ± 0.8. Stricter correlation cuts (lower values) will eliminate more variables from the list, so for each cut a different number of variables is used; six for the nominal (± 0.4) cut, and eight and twelve for the other cuts, respectively. The correlation scores for all the variables in the momentum bins 105-125 and 500-600 GeV are shown in figures 4.17 and 4.18. The correlation coefficients between two variables A and B are calculated as

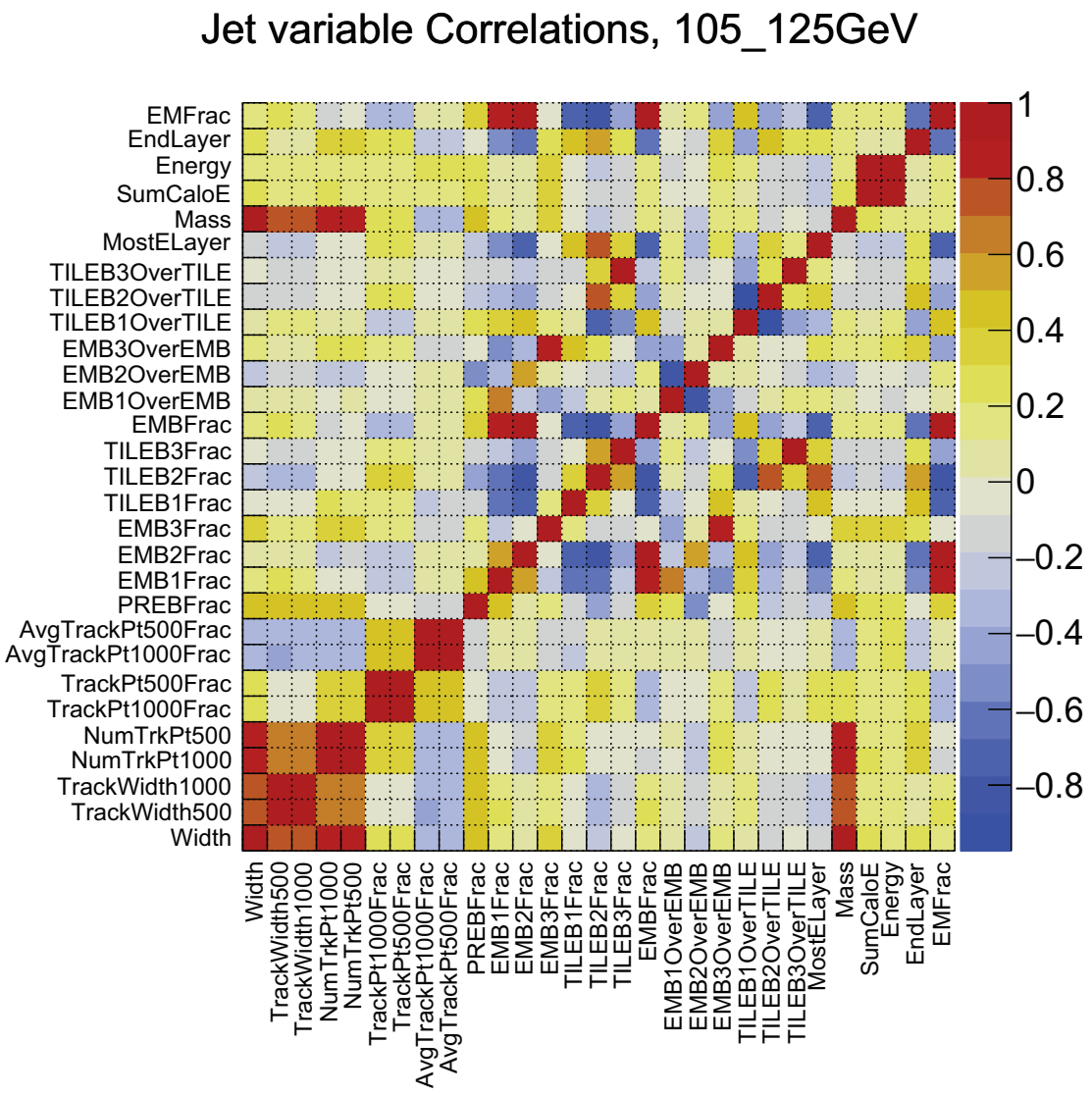

Figure 4.17: Correlation scores between each jet property at 105-125 GeV

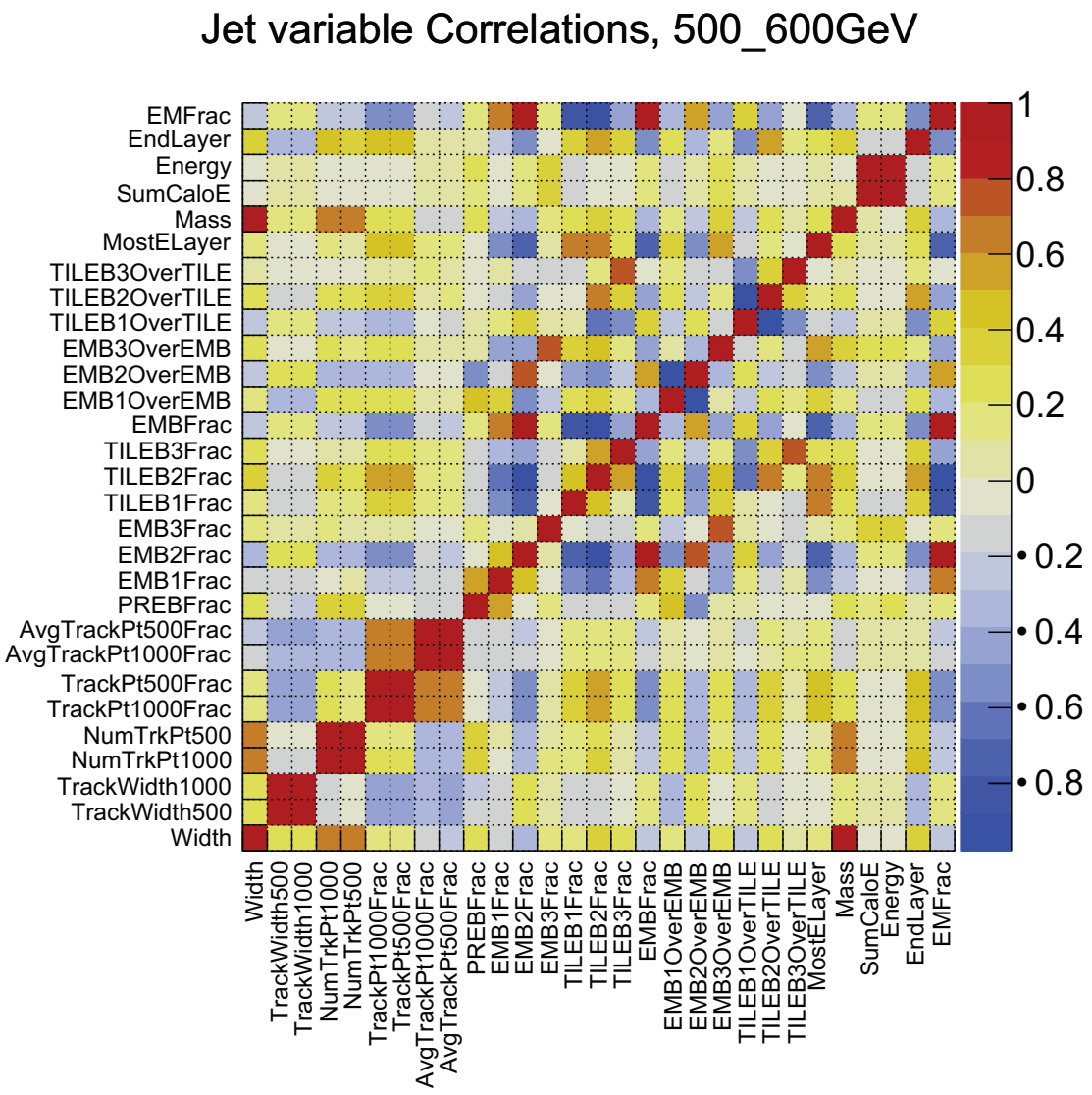

Figure 4.18: Correlation scores between each jet property at 500-600 GeV

105-125 GeV	500-600 GeV
NumTrkPt1000	Mass
TrackPt500Frac	TrackPt500Frac
TILEB1Frac	EMB3OverEMB
EMB3Frac	TILEB1Frac
TILEB2OverTILE	TILEB2OverTILE
EMB2OverEMB	EMB2OverEMB

Table 4.2: Selected jet properties for 105-125 and 500-600 GeV. The properties used in the other momentum bins are listed in appendix F.

$$Corr(A, B) = \frac{Cov(A, B)}{\sigma_A \sigma_B} \tag{4.6}$$

where $Cov(A, B)$ is the covariance of the two variables. Some of the correlations have been discussed above: The fraction of the total energy deposited in the EMB(TILEB) absorbed in each EMB (TILEB) layer, and the relationship between mass and width. Of course, each EMBXFrac (TILEBXFrac) variable correlates with the EMBXOverEMB (TILEBXOverTILEB) variable for the same layer, and anti-correlates with those of the other layers. All of the track variables correlate with the alternative p_T cut version of the same variable, e.g. TrackWidth500 is highly correlated with TrackWidth1000. Most of the track variables correlate at some level with the others, except for AvgTrackPtXFrac which anti-correlates with NumTrackPtX as it is constructed by dividing by the number of tracks.

While EndLayer and MostELayer are interesting and they provide some confirmation of the differences between high and low response jets, they are not used further in the study. For highly discrete variables such as these, the statistical methods struggle to provide an accurate measure of the signal-to-background separation. The different integrated probabilities end up with many bins giving either very high or low probability, and in variables with only six usable bins, these contribute greatly to the integrated values. Additionally, for so few bins the Chi2 test is unreliable. The correlation factors of EndLayer and MostELayer are included in the charts of correlation scores, but the variables are not included in creating ranked variable lists.

With the variables ranked and a correlation cut applied, a list of jet properties providing the best discrimination between high and low response jets is produced for each of the p_T bins. These lists are shown in table 4.2 for select p_T bins.

4.2 Creating a Correction Factor

To create a correction for the jet momentum, a likelihood function is used, defined as

$$L = \Pi_V P_{V(x)}, \tag{4.7}$$

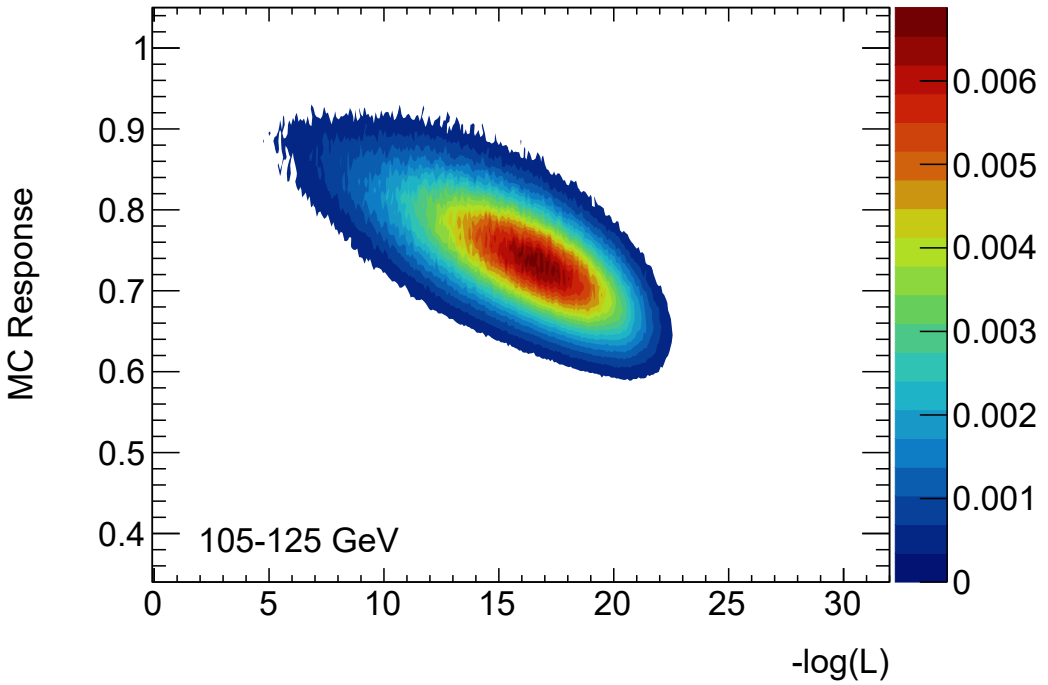

Figure 4.19: MC response versus $-log(L)$ for the p_T range of 105-125 GeV.

where P is the probability that when a variable V has the value x, the jet has a high response. For each variable in the list for a given p_T bin, the probability of a high response is calculated for each histogram bin. The probabilities discussed here and in equations 4.2-4.6 use the non-normalized jet variables, unlike the plotted jet variables which were normalized to unit integral to be viewable. This ensures the correct ratios of signal and background jets are used.

Each jet in the analysis is sorted into the appropriate p_T bin, and variables from the corresponding list are recorded. These variable values are then checked against the histogram bins for that variable, and the closest histogram bin is used to select the high response probability. For a list with six variables then, each jet builds the likelihood L as the multiplicative combination of six probabilities. The likelihood is then binned as $-log(L)$, and this value is compared with the jet response, as calculated from equation 4.1. Response versus $-log(L)$ plots are displayed in figures 4.19 and 4.20 for select momentum bins.

There are some important features to the response versus $-log(L)$ distribution. First, there must be some correlation between the response and the likelihood. This is clearly present in figures 4.19 and 4.20. The general trend is simple: Jets with a smaller $-log(L)$ have a higher response. $-log(L)$ is, of course, smaller at a higher combined probability of high response, so this behaviour is expected. The correction factor for a jet is determined by fitting bins of $-log(L)$ with a double Gaussian, seen in figure 4.21. The response, projected into $-log(L)$ bins, is fit to a Gaussian and re-fit in the interval of $\pm 2\sigma$ of the first fit. The

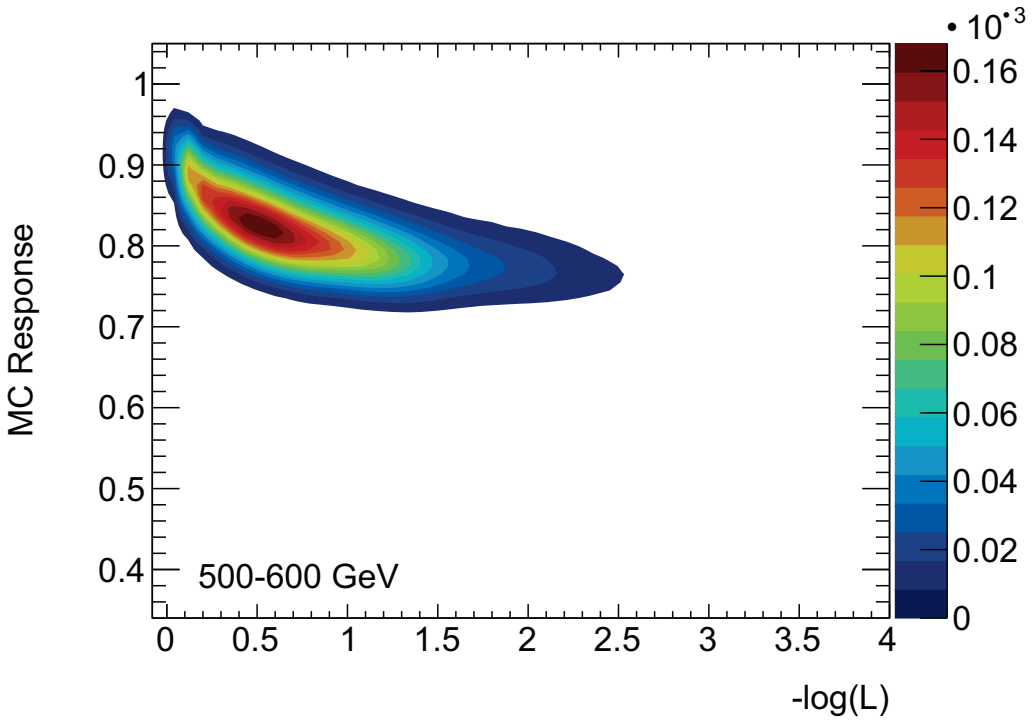

Figure 4.20: MC response versus $-log(L)$ for the p_T range of 500-600 GeV.

mean of this fit, essentially the average response of jets in a select $-log(L)$ and p_T range, is the correction factor. This factor is known as the alpha correction, α.

While a correlation is seen between the response and the likelihood, the distributions are unfortunately very broad. This is a result of the dynamics of jet formation and the response of the calorimeters, and is a limitation of this technique for correcting the energy of jets.

Dividing the pileup-corrected p_t of a jet by the corresponding alpha correction gives an estimate of the true momentum, but it can be improved further. In each momentum bin, the corrected p_T is compared to the truth p_T by the alpha closure, α_c, defined as

$$\alpha_c = \frac{p_T^{\alpha} - p_T^{Truth}}{p_T^{Truth}}, \tag{4.8}$$

where p_T^{α} is the jet p_T after the application of the original α correction. The α_c distribution is fitted to a double Gaussian in each momentum bin. The difference between the mean of each α_c fit and zero is applied as an additional multiplicative correction to the jet momentum (figure 4.22). This residual correction ensures the corrected jet p_T is equivalent to the particle level transverse momentum. This second correction brings the mean of the α distribution closer to the true jet p_T, but it does not improve the width.

The uncertainty of the correction is provided by the standard deviation of the alpha closure distributions (figure 4.23). This uncertainty is largest at low p_T, roughly 14%, and lowers with increasing momentum to around 4-5%. With this uncertainty in mind, a second

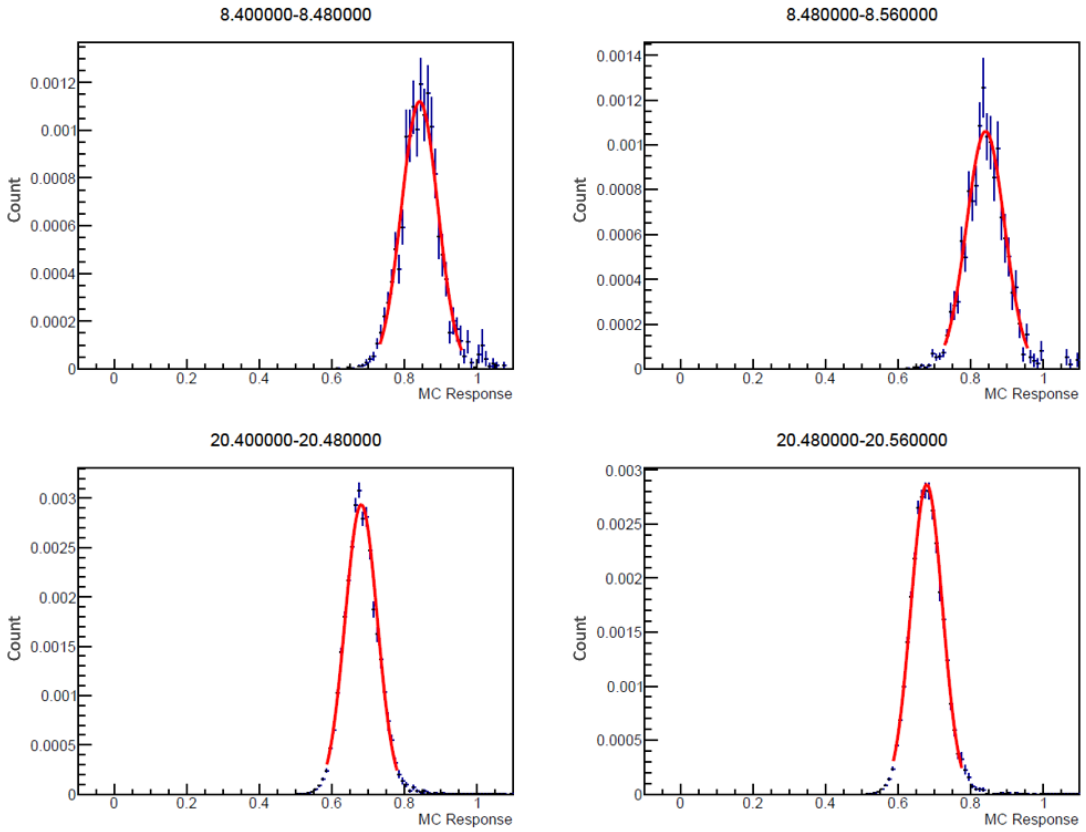

Figure 4.21: Distributions of jet response at 105-125 GeV in selected $-log(L)$ bins. The distributions are fit with a double Gaussian (outlined in the text), which removes the effects of large tails. The mean of each fit provides a correction factor (α) for jets with the corresponding p_T and $-log(L)$. Comparing the upper plots with the lower ones, it is clear that the average response decreases with increasing $-log(L)$.

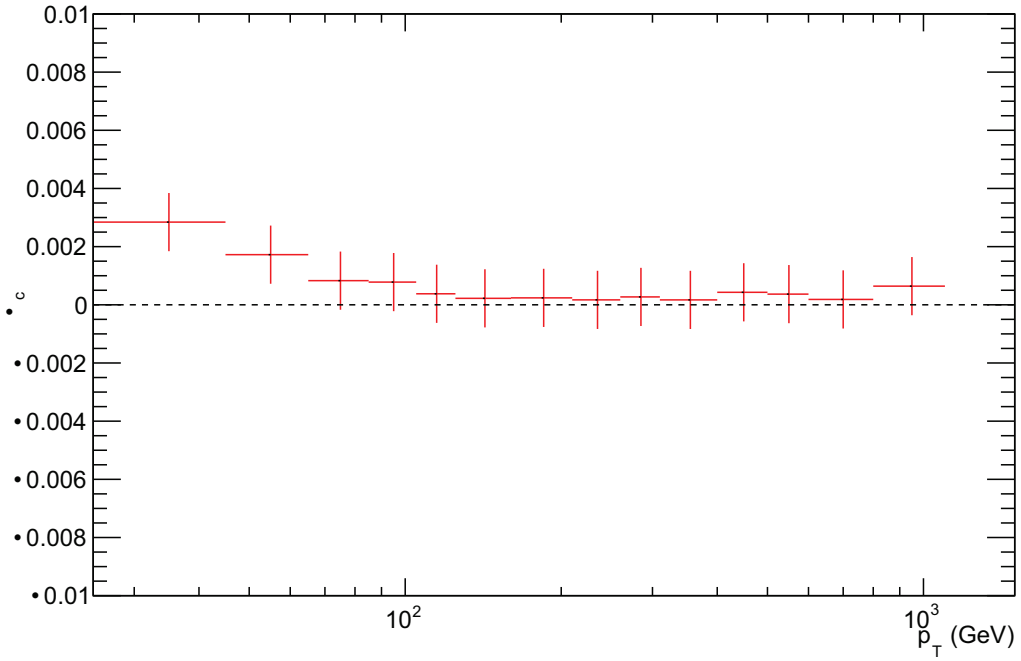

Figure 4.22: The secondary α_c correction used in each momentum bin. The corrections are well below 1% in all the p_T bins, showing that the initial correction generally brings jets very close to their truth level momentum.

important feature of figures 4.19 and 4.20 can be seen. The width of the plots with respect to response translates into the uncertainty of α_c. If the distribution of responses in a $-log(L)$ bin is broad, the correction factor will be less effective, as the tails of the distribution can have very different responses than the mean, and the α_c distribution will be broader.

The width of the response versus $-log(L)$ plots decreases with increasing jet momentum, as seen by comparing figures 4.19 and 4.20, where the 500-600 GeV plot is narrower with respect to response than the lower p_T plot and is shifted upward overall in MC response. This corresponds to the general increase in jet response with increasing momentum, and the greater variation in jet response at low p_T, where more jets are produced.

From the study of jet properties, a correction for the jet p_T has been obtained. Since the correction value depends on $-log(L)$, all that is needed to determine a given jet's correction is the jet properties. Jet properties are readily available in data, and thus the study of properties that has to this point been conducted in MC can be carried over to data. With the correction factor applied, the leading jet from a dijet event, i.e. the one with the highest energy, is ready to be used as a reference object in the MPF calculation.

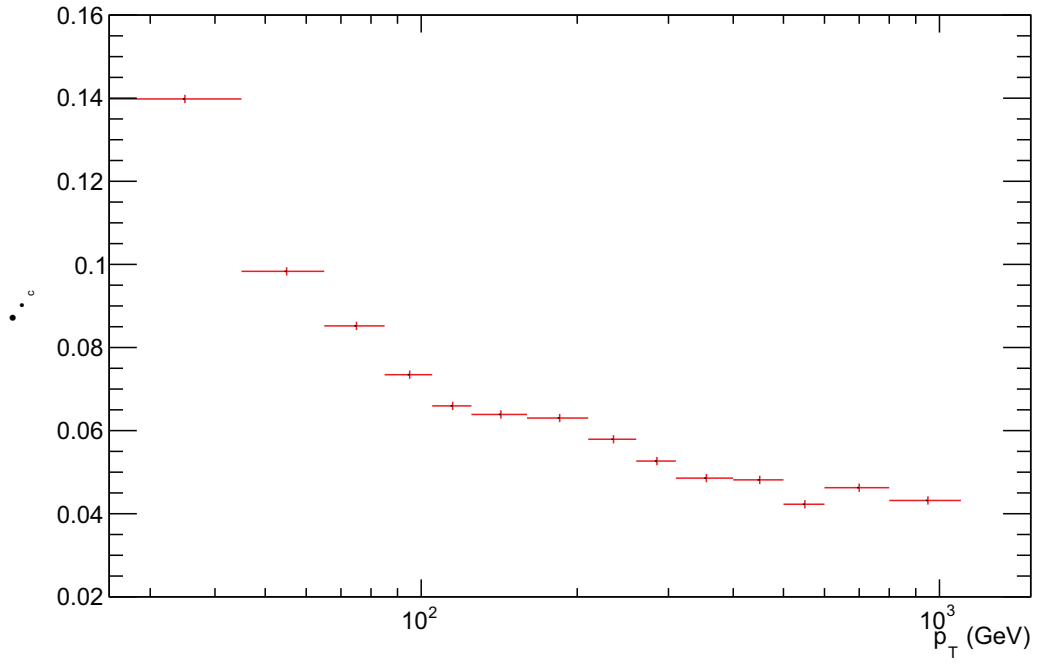

Figure 4.23: The standard deviation of α_c, ranging from 14% at low p_T to as little as 4-5% at high p_T. These values are taken as an uncertainty in each p_T bin and show that even though the average jet is corrected well, there can be significant deviations.

Chapter 5

Calibration and Jet Response

5.1 Data and Selections

The correction factors α and α_c from the previous section were derived in MC, where truth level information and the jet response are known. Since the correction factors are selected based on pileup corrected p_T and the $-log(L)$, which comes from the jet properties, the same correction factors can be applied in data.

This thesis makes use of the entire Run 2 dataset, 139 fb^{-1} of collision data at 13 TeV centre of mass energy, recorded from 2015-18. Two event types are studied, Dijet and Z + jet.

Pythia8 MC dijet samples were used in the previous section to develop the jet p_T corrections, and they are used here as a reference for the data results.

Z + jet MPF has been very extensively researched (see [48, 49]). Here, the MPF response of Z + jet events is determined in data as well as MadGraph-Pythia8 MC for reference. The Z + jet and dijet uncertainties are detailed in section 5.2.2.

ATLAS provides a level of pre-selection for different event types through the use of Derived Analysis Object Data (DAOD) files. Different DAODs are used for different analyses, and for dijet and Z + jet events the DAODs are known as JETM1 and JETM3. While these DAODs have been somewhat filtered through the ATLAS analysis framework to select only the desired events, additional cuts on the events and the physics objects within are required.

5.1.1 Dijet Events

For the study of dijets, several cuts on the event topology are needed. These cuts are performed using jets that are fully calibrated using the procedures described in section 3.2. First, both the leading and sub-leading jets in the event must be within the calorimeter barrel region, $|\eta| \leq 0.8$. The same two jets must be relatively back-to-back in the detector; $\Delta\phi^{J_1,J_2} > 2.9$. The third jet in a dijet event must not have p_T exceeding 12 GeV or $0.2 \times p_T^{J_1}$, whichever is greater. These final two cuts ensure the event has a dijet topology, with p_T balance.

Trigger Label	Working Point (GeV)
HLT_j15	20
HLT_j25	37
HLT_j35	50
HLT_j45	62
HLT_j60	76
HLT_j85	106
HLT_j110	132
HLT_j175	206
HLT_j260	300
HLT_j360	420
HLT_j420	470

Table 5.1: Jet triggers and working points. The name of each trigger indicates the threshold energy, though for 99% efficiency a higher p_T is needed.

The $\Delta\phi$ and third jet cuts reduce the effects of initial and final state radiation (ISR/FSR). ISR occurs when a parton is radiated by the incoming partons, and FSR is the same process but from the outgoing partons (after the collision). Both of these effects can ruin the assumption of the MPF calculation, that a reference object perfectly balances the recoil object.

Both the leading and sub-leading jets were required to have at least 8 GeV of p_T, and jets also had to pass the jet vertex tagger (JVT). The JVT tool performs a two-dimensional likelihood analysis to determine if a jet originates from the hard-scatter point, and not from in-time pileup. The output ranges from 0 to 1, with one being a guaranteed hard scatter jet. For the EMTopo jets used in this thesis, JVT > 0.59 is required. Jets must also pass overlap cuts. Other physics objects, such as electrons, can be reconstructed as jets, thus any jet within $\Delta R < 0.3$ of a reconstructed electron is rejected as a jet.

Finally, there are the jet triggers. Each event is required to pass a jet trigger using the average p_T of the leading and sub-leading jet. Each trigger has a 99% efficiency working point, and the trigger used is determined by comparing the working points to the average p_T of the first two jets. The triggers used, and their working points, are shown in table 5.1.

5.1.2 Z + Jet Events

Many of the cuts for Z + jet events are similar to the dijet cuts. The reconstructed Z boson must have a $\Delta\phi > 2.9$ with the leading jet, and the sub-leading jet cannot have more than 12 GeV or $0.3 \times p_T^{J_1}$. The leading jet must have $p_T > 12$ GeV, pass the same JVT cut as in the dijet events, and survive overlap removal.

Z + jet events, in the form of either Z→ ee or Z→ $\mu\mu$, must pass either electron or muon triggers. Electrons and muons must also pass likelihood and isolation conditions, which ensure the reconstructed leptons are not fakes and are well separated from other objects.

For each Z + jet event, there must be exactly two leptons representing the Z boson decay. The combined mass of these leptons must be within 66-116 GeV, which is loosely fixed around the mass of the Z, 91.19 GeV.

Further detail on the selections for Z + jet events can be found in [53], a dedicated Z + jet analysis.

5.2 Response Calculation

5.2.1 ClusterMET

Calculation of the dijet response requires a well defined reference object, which has been created using the correction factors. The other item needed is the missing transverse energy. ATLAS provides software tools for determining the MET (METMaker), but these tools do not correctly account for the energy loss of muons. However, the properties of the MET allow for a simple calculation to be performed.

To remedy the issues in the METMaker tool, a simple algorithm is used to calculate the missing transverse energy from clusters. First, the transverse momentum of every cluster is summed:

$$\vec{E}_T^{miss} = -\sum \vec{p}_T^{clusters} \tag{5.1}$$

Then, clusters associated with leptons are removed. Clusters do not describe muons well, so they and electrons are replaced by the leptons calibrated using the calorimeter and other parts of the detector. Clusters within $\Delta R = 0.2$ of the calibrated lepton are removed:

$$\vec{p}_{EM} = \sum^{\Delta R<0.2} \vec{p}_T^{clusters} \tag{5.2}$$

Adding the calibrated leptons:

$$\vec{E}_T^{miss} = -\sum \vec{p}_T^{clusters} + \sum(\vec{p}_{EM} - \vec{P}_T^l) \tag{5.3}$$

In removing the clusters earlier, pileup was also removed from those regions. To ensure the vector sum of pileup remains zero, an estimate of the pileup must be added back. This is typically done by estimating the pileup energy density in low occupancy regions of the detector and projecting this energy around the leptons.

$$\vec{E}_T^{miss} = -\sum \vec{p}_t^{clusters} + \sum(\vec{p}_{EM} - \vec{P}_t^l - \hat{P}_t^l \cdot \rho \cdot \pi(0.2)^2) \tag{5.4}$$

where ρ is the pileup energy density. This provides a simple calculation of the MET, improving on the METMaker tool by re-incorporating the pileup previously removed. Cluster association is done here by ΔR, while in METMaker it is done with ghost association. This MET calculation has been implemented in multiple studies and is used in MPF calculations to provide the primary ATLAS insitu jet calibration.

Clusters are not available in JETM1 DAODs, as these events are exceedingly large already. Thus, a clusterMET tool was developed at derivation level to save the MET in the x and y direction as simple variables to be accessed in DAODs. This allows the proven clusterMET algorithm to be implemented in the dijet MPF calculation. Unfortunately, limitations in the derivation framework mean that uncalibrated leptons had to be used in the clusterMET tool. Because of this, the tool is only applicable to dijets at this time, with the use of an offline correction.

Since one of the jets in a dijet event is corrected to truth level using the alpha correction, the contribution to the MET from this jet must be adjusted. The difference in p_T between the pileup-subtracted reference jet and the alpha-corrected reference jet is subtracted from the clusterMET in each event.

5.2.2 Uncertainty

There are large uncertainties associated with the likelihood/α-correction technique, caused by the very broad response distributions of jets in the detector. In the 2016 version of this study the uncertainty on the dijet response and the final quark and gluon responses was quite large [56]. Here, the same sources of uncertainty are considered to see if the increase in available data has reduced their scale.

In the standard MPF calculation with Z + jet events, such as in the precision recommendations for ATLAS jet calibrations [49], the uncertainty in the response measurement is a combination of lepton scale/resolution, variation of ISR/FSR, variation of the JVT, and a statistical component. There is also an uncertainty from differences in the results of different MC generators.

The dijet response uncertainty is a combination of the σ_{α_c} (the α_c uncertainty) from the previous chapter with variations of the high and low response cuts, variations of the correlation cut, and ISR/FSR cut variations. Varying the high/low response and correlation cuts creates different variable lists used in the likelihood/response relationship. This gives different correction factors as well as a different set of α_c values. The α_c uncertainty (from the nominal cuts) is taken as symmetric in the positive and negative direction. The uncertainties for the three variations mentioned are quite small, so the largest deviation in either direction is taken as the uncertainty, as opposed to using a different uncertainty for the positive and negative directions.

The α_c uncertainty ranges from 14 to 5% (relative to the dijet response) across the p_T range (figure 4.23), and is the largest uncertainty on the dijet response. It is important to

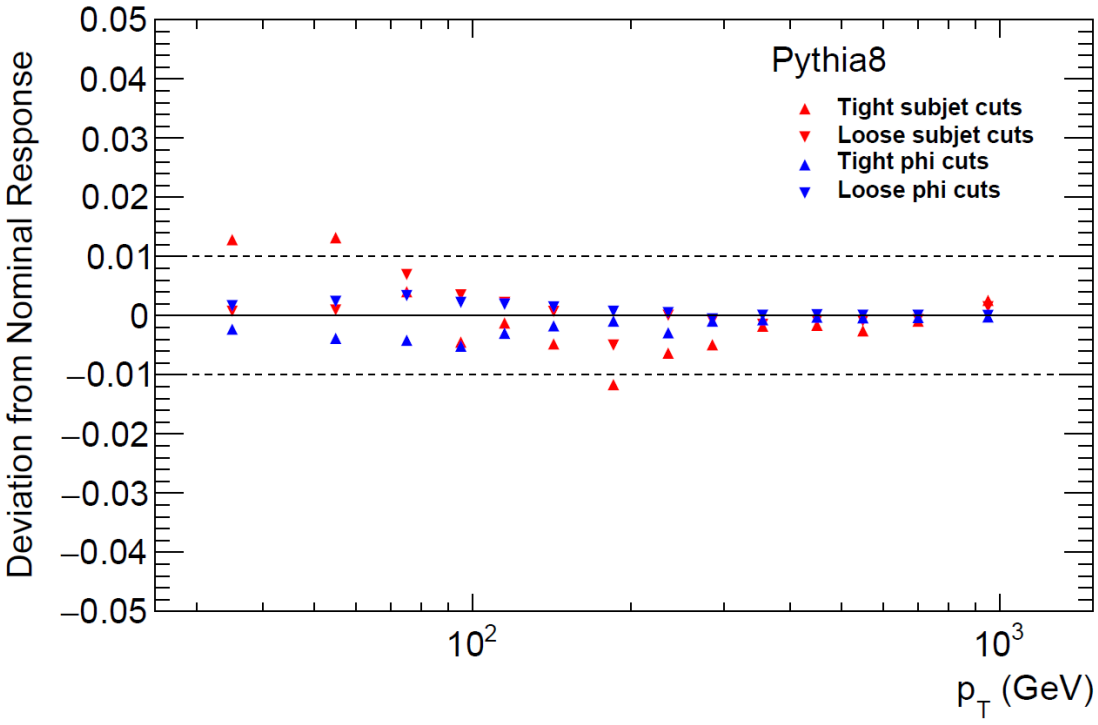

Figure 5.1: Relative dijet MPF response difference between the nominal and varied ISR/FSR cuts in Pythia8 Monte Carlo.

note that this is less an inaccuracy in the correction factor, but an effect of the fluctuations in jet development.

The ISR/FSR cuts on $\Delta\phi$ and the momentum of the third jet in the event are varied between tight and loose selection criteria. The $\Delta\phi$ cut, nominally 2.9 between the leading and sub-leading jet in a dijet event, is tightened and loosened to 3.0 and 2.8, respectively. The cut on the third jet is varied to a tighter selection of 0.1 $\times p_T^{lead}$ or 10 GeV, and a looser selection of 0.3 $\times p_T^{lead}$, from a nominal selection of 0.2 $\times p_T^{lead}$ or 12 GeV. The effects of these variations are shown in MC in figure 5.1 and in data in figure 5.2. The largest deviation for each of the ISR/FSR cuts is used as an uncertainty. For MC, the uncertainties are highest at low p_T (with some exceptions) and rarely greater than 1%. In data the uncertainties also trend downward with p_T, but here they are as high as 3%.

Variation of the response classification, the definition of what is considered a high response or low response jet, had little effect on the MPF results. The nominal result using jets with a response greater than 0.9 as high response and less than 0.7 as low response is known as 9070. The response cuts were varied three times; to 9050, 8070, and 8050. Figures 5.3 and 5.4 show the results of these variations on the MPF in MC and data, respectively. The results are similar for both MC and data, and the uncertainty is less than 0.1% across the full p_T range in both, and does not show significant dependence on the jet momentum.

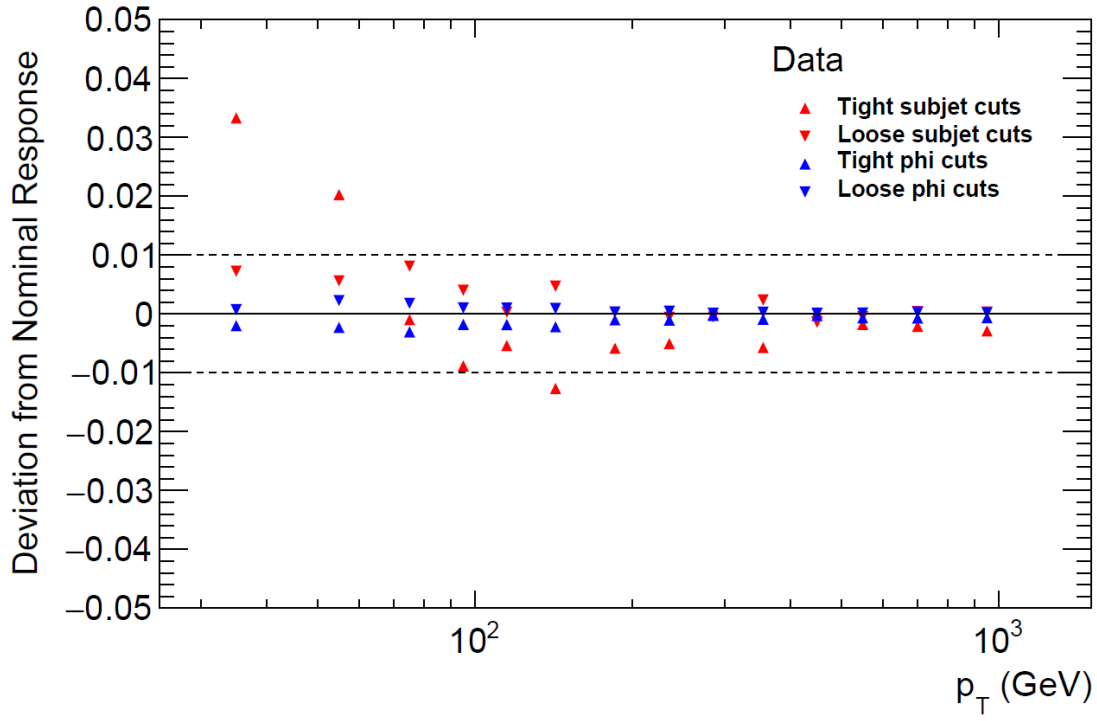

Figure 5.2: Relative dijet MPF response difference between the nominal and varied ISR/FSR cuts in data.

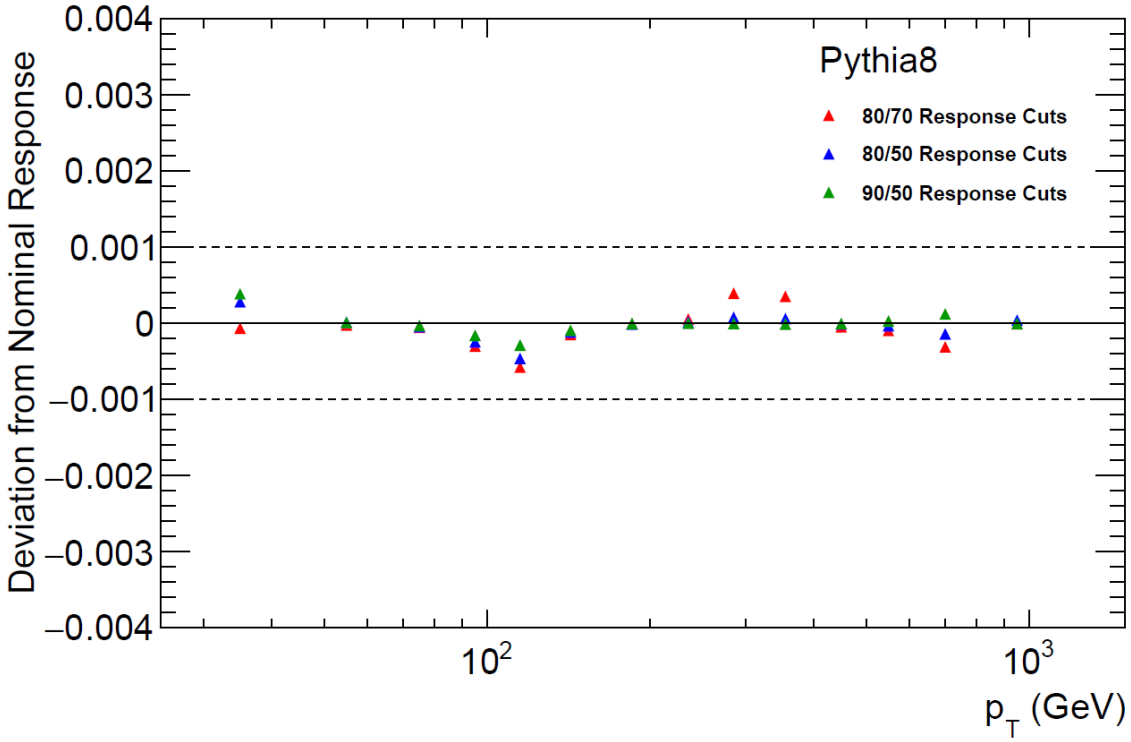

Figure 5.3: Relative dijet MPF response difference between the nominal and varied response classification cuts in Pythia8 Monte Carlo.

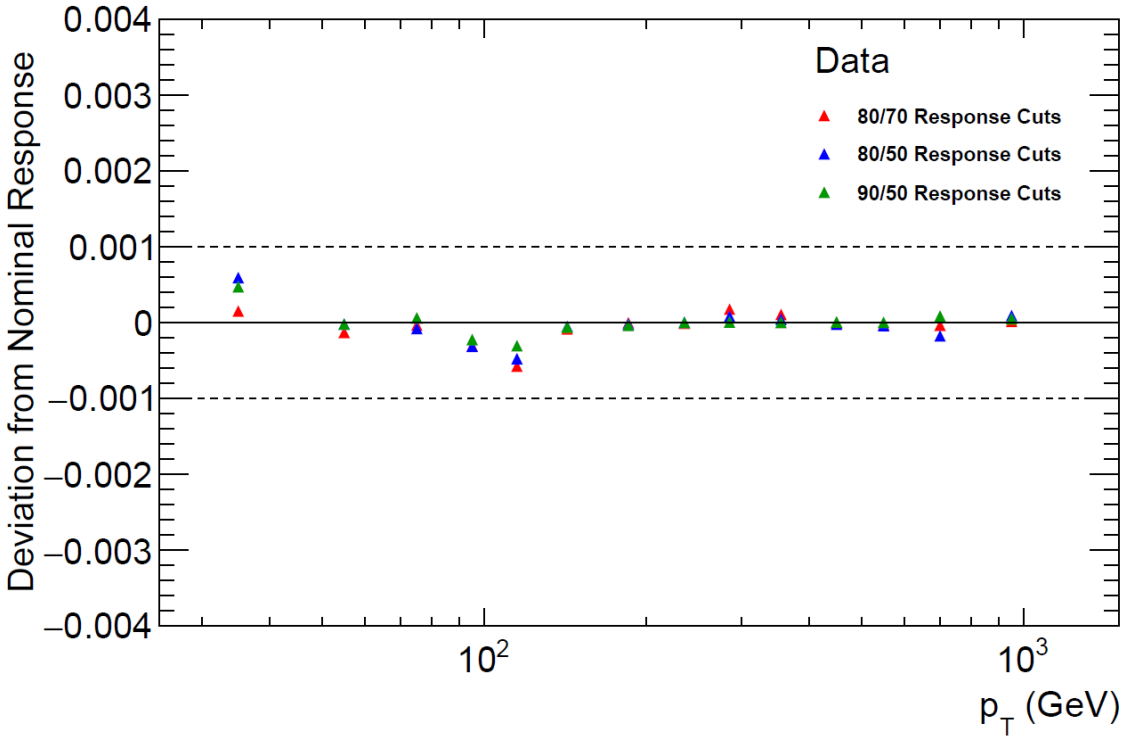

Figure 5.4: Relative dijet MPF response difference between the nominal and varied response classification cuts in data.

Lastly, the correlation cut used in the selection of jet variables for the likelihood function is varied. Not only does this change the variables used in the likelihood function, but it increases the number that can be used. With the nominal correlation cut of ± 0.4 only six variables could be used in each likelihood, as the others would be eliminated by the correlations[1]. With looser cuts of ± 0.6 and ± 0.8, eight and ten variables could be used. The MPF calculated with these variations is shown in MC in figure 5.5 and in data in figure 5.6. Once again the uncertainties are very small, below 1% in MC with little dependence on p_T. In data the results are also small, and only the lowest p_T bin has an uncertainty greater than 1%.

Overall, the uncertainty in the dijet response is dominated by σ_{α_c}. The four uncertainties described here are added in quadrature to provide the total uncertainty on the dijet response.

For the Z+jet MPF response, the uncertainty is derived within the insitu framework mentioned above. This uncertainty has several components, including lepton scale and resolution, variations of the jet vertex tool, $\Delta\phi$, and sub-jet cuts. The framework also includes a statistical uncertainty and a component from variations between a nominal and alternative MC. The combined effects of these uncertainties, as well as of the individual components,

[1]Some momentum bins may have had more variables available after the cuts, but it was decided that each bin should use the same number of jet properties.

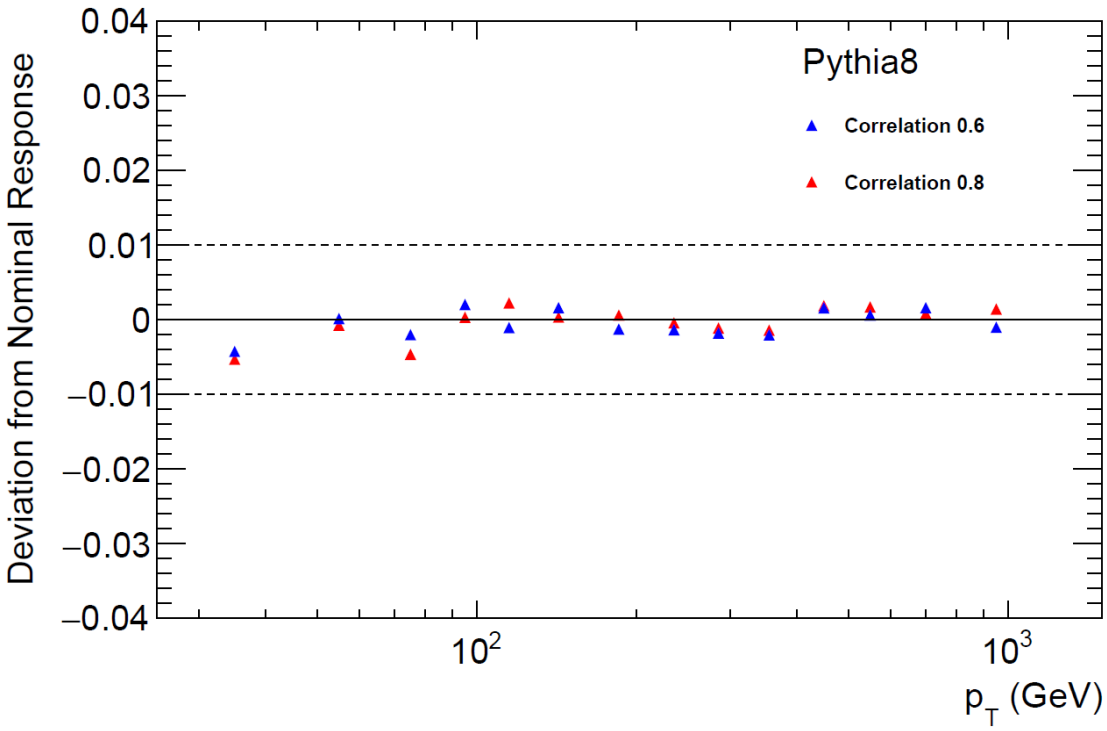

Figure 5.5: Relative dijet MPF response difference between the nominal and varied correlation cuts in Pythia8 Monte Carlo.

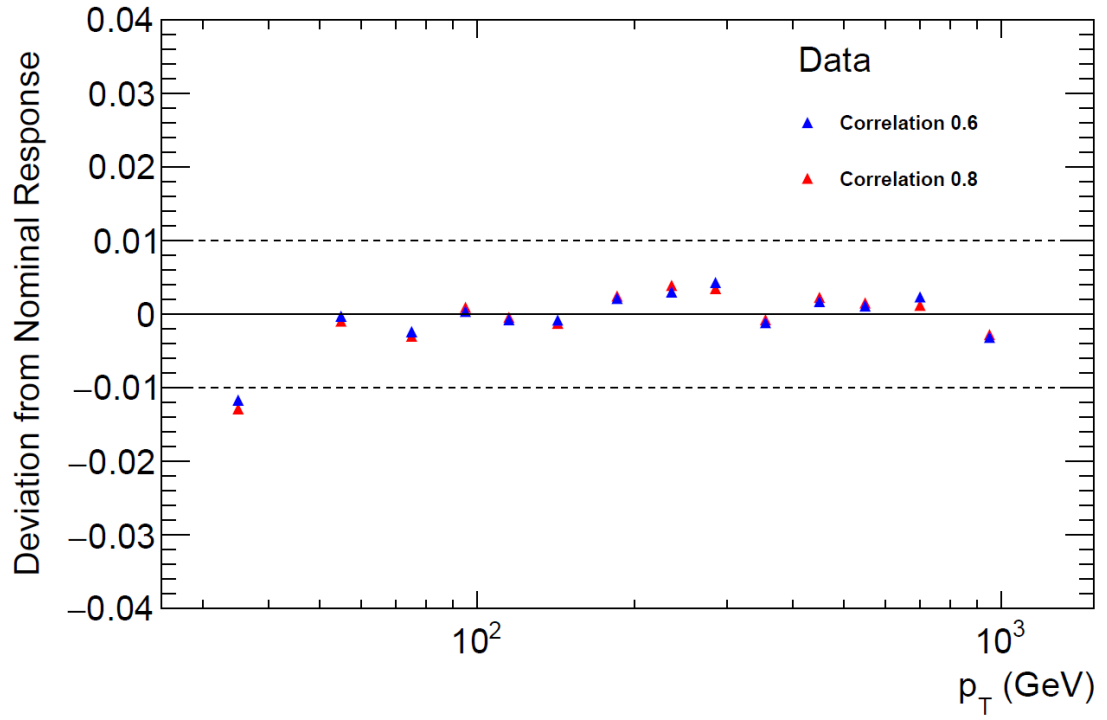

Figure 5.6: Relative dijet MPF response difference between the nominal and varied correlation cuts in Data.

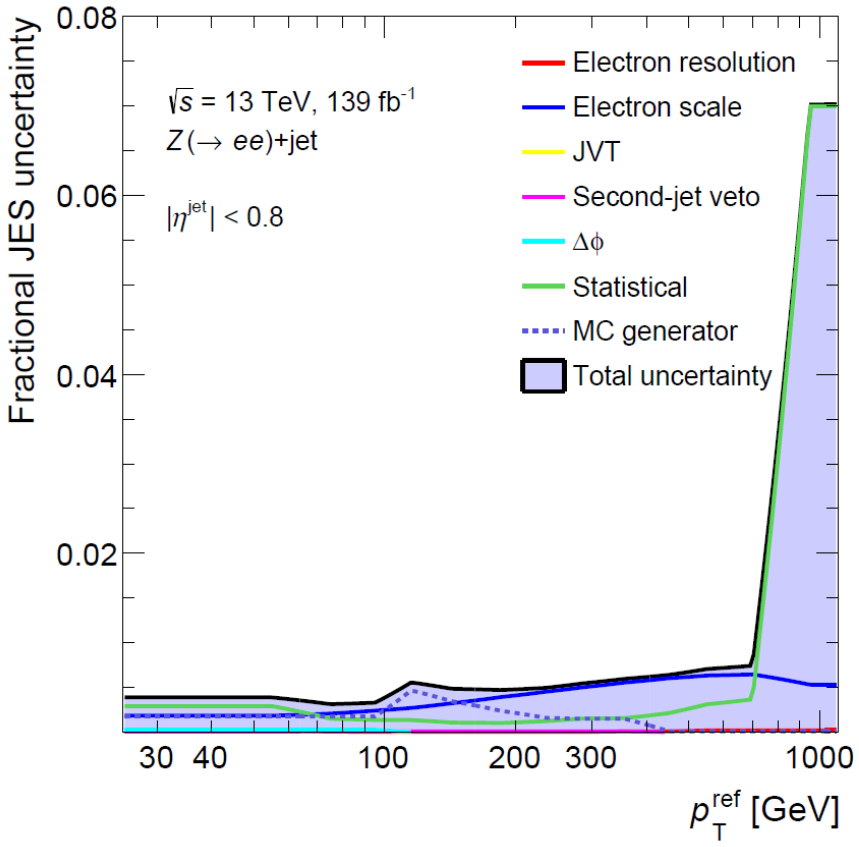

Figure 5.7: Z + jet MPF uncertainties.

are shown in figure 5.7. The combined uncertainty is typically below 1%, except for the highest momentum bin which includes a large statistical uncertainty due to a drop off in available data, owing to the falling Z+jet cross-section as a function of p_T.

5.2.3 Results

Calculation of the dijet MPF depends on whether the leading or sub-leading jet is selected as the reference object. If the leading jet is used as the reference, then the probe jet is the sub-leading jet, and vice-versa. This is not a problem in Z + jet events, where only one jet is considered in the momentum balance. Here the leading jet in each dijet event was selected to act as the reference object. Generally, the higher-p_T leading jet will have a higher response and thus will require less of a correction using the likelihood technique. The probe jet, for which the MPF response is calculated, is then the sub-leading jet. The above jet property/likelihood study was completed specifically on the leading jets, to ensure the correction factors were accurate. Additionally, calculation of the quark and gluon jet responses in the next section accounts for the selection of the leading jet as the reference. Since the dijet response is calculated for the sub-leading jet, the dijet flavour fractions

are also calculated for the sub-leading jet. Appendix B shows the results of an alternative calculation with the MPF calculated twice per event using each jet as the reference.

Calculation of the MPF is performed using both transverse directions, x and y in figure 2.3a. With this in mind, equation 3.7 becomes:

$$R_{MPF} = 1 + \frac{(E_{T,x}^{miss,\,corr} \cdot p_{T,x}^{ref,\,corr})(E_{T,y}^{miss,\,corr} \cdot p_{T,y}^{ref,\,corr})}{(p_T^{ref,\,corr})^2} \tag{5.5}$$

This is essentially $E^{measured}/E^{true}$ for the recoil. The dijet response (figure 5.8) is recorded in momentum-binned histograms and extracted using the same double-fitting technique described earlier, where the MPF histogram is fitted to a Gaussian and refitted to $\pm 2\sigma$. Both the data and the MC trend upward with p_T, from around 0.55 to nearly 0.8, as expected from previous studies. The data and MC results agree well within uncertainties, with the greatest differences occurring in the second p_T bin and from roughly 100 to 300 GeV. Both data and MC results have large uncertainties at low p_T, greater than 10%, primarily due to the alpha closure. The uncertainty reduces with increasing p_T. This result agrees with the earlier results from [56] well within uncertainties.

While the variable-likelihood-based correction can generally bring the reference jet p_T to within 1% of truth level, it varies greatly between events due to fluctuations in jet formation and calorimeter interactions. As was seen in the previous chapter, even the variables that provide the best separation between signal and background jets have broad distributions with significant overlap, which propagates through to the alpha corrections.

The Z+jet response (fig. 5.9) derived here agrees well with earlier derivations for EM-Topo jets, such as in ref. [53]. The response increases from roughly 0.45 to 0.8 over the p_T spectra. The data are generally less than 5% lower than the MC, decreasing with increasing p_T. The large uncertainty in the final bin, from the drop in available data, is visible in the response curve.

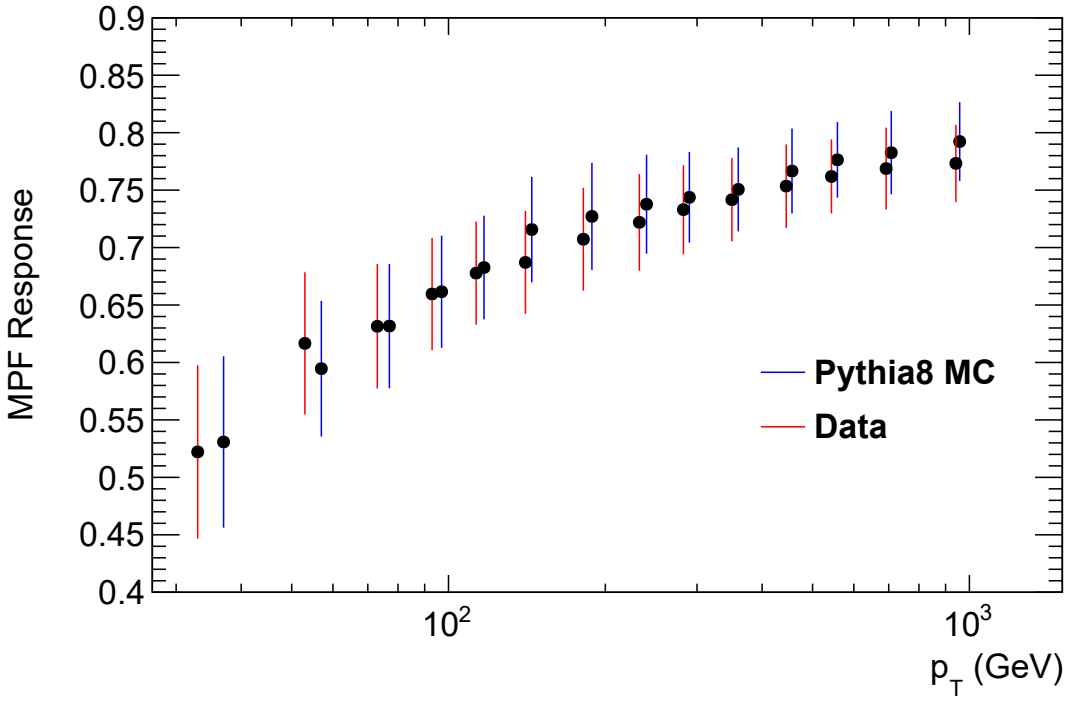

Figure 5.8: The dijet MPF response calculated in Pythia8 MC and data using a jet property likelihood function.

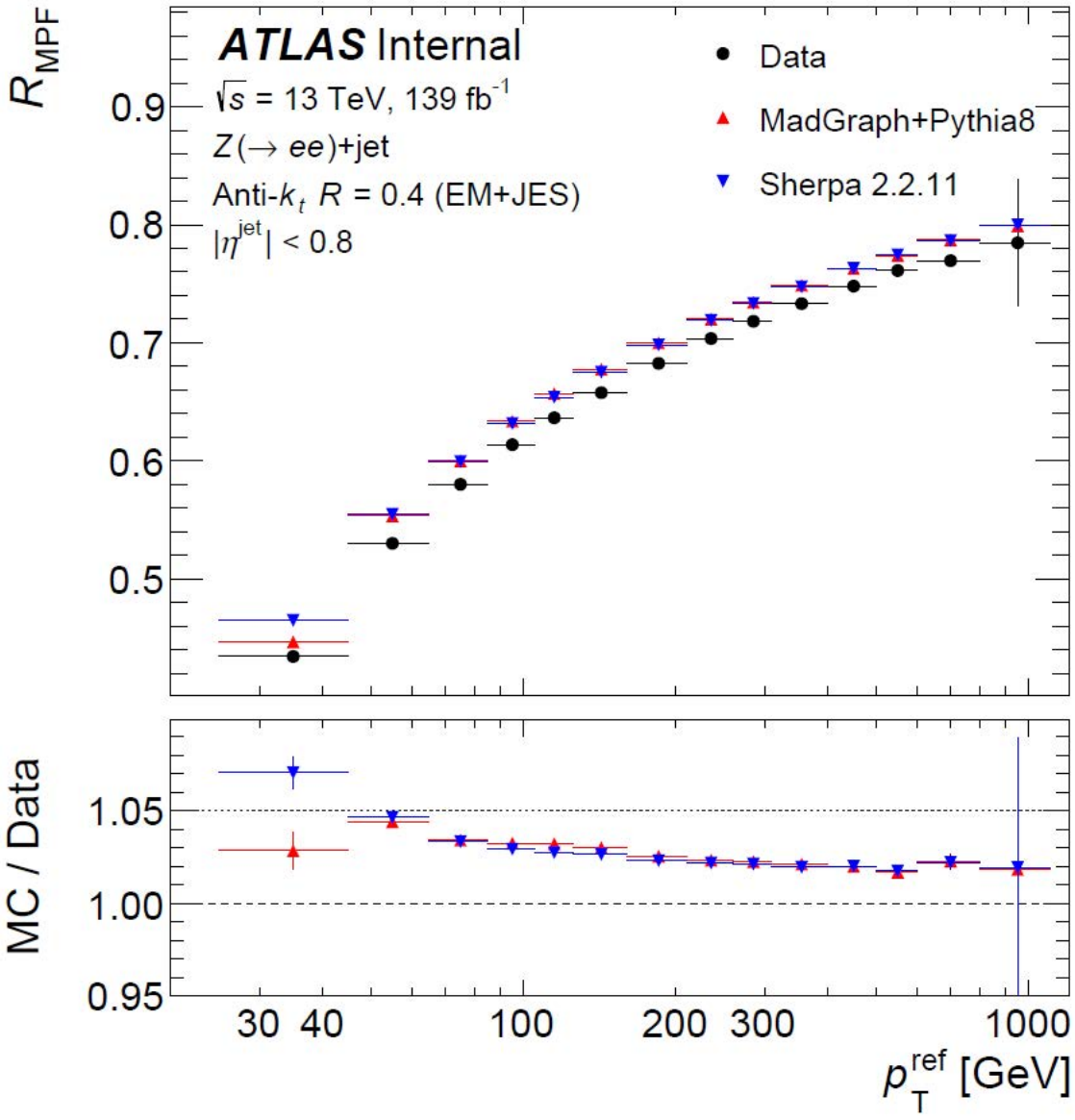

Figure 5.9: Jet MPF response in Z + jet events, shown in data and two MC generators.

Chapter 6

Quark and Gluon Response

With the Dijet and Z + jet responses determined, all that is needed to calculate the light quark and gluon jet responses are the flavour fractions and charm quark jet response. These are determined in MC, where parton/particle-level information allows the jet flavour to be known.

To estimate an uncertainty on the flavour fractions, alternative MC generators are used in both event topologies. The relative variation between the nominal and alternative MC is taken as an uncertainty in each p_T bin.

Figures 6.1 and 6.2 show the parton flavour fractions in dijets and Z + jet events. In both plots it is clear that charm quarks are overshadowed by lighter quarks and gluons, which is expected. In Z + jet events the light quark and gluon fractions are similar at low p_T and diverge as the transverse momentum increases, with light quarks becoming the majority. In dijets, the gluon fraction is much larger than the light quark fraction at low p_T and falls with increasing p_T. The two fractions cross at roughly 400 GeV, from which point the light quark fraction is the largest. The dijet flavour fractions determined here are consistent with the results from the 2016 study, and the flavour fractions of both events are compatible with $\sqrt{s} = 8$ TeV results from [57].

The charm quark jet response, determined by $p_T^{PileCorr}/p_T^{truth}$ for jets labelled as charm initiated in MC, is shown in figure 6.3. The charm response increases from 0.67 (0.60) to 0.85 in Pythia8 (Herwig7) over the p_T range. Pythia7 is the nominal MC, and these values will be used in further calculations. Herwig7 provides the uncertainty on the charm jet response through its relative variation from Pythia. The two MC generators show less than 3% variation in all but the lowest momentum bin, where the Pythia charm jet response is 10% higher.

6.1 Uncertainty

For the uncertainty on the final results, the fluctuation in the responses with respect to the different inputs must be considered. Some assumptions are made to simplify the propagation

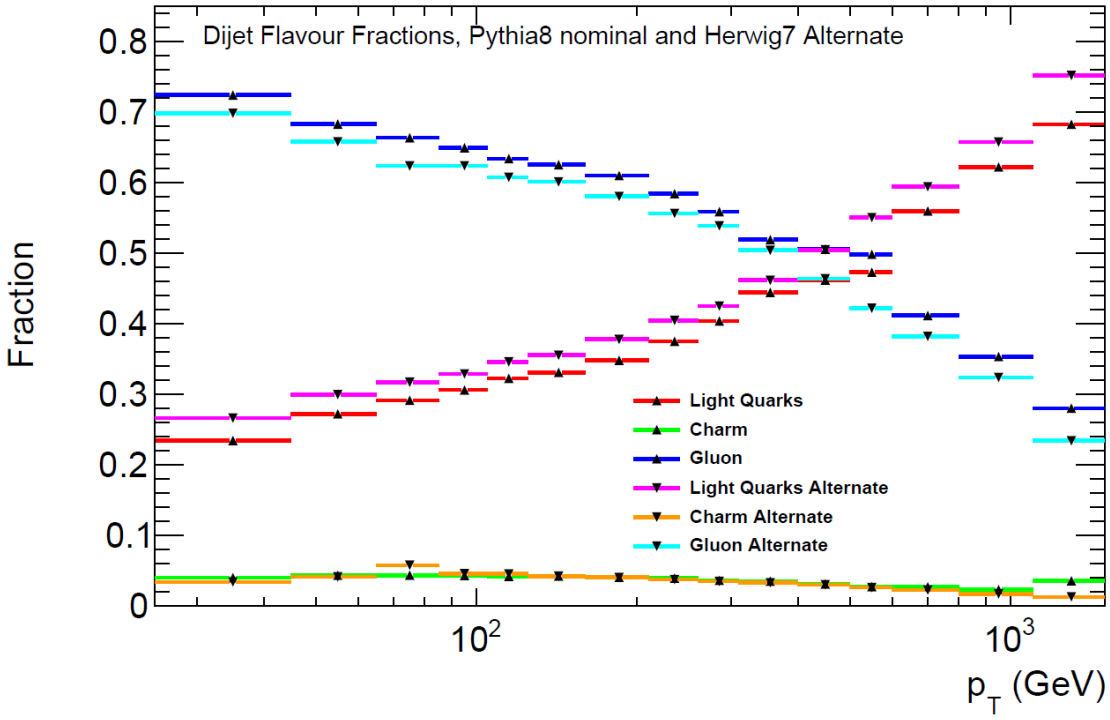

Figure 6.1: Parton flavour fractions in dijet events. A second MC, Herwig7, was used in addition to the nominal Pythia8 to determine the uncertainty in the flavour fractions.

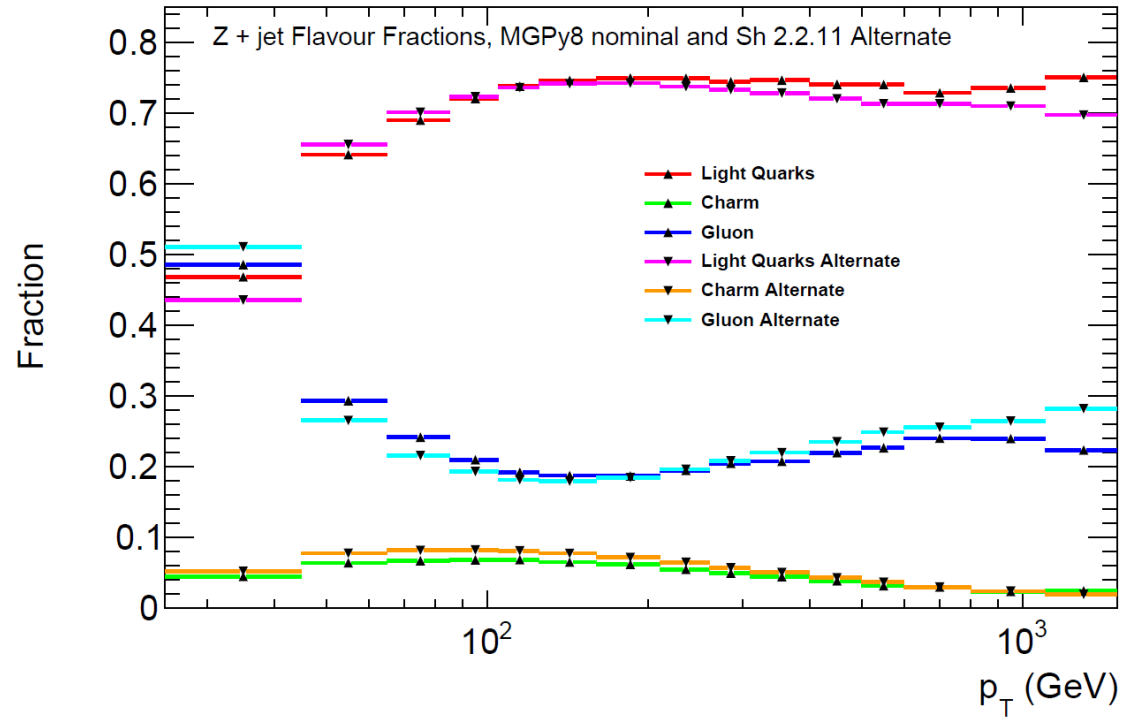

Figure 6.2: Parton flavour fractions in Z + jet events. The nominal MC here is Madgraph Pythia8, while Sherpa 2.2.11 is used to determine the uncertainty.

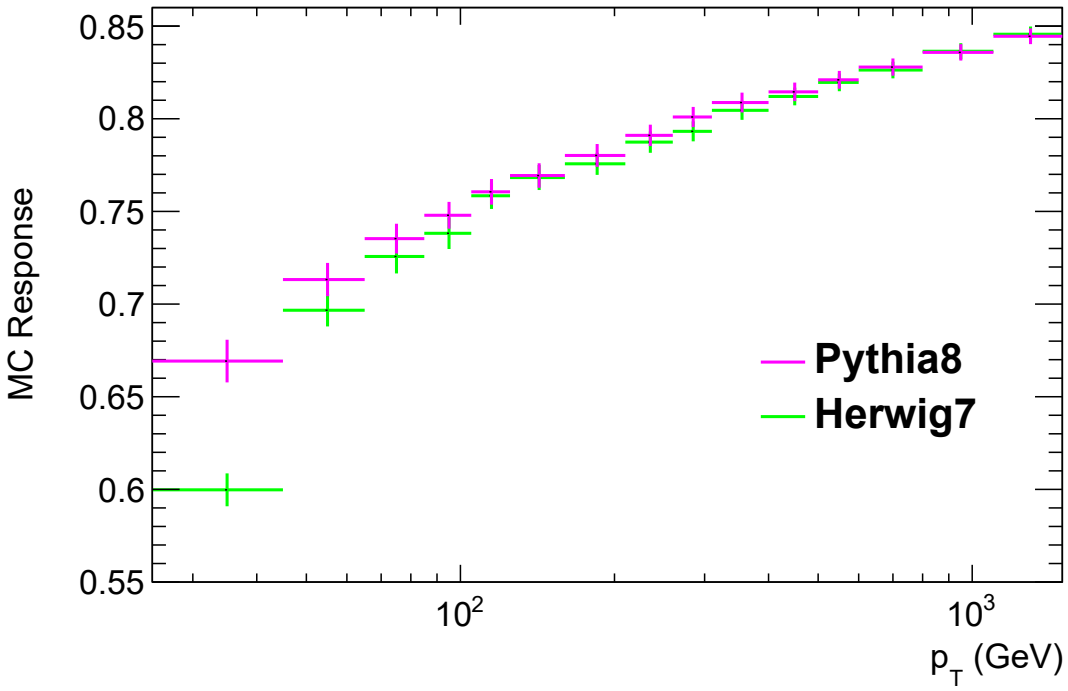

Figure 6.3: The response of charm jets in Pythia8 and Herwig7 MC.

of uncertainties. First, the charm quark fractions are assumed to be small enough and known well enough to ignore the uncertainties. This in turn allows the light quark and gluon fractions to be treated as fully anti-correlated, and the relationship

$$f_{lq} + f_g + f_c = 1, \tag{6.1}$$

means that one of the quark or gluon fractions can be substituted in 3.13 and 3.12. Thus, only the larger of the light quark and gluon fraction uncertainties is used for each event topology. Second, the jet responses of dijet and Z + jet events are considered independent for this study.

These assumptions allow the final quark and gluon jet response uncertainties to be constructed from five factors: The dijet and Z + jet response uncertainties, the dijet quark fraction and Z + jet gluon fraction uncertainties, and the MC charm quark response uncertainty.

The uncertainties are propagated using partial derivatives through equations 3.13 and 3.12. For example, the dijet response uncertainty component for the quark(gluon) jet response is given by:

$$\Delta R^{q/g}(\Delta R_{DJ}) = \frac{\partial R^{q/g}}{\partial R_{DJ}} \Delta R_{DJ} \tag{6.2}$$

This and the other uncertainty terms are derived in greater detail in appendix A. The five uncertainty terms are combined in quadrature for each of the final quark and gluon response uncertainties.

6.2 Results

Combining the previous results for jet response and flavour fractions, the quark and gluon jet response can be determined. Figures 6.4 and 6.5 show the response for quark and gluon-initiated jets, respectively. The quark response behaves as expected after the first momentum bin, rising from approximately 0.5 to 0.8 over the momentum range. For all points, MC and data agree within uncertainty. The uncertainties are largest in the lowest and highest momentum bins, and smallest in the middle of the p_T range. Overall, the results for quark jet responses are similar to those seen in the 2016 study, though the uncertainties are smaller here aside from the highest p_T bin.

The gluon response in figure 6.5 includes some unexpected features. It starts considerably higher than the quark response at low p_T, around 0.6. It was expected, based on the physics of jet development, that the gluon response would be lower than that of the quark, but this is not the case here. Both data and MC increase over the momentum range and agree with each other within uncertainties. The central p_T region has the smallest uncertainties, though they are larger than in the quark response, while the lowest and highest bins have larger errors.

The large uncertainties in the first and last bins of both parton responses can be explained by the sources of uncertainty. σ_{α_c} represents the difficulties in labelling jets as high or low response based on their properties in the detector, and in the lowest momentum bin, where jet fluctuations are relatively larger, this has a large effect on the uncertainty. In the flavour plots (figures 6.1 and 6.2), It is clear that the largest variations in the light quark and gluon fractions occur at the highest and lowest p_T bins. The statistical uncertainty in the Z+jet response at high p_T (fig. 5.7) contributes significantly to the large uncertainties in the highest momentum bin. Overall, the uncertainties are similar to or smaller than previous studies.

Looking back to the equations for quark and gluon response (3.13, 3.12), it is useful to consider how the various inputs affect the final results. In each bin, the gluon response increases with increasing dijet response and decreases with increasing Z + jet response. The opposite is true for the quark response. The dijet and Z + jet responses determined in Chapter 5 are consistent with existing results. The charm jet response has positive and negative contributions to both the quark and gluon jet responses, and the small charm fractions minimize these effects regardless. The flavour fractions are also consistent with other studies. Thus, all of the inputs to the quark and gluon jet responses have been verified, and these measurements do not appear to be the issue.

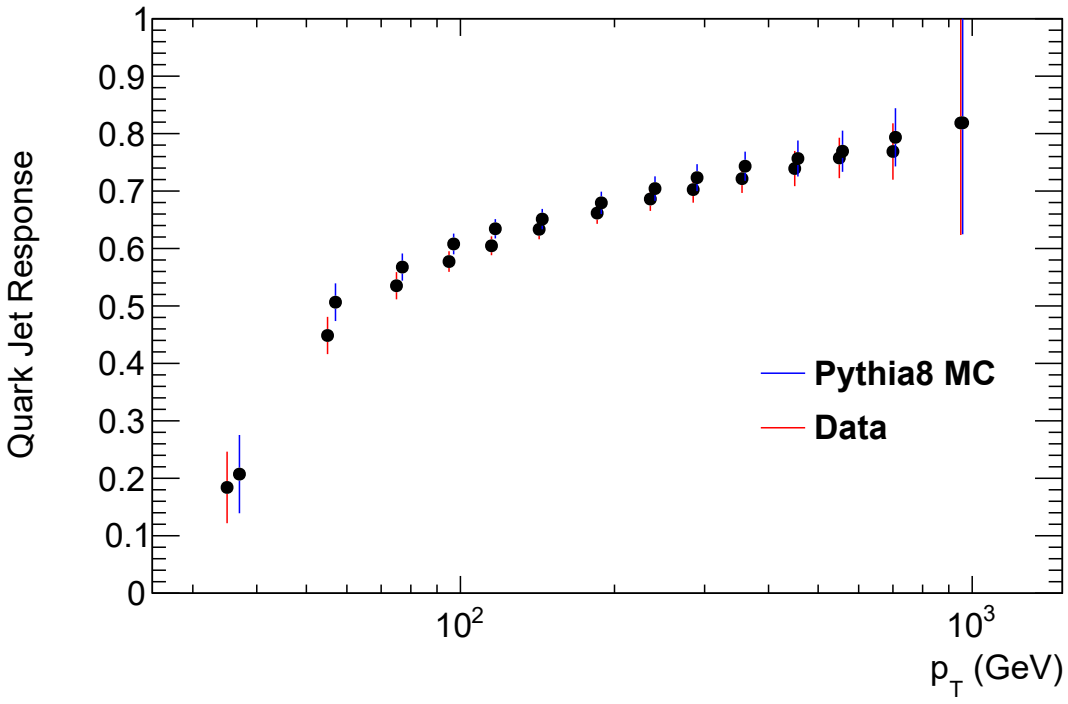

Figure 6.4: The calculated response of quark-initiated jets in MC and data. The response calculated here behaves as expected, increasing with pt. MC and data agree well within the uncertainties.

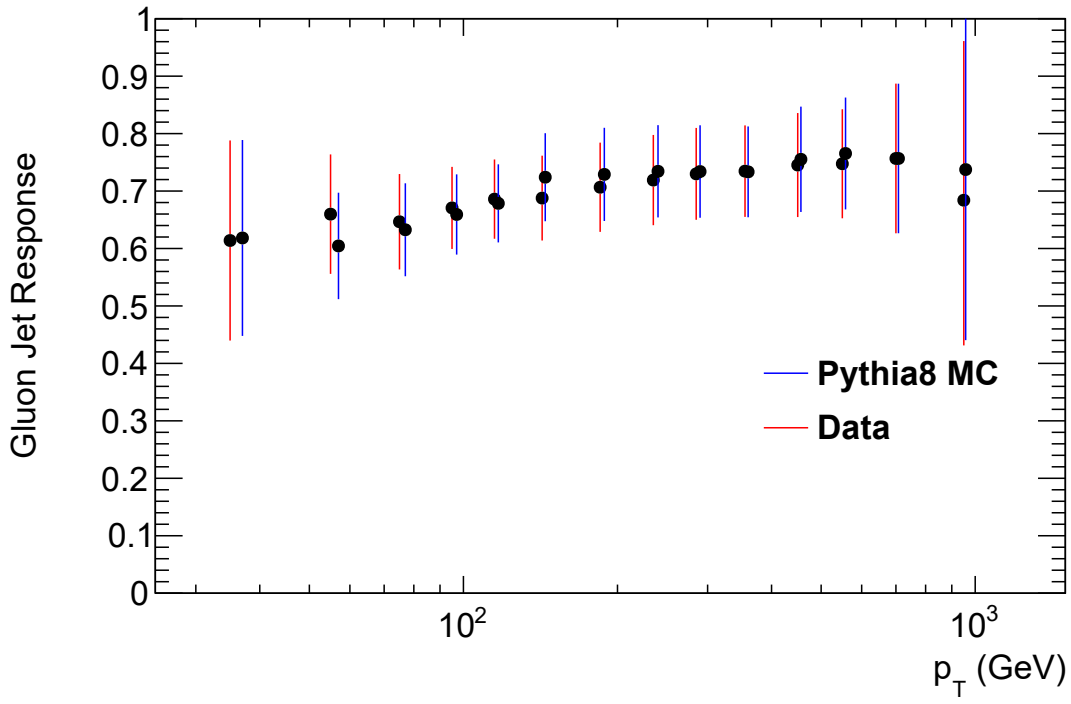

Figure 6.5: The gluon initiated jet response calculated in MC and data. While the data and MC results agree within the uncertainties, the overall behaviour is not consistent with previous studies. The response is considerably higher than expected at low p_t.

The choice of Z + jet as the second event type (instead of γ + jet) may be an issue in itself. The kinematics of creating a massive Z boson versus a massless photon are very different, which changes how the partons are sampled and leads to different flavour fractions. Comparing the flavour fractions in Z + jet events (fig. 6.2) with the flavour fractions in γ + jet events (fig. 6.6), large differences are seen in the low p_T region. Over the momentum range studied, photon plus jet production is always dominated by quark-gluon Compton scattering (see figure 3.6, left side) which produces quark jets, while for Z + jet production quark/antiquark annihilation (figure 3.6, right side) plays a much larger role at low p_T, and produces gluon jets. The light-quark and gluon fractions that begin close together in Z + jet events are much more separated in γ + jet events. While neither appears particularly similar to the dijet flavour fractions at low p_T, the γ + jet is almost the opposite, while the Z + jet is closer.

Two observables (in this case, dijet and Z + jet events) which are too similar in representing the physics make for poor discriminants. Here, the parton flavour fractions of Z + jet events are too similar to those of dijet events. No improvement in the measurement of the dijet response can change this, and this method of quark and gluon jet response calculation will always work better with γ + jet events rather than Z + jet.

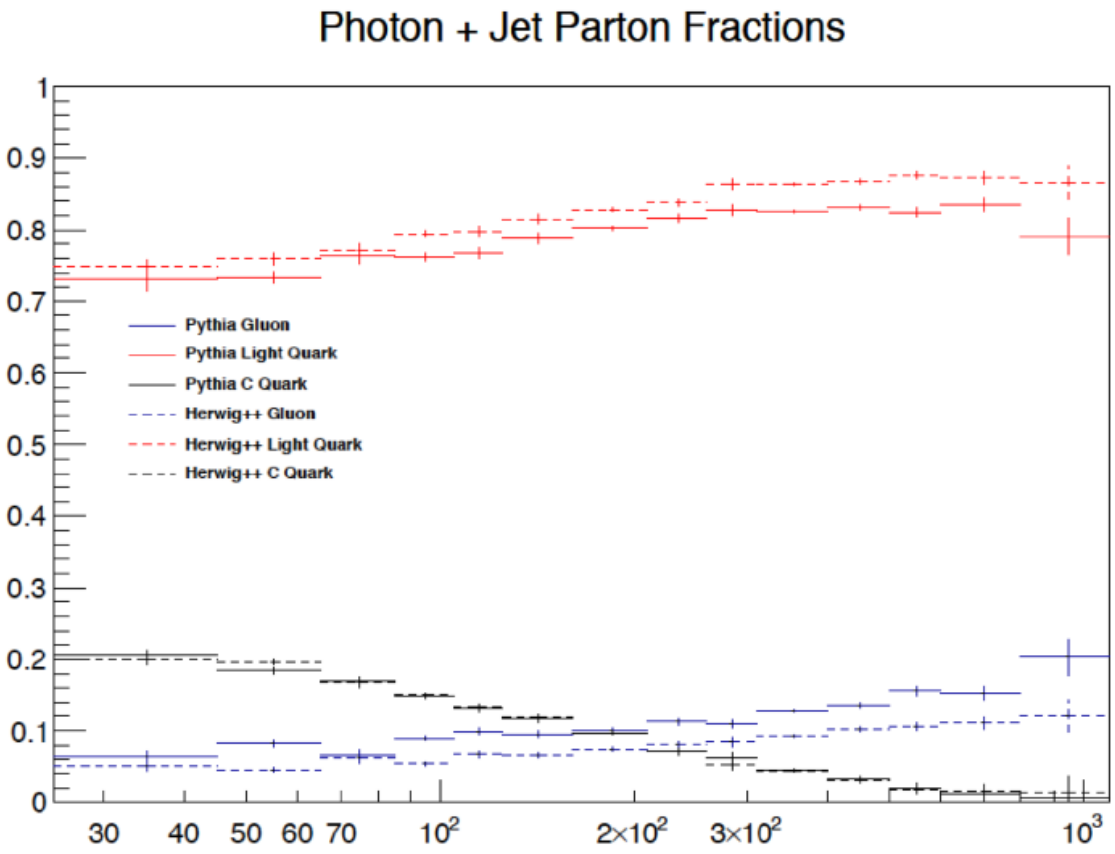

Figure 6.6: Parton flavour fractions in γ + jet events, from [56]. The difference between this and the Z + jet events at low p_T contributes to the discrepancies seen in the quark and gluon response.

Chapter 7

Conclusion

The primary objective of this thesis was to determine the responses of jets initiated by quarks and gluons. While a reasonable result was obtained for quark jets, the calculated response of gluon jets was larger than expected. The gluon jet response should be lower than that of the quark, as jets initiated by gluons generally have more, lower-energy particles due to colour factors and the physics of jet development. This should result in a lower measured jet response. Only in the highest momentum ranges probed in this study did the quark jet response surpass the gluon. The uncertainties in the highest and lowest momentum bins were large, roughly 30%, but the central momentum region had a more reasonable 5-10% uncertainty.

The quark and gluon responses were calculated using the jet responses and flavour fractions of two different event types, Z + jet and dijets. The flavour fractions were determined in MC through existing parton labels, and the Z + jet response was calculated using the established ATLAS in-situ MPF framework. For dijets, the standard MPF calculation was not immediately usable as no clear reference object existed. The other focus of this research was to modify dijet events to make them suitable for the MPF calculation.

An array of jet properties were studied in MC and ranked depending on how well they discriminated between high and low-response jets. The probabilities of high response across multiple variables were combined to create a likelihood function that showed a clear correlation with jet response. Fitting this likelihood function provided a map between jet response and jet properties. This allowed for jets in data, where the response was not known, to be corrected to their true momentum. Once one of the jets in a dijet was corrected, it could serve as a reference for an MPF calculation of the other jet's response.

Here the study was successful. It was shown that on average the correction factors bring the jets very close to their true momentum, and the dijet response calculated this way was well within expectations. The same sources of uncertainty were considered as in earlier studies, and the resulting calculated uncertainty was significantly lower than before, ranging from roughly 14-4% with increasing p_T. Also, a new Missing Transverse Energy algorithm was created and tested at the derivation level of the ATLAS analysis chain. The algorithm

provides a simple and efficient MET calculation that would otherwise not be available in certain data types, and the saved results are space-efficient. Though more work is needed regarding leptons to improve the algorithm, the ClusterMET tool is a useful starting point for a derivation-level, cluster-based MET calculation.

Jet properties show significant overlap when discriminating between high and low response jets, which resulted in a large uncertainty. Improving the resolution of the alpha correction *would* allow the dijet response to be known with much greater certainty, but the inaccuracies in the alpha correction are more a result of physics than of technique. Fluctuations in jet properties and response are the largest contributors to the uncertainty in the dijet response, and these are inherent to the measurement of jets. The statistical methods used here to rank the variables could be improved upon to create a more accurate likelihood function, though it is unlikely this would improve the final result significantly. The same methods were used here as in earlier studies to allow for a more direct comparison with earlier results.

There are different ways the quark and gluon response can be determined after the dijet response is calculated. This thesis only considered light quarks, gluons, and charm quarks, though bottom quarks could also be included (though this would likely be a small effect). In both event types, the charm quark fraction was low and indeed the bottom quark fraction would be lower still, but it should be investigated nonetheless.

There is also the matter of which secondary event type to use. Z + jet events could be replaced here by γ + jet events, as were used in the previous study. Based on the flavour fractions of these event types, photon events appear to be a better candidate for comparison against dijets. The Z + jet flavour profile is too similar to that of the dijet at low p_T. It would be valuable to attempt this study again using γ + jet events, or even with all three event types used together. This, along with the inclusion of bottom quarks, would add more sources of uncertainty, but would also increase the available information and allow for a more complete picture of the quark and gluon responses.

Overall, the research here succeeded in showcasing the efficacy of the likelihood/α-correction method of preparing dijets for MPF calibration. The research also demonstrates the complexities of working with jets and the difficulties of using measured jet properties to determine parton level information.

Bibliography

[1] Mark Thomson. *Modern particle physics*. Cambridge University Press, Cambridge, United Kingdom; New York, 2013.

[2] Wikipedia User: MissMJ. Standard model of elementary particles.svg. Online, accessed 19 September 2022 from `https://en.m.wikipedia.org/wiki/File:Standard_Model_of_Elementary_Particles.svg`.

[3] David J. Griffiths. *Introduction to elementary particles*. Physics textbook. Wiley-VCH, Weinheim, 2., rev. ed., 5. reprint edition, 2011.

[4] Wikipedia User: Ponor. All standard model vertices.svg. Online, accessed 8 May 2023 from `https://commons.wikimedia.org/wiki/File:Standard_Model_%E2%80%93_All_Feynman_diagram_vertices.svg`.

[5] Particle Data Group. Review of Particle Physics. *Progress of Theoretical and Experimental Physics*, 2022(8):083C01, August 2022.

[6] Luigi Di Lella and Carlo Rubbia. The Discovery of the W and Z Particles. In *Advanced Series on Directions in High Energy Physics*, volume 23, pages 137–163. WORLD SCIENTIFIC, September 2015.

[7] C. S. Wu, E. Ambler, R. W. Hayward, D. D. Hoppes, and R. P. Hudson. Experimental test of parity conservation in beta decay. *Phys. Rev.*, 105:1413–1415, Feb 1957.

[8] Peter W. Higgs. Broken Symmetries and the Masses of Gauge Bosons. *Physical Review Letters*, 13(16):508–509, October 1964. Publisher: American Physical Society.

[9] F. Englert and R. Brout. Broken Symmetry and the Mass of Gauge Vector Mesons. *Physical Review Letters*, 13(9):321–323, August 1964. Publisher: American Physical Society.

[10] Steven Weinberg. A model of leptons. *Phys. Rev. Lett.*, 19:1264–1266, Nov 1967.

[11] ATLAS collaboration. Observation of a new particle in the search for the standard model higgs boson with the atlas detector at the lhc. *Physics Letters B*, 716(1):1–29, 2012.

[12] The CMS Collaboration. Observation of a new boson at a mass of 125 GeV with the CMS experiment at the LHC. *Physics Letters B*, 716(1):30–61, 2012.

[13] F. Halzen and Alan D. Martin. *Quarks and leptons: an introductory course in modern particle physics*. Wiley, New York, 1984.

[14] Richard Wigmans. *Calorimetry: Energy Measurement in Particle Physics*. Oxford Academic, September 2017.

[15] Richard Clinton Fernow. *Introduction to experimental particle physics*. Cambridge Univ. Press, Cambridge, transferred to digital printing 2001 edition, 2001.

[16] K.A. Olive et al (Particle Data Group). Review of Particle Physics. *Chinese Physics C*, 38(9):090001, August 2014.

[17] Claus Grupen and Boris Shwartz. *Particle Detectors*. Cambridge Monographs on Particle Physics, Nuclear Physics and Cosmology. Cambridge University Press, Cambridge, 2 edition, 2008.

[18] Cristina Biino. The CMS Electromagnetic Calorimeter: overview, lessons learned during Run 1 and future projections. *Journal of Physics: Conference Series*, 587:012001, February 2015.

[19] G. Gaudio, M. Livan, and R. Wigmans. The art of calorimetry. In S. Bertolucci, U. Bottigli, and P. Oliva, editors, *Radiation and Particle Detectors*, pages 31–77. IOS Press, Incorporated, 2010.

[20] ATLAS collaboration. Electron and photon performance measurements with the ATLAS detector using the 2015–2017 LHC proton-proton collision data. *Journal of Instrumentation*, 14(12):P12006–P12006, December 2019. Publisher: IOP Publishing.

[21] G J Russ, E J Pitcher, and L L Daemen. Introduction to spallation physics and spallation–target design. In *Summary of the Accelerator-Driven Transmutation Technologies and their applications*, pages 93–105. Los Alamos National Laboratory, October 1995.

[22] Sehwook Lee, Michele Livan, and Richard Wigmans. On the limits of the hadronic energy resolution of calorimeters. *Nuclear Instruments and Methods in Physics Research Section A: Accelerators, Spectrometers, Detectors and Associated Equipment*, 882:148–157, February 2018. arXiv:1710.10535 [hep-ex, physics:physics].

[23] J.C. David. Spallation reactions. A successful interplay between modelingand applications. working paper or preprint, `https://hal.archives-ouvertes.fr/hal-01154286`, May 2015.

[24] Joao Pequenao and Paul Schaffner. How ATLAS detects particles: diagram of particle paths in the detector. 2013.

[25] Yoichiro Suzuki. The Super-Kamiokande experiment. *The European Physical Journal C*, 79(4):298, April 2019.

[26] Beate Heinemann. LuminosityPublicResults, Atlas Public Twiki. `https://twiki.cern.ch/twiki/bin/view/AtlasPublic/LuminosityPublicResults`.

[27] Eric Torrence. LuminosityPublicResultsRun2, Atlas Public Twiki. `https://twiki.cern.ch/twiki/bin/view/AtlasPublic/LuminosityPublicResultsRun2`.

[28] Arpad Horvath. Lhc.svg. Online, accessed 4 October 2022 from `https://en.m.wikipedia.org/wiki/File:LHC.svg`.

[29] The ATLAS Collaboration. The ATLAS Experiment at the CERN Large Hadron Collider. *Journal of Instrumentation*, 3(08):S08003–S08003, August 2008.

[30] Matthias Schott and Monica Dunford. Review of single vector boson production in pp collisions at $\sqrt{s} = 7$ TeV. *The European Physical Journal C*, 74(7), jul 2014.

[31] ATLAS collaboration. Track Reconstruction Performance of the ATLAS Inner Detector at $\sqrt{s} = 13$ TeV. Technical Report ATL-PHYS-PUB-2015-018, ATL-COM-PHYS-2015-596, July 2015. Publication Title: CERN Document Server.

[32] Bartosz Mindur. ATLAS Transition Radiation Tracker (TRT): Straw tubes for tracking and particle identification at the Large Hadron Collider. *Nuclear Instruments and Methods in Physics Research Section A: Accelerators, Spectrometers, Detectors and Associated Equipment*, 845:257–261, February 2017.

[33] Martin Kocian. Operational experience and performance with the atlas pixel detector at the large hadron collider. In *The 28th International Workshop on Vertex Detectors*, 2019. `https://cds.cern.ch/record/2693451/files/ATL-INDET-SLIDE-2019-765.pdf`.

[34] ATLAS collaboration. ATLAS inner detector : Technical Design Report, 1. Technical Report CERN-LHCC-97-016, CERN, 1997. ISBN: 9789290831020 Publication Title: CERN Document Server.

[35] ATLAS collaboration. ATLAS detector and physics performance technical design report. Technical Report BNL–52570, KA0401, 752144, CERN, June 1999.

[36] Henric Wilkens and the ATLAS LArg Collaboration. The ATLAS Liquid Argon calorimeter: An overview. *Journal of Physics: Conference Series*, 160:012043, April 2009. Publisher: IOP Publishing.

[37] ATLAS collaboration. Technical Design Report for the Phase-II Upgrade of the ATLAS Muon Spectrometer, September 2017. Number: CERN-LHCC-2017-017.

[38] Trigger and Data Acquisition System, Official public website for the ATLAS Experiment at CERN. `https://atlas.cern/Discover/Detector/Trigger-DAQ`.

[39] Yu Nakahama and on behalf of the ATLAS Collaboration. The ATLAS Trigger System: Ready for Run-2. *Journal of Physics: Conference Series*, 664(8):082037, December 2015. Publisher: IOP Publishing.

[40] Geoff Brumfiel. High-energy physics: Down the petabyte highway. *Nature*, 469(7330):282–283, January 2011. Number: 7330 Publisher: Nature Publishing Group.

[41] Gavin P. Salam. Towards jetography. *The European Physical Journal C*, 67(3-4):637–686, June 2010.

[42] ATLAS Collaboration. Topological cell clustering in the ATLAS calorimeters and its performance in LHC Run 1. *The European Physical Journal C*, 77(7):490, July 2017. arXiv:1603.02934 [hep-ex].

[43] Gerald C. Blazey, Jay R. Dittmann, Stephen D. Ellis, V. Daniel Elvira, K. Frame, S. Grinstein, Robert Hirosky, R. Piegaia, H. Schellman, R. Snihur, V. Sorin, and Dieter Zeppenfeld. Run II Jet Physics: Proceedings of the Run II QCD and Weak Boson Physics Workshop. *arXiv:hep-ex/0005012*, May 2000.

[44] Matteo Cacciari, Gavin P Salam, and Gregory Soyez. The anti-k_t jet clustering algorithm. *Journal of High Energy Physics*, 2008(04):063–063, April 2008.

[45] Ryan Atkin. Review of jet reconstruction algorithms. *Journal of Physics: Conference Series*, 645(1):012008, September 2015. Publisher: IOP Publishing.

[46] Stefan Weinzierl. The SISCone jet algorithm optimised for low particle multiplicities. *Computer Physics Communications*, 183(3):813–820, March 2012. arXiv:1108.1934 [hep-ph].

[47] ATLAS collaboration. Measurement of jet-substructure observables in top quark, W boson and light jet production in proton-proton collisions at $\sqrt{s} = 13$ TeV with the ATLAS detector. *Journal of High Energy Physics*, 2019(8):33, August 2019. arXiv:1903.02942 [hep-ex].

[48] ATLAS Collaboration. Jet energy scale and resolution measured in proton-proton collisions at $\sqrt{s} = 13$ TeV with the ATLAS detector. *arXiv:2007.02645 [hep-ex]*, July 2020.

[49] ATLAS Collaboration. New techniques for jet calibration with the ATLAS detector, March 2023.

[50] ATLAS Collaboration. Jet energy scale measurements and their systematic uncertainties in proton-proton collisions at $\sqrt{s} = 13$ TeV with the ATLAS detector. *Physical Review D*, 96(7):072002, October 2017.

[51] ATLAS collaboration. Pile-up subtraction and suppression for jets in ATLAS. *Inspire HEP*, August 2013. ATLAS-CONF-2013-083.

[52] F. Abe et al. Dijet angular distribution in $p\bar{p}$ collisions at $\sqrt{s} = 1.8$ TeV. *Physical Review Letters*, 69(20):2896–2900, November 1992. American Physical Society.

[53] Sundeep Singh. Determining the Jet Energy Scale for ATLAS in the Z+Jet Channel. Master's thesis, Simon Fraser University, Burnaby, Canada, November 2020.

[54] ATLAS Collaboration. Light-quark and gluon jet discrimination in pp collisions at $\sqrt{s} = 7$ TeV with the ATLAS detector. *The European Physical Journal C*, 74(8):3023, August 2014. arXiv:1405.6583 [hep-ex].

[55] Wanyun Su, Ben Nachman, Evan Robert Saraivanov, Htet Aung Myin, Rongqian Qian, Haoran Zhao, Shih-Chieh Hsu, and Shu Li. Calibration of the quark/gluon jet tagging variables using matrix method with the ATLAS detector, 2022. Geneva.

[56] James Beare. Reconstructing a Quark and Gluon Response at ATLAS. Master's thesis, Simon Fraser University, Burnaby, Canada, September 2016.

[57] ATLAS collaboration. Discrimination of Light Quark and Gluon Jets in pp collisions at $\sqrt{s} = 8$ TeV with the ATLAS Detector, 2016. Geneva.

Appendix A

Quark and Gluon Response Uncertainties

Partial derivatives are used to determine how the quark and gluon responses react to changes in their inputs. It is assumed that the inputs are uncorrelated, and the relationship $f^q + f^g + f^c = 1$ is used to substitute out the flavour fraction with lower uncertainty. The quark fraction uncertainty is used for dijets, and the gluon fraction uncertainty is used for Z + jet events. After making these substitutions, equations 3.13 and 3.12 become:

$$R^q = \frac{(1 - f^q_{DJ} - f^c_{DJ})(R_{ZJ} - R^c f^c_{ZJ}) - f^g_{ZJ}(R_{DJ} - R^c f^c_{DJ})}{1 - f^q_{DJ} + f^c_{ZJ} f^q_{DJ} - f^g_{ZJ} + f^c_{DJ} f^g_{ZJ} - f^c_{ZJ} - f^c_{DJ} + f^c_{ZJ} f^c_{DJ}} \tag{A.1}$$

and

$$R^g = \frac{-f^q_{DJ}(R_{ZJ} - R^c f^c_{ZJ}) + (1 - f^g_{ZJ} - f^c_{ZJ})(R_{DJ} - R^c f^c_{DJ})}{1 - f^q_{DJ} + f^c_{ZJ} f^q_{DJ} - f^g_{ZJ} + f^c_{DJ} f^g_{ZJ} - f^c_{ZJ} - f^c_{DJ} + f^c_{ZJ} f^c_{DJ}} \tag{A.2}$$

For these response calculations there are five uncertainties: Δf^q_{DJ}, Δf^g_{ZJ}, ΔR_{ZJ}, ΔR_{ZJ}, and ΔR^c. Each uncertainty is calculated as a partial derivative. For an input x, the uncertainty in the response is given by

$$\Delta R(\Delta x) = \frac{\partial R}{\partial x} \Delta x. \tag{A.3}$$

The derivatives are straightforward as many terms cancel or reduce to zero. For the quark response, the uncertainties are:

$$\Delta R^q(\Delta f^q_{DJ}) = \frac{f^g_Z(f^c_Z R_D - f^c_Z R^c - f^c_D R_Z + f^c_D R^c - R_D + R_Z}{D^2} \Delta f^q_D \tag{A.4}$$

$$\Delta R^q(\Delta f^g_{ZJ}) = \frac{f^g_D(f^c_Z R_D - f^c_Z R^c - f^c_D R_Z + f^c_D R^c - R_D + R_Z)}{D^2} \Delta f^g_Z \tag{A.5}$$

$$\Delta R^q(\Delta R_{DJ}) == \frac{-f_Z^q}{D}\Delta R_D \tag{A.6}$$

$$\Delta R^q(\Delta R_{ZJ}) = \frac{f_D^g}{D}\Delta R_Z \tag{A.7}$$

$$\Delta R^q(\Delta R^c) = \frac{f_Z^c f_D^q + f_Z^c f_D^c - f_Z^c + f_D^c f_Z^g}{D}\Delta R^c \tag{A.8}$$

Where D is the denominator from equations A.1 and A.2. f_D^g and f_Z^q have been substituted back into several of the expressions. For the Gluon:

$$\Delta R^g(\Delta f_{DJ}^q) = \frac{f_Z^q(-f_Z^c R_D + f_Z^c R^c + f_D^c R_Z - f_D^c R^c + R_D - R_Z)}{D^2}\Delta f_D^q \tag{A.9}$$

$$\Delta R^g(\Delta f_{ZJ}^g) = \frac{f_D^q(-f_Z^c R_D + f_Z^c R^c + f_D^c R_Z - f_D^c R^c + R_D - R_Z)}{D^2}\Delta f_Z^g \tag{A.10}$$

$$\Delta R^g(\Delta R_{DJ}) = \frac{f_Z^q}{D}\Delta R_D \tag{A.11}$$

$$\Delta R^g(\Delta R_{ZJ}) = \frac{-f_D^q}{D}\Delta R_Z \tag{A.12}$$

$$\Delta R^g(\Delta R^c) = \frac{f_D^c f_Z^g + f_D^c f_Z^c - f_D^c + f_Z^c f_D^q}{D}\Delta R^c \tag{A.13}$$

Appendix B

Additional Dijet MPF Results

While investigating the higher-than-expected gluon response, the primary suspect was the dijet MPF. The Z + jet MPF comes from a thoroughly tested software framework, and the flavour fractions come from simple tags on the jets in MC.

Several avenues were taken to explore the dijet MPF and its effect on the quark and gluon responses. One investigation was to try the MPF calculation with each of the jets as the reference and the probe. In chapter 5, the dijet MPF was calculated using the leading jet as the reference and the sub-leading jet as the probe. Figure B.1 shows the dijet MPF calculation performed twice per event, once with the leading jet as the reference and once with the sub-leading jet as the reference. After fitting, the calculated MPF is the average of the two methods. The dijet MPF calculated this way is higher across the p_T range, and would be higher still if only the sub-leading jet were used as the reference. Since the gluon response rises with climbing dijet response, the method used in chapter 5 is optimal for the lowest gluon response.

Figure B.1 also shows a significant difference between data and MC before roughly 400 GeV. A potential cause of this was an uneven application of the triggers, where more than one trigger was being implemented in certain pt bins. The point where the data and MC begin to agree again coincides with the last trigger, where by default only that trigger can be applied. This was resolved in the main analyses.

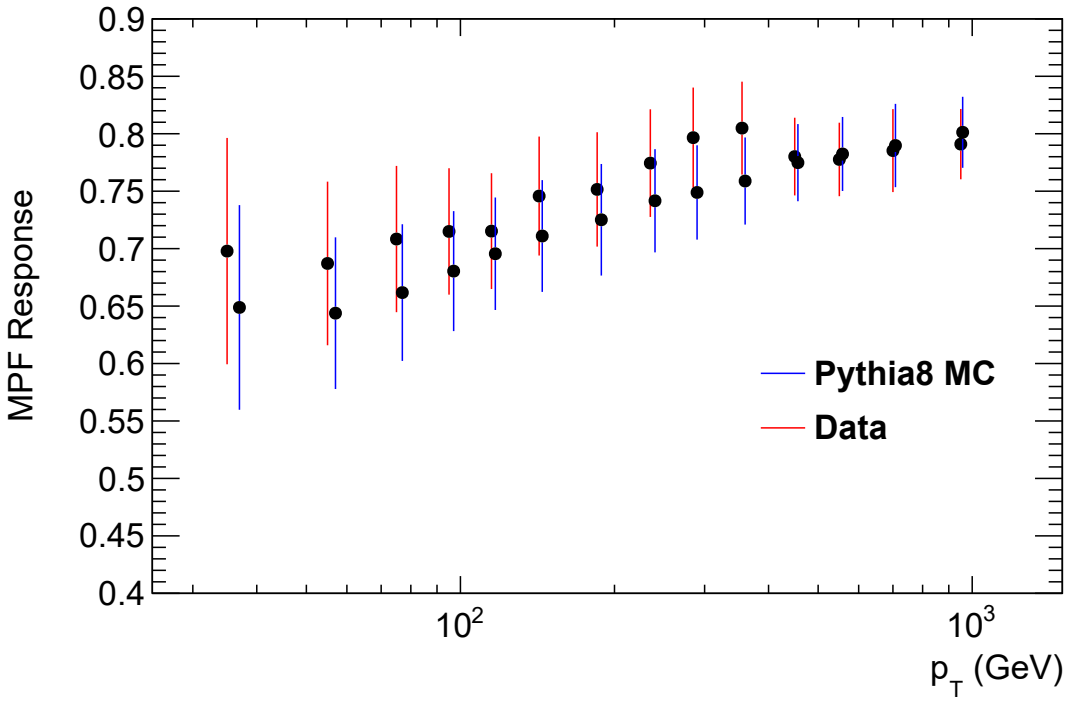

Figure B.1: The dijet MPF response calculated using both jets in the event.

Appendix C

Jet Property Signal/Background Plots

Shown here are the signal and background distributions for the jet variables used in this thesis, across the p_T range 25-1100 GeV. The results are normalized to unit integrals to better show the less frequent high response signal jets.

C.1 25-45 GeV

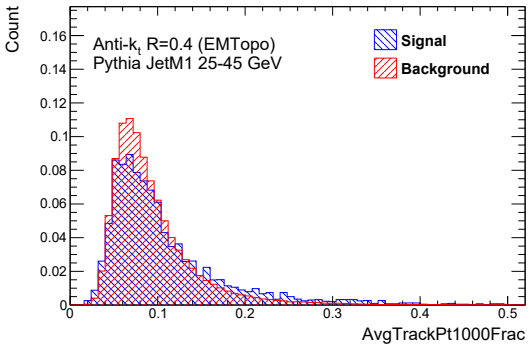
Count
Anti-k$_t$ R=0.4 (EMTopo)
Pythia JetM1 25-45 GeV
Signal
Background
AvgTrackPt1000Frac

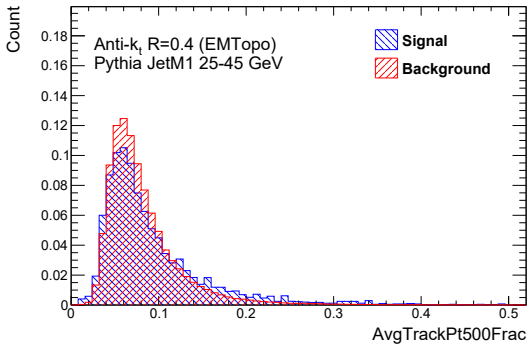
Count
Anti-k$_t$ R=0.4 (EMTopo)
Pythia JetM1 25-45 GeV
Signal
Background
AvgTrackPt500Frac

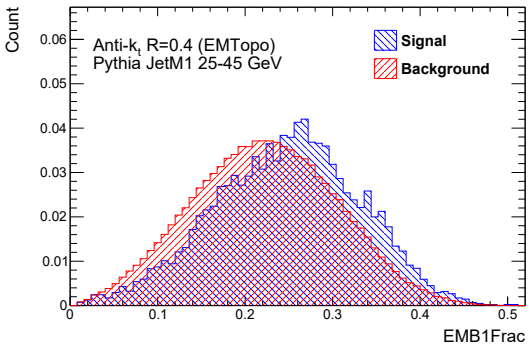
Count
Anti-k$_t$ R=0.4 (EMTopo)
Pythia JetM1 25-45 GeV
Signal
Background
EMB1Frac

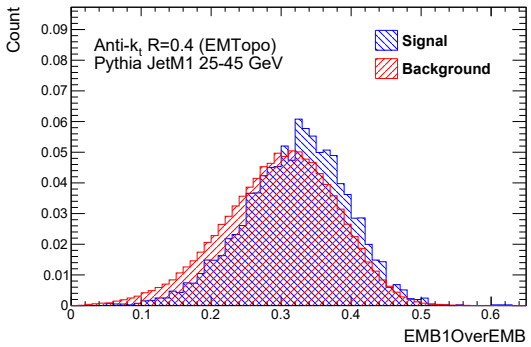
Count
Anti-k$_t$ R=0.4 (EMTopo)
Pythia JetM1 25-45 GeV
Signal
Background
EMB1OverEMB

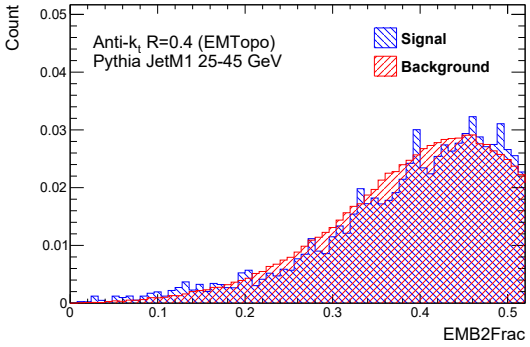
Count
Anti-k$_t$ R=0.4 (EMTopo)
Pythia JetM1 25-45 GeV
Signal
Background
EMB2Frac

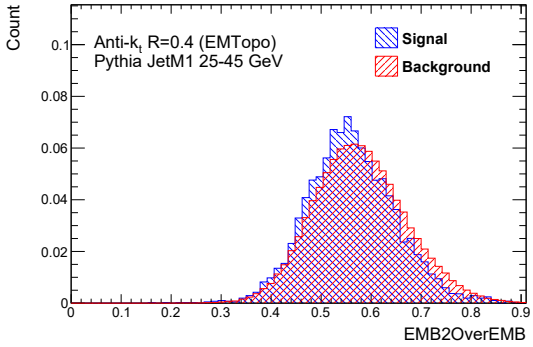
Count
Anti-k$_t$ R=0.4 (EMTopo)
Pythia JetM1 25-45 GeV
Signal
Background
EMB2OverEMB

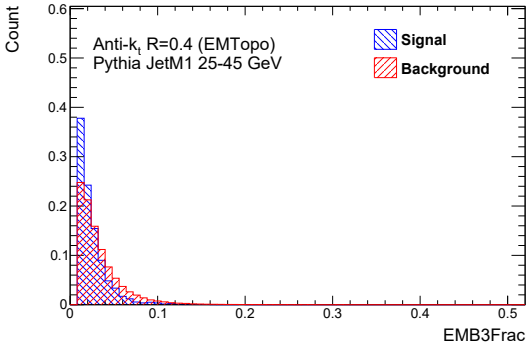
Count
Anti-k$_t$ R=0.4 (EMTopo)
Pythia JetM1 25-45 GeV
Signal
Background
EMB3Frac

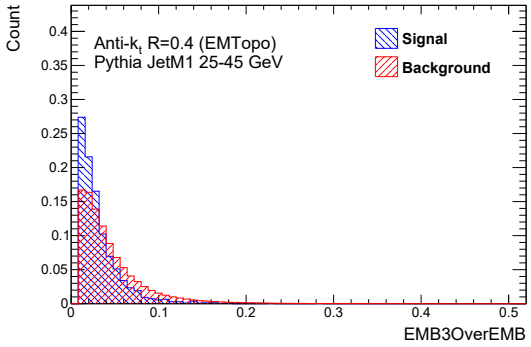
Count
Anti-k$_t$ R=0.4 (EMTopo)
Pythia JetM1 25-45 GeV
Signal
Background
EMB3OverEMB

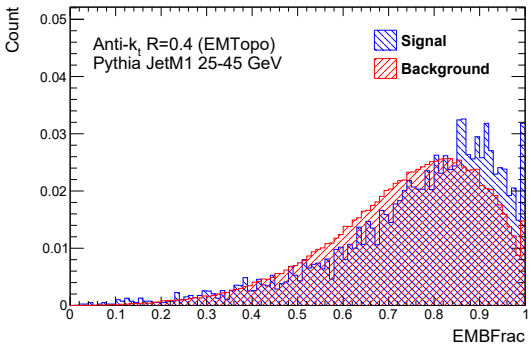
Count
Anti-k$_t$ R=0.4 (EMTopo)
Pythia JetM1 25-45 GeV
Signal
Background
EMBFrac

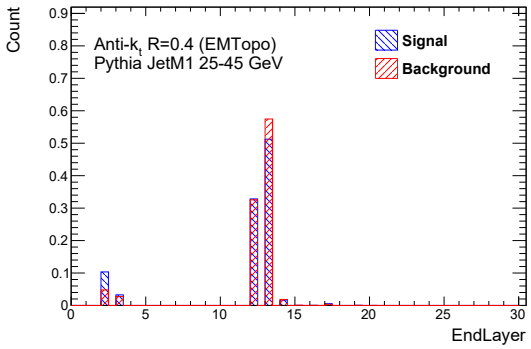
Count
Anti-k$_t$ R=0.4 (EMTopo)
Pythia JetM1 25-45 GeV
Signal
Background
EndLayer

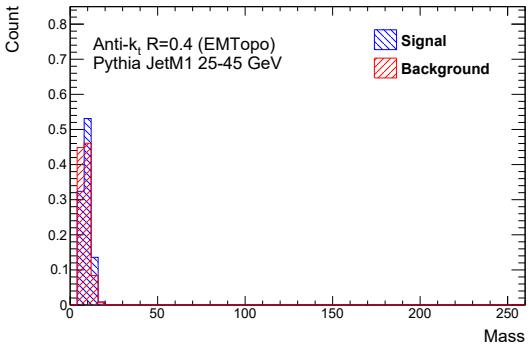
Count
Anti-k$_t$ R=0.4 (EMTopo)
Pythia JetM1 25-45 GeV
Signal
Background
Mass

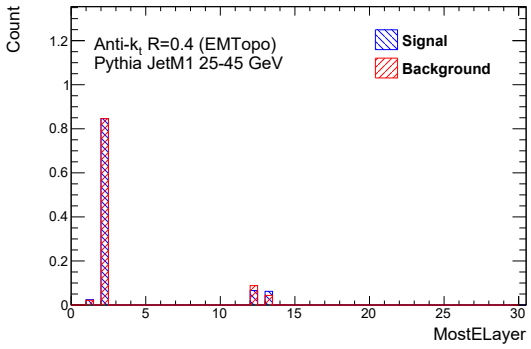
Count
Anti-k$_t$ R=0.4 (EMTopo)
Pythia JetM1 25-45 GeV
Signal
Background
MostELayer

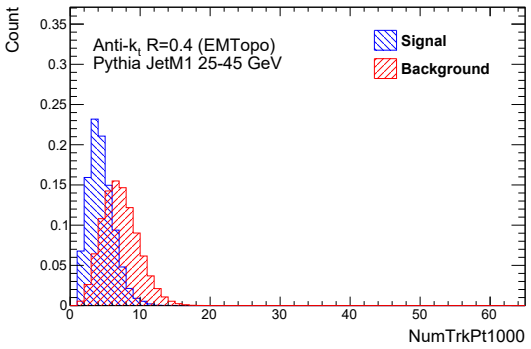
Count
Anti-k$_t$ R=0.4 (EMTopo)
Pythia JetM1 25-45 GeV
Signal
Background
NumTrkPt1000

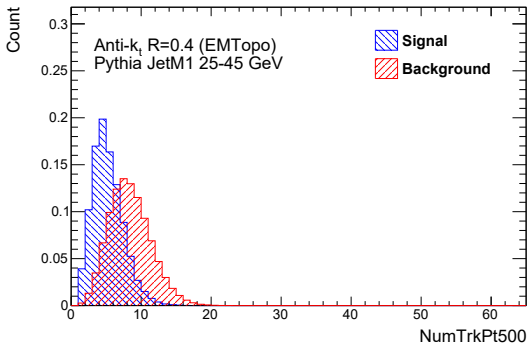
Count
Anti-k$_t$ R=0.4 (EMTopo)
Pythia JetM1 25-45 GeV
Signal
Background
NumTrkPt500

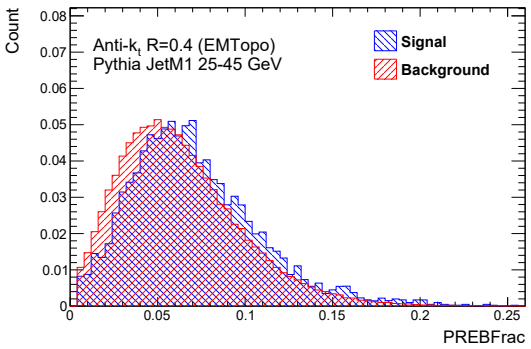
Count
Anti-k$_t$ R=0.4 (EMTopo)
Pythia JetM1 25-45 GeV
Signal
Background
PREBFrac

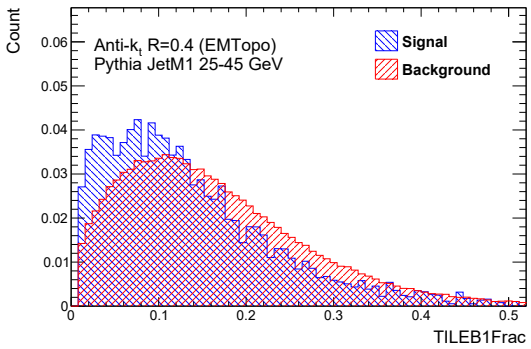
Count
Anti-k$_t$ R=0.4 (EMTopo)
Pythia JetM1 25-45 GeV
Signal
Background
TILEB1Frac

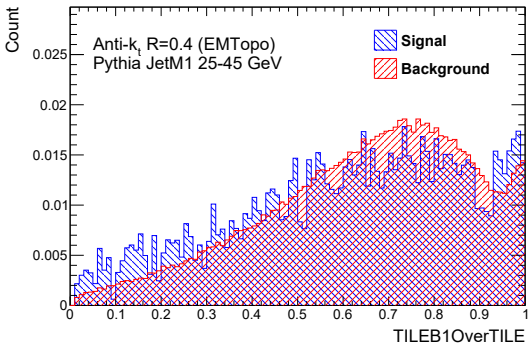
Count
Anti-k$_t$ R=0.4 (EMTopo)
Pythia JetM1 25-45 GeV
Signal
Background
TILEB1OverTILE

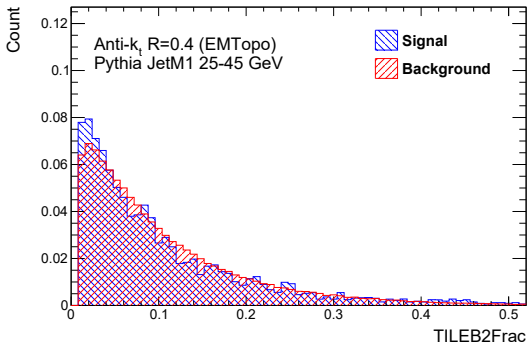
Count
Anti-k$_t$ R=0.4 (EMTopo)
Pythia JetM1 25-45 GeV
Signal
Background
TILEB2Frac

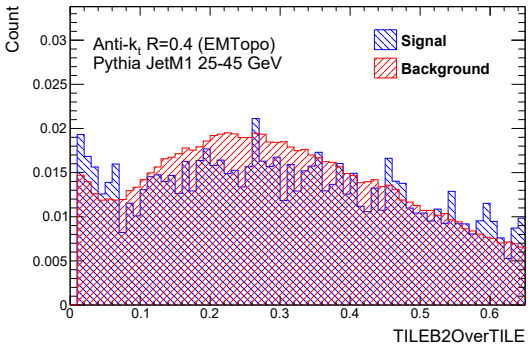
Count
Anti-k$_t$ R=0.4 (EMTopo)
Pythia JetM1 25-45 GeV
Signal
Background
TILEB2OverTILE

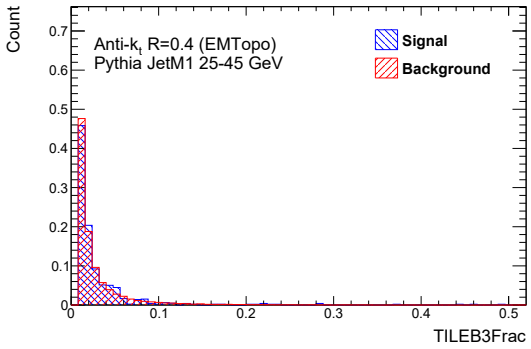
Count
Anti-k$_t$ R=0.4 (EMTopo)
Pythia JetM1 25-45 GeV
Signal
Background
TILEB3Frac

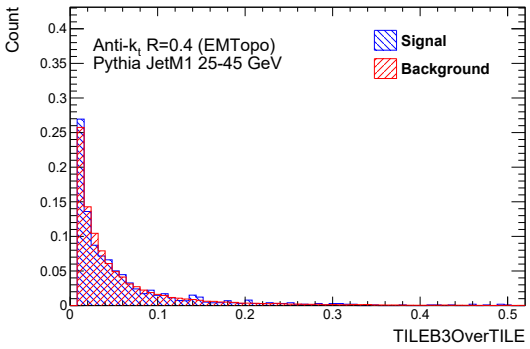
Count
Anti-k$_t$ R=0.4 (EMTopo)
Pythia JetM1 25-45 GeV
Signal
Background
TILEB3OverTILE

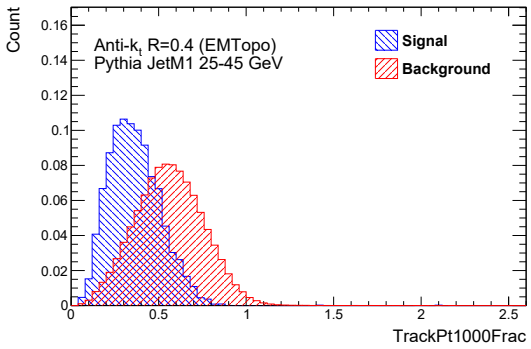
Count
Anti-k$_t$ R=0.4 (EMTopo)
Pythia JetM1 25-45 GeV
Signal
Background
TrackPt1000Frac

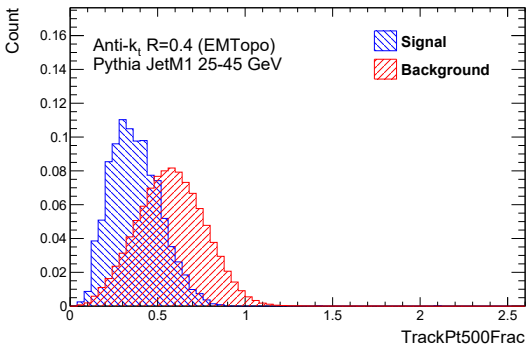
Count
Anti-k$_t$ R=0.4 (EMTopo)
Pythia JetM1 25-45 GeV
Signal
Background
TrackPt500Frac

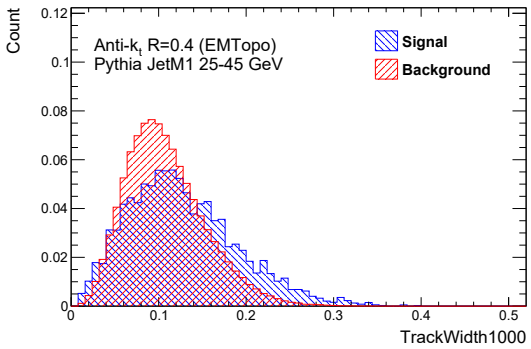
Count
Anti-k$_t$ R=0.4 (EMTopo)
Pythia JetM1 25-45 GeV
Signal
Background
TrackWidth1000

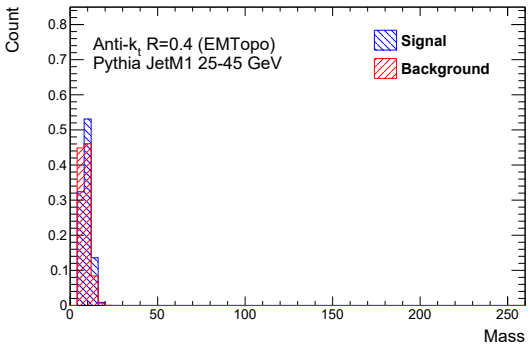
Count
Anti-k$_t$ R=0.4 (EMTopo)
Pythia JetM1 25-45 GeV
Signal
Background
Mass

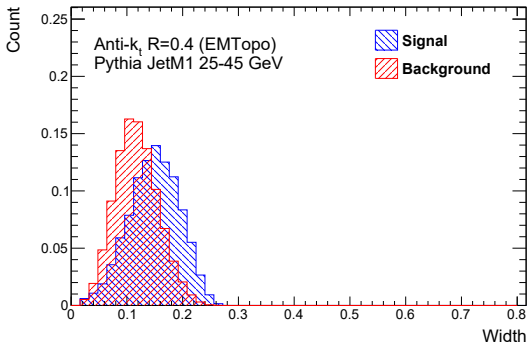
Count
Anti-k$_t$ R=0.4 (EMTopo)
Pythia JetM1 25-45 GeV
Signal
Background
Width

C.2 45-65 GeV

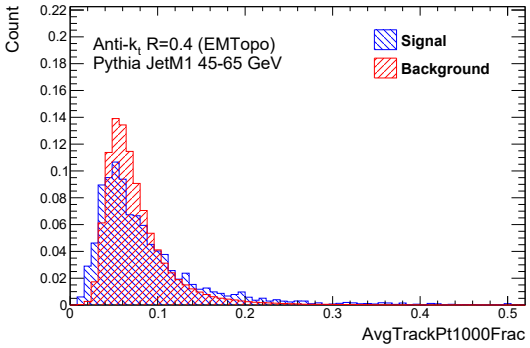
Count
Anti-k$_t$ R=0.4 (EMTopo)
Pythia JetM1 45-65 GeV
Signal
Background
AvgTrackPt1000Frac

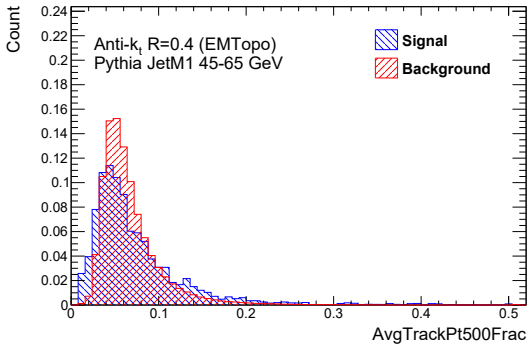
Count
Anti-k$_t$ R=0.4 (EMTopo)
Pythia JetM1 45-65 GeV
Signal
Background
AvgTrackPt500Frac

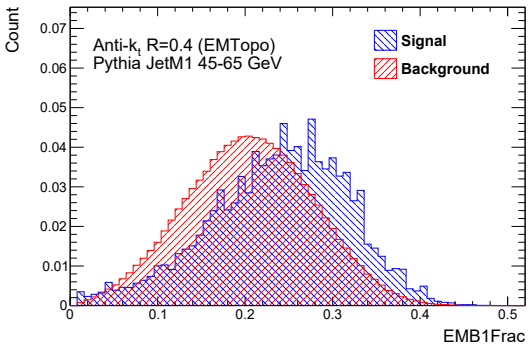
Count
Anti-k$_t$ R=0.4 (EMTopo)
Pythia JetM1 45-65 GeV
Signal
Background
EMB1Frac

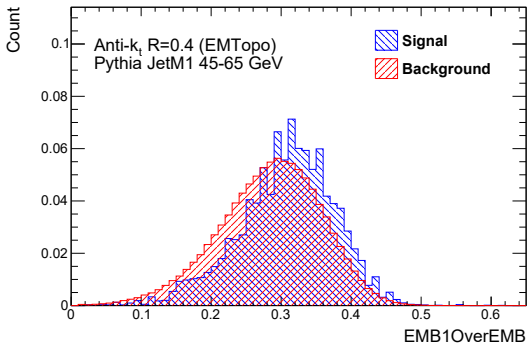
Count
Anti-k$_t$ R=0.4 (EMTopo)
Pythia JetM1 45-65 GeV
Signal
Background
EMB1OverEMB

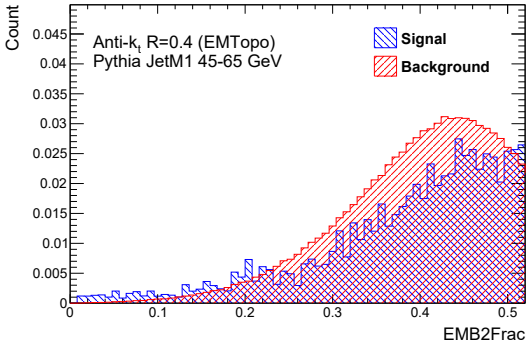
Count
Anti-k$_t$ R=0.4 (EMTopo)
Pythia JetM1 45-65 GeV
Signal
Background
EMB2Frac

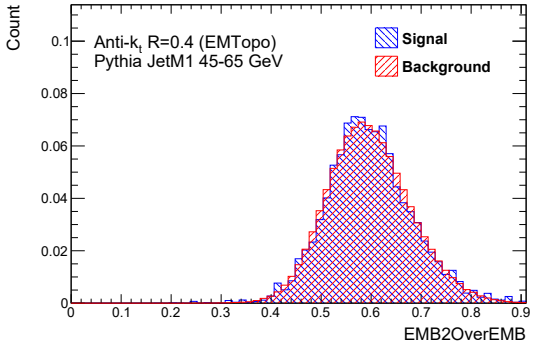
Count
Anti-k$_t$ R=0.4 (EMTopo)
Pythia JetM1 45-65 GeV
Signal
Background
EMB2OverEMB

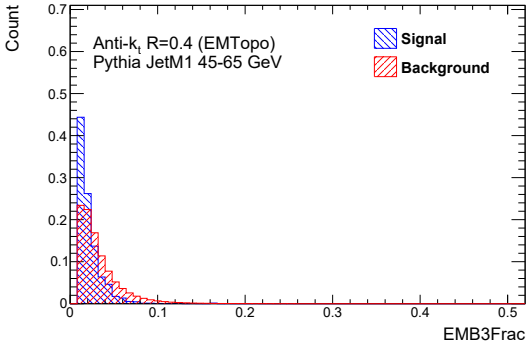
Count
Anti-k$_t$ R=0.4 (EMTopo)
Pythia JetM1 45-65 GeV
Signal
Background
EMB3Frac

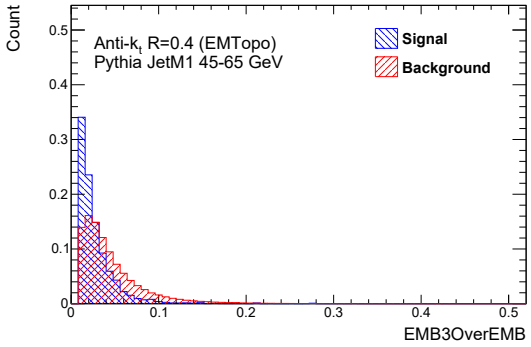
Count
Anti-k$_t$ R=0.4 (EMTopo)
Pythia JetM1 45-65 GeV
Signal
Background
EMB3OverEMB

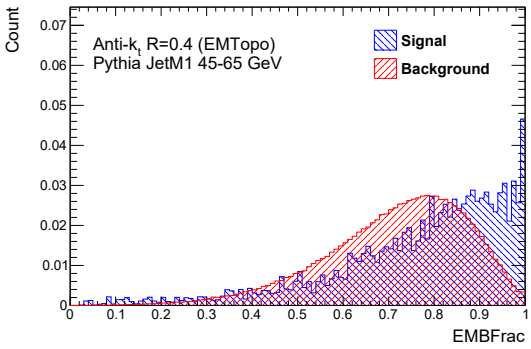
Count
Anti-k$_t$ R=0.4 (EMTopo)
Pythia JetM1 45-65 GeV
Signal
Background
EMBFrac

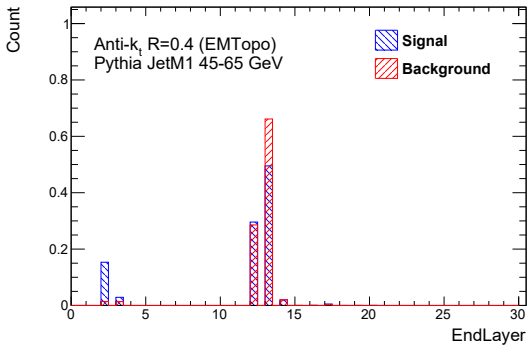
Count
Anti-k$_t$ R=0.4 (EMTopo)
Pythia JetM1 45-65 GeV
Signal
Background
EndLayer

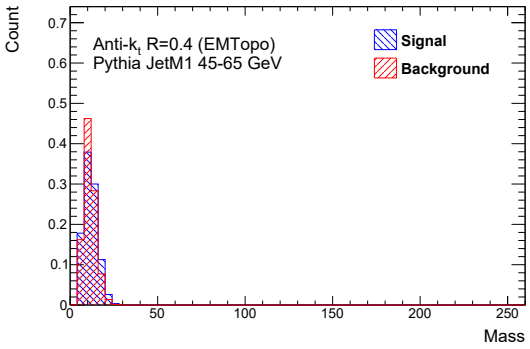
Count
Anti-k$_t$ R=0.4 (EMTopo)
Pythia JetM1 45-65 GeV
Signal
Background
Mass

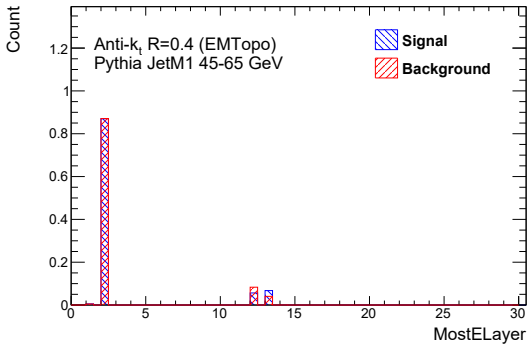
Count
Anti-k$_t$ R=0.4 (EMTopo)
Pythia JetM1 45-65 GeV
Signal
Background
MostELayer

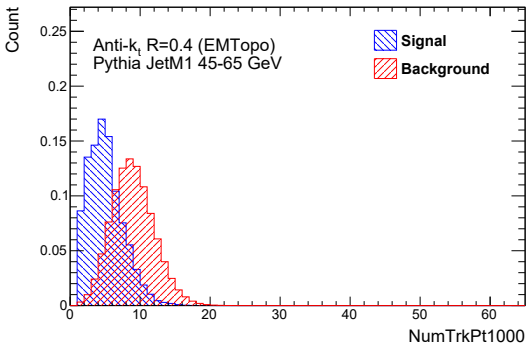
Count
Anti-k$_t$ R=0.4 (EMTopo)
Pythia JetM1 45-65 GeV
Signal
Background
NumTrkPt1000

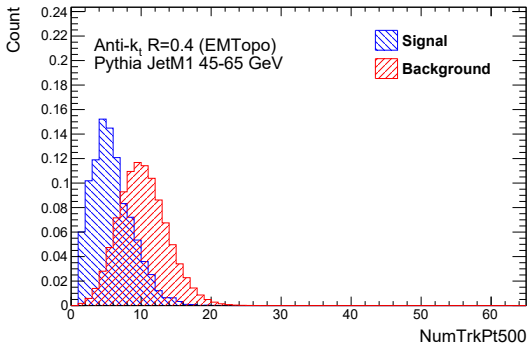
Count
Anti-k$_t$ R=0.4 (EMTopo)
Pythia JetM1 45-65 GeV
Signal
Background
NumTrkPt500

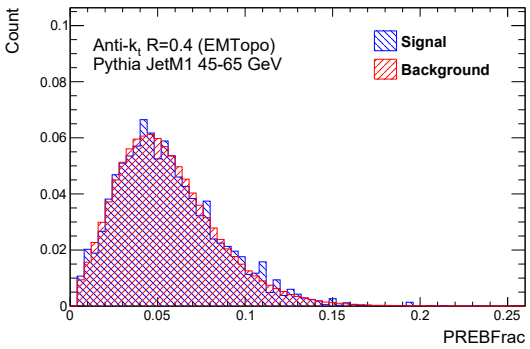
Count
Anti-k$_t$ R=0.4 (EMTopo)
Pythia JetM1 45-65 GeV
Signal
Background
PREBFrac

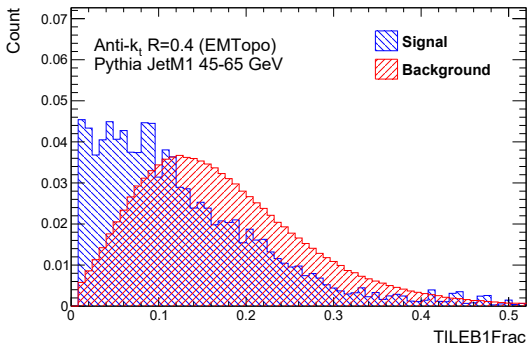
Count
Anti-k$_t$ R=0.4 (EMTopo)
Pythia JetM1 45-65 GeV
Signal
Background
TILEB1Frac

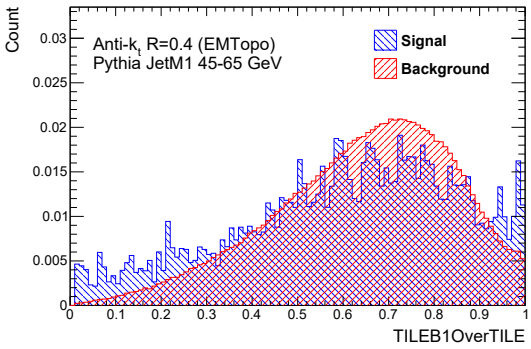
Count
Anti-k$_t$ R=0.4 (EMTopo)
Pythia JetM1 45-65 GeV
Signal
Background
TILEB1OverTILE

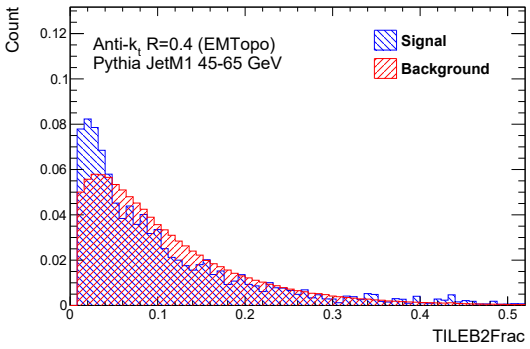
Count
Anti-k$_t$ R=0.4 (EMTopo)
Pythia JetM1 45-65 GeV
Signal
Background
TILEB2Frac

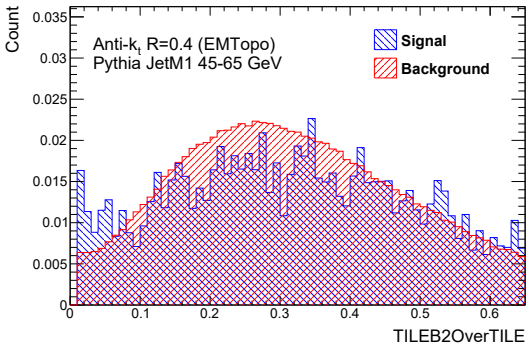
Count
Anti-k$_t$ R=0.4 (EMTopo)
Pythia JetM1 45-65 GeV
Signal
Background
TILEB2OverTILE

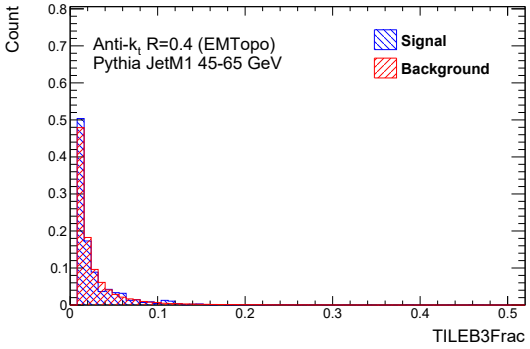
Count
Anti-k$_t$ R=0.4 (EMTopo)
Pythia JetM1 45-65 GeV
Signal
Background
TILEB3Frac

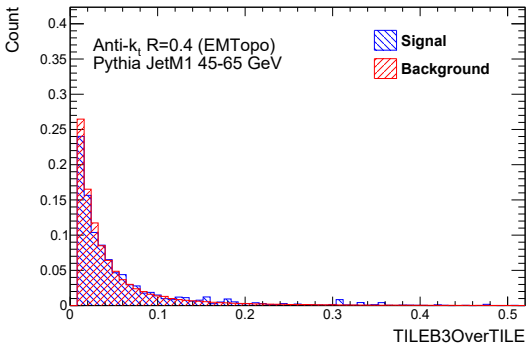
Count
Anti-k$_t$ R=0.4 (EMTopo)
Pythia JetM1 45-65 GeV
Signal
Background
TILEB3OverTILE

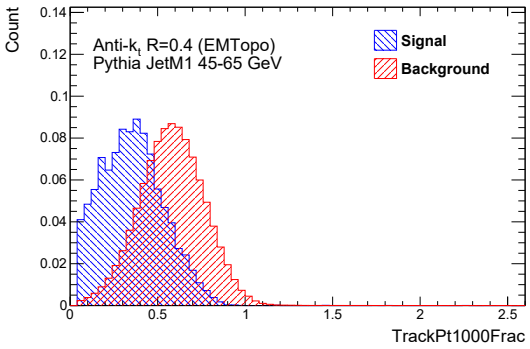
Count
Anti-k$_t$ R=0.4 (EMTopo)
Pythia JetM1 45-65 GeV
Signal
Background
TrackPt1000Frac

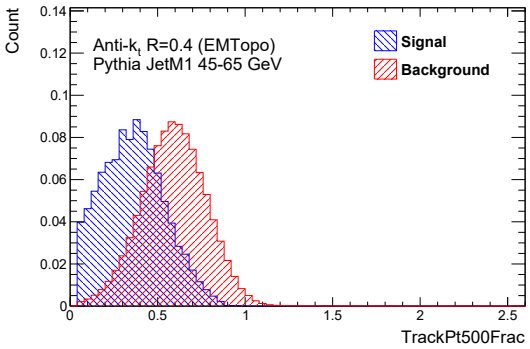
Count
Anti-k$_t$ R=0.4 (EMTopo)
Pythia JetM1 45-65 GeV
Signal
Background
TrackPt500Frac

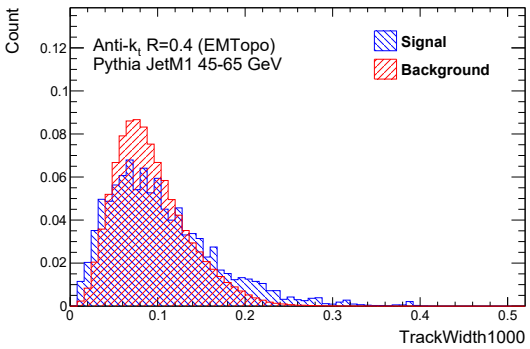
Count
Anti-k$_t$ R=0.4 (EMTopo)
Pythia JetM1 45-65 GeV
Signal
Background
TrackWidth1000

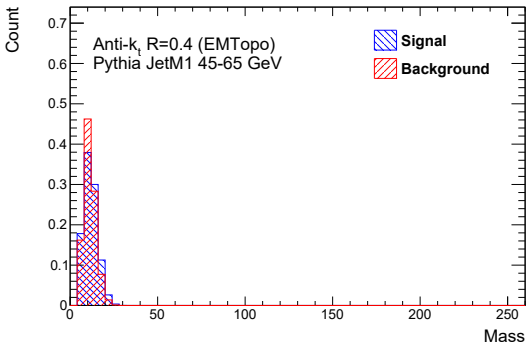
Count
Anti-k$_t$ R=0.4 (EMTopo)
Pythia JetM1 45-65 GeV
Signal
Background
Mass

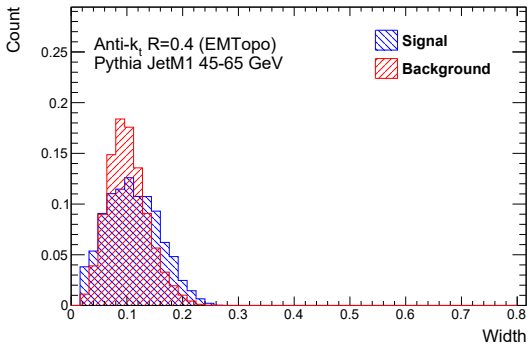
Count
Anti-k$_t$ R=0.4 (EMTopo)
Pythia JetM1 45-65 GeV
Signal
Background
Width

C.3 65-85 GeV

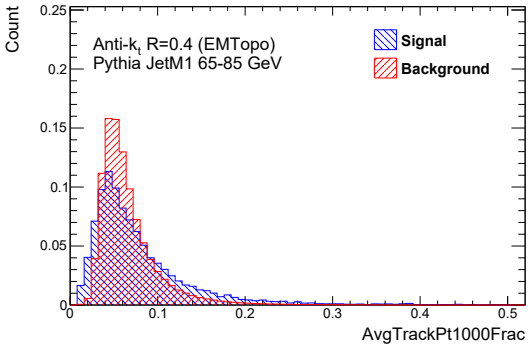
Count
Anti-k$_t$ R=0.4 (EMTopo)
Pythia JetM1 65-85 GeV
Signal
Background
AvgTrackPt1000Frac

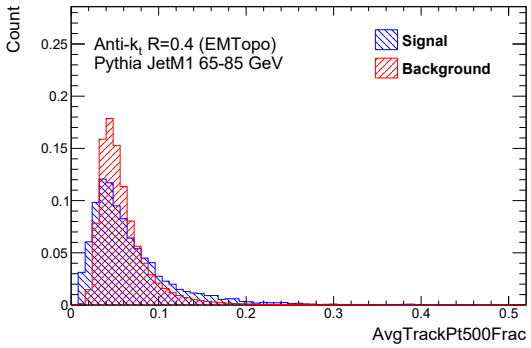
Count
Anti-k$_t$ R=0.4 (EMTopo)
Pythia JetM1 65-85 GeV
Signal
Background
AvgTrackPt500Frac

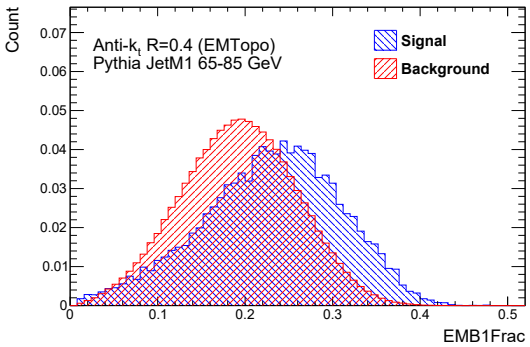
Count
Anti-k$_t$ R=0.4 (EMTopo)
Pythia JetM1 65-85 GeV
Signal
Background
EMB1Frac

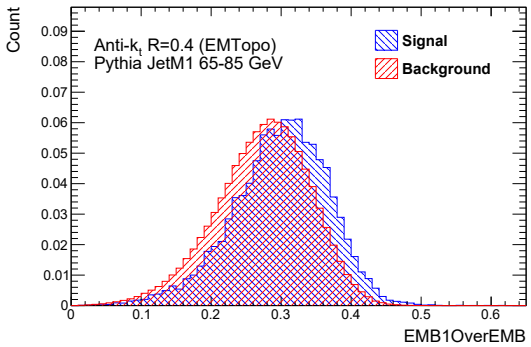
Count
Anti-k$_t$ R=0.4 (EMTopo)
Pythia JetM1 65-85 GeV
Signal
Background
EMB1OverEMB

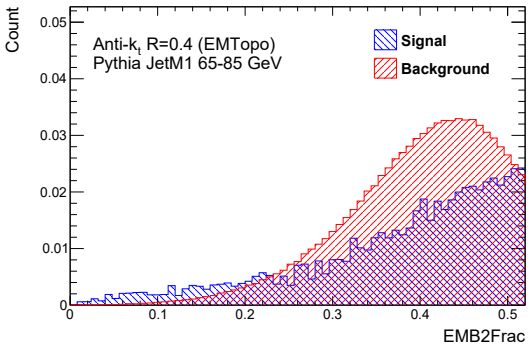
Count
Anti-k$_t$ R=0.4 (EMTopo)
Pythia JetM1 65-85 GeV
Signal
Background
EMB2Frac

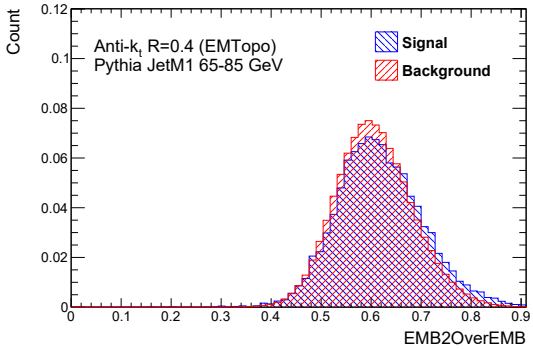
Count
Anti-k$_t$ R=0.4 (EMTopo)
Pythia JetM1 65-85 GeV
Signal
Background
EMB2OverEMB

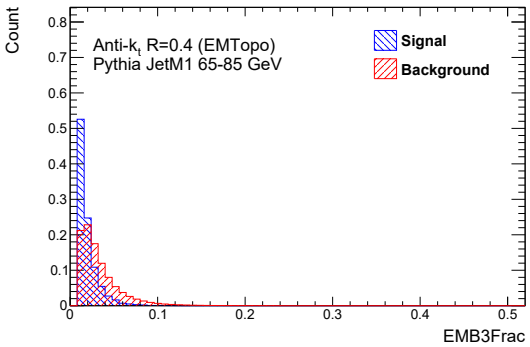
Count
Anti-k$_t$ R=0.4 (EMTopo)
Pythia JetM1 65-85 GeV
Signal
Background
EMB3Frac

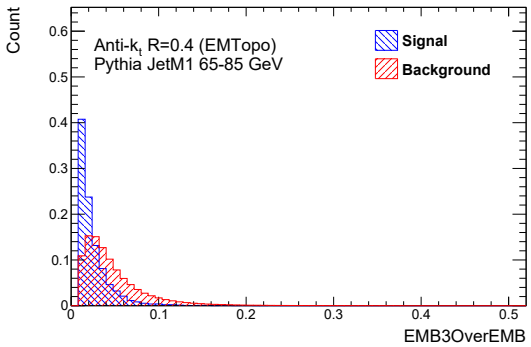
Count
Anti-k$_t$ R=0.4 (EMTopo)
Pythia JetM1 65-85 GeV
Signal
Background
EMB3OverEMB

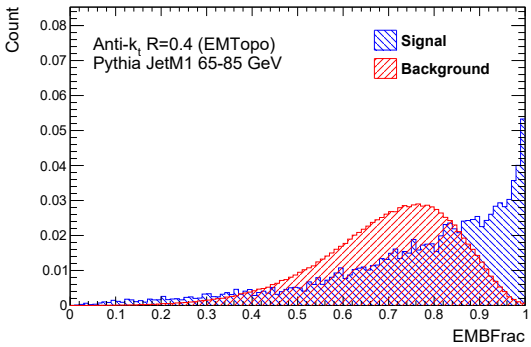
Count
Anti-k$_t$ R=0.4 (EMTopo)
Pythia JetM1 65-85 GeV
Signal
Background
EMBFrac

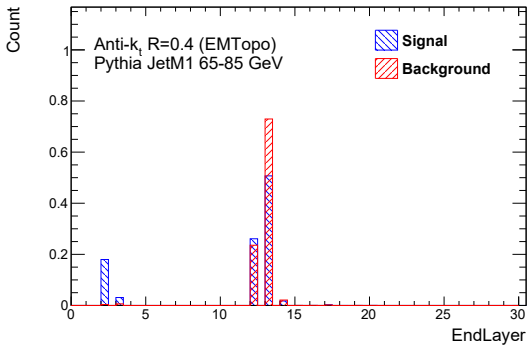
Count
Anti-k$_t$ R=0.4 (EMTopo)
Pythia JetM1 65-85 GeV
Signal
Background
EndLayer

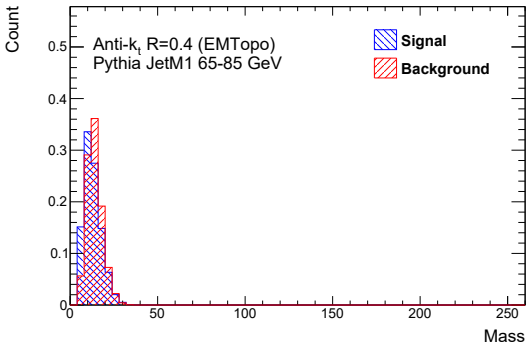
Count
Anti-k$_t$ R=0.4 (EMTopo)
Pythia JetM1 65-85 GeV
Signal
Background
Mass

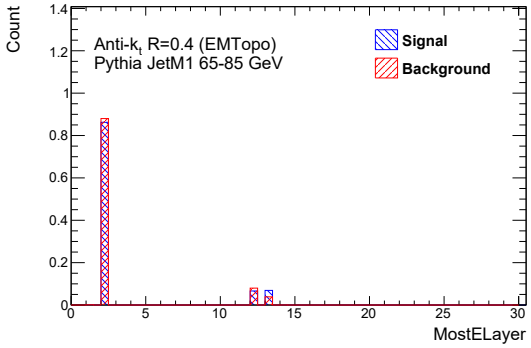
Count
Anti-k$_t$ R=0.4 (EMTopo)
Pythia JetM1 65-85 GeV
Signal
Background
MostELayer

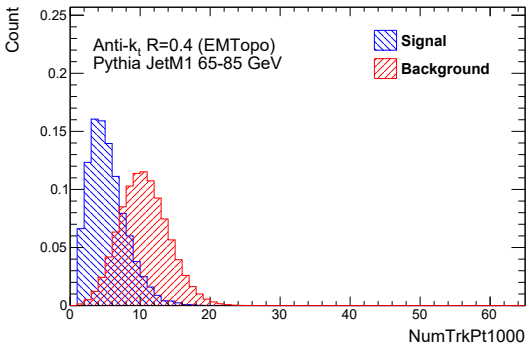
Count
Anti-k$_t$ R=0.4 (EMTopo)
Pythia JetM1 65-85 GeV
Signal
Background
NumTrkPt1000

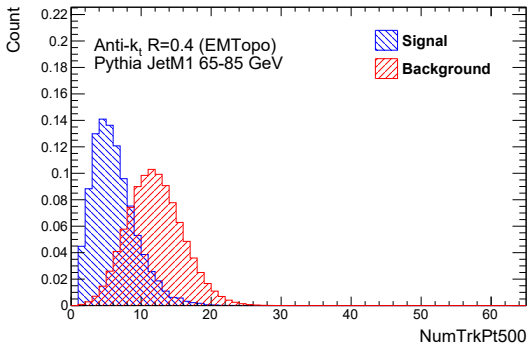
Count
Anti-k$_t$ R=0.4 (EMTopo)
Pythia JetM1 65-85 GeV
Signal
Background
NumTrkPt500

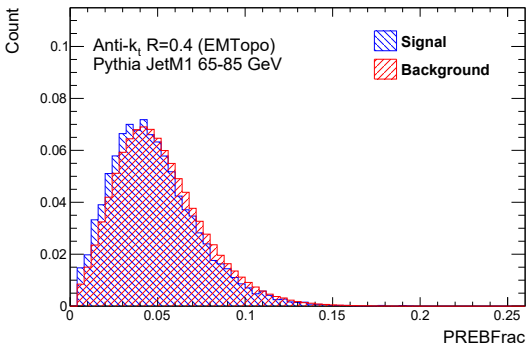
Count
Anti-k$_t$ R=0.4 (EMTopo)
Pythia JetM1 65-85 GeV
Signal
Background
PREBFrac

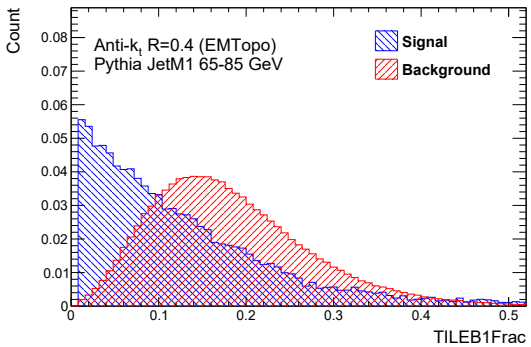
Count
Anti-k$_t$ R=0.4 (EMTopo)
Pythia JetM1 65-85 GeV
Signal
Background
TILEB1Frac

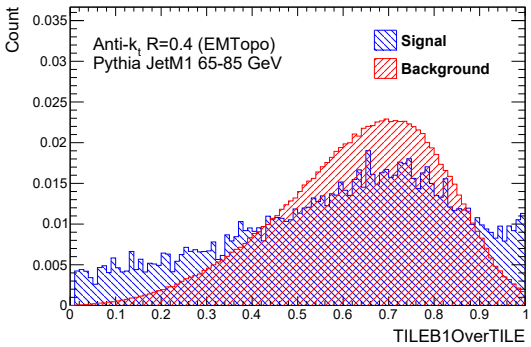
Count
Anti-k$_t$ R=0.4 (EMTopo)
Pythia JetM1 65-85 GeV
Signal
Background
TILEB1OverTILE

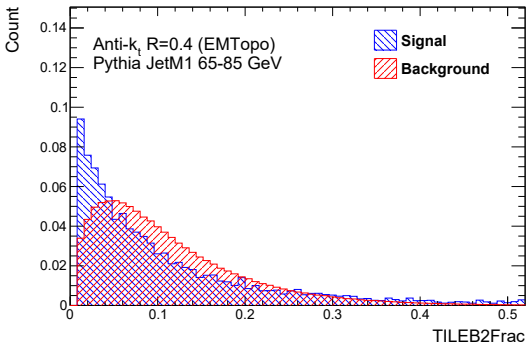
Count
Anti-k$_t$ R=0.4 (EMTopo)
Pythia JetM1 65-85 GeV
Signal
Background
TILEB2Frac

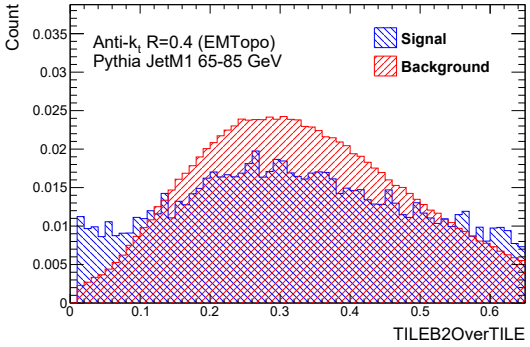
Count
Anti-k$_t$ R=0.4 (EMTopo)
Pythia JetM1 65-85 GeV
Signal
Background
TILEB2OverTILE

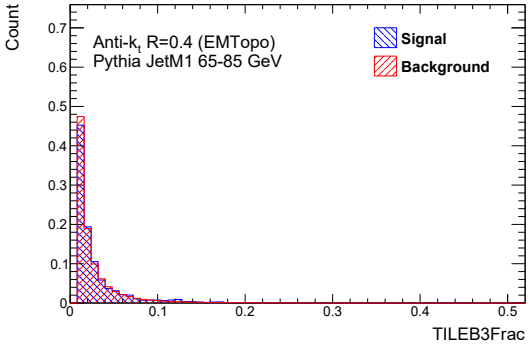
Count
Anti-k$_t$ R=0.4 (EMTopo)
Pythia JetM1 65-85 GeV
Signal
Background
TILEB3Frac

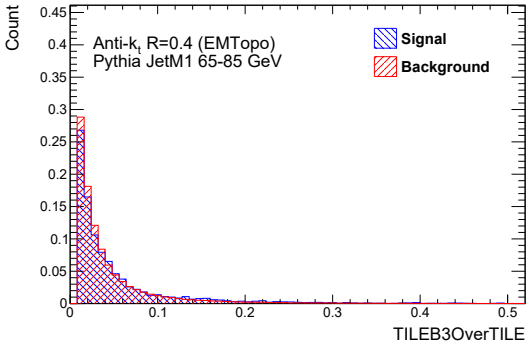
Count
Anti-k$_t$ R=0.4 (EMTopo)
Pythia JetM1 65-85 GeV
Signal
Background
TILEB3OverTILE

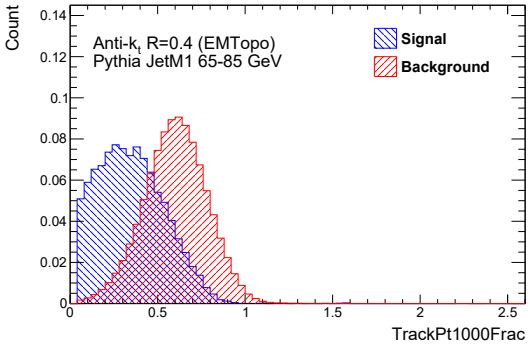
Count
Anti-k$_t$ R=0.4 (EMTopo)
Pythia JetM1 65-85 GeV
Signal
Background
TrackPt1000Frac

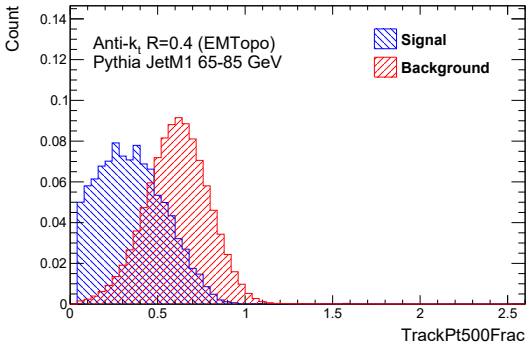
Count
Anti-k$_t$ R=0.4 (EMTopo)
Pythia JetM1 65-85 GeV
Signal
Background
TrackPt500Frac

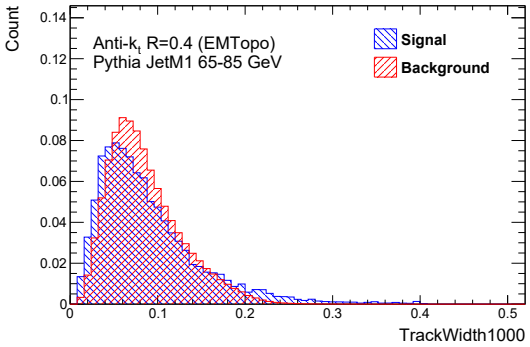
Count
Anti-k$_t$ R=0.4 (EMTopo)
Pythia JetM1 65-85 GeV
Signal
Background
TrackWidth1000

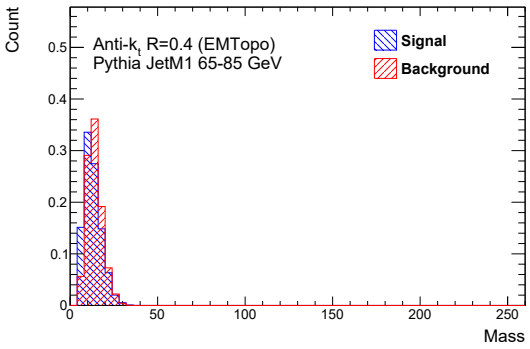
Count
Anti-k$_t$ R=0.4 (EMTopo)
Pythia JetM1 65-85 GeV
Signal
Background
0.5
0.4
0.3
0.2
0.1
0
0
50
100
150
200
250
Mass

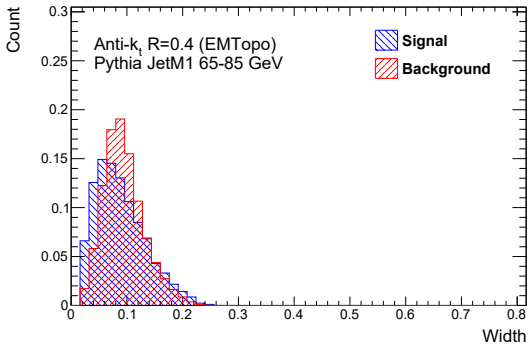
Count
Anti-k$_t$ R=0.4 (EMTopo)
Pythia JetM1 65-85 GeV
Signal
Background
0.3
0.25
0.2
0.15
0.1
0.05
0
0
0.1
0.2
0.3
0.4
0.5
0.6
0.7
0.8
Width

C.4 85-105 GeV

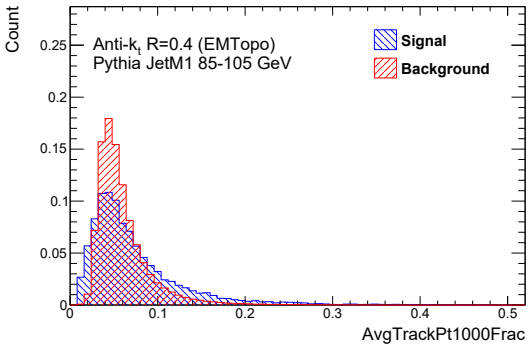
Count
Anti-k$_t$ R=0.4 (EMTopo)
Pythia JetM1 85-105 GeV
Signal
Background
AvgTrackPt1000Frac

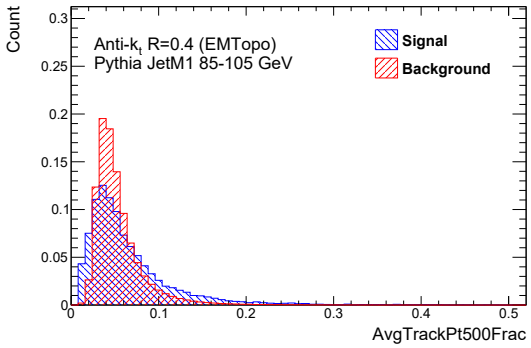
Count
Anti-k$_t$ R=0.4 (EMTopo)
Pythia JetM1 85-105 GeV
Signal
Background
AvgTrackPt500Frac

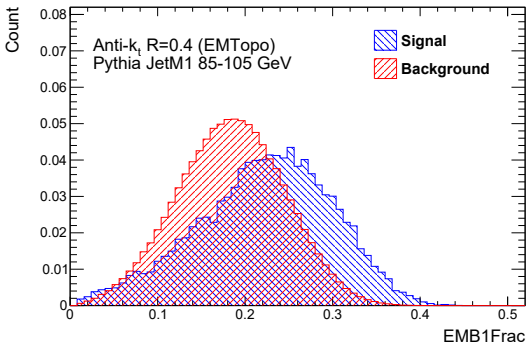
Count
Anti-k$_t$ R=0.4 (EMTopo)
Pythia JetM1 85-105 GeV
Signal
Background
EMB1Frac

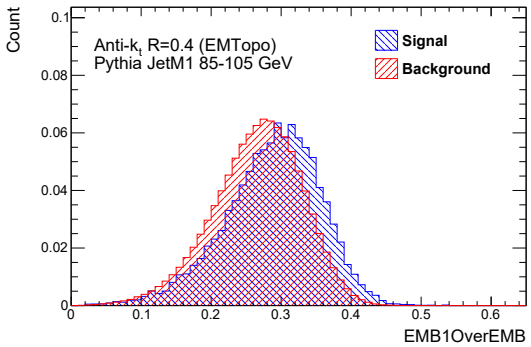
Count
Anti-k$_t$ R=0.4 (EMTopo)
Pythia JetM1 85-105 GeV
Signal
Background
EMB1OverEMB

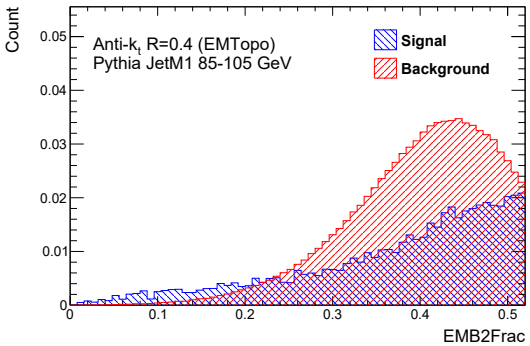
Count
Anti-k$_t$ R=0.4 (EMTopo)
Pythia JetM1 85-105 GeV
Signal
Background
EMB2Frac

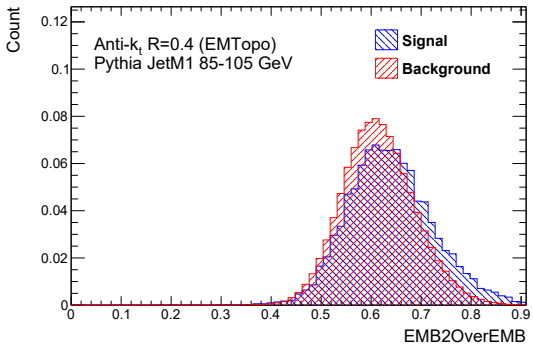
Count
Anti-k$_t$ R=0.4 (EMTopo)
Pythia JetM1 85-105 GeV
Signal
Background
EMB2OverEMB

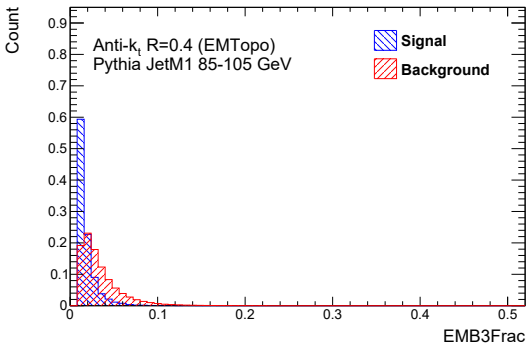
Count
Anti-k$_t$ R=0.4 (EMTopo)
Pythia JetM1 85-105 GeV
Signal
Background
EMB3Frac

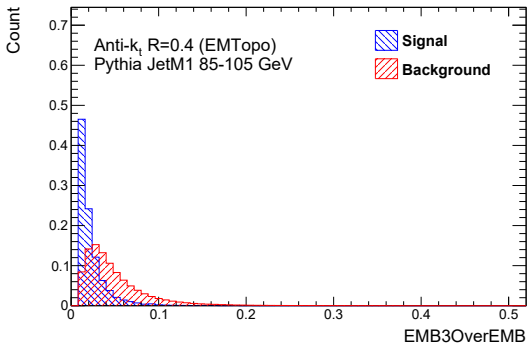
Count
Anti-k$_t$ R=0.4 (EMTopo)
Pythia JetM1 85-105 GeV
Signal
Background
EMB3OverEMB

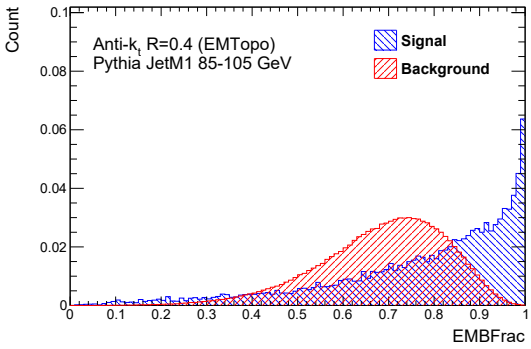
Count
Anti-k$_t$ R=0.4 (EMTopo)
Pythia JetM1 85-105 GeV
Signal
Background
EMBFrac

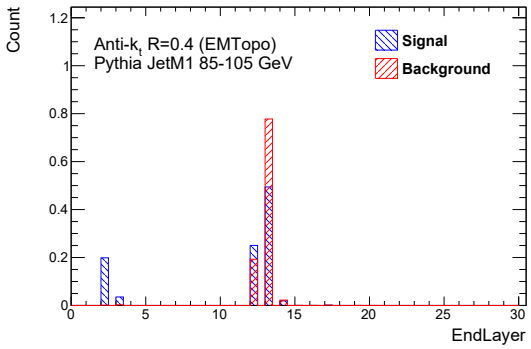
Count
Anti-k$_t$ R=0.4 (EMTopo)
Pythia JetM1 85-105 GeV
Signal
Background
EndLayer

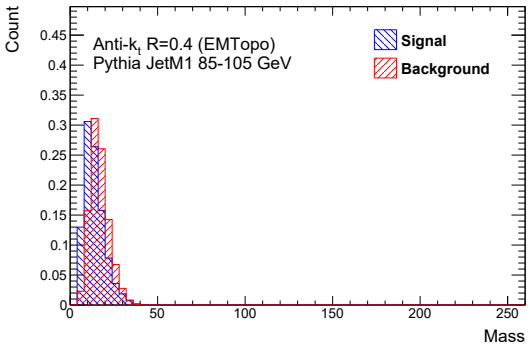
Count
Anti-k$_t$ R=0.4 (EMTopo)
Pythia JetM1 85-105 GeV
Signal
Background
Mass

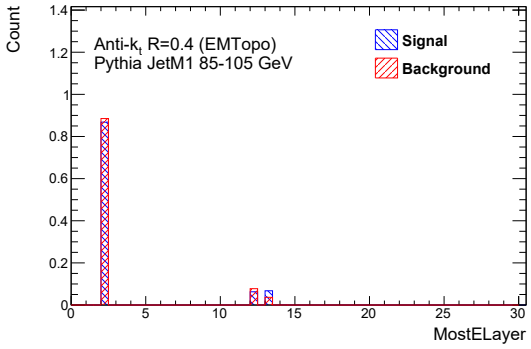
Count
Anti-k$_t$ R=0.4 (EMTopo)
Pythia JetM1 85-105 GeV
Signal
Background
MostELayer

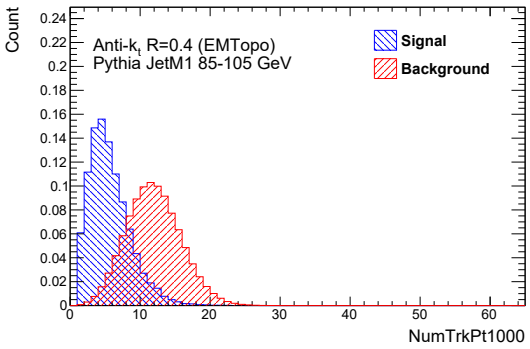
Count
Anti-k$_t$ R=0.4 (EMTopo)
Pythia JetM1 85-105 GeV
Signal
Background
NumTrkPt1000

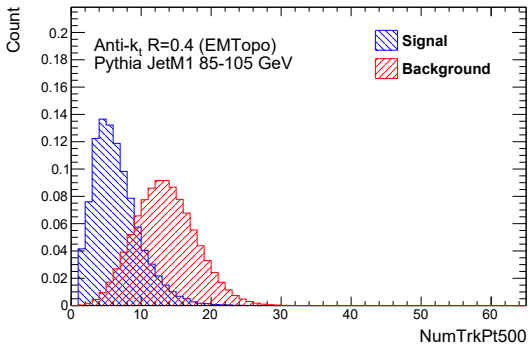
Count
Anti-k$_t$ R=0.4 (EMTopo)
Pythia JetM1 85-105 GeV
Signal
Background
NumTrkPt500

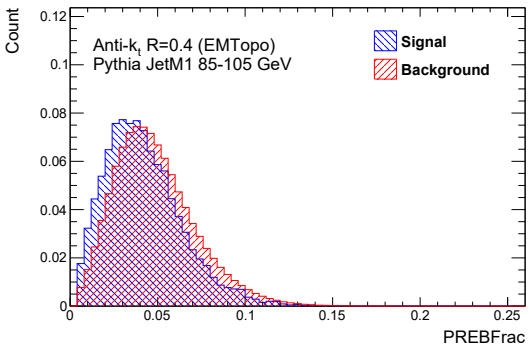
Count
Anti-k$_t$ R=0.4 (EMTopo)
Pythia JetM1 85-105 GeV
Signal
Background
PREBFrac

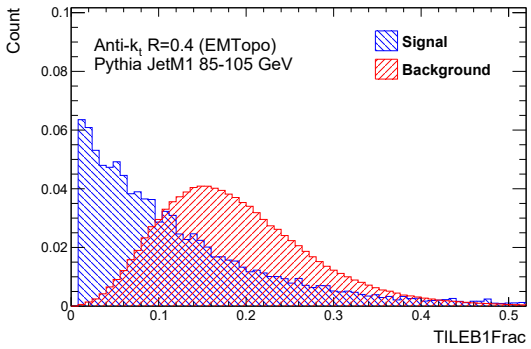
Count
Anti-k$_t$ R=0.4 (EMTopo)
Pythia JetM1 85-105 GeV
Signal
Background
TILEB1Frac

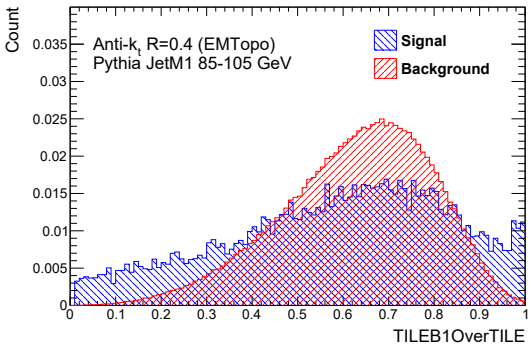
Count
Anti-k$_t$ R=0.4 (EMTopo)
Pythia JetM1 85-105 GeV
Signal
Background
TILEB1OverTILE

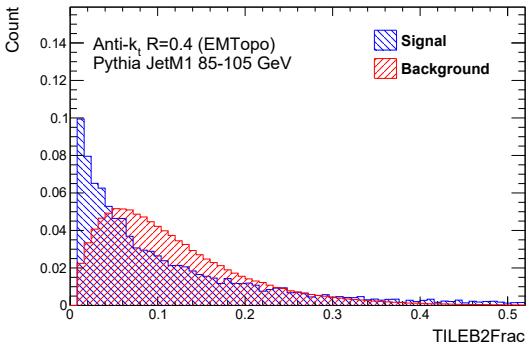
Count
Anti-k$_t$ R=0.4 (EMTopo)
Pythia JetM1 85-105 GeV
Signal
Background
TILEB2Frac

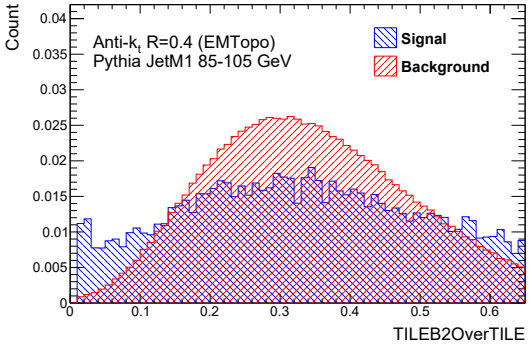
Count
Anti-k$_t$ R=0.4 (EMTopo)
Pythia JetM1 85-105 GeV
Signal
Background
TILEB2OverTILE

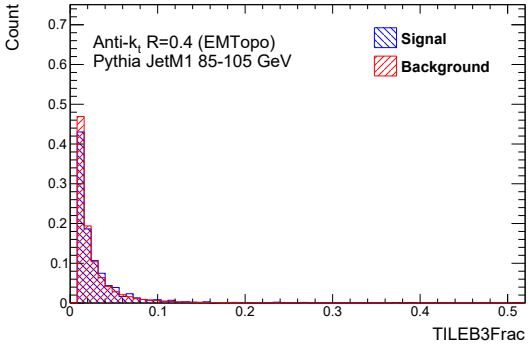
Count
Anti-k$_t$ R=0.4 (EMTopo)
Pythia JetM1 85-105 GeV
Signal
Background
TILEB3Frac

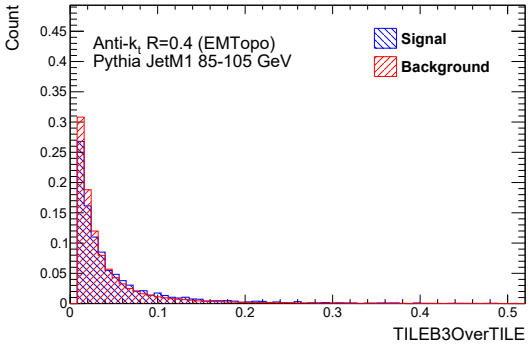
Count
Anti-k$_t$ R=0.4 (EMTopo)
Pythia JetM1 85-105 GeV
Signal
Background
TILEB3OverTILE

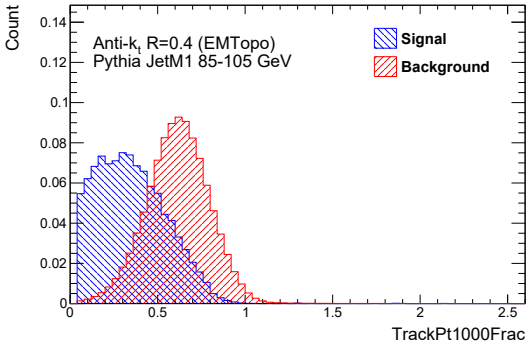
Count
Anti-k$_t$ R=0.4 (EMTopo)
Pythia JetM1 85-105 GeV
Signal
Background
TrackPt1000Frac

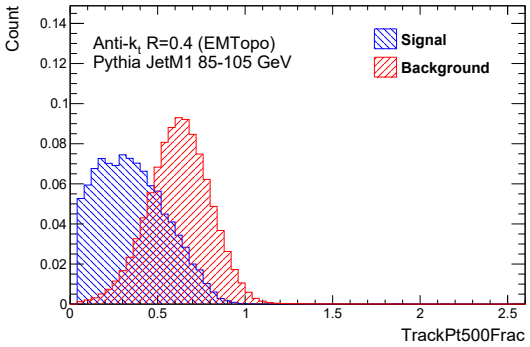
Count
Anti-k$_t$ R=0.4 (EMTopo)
Pythia JetM1 85-105 GeV
Signal
Background
TrackPt500Frac

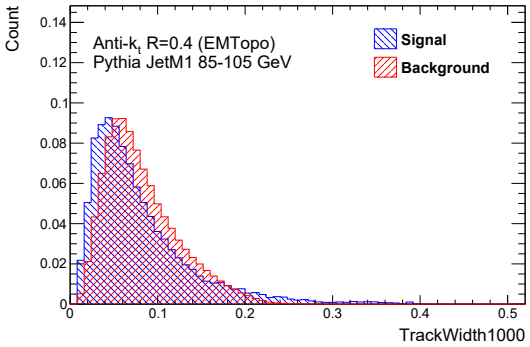
Count
Anti-k$_t$ R=0.4 (EMTopo)
Pythia JetM1 85-105 GeV
Signal
Background
TrackWidth1000

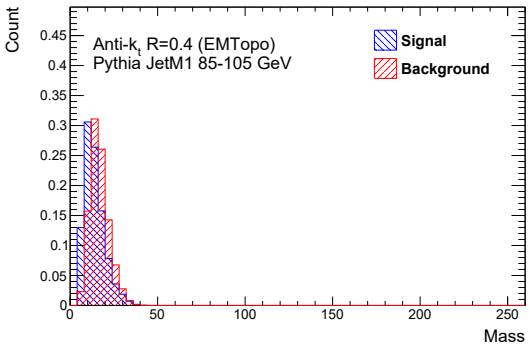
Count
Anti-k$_t$ R=0.4 (EMTopo)
Pythia JetM1 85-105 GeV
Signal
Background
Mass

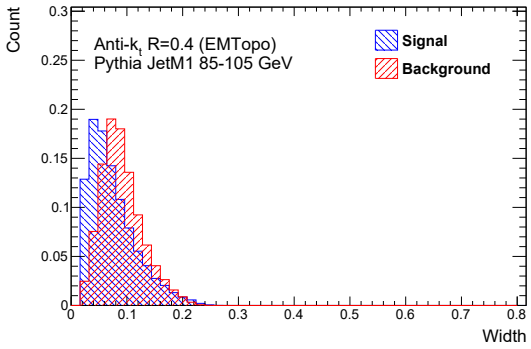
Count
Anti-k$_t$ R=0.4 (EMTopo)
Pythia JetM1 85-105 GeV
Signal
Background
Width

C.5 105-125 GeV

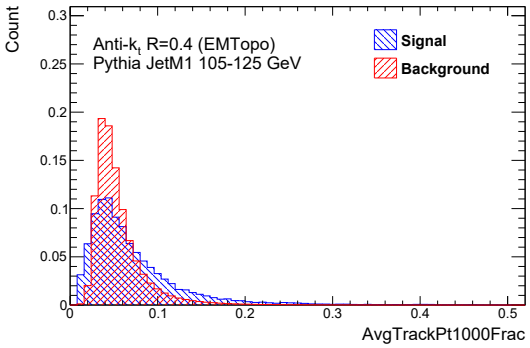

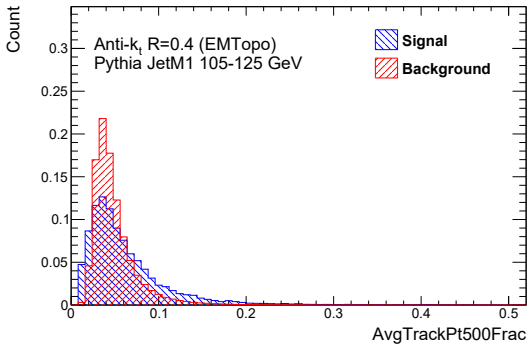

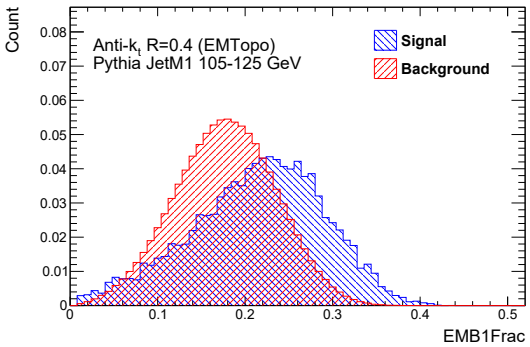

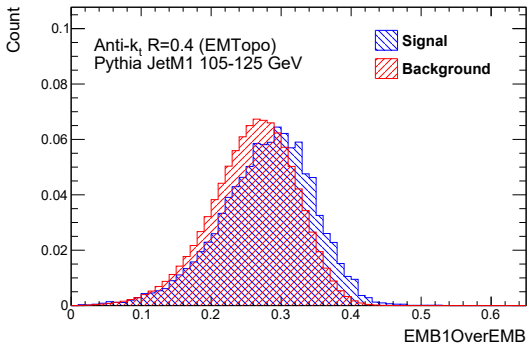

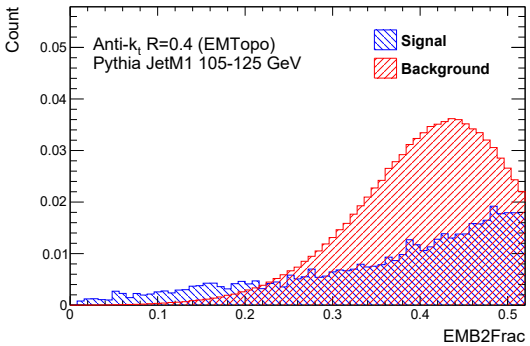

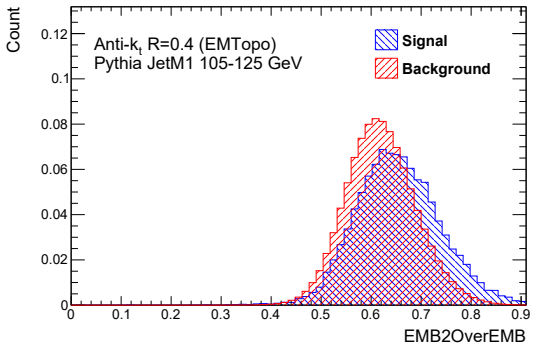

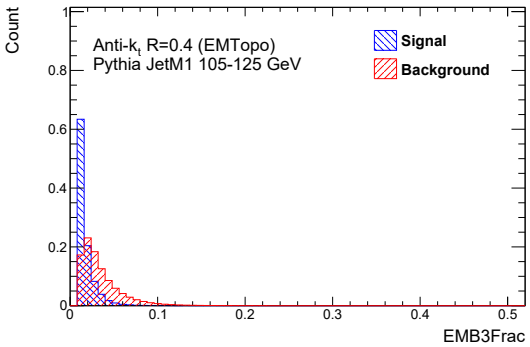

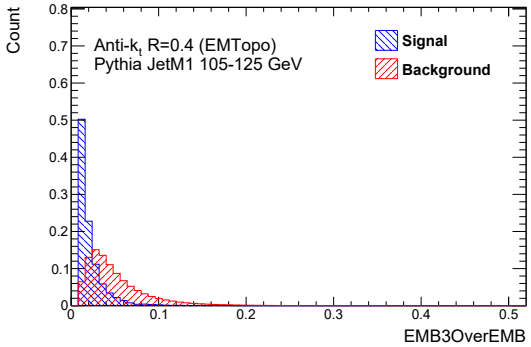

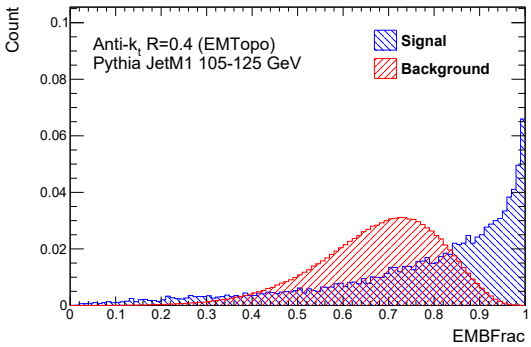
Count
Anti-k$_t$ R=0.4 (EMTopo)
Pythia JetM1 105-125 GeV
Signal
Background
EMBFrac

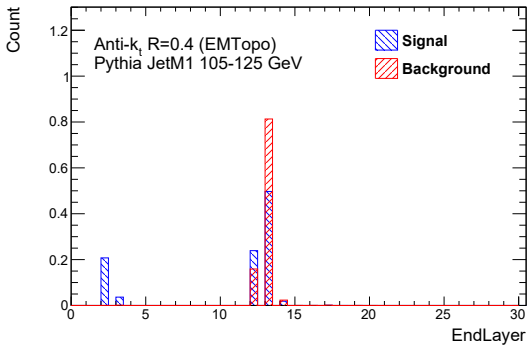
Count
Anti-k$_t$ R=0.4 (EMTopo)
Pythia JetM1 105-125 GeV
Signal
Background
EndLayer

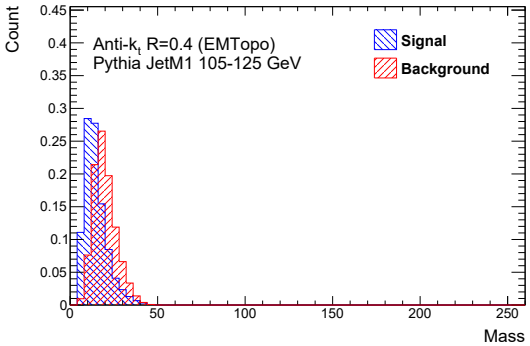
Count
Anti-k$_t$ R=0.4 (EMTopo)
Pythia JetM1 105-125 GeV
Signal
Background
Mass

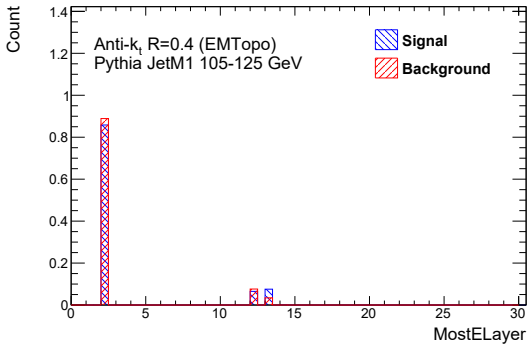
Count
Anti-k$_t$ R=0.4 (EMTopo)
Pythia JetM1 105-125 GeV
Signal
Background
MostELayer

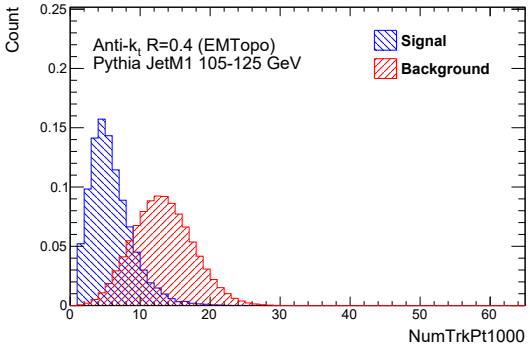
Count
Anti-k$_t$ R=0.4 (EMTopo)
Pythia JetM1 105-125 GeV
Signal
Background
NumTrkPt1000

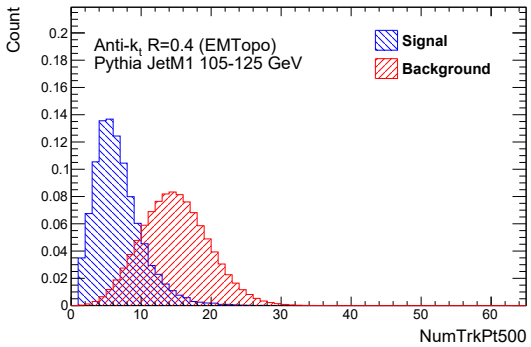
Count
Anti-k$_t$ R=0.4 (EMTopo)
Pythia JetM1 105-125 GeV
Signal
Background
NumTrkPt500

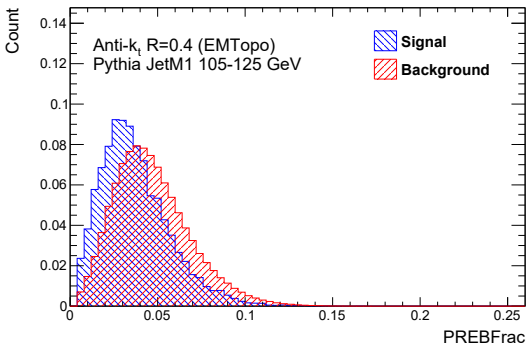
Count
Anti-k$_t$ R=0.4 (EMTopo)
Pythia JetM1 105-125 GeV
Signal
Background
PREBFrac

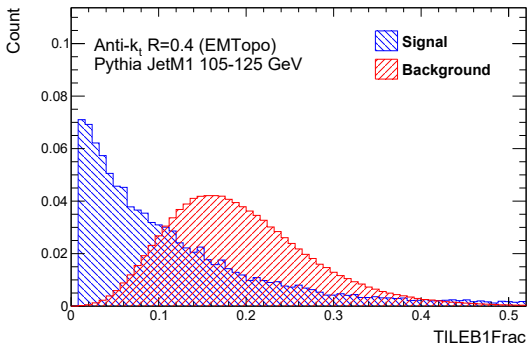
Count
Anti-k$_t$ R=0.4 (EMTopo)
Pythia JetM1 105-125 GeV
Signal
Background
TILEB1Frac

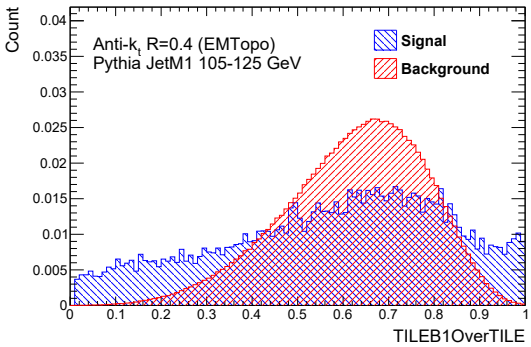
Count
Anti-k$_t$ R=0.4 (EMTopo)
Pythia JetM1 105-125 GeV
Signal
Background
TILEB1OverTILE

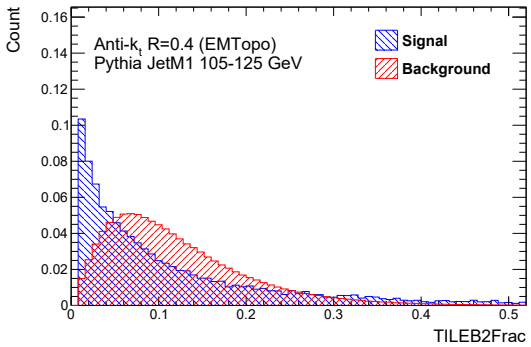
Count
Anti-k$_t$ R=0.4 (EMTopo)
Pythia JetM1 105-125 GeV
Signal
Background
TILEB2Frac

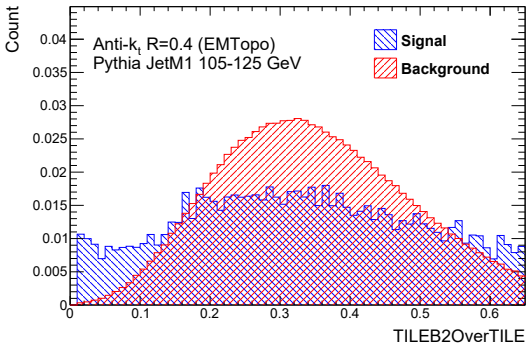
Count
Anti-k$_t$ R=0.4 (EMTopo)
Pythia JetM1 105-125 GeV
Signal
Background
TILEB2OverTILE

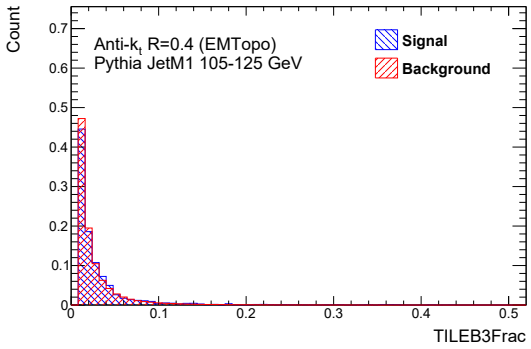
Count
Anti-k$_t$ R=0.4 (EMTopo)
Pythia JetM1 105-125 GeV
Signal
Background
TILEB3Frac

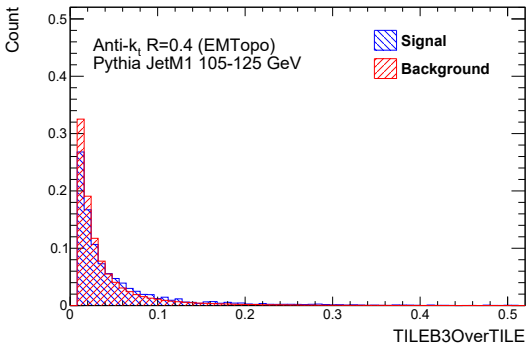
Count
Anti-k$_t$ R=0.4 (EMTopo)
Pythia JetM1 105-125 GeV
Signal
Background
TILEB3OverTILE

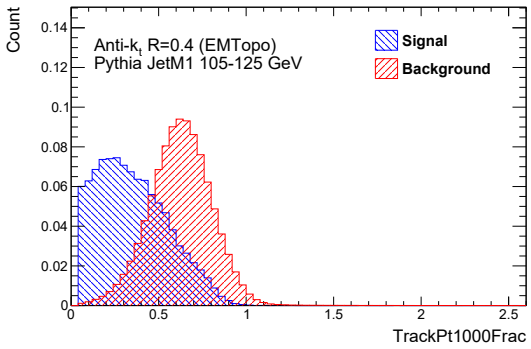
Count
Anti-k$_t$ R=0.4 (EMTopo)
Pythia JetM1 105-125 GeV
Signal
Background
TrackPt1000Frac

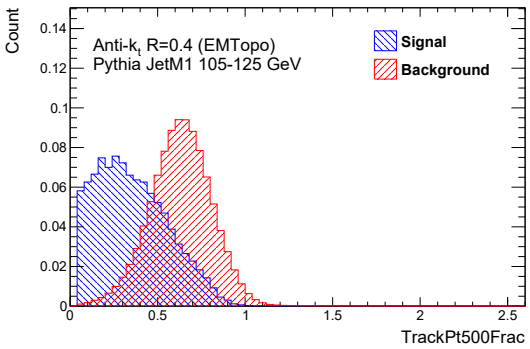
Count
Anti-k$_t$ R=0.4 (EMTopo)
Pythia JetM1 105-125 GeV
Signal
Background
TrackPt500Frac

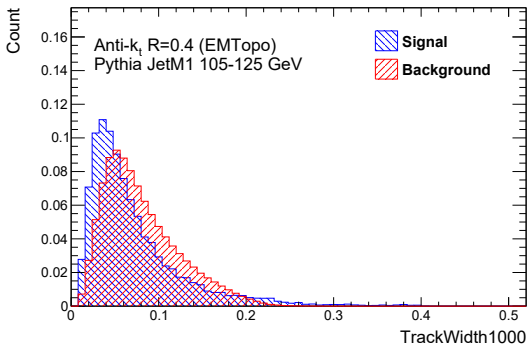
Count
Anti-k$_t$ R=0.4 (EMTopo)
Pythia JetM1 105-125 GeV
Signal
Background
TrackWidth1000

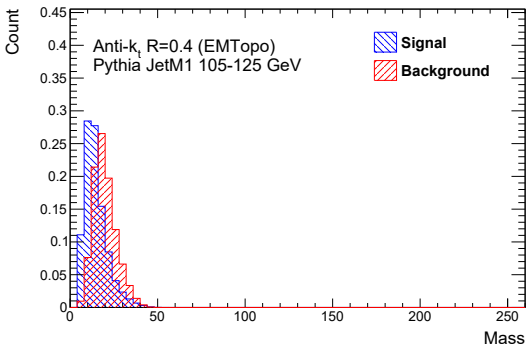
Count
Anti-k$_t$ R=0.4 (EMTopo)
Pythia JetM1 105-125 GeV
Signal
Background
Mass

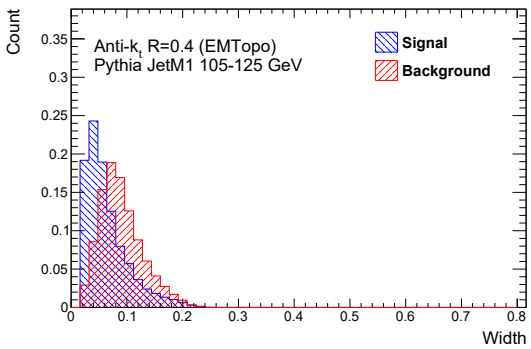
Count
Anti-k$_t$ R=0.4 (EMTopo)
Pythia JetM1 105-125 GeV
Signal
Background
Width

C.6 125-160 GeV

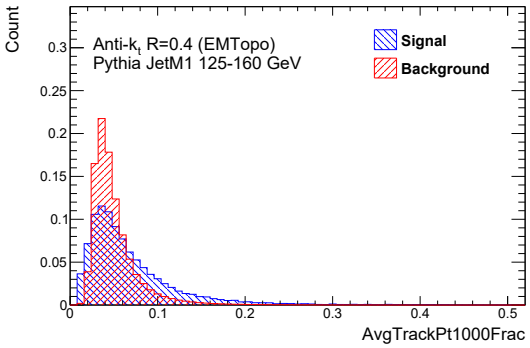

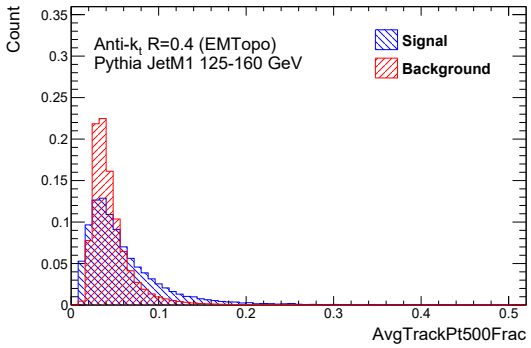

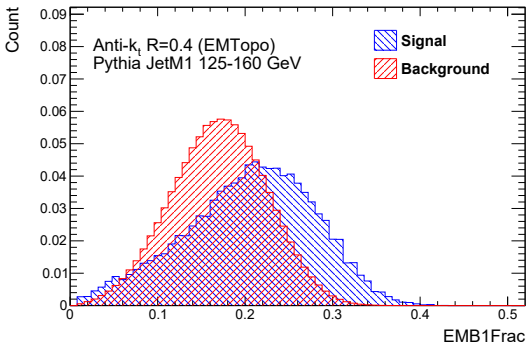

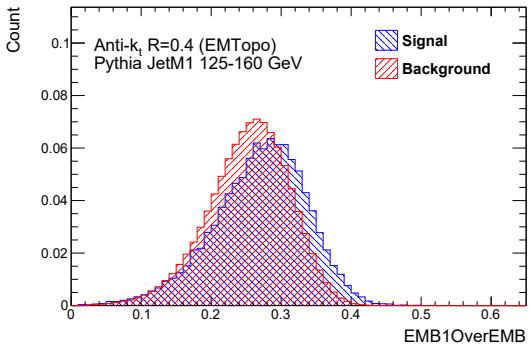

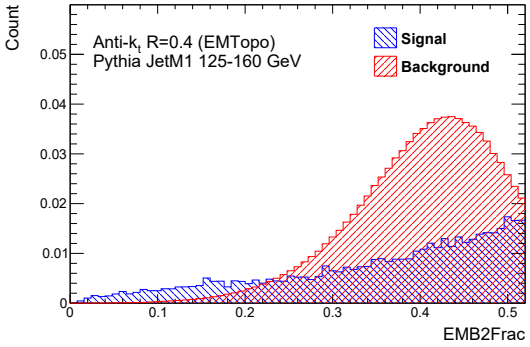

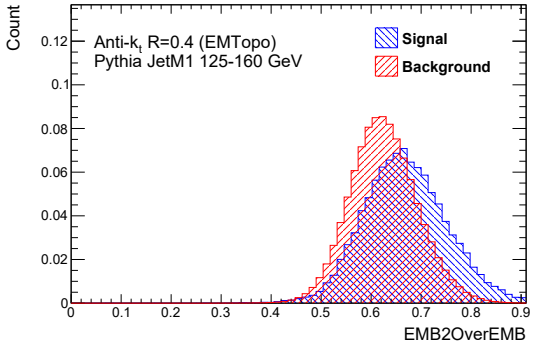

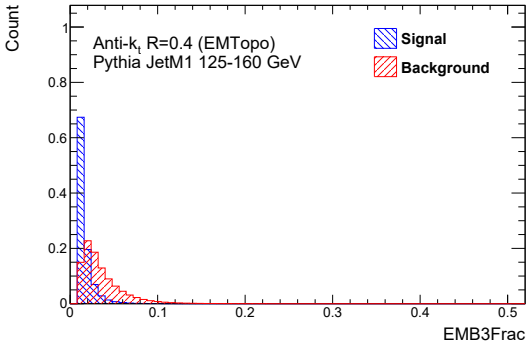

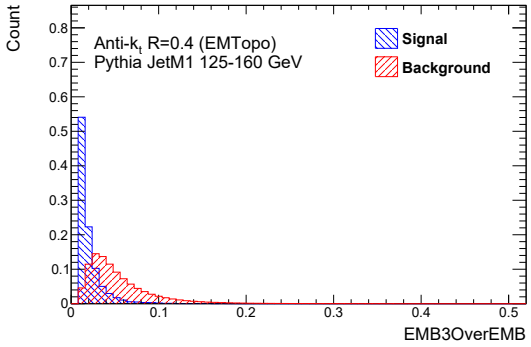

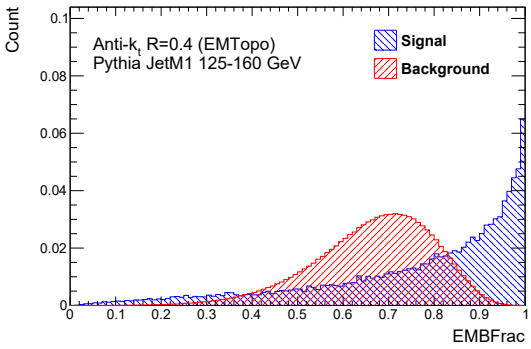
Count
Anti-k$_t$ R=0.4 (EMTopo)
Pythia JetM1 125-160 GeV
Signal
Background
EMBFrac

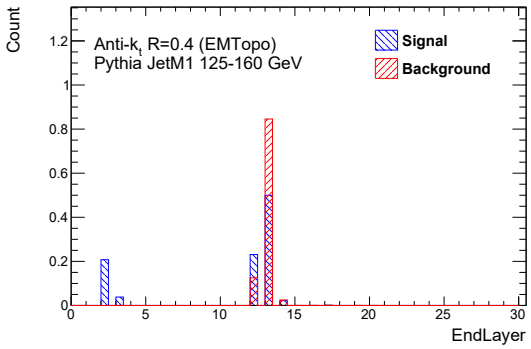
Count
Anti-k$_t$ R=0.4 (EMTopo)
Pythia JetM1 125-160 GeV
Signal
Background
EndLayer

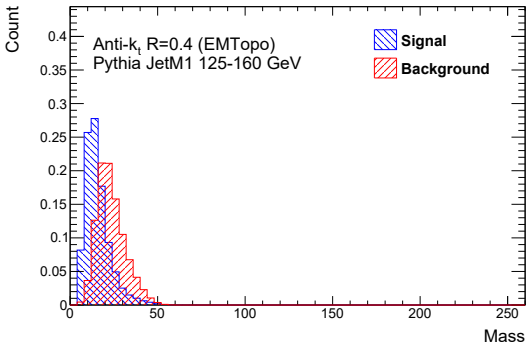
Count
Anti-k$_t$ R=0.4 (EMTopo)
Pythia JetM1 125-160 GeV
Signal
Background
Mass

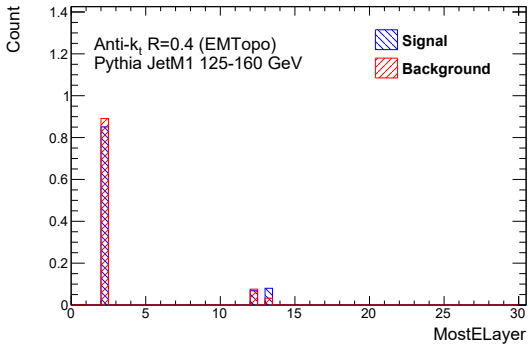
Count
Anti-k$_t$ R=0.4 (EMTopo)
Pythia JetM1 125-160 GeV
Signal
Background
MostELayer

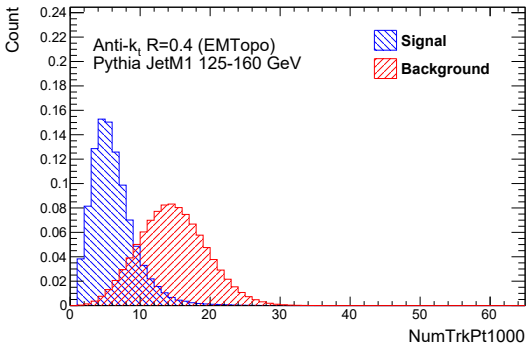
Count
Anti-k$_t$ R=0.4 (EMTopo)
Pythia JetM1 125-160 GeV
Signal
Background
NumTrkPt1000

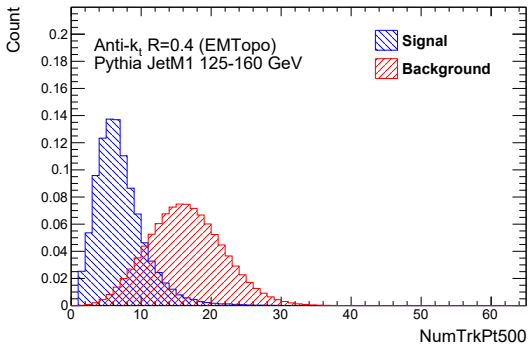
Count
Anti-k$_t$ R=0.4 (EMTopo)
Pythia JetM1 125-160 GeV
Signal
Background
NumTrkPt500

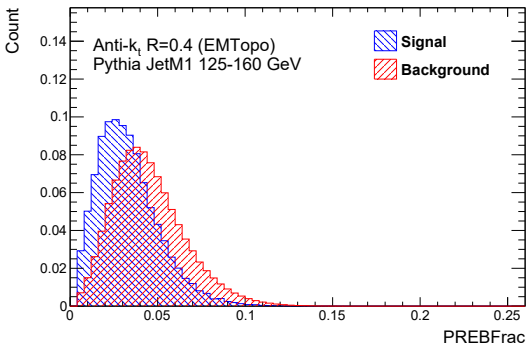
Count
Anti-k$_t$ R=0.4 (EMTopo)
Pythia JetM1 125-160 GeV
Signal
Background
PREBFrac

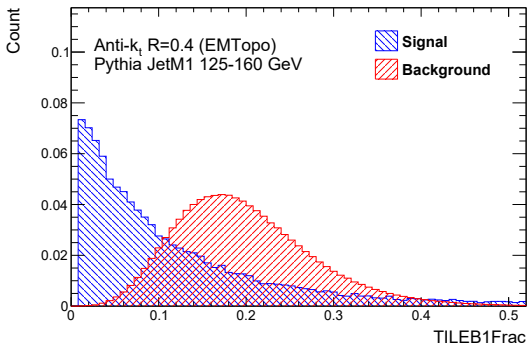
Count
Anti-k$_t$ R=0.4 (EMTopo)
Pythia JetM1 125-160 GeV
Signal
Background
TILEB1Frac

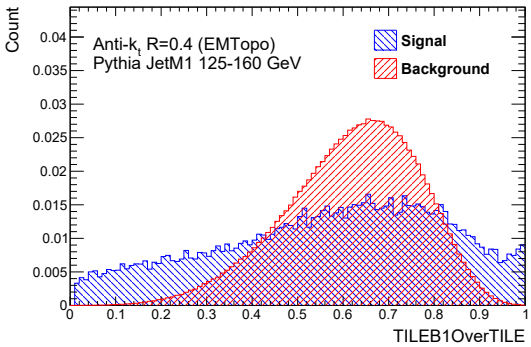
Count
Anti-k$_t$ R=0.4 (EMTopo)
Pythia JetM1 125-160 GeV
Signal
Background
TILEB1OverTILE

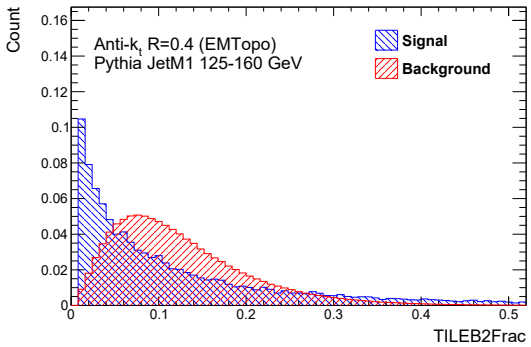
Count
Anti-k$_t$ R=0.4 (EMTopo)
Pythia JetM1 125-160 GeV
Signal
Background
TILEB2Frac

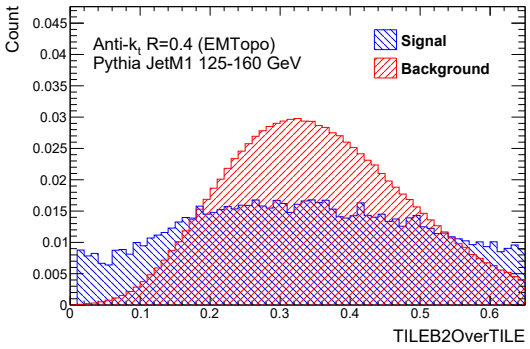
Count
Anti-k$_t$ R=0.4 (EMTopo)
Pythia JetM1 125-160 GeV
Signal
Background
TILEB2OverTILE

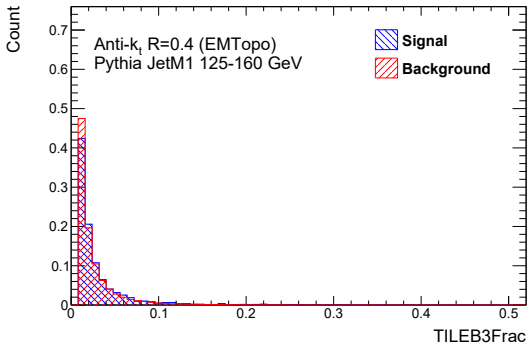
Count
Anti-k$_t$ R=0.4 (EMTopo)
Pythia JetM1 125-160 GeV
Signal
Background
TILEB3Frac

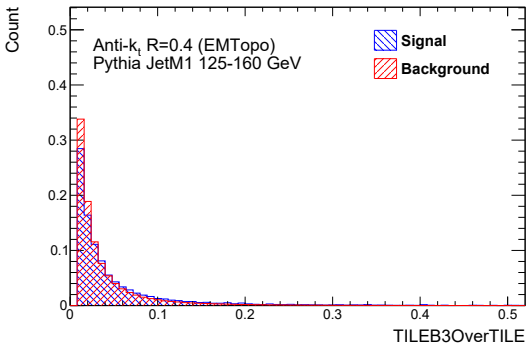
Count
Anti-k$_t$ R=0.4 (EMTopo)
Pythia JetM1 125-160 GeV
Signal
Background
TILEB3OverTILE

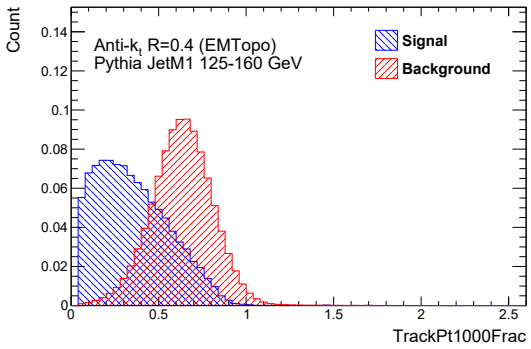
Count
Anti-k$_t$ R=0.4 (EMTopo)
Pythia JetM1 125-160 GeV
Signal
Background
TrackPt1000Frac

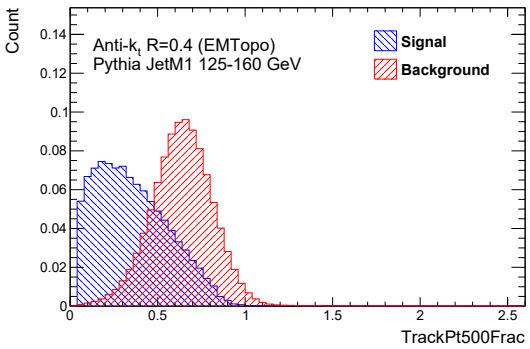
Count
Anti-k$_t$ R=0.4 (EMTopo)
Pythia JetM1 125-160 GeV
Signal
Background
TrackPt500Frac

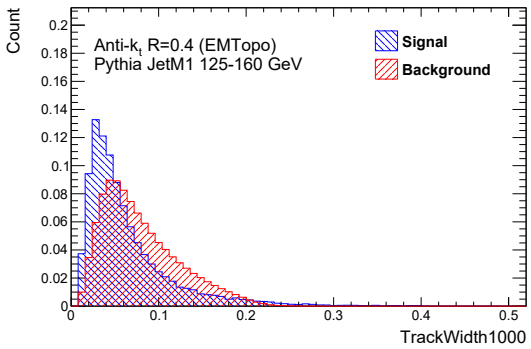
Count
Anti-k$_t$ R=0.4 (EMTopo)
Pythia JetM1 125-160 GeV
Signal
Background
TrackWidth1000

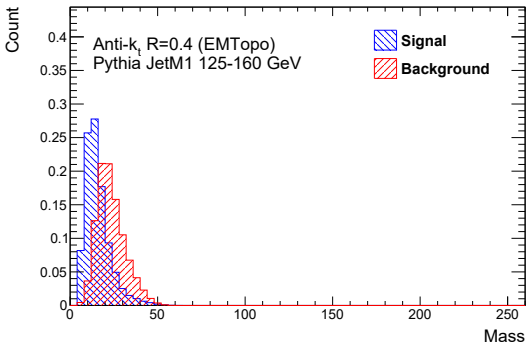
Count
Anti-k$_t$ R=0.4 (EMTopo)
Pythia JetM1 125-160 GeV
Signal
Background
Mass

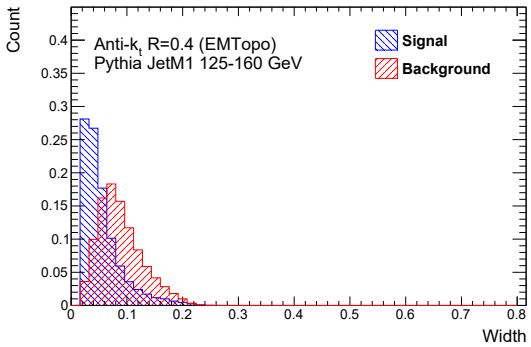
Count
Anti-k$_t$ R=0.4 (EMTopo)
Pythia JetM1 125-160 GeV
Signal
Background
Width

C.7 160-210 GeV

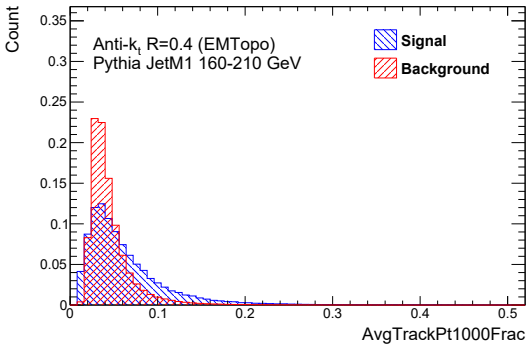

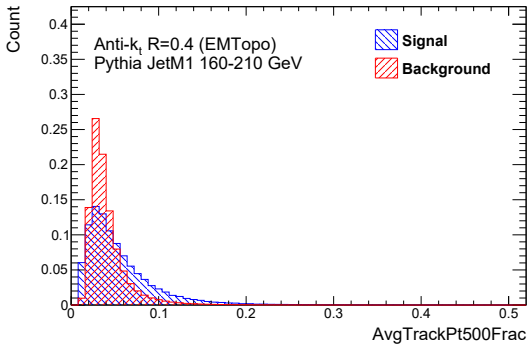

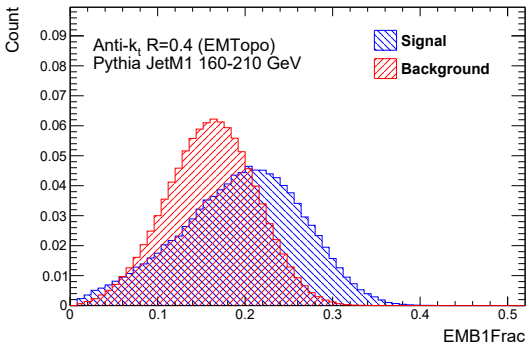

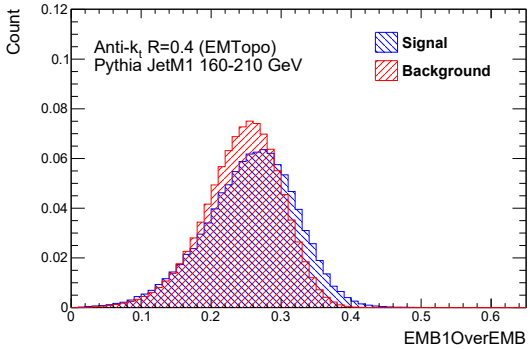

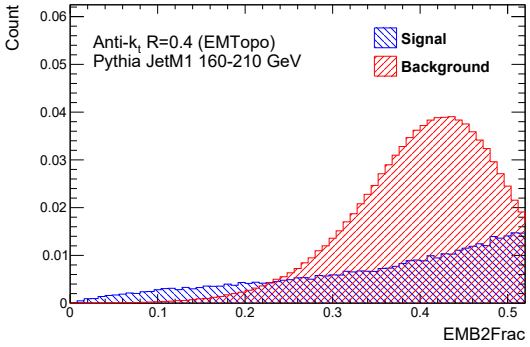

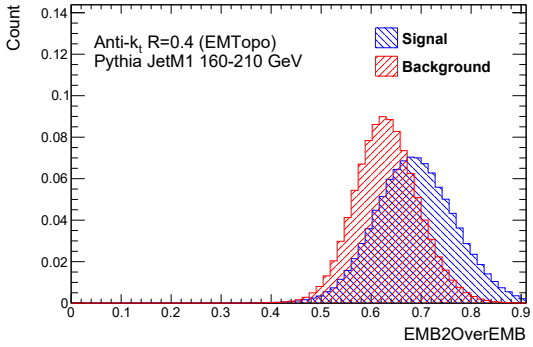

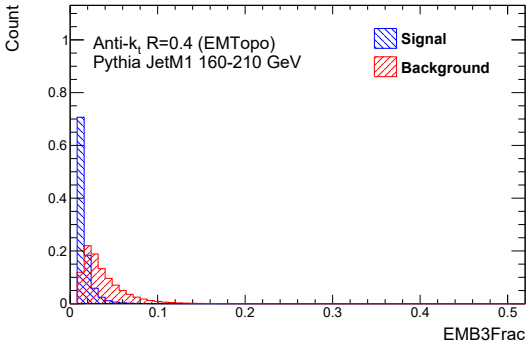

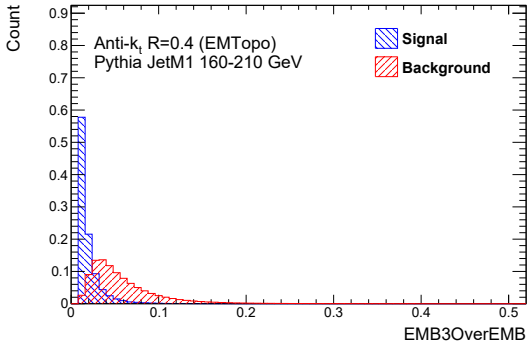

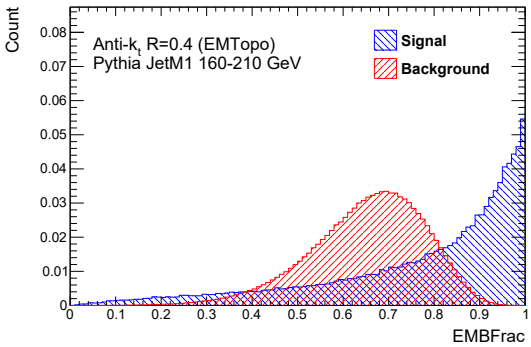
Count
Anti-k$_t$ R=0.4 (EMTopo)
Pythia JetM1 160-210 GeV
Signal
Background
EMBFrac

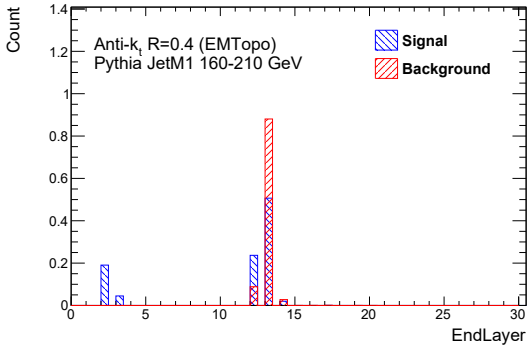
Count
Anti-k$_t$ R=0.4 (EMTopo)
Pythia JetM1 160-210 GeV
Signal
Background
EndLayer

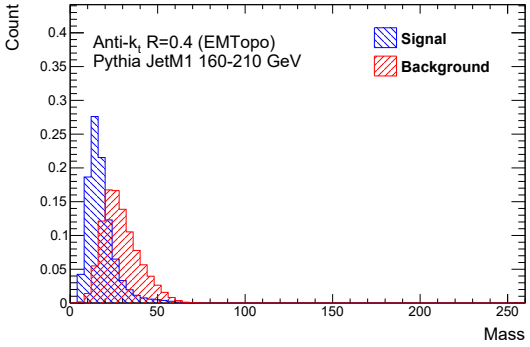
Count
Anti-k$_t$ R=0.4 (EMTopo)
Pythia JetM1 160-210 GeV
Signal
Background
Mass

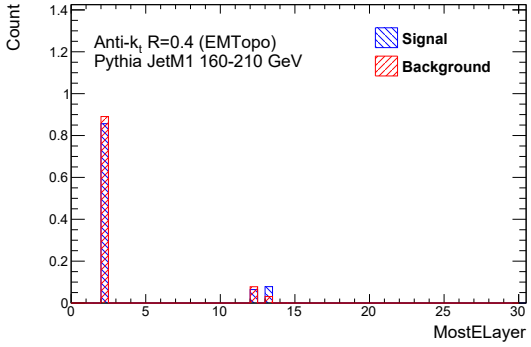
Count
Anti-k$_t$ R=0.4 (EMTopo)
Pythia JetM1 160-210 GeV
Signal
Background
MostELayer

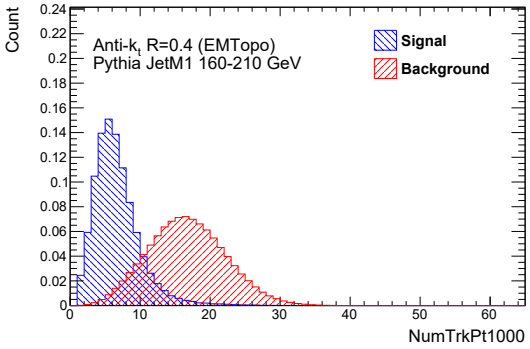
Count
Anti-k$_t$ R=0.4 (EMTopo)
Pythia JetM1 160-210 GeV
Signal
Background
NumTrkPt1000

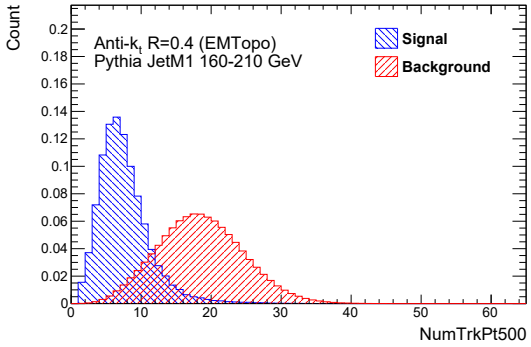
Count
Anti-k$_t$ R=0.4 (EMTopo)
Pythia JetM1 160-210 GeV
Signal
Background
NumTrkPt500

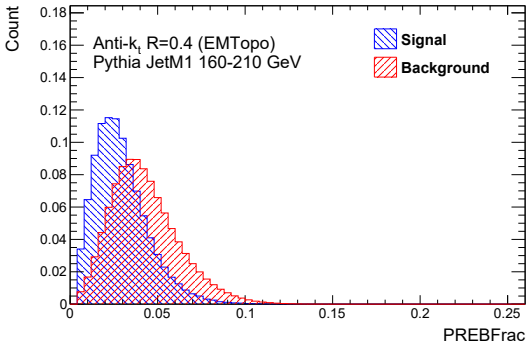
Count
Anti-k$_t$ R=0.4 (EMTopo)
Pythia JetM1 160-210 GeV
Signal
Background
PREBFrac

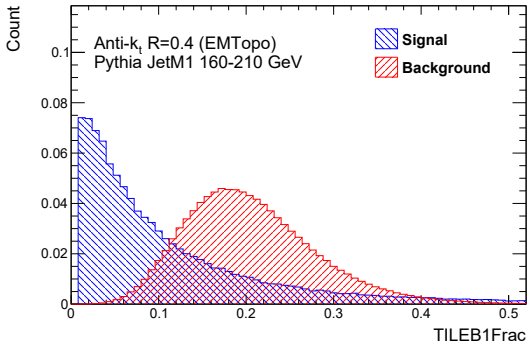
Count
Anti-k$_t$ R=0.4 (EMTopo)
Pythia JetM1 160-210 GeV
Signal
Background
TILEB1Frac

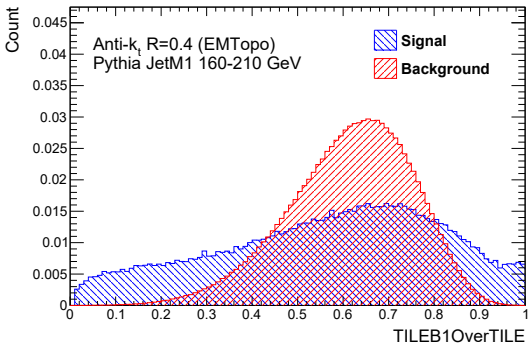
Count
Anti-k$_t$ R=0.4 (EMTopo)
Pythia JetM1 160-210 GeV
Signal
Background
TILEB1OverTILE

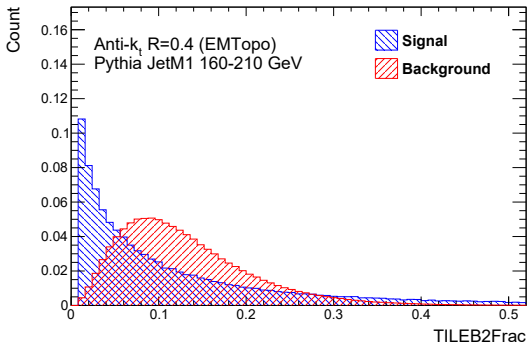
Count
Anti-k$_t$ R=0.4 (EMTopo)
Pythia JetM1 160-210 GeV
Signal
Background
TILEB2Frac

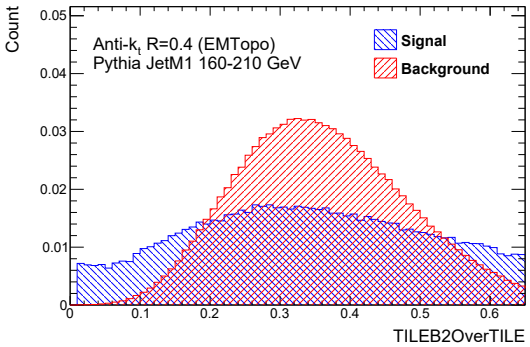
Count
Anti-k$_t$ R=0.4 (EMTopo)
Pythia JetM1 160-210 GeV
Signal
Background
TILEB2OverTILE

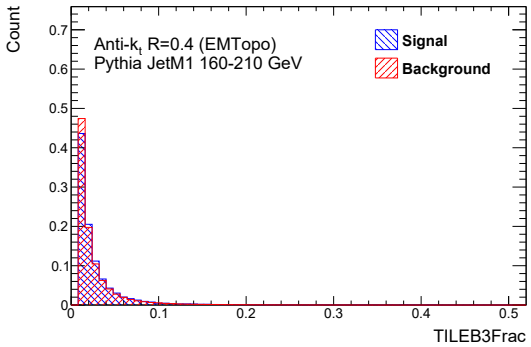
Count
Anti-k$_t$ R=0.4 (EMTopo)
Pythia JetM1 160-210 GeV
Signal
Background
TILEB3Frac

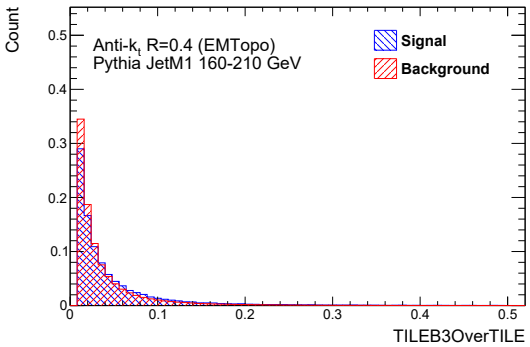
Count
Anti-k$_t$ R=0.4 (EMTopo)
Pythia JetM1 160-210 GeV
Signal
Background
TILEB3OverTILE

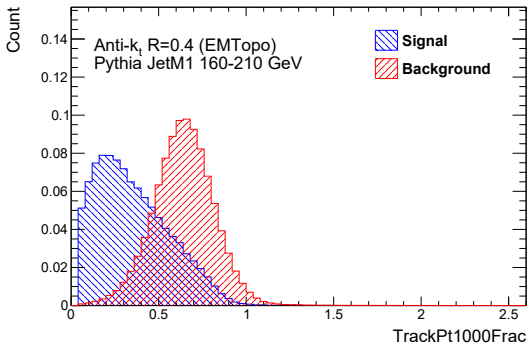
Count
Anti-k$_t$ R=0.4 (EMTopo)
Pythia JetM1 160-210 GeV
Signal
Background
TrackPt1000Frac

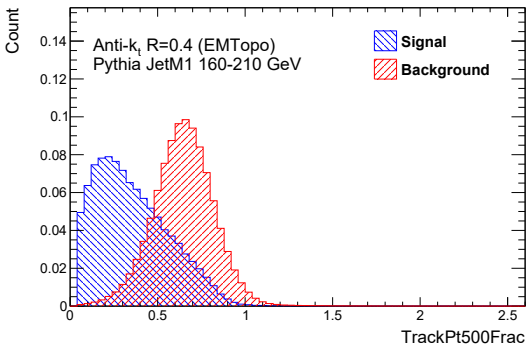
Count
Anti-k$_t$ R=0.4 (EMTopo)
Pythia JetM1 160-210 GeV
Signal
Background
TrackPt500Frac

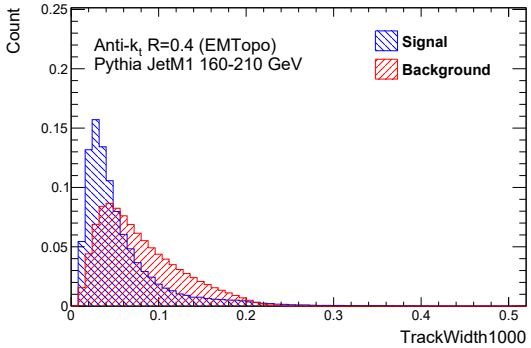
Count
Anti-k$_t$ R=0.4 (EMTopo)
Pythia JetM1 160-210 GeV
Signal
Background
TrackWidth1000

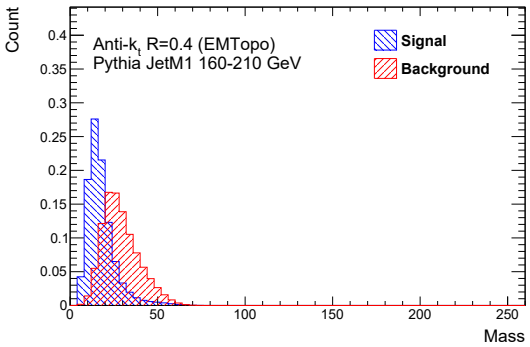
Count
Anti-k$_t$ R=0.4 (EMTopo)
Pythia JetM1 160-210 GeV
Signal
Background
Mass

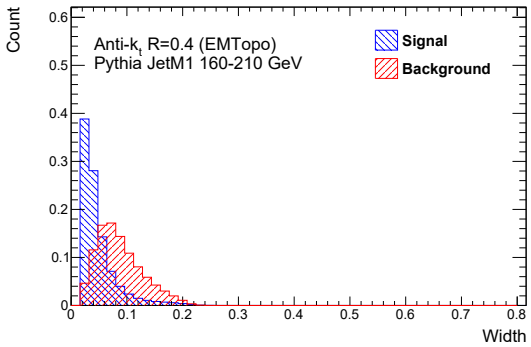
Count
Anti-k$_t$ R=0.4 (EMTopo)
Pythia JetM1 160-210 GeV
Signal
Background
Width

C.8 210-260 GeV

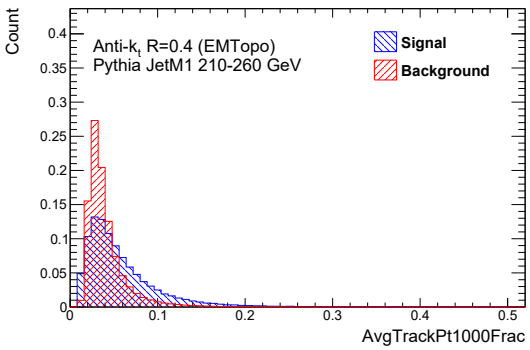

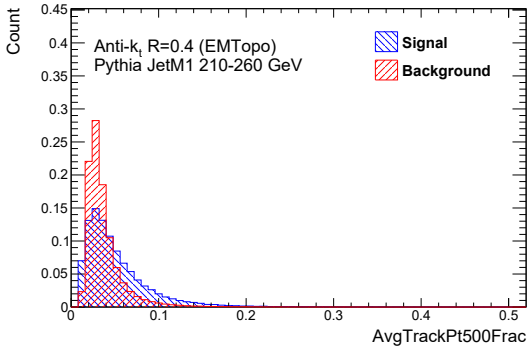

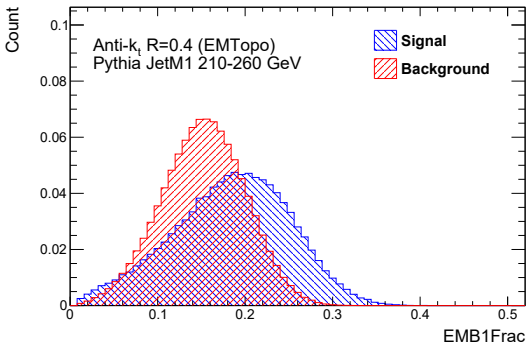

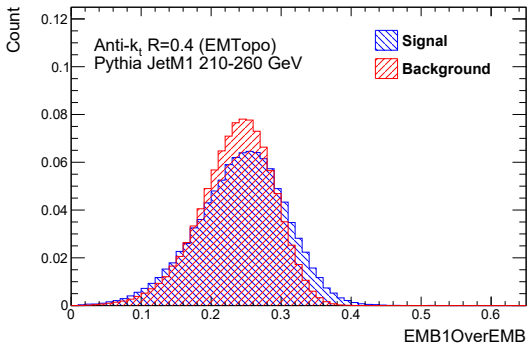

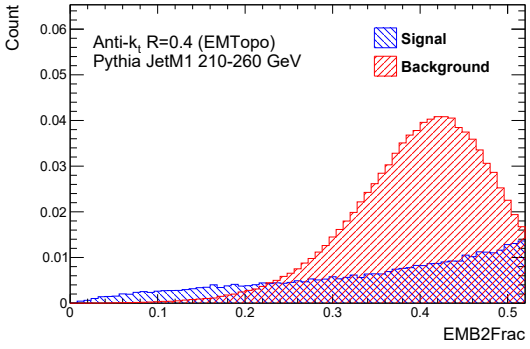

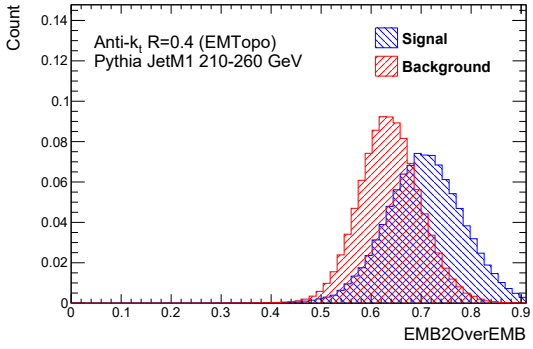

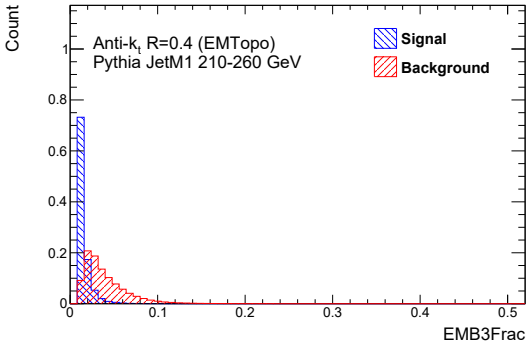

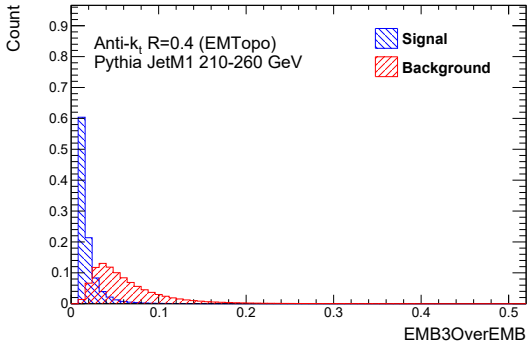

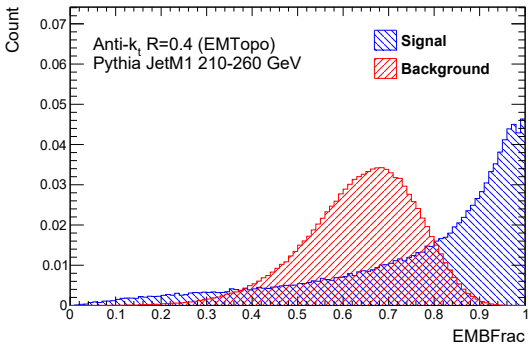
Count
Anti-k$_t$ R=0.4 (EMTopo)
Pythia JetM1 210-260 GeV
Signal
Background
EMBFrac

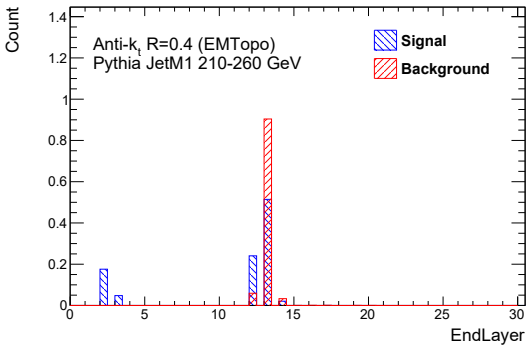
Count
Anti-k$_t$ R=0.4 (EMTopo)
Pythia JetM1 210-260 GeV
Signal
Background
EndLayer

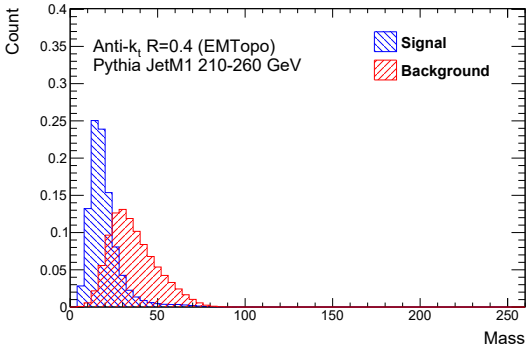
Count
Anti-k$_t$ R=0.4 (EMTopo)
Pythia JetM1 210-260 GeV
Signal
Background
Mass

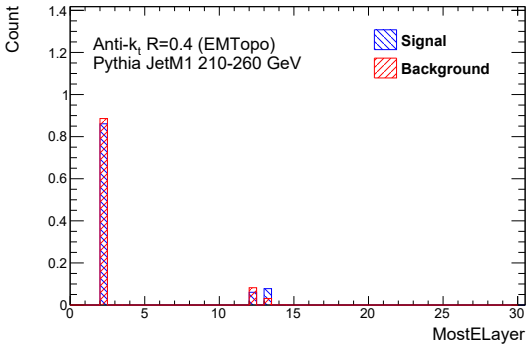
Count
Anti-k$_t$ R=0.4 (EMTopo)
Pythia JetM1 210-260 GeV
Signal
Background
MostELayer

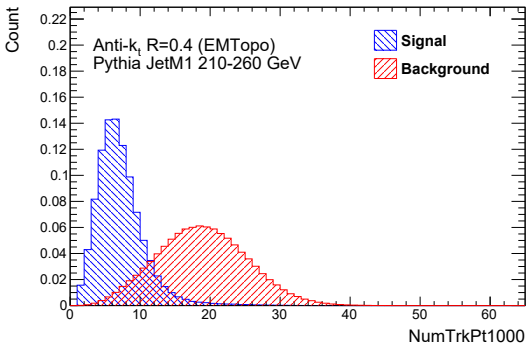
Count
Anti-k$_t$ R=0.4 (EMTopo)
Pythia JetM1 210-260 GeV
Signal
Background
NumTrkPt1000

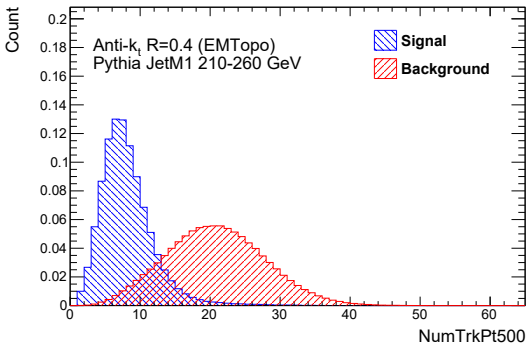
Count
Anti-k$_t$ R=0.4 (EMTopo)
Pythia JetM1 210-260 GeV
Signal
Background
NumTrkPt500

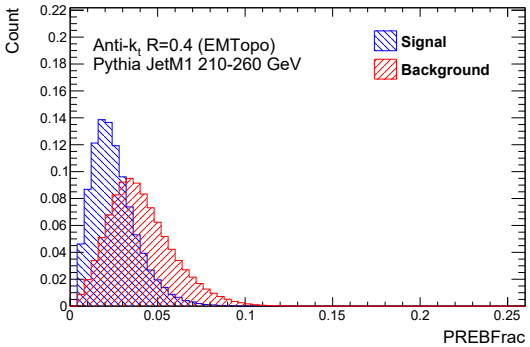
Count
Anti-k$_t$ R=0.4 (EMTopo)
Pythia JetM1 210-260 GeV
Signal
Background
PREBFrac

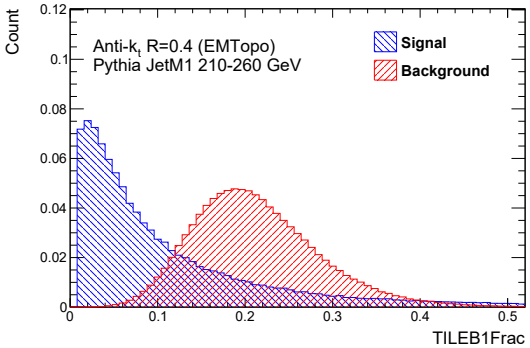
Count
Anti-k$_t$ R=0.4 (EMTopo)
Pythia JetM1 210-260 GeV
Signal
Background
TILEB1Frac

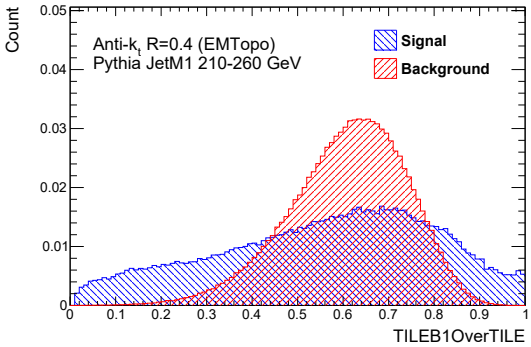
Count
Anti-k$_t$ R=0.4 (EMTopo)
Pythia JetM1 210-260 GeV
Signal
Background
TILEB1OverTILE

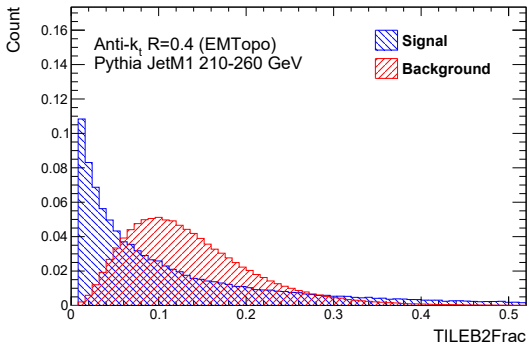
Count
Anti-k$_t$ R=0.4 (EMTopo)
Pythia JetM1 210-260 GeV
Signal
Background
TILEB2Frac

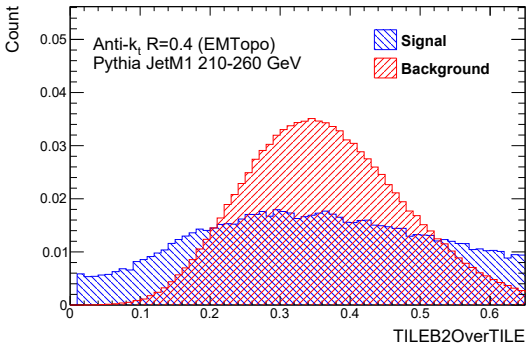
Count
Anti-k$_t$ R=0.4 (EMTopo)
Pythia JetM1 210-260 GeV
Signal
Background
TILEB2OverTILE

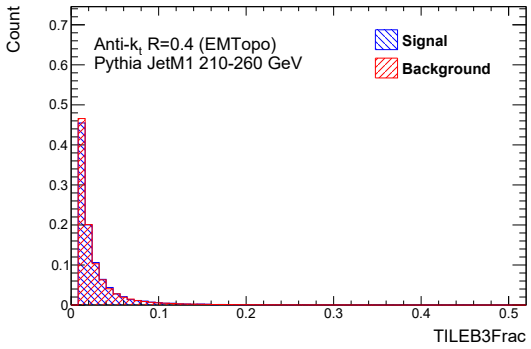
Count
Anti-k$_t$ R=0.4 (EMTopo)
Pythia JetM1 210-260 GeV
Signal
Background
TILEB3Frac

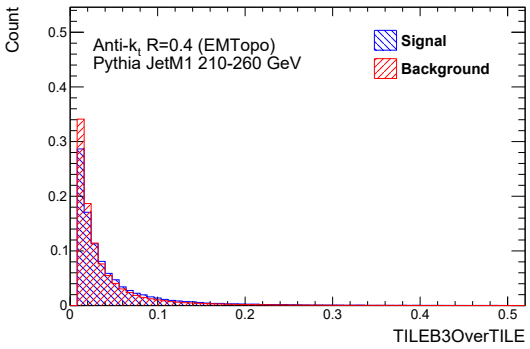
Count
Anti-k$_t$ R=0.4 (EMTopo)
Pythia JetM1 210-260 GeV
Signal
Background
TILEB3OverTILE

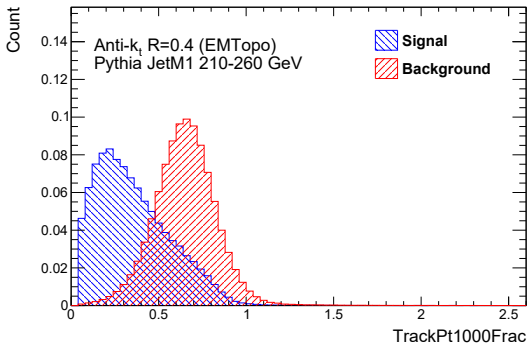
Count
Anti-k$_t$ R=0.4 (EMTopo)
Pythia JetM1 210-260 GeV
Signal
Background
TrackPt1000Frac

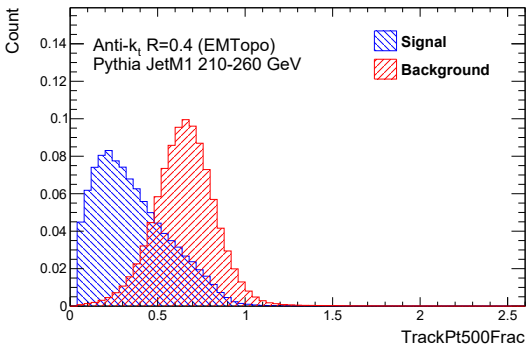
Count
Anti-k$_t$ R=0.4 (EMTopo)
Pythia JetM1 210-260 GeV
Signal
Background
TrackPt500Frac

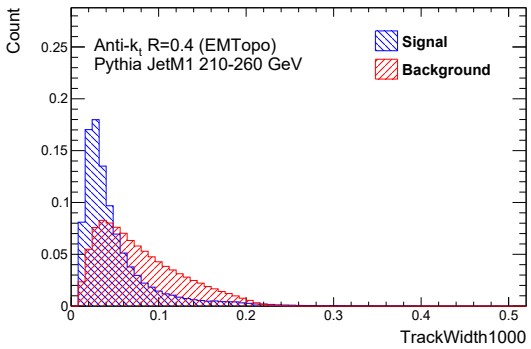
Count
Anti-k$_t$ R=0.4 (EMTopo)
Pythia JetM1 210-260 GeV
Signal
Background
TrackWidth1000

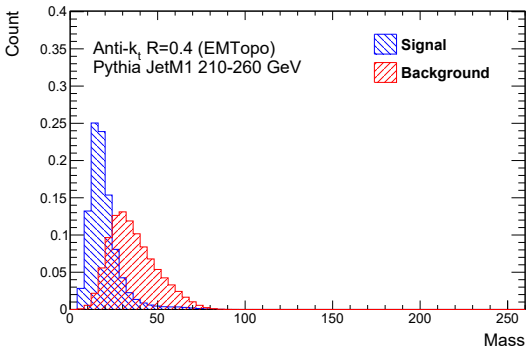
Count
Anti-k$_t$ R=0.4 (EMTopo)
Pythia JetM1 210-260 GeV
Signal
Background
Mass

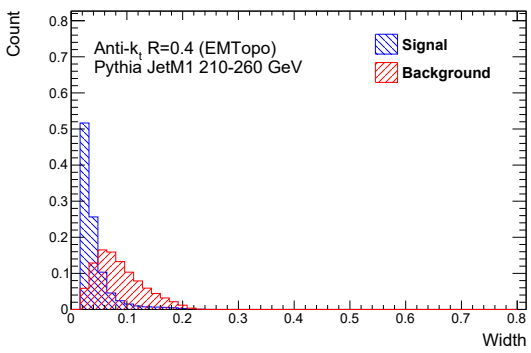
Count
Anti-k$_t$ R=0.4 (EMTopo)
Pythia JetM1 210-260 GeV
Signal
Background
Width

C.9 260-310 GeV

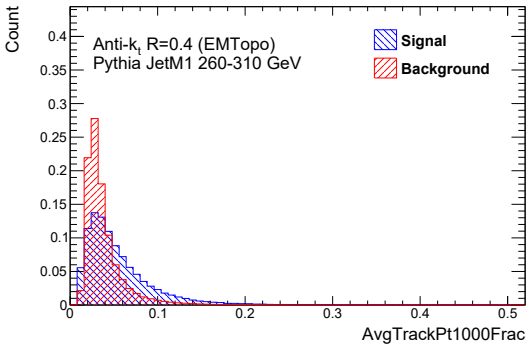

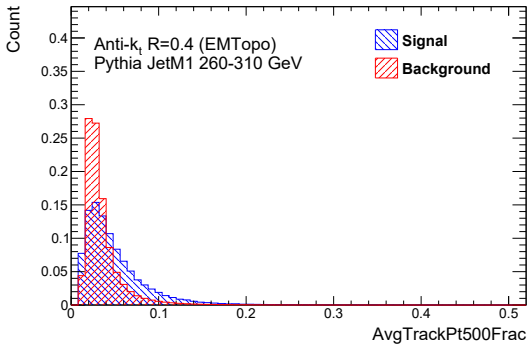

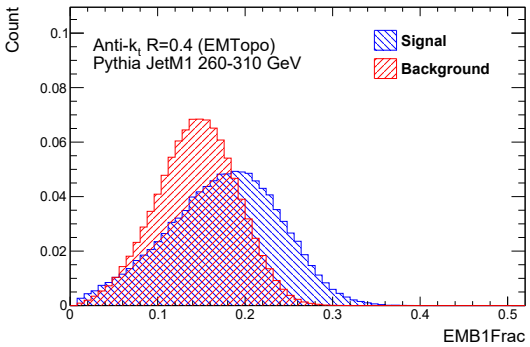

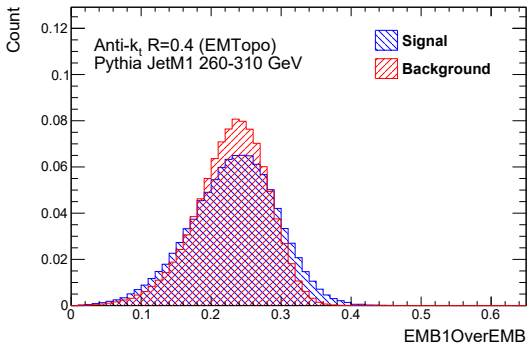

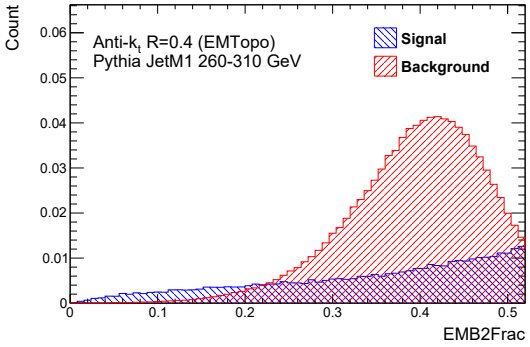

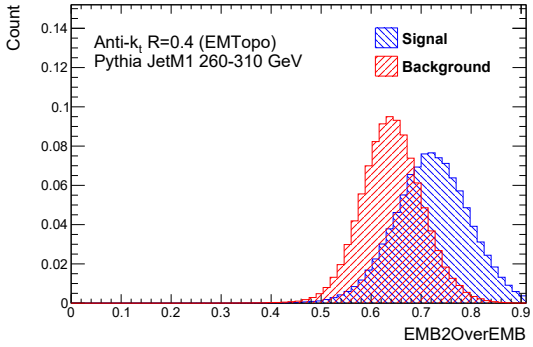

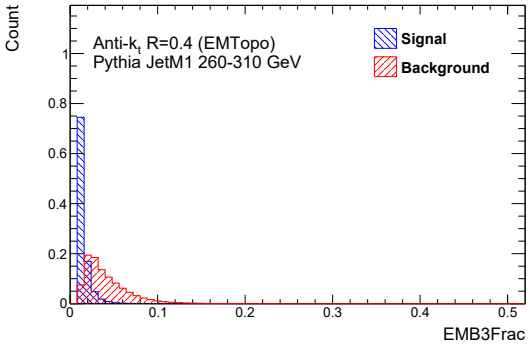

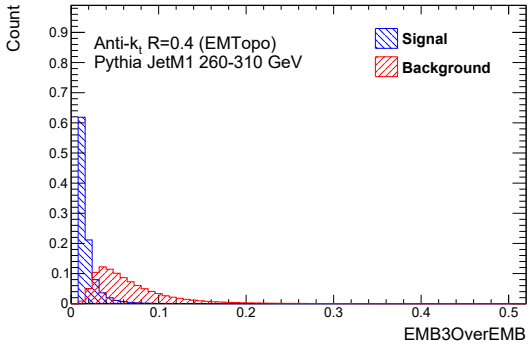

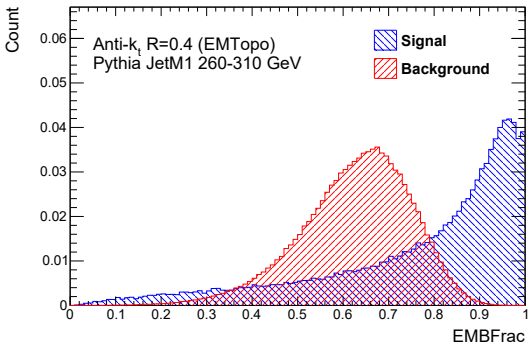
Count
Anti-k$_t$ R=0.4 (EMTopo)
Pythia JetM1 260-310 GeV
Signal
Background
EMBFrac

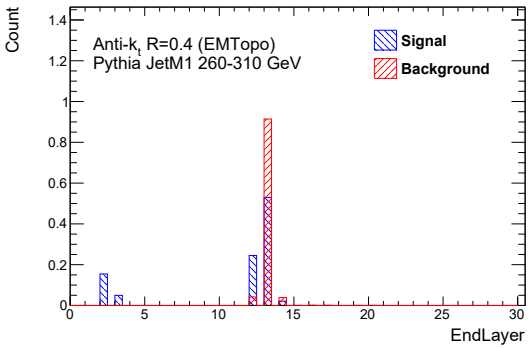
Count
Anti-k$_t$ R=0.4 (EMTopo)
Pythia JetM1 260-310 GeV
Signal
Background
EndLayer

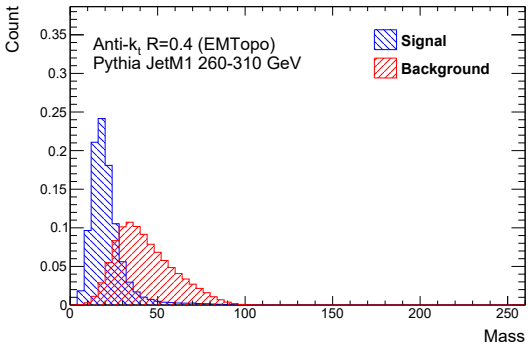
Count
Anti-k$_t$ R=0.4 (EMTopo)
Pythia JetM1 260-310 GeV
Signal
Background
Mass

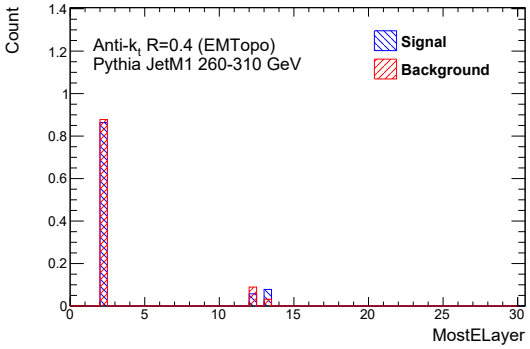
Count
Anti-k$_t$ R=0.4 (EMTopo)
Pythia JetM1 260-310 GeV
Signal
Background
MostELayer

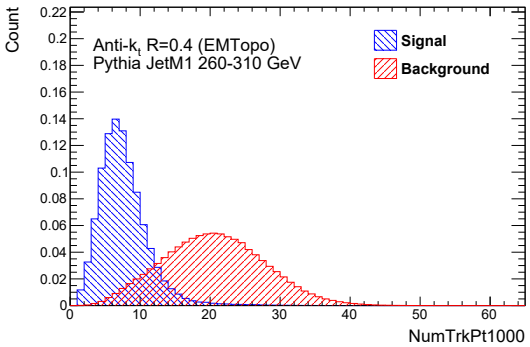
Count
Anti-k$_t$ R=0.4 (EMTopo)
Pythia JetM1 260-310 GeV
Signal
Background
NumTrkPt1000

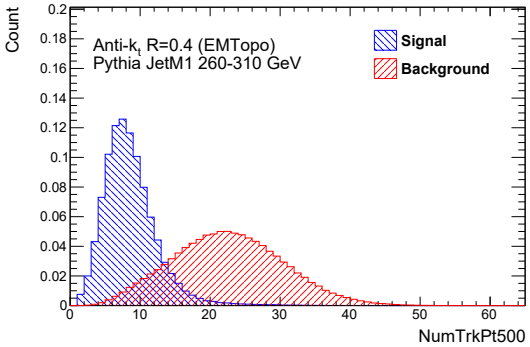
Count
Anti-k$_t$ R=0.4 (EMTopo)
Pythia JetM1 260-310 GeV
Signal
Background
NumTrkPt500

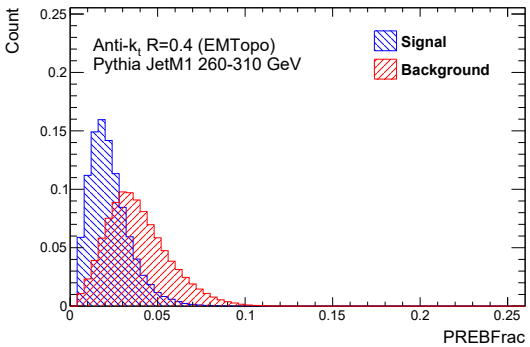
Count
Anti-k$_t$ R=0.4 (EMTopo)
Pythia JetM1 260-310 GeV
Signal
Background
PREBFrac

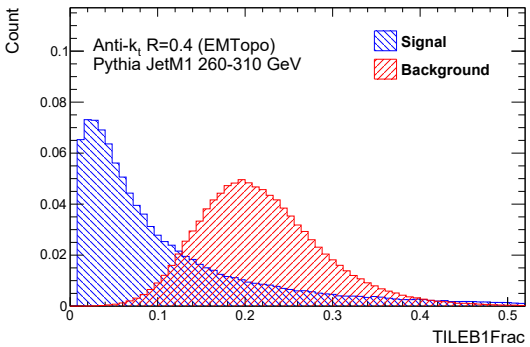
Count
Anti-k$_t$ R=0.4 (EMTopo)
Pythia JetM1 260-310 GeV
Signal
Background
TILEB1Frac

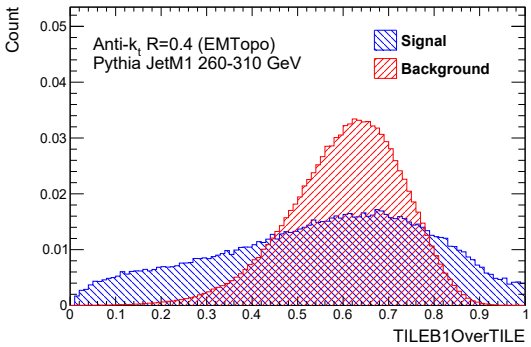
Count
Anti-k$_t$ R=0.4 (EMTopo)
Pythia JetM1 260-310 GeV
Signal
Background
TILEB1OverTILE

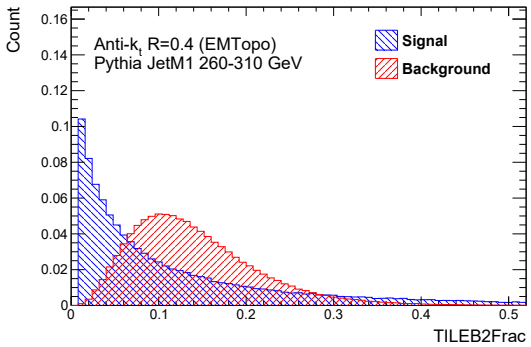
Count
Anti-k$_t$ R=0.4 (EMTopo)
Pythia JetM1 260-310 GeV
Signal
Background
TILEB2Frac

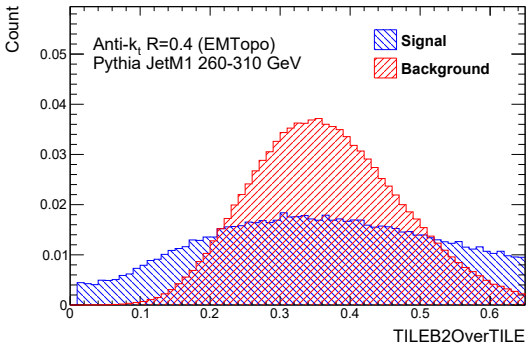
Count
Anti-k$_t$ R=0.4 (EMTopo)
Pythia JetM1 260-310 GeV
Signal
Background
TILEB2OverTILE

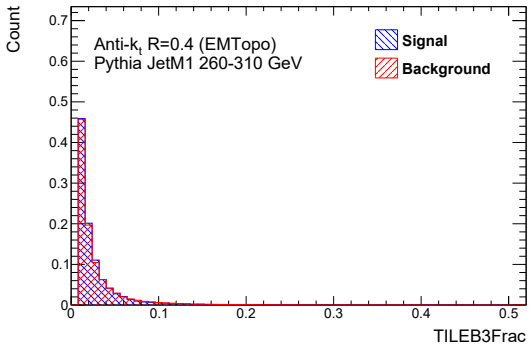
Count
Anti-k$_t$ R=0.4 (EMTopo)
Pythia JetM1 260-310 GeV
Signal
Background
TILEB3Frac

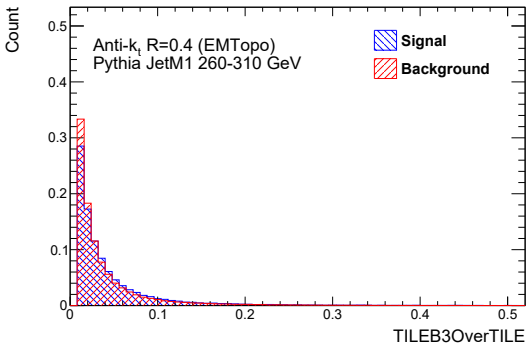
Count
Anti-k$_t$ R=0.4 (EMTopo)
Pythia JetM1 260-310 GeV
Signal
Background
TILEB3OverTILE

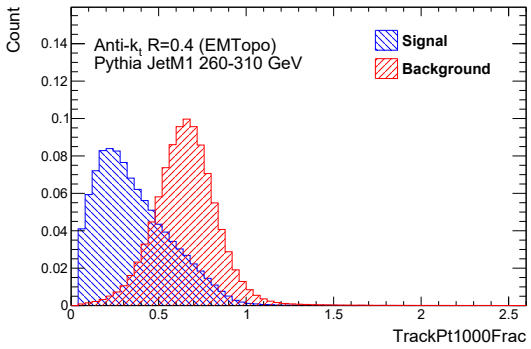
Count
Anti-k$_t$ R=0.4 (EMTopo)
Pythia JetM1 260-310 GeV
Signal
Background
TrackPt1000Frac

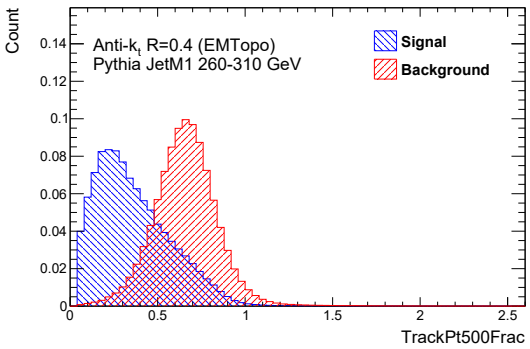
Count
Anti-k$_t$ R=0.4 (EMTopo)
Pythia JetM1 260-310 GeV
Signal
Background
TrackPt500Frac

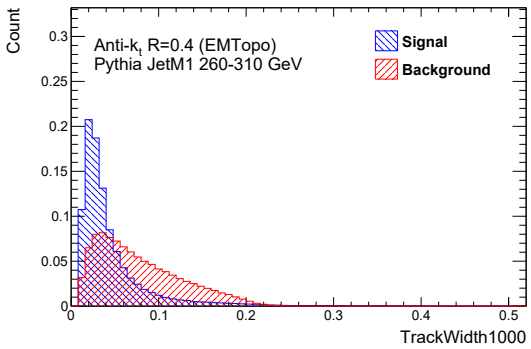
Count
Anti-k$_t$ R=0.4 (EMTopo)
Pythia JetM1 260-310 GeV
Signal
Background
TrackWidth1000

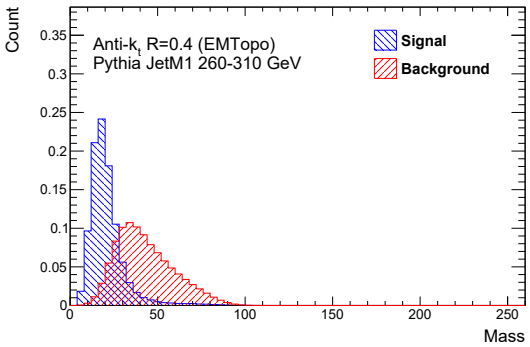
Count
Anti-k$_t$ R=0.4 (EMTopo)
Pythia JetM1 260-310 GeV
Signal
Background
Mass

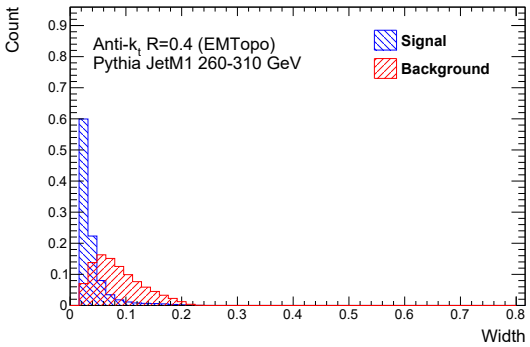
Count
Anti-k$_t$ R=0.4 (EMTopo)
Pythia JetM1 260-310 GeV
Signal
Background
Width

C.10 310-400 GeV

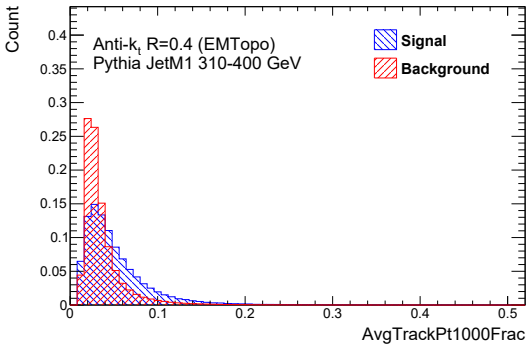

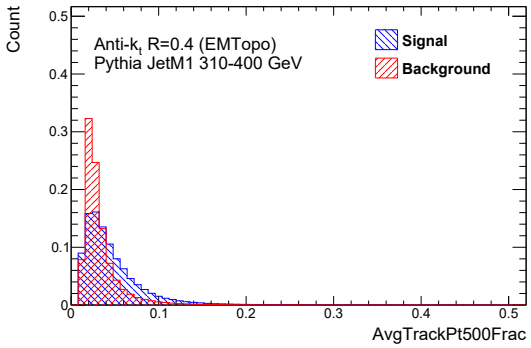

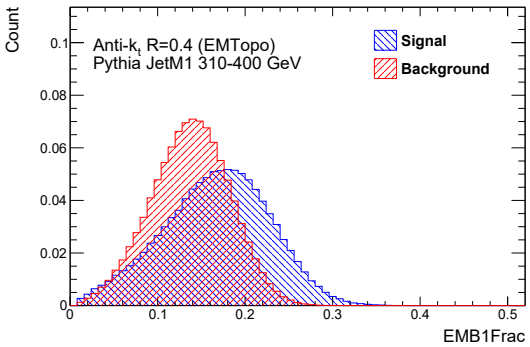

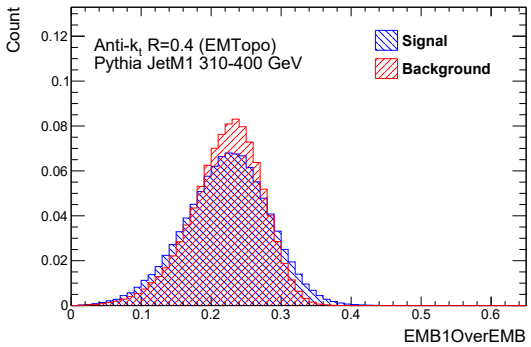

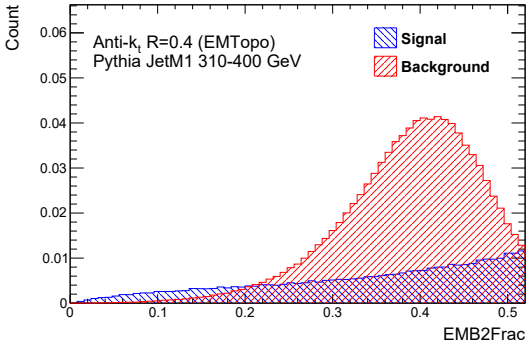

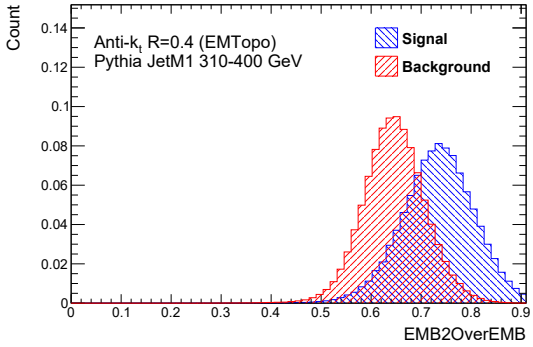

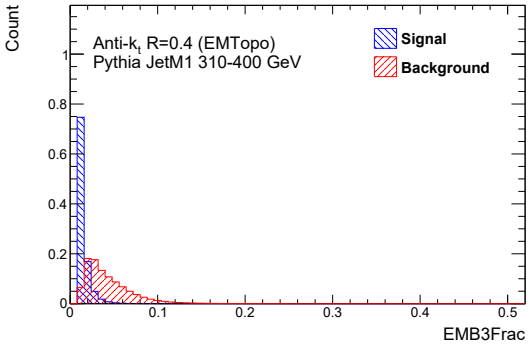

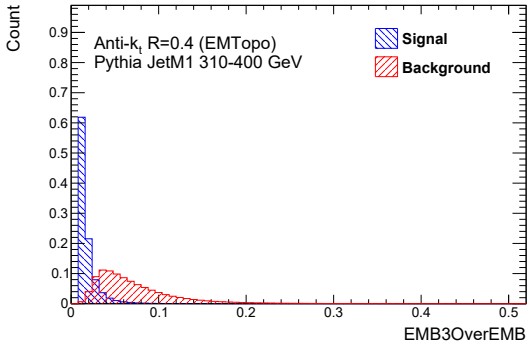

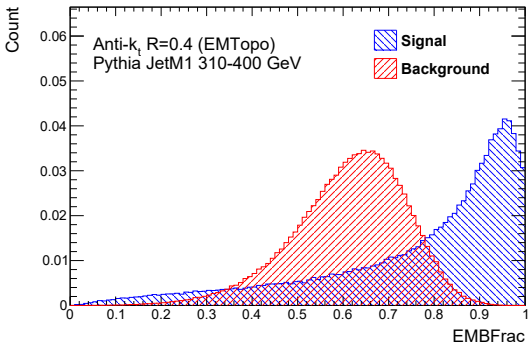
Count
Anti-k$_t$ R=0.4 (EMTopo)
Pythia JetM1 310-400 GeV
Signal
Background
EMBFrac

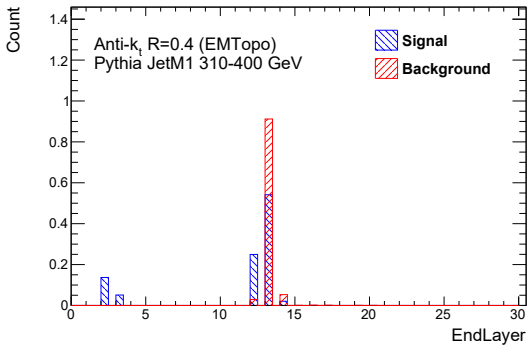
Count
Anti-k$_t$ R=0.4 (EMTopo)
Pythia JetM1 310-400 GeV
Signal
Background
EndLayer

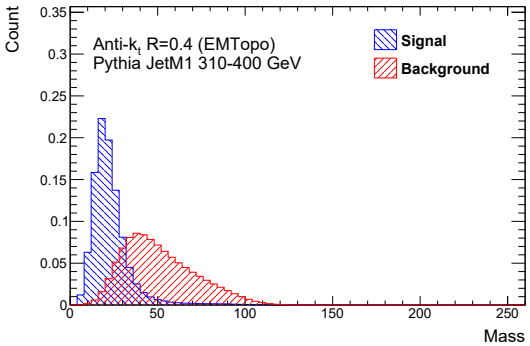
Count
Anti-k$_t$ R=0.4 (EMTopo)
Pythia JetM1 310-400 GeV
Signal
Background
Mass

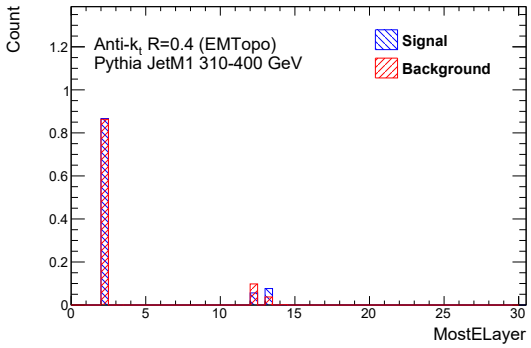
Count
Anti-k$_t$ R=0.4 (EMTopo)
Pythia JetM1 310-400 GeV
Signal
Background
MostELayer

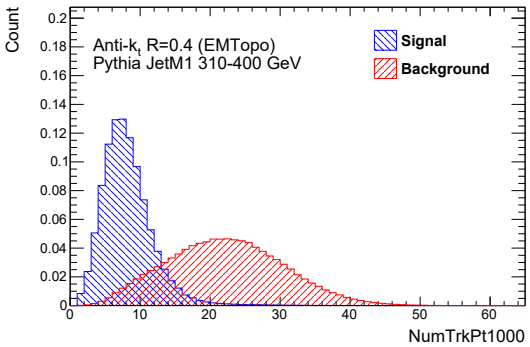
Count
Anti-k$_t$ R=0.4 (EMTopo)
Pythia JetM1 310-400 GeV
Signal
Background
NumTrkPt1000

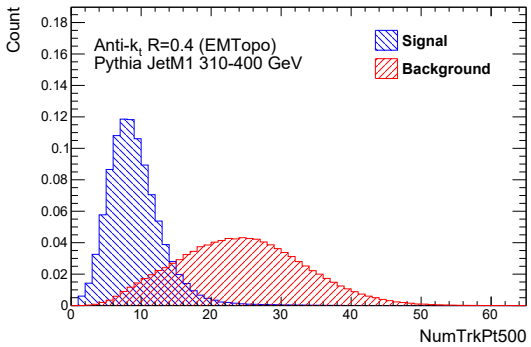
Count
Anti-k$_t$ R=0.4 (EMTopo)
Pythia JetM1 310-400 GeV
Signal
Background
NumTrkPt500

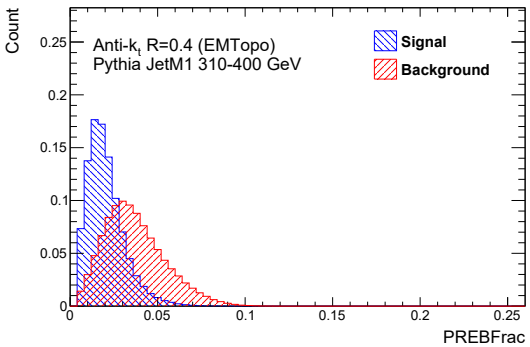
Count
Anti-k$_t$ R=0.4 (EMTopo)
Pythia JetM1 310-400 GeV
Signal
Background
PREBFrac

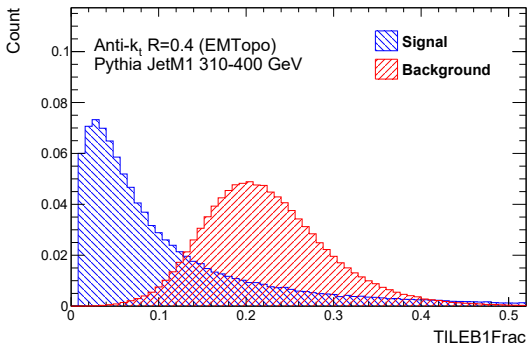
Count
Anti-k$_t$ R=0.4 (EMTopo)
Pythia JetM1 310-400 GeV
Signal
Background
TILEB1Frac

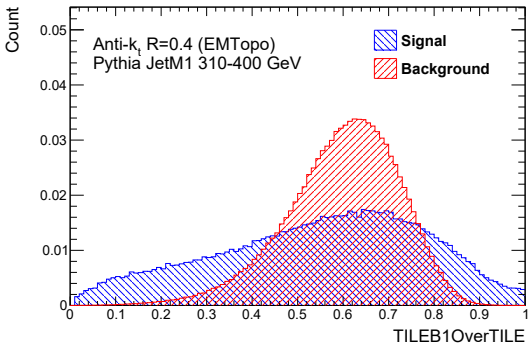
Count
Anti-k$_t$ R=0.4 (EMTopo)
Pythia JetM1 310-400 GeV
Signal
Background
TILEB1OverTILE

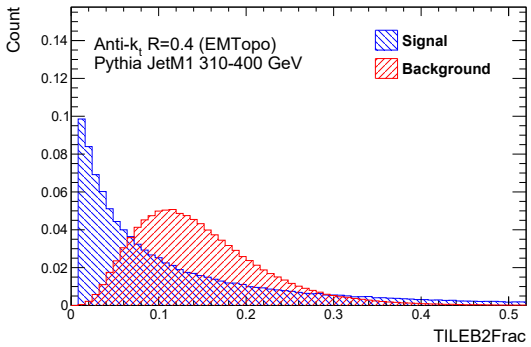
Count
Anti-k$_t$ R=0.4 (EMTopo)
Pythia JetM1 310-400 GeV
Signal
Background
TILEB2Frac

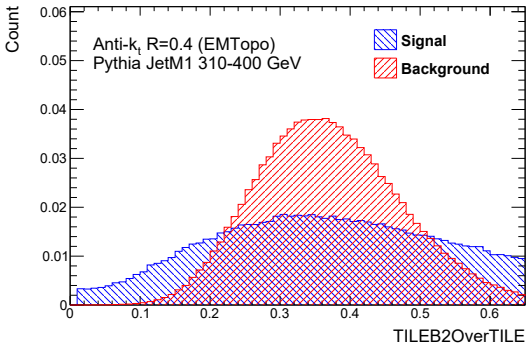
Count
Anti-k$_t$ R=0.4 (EMTopo)
Pythia JetM1 310-400 GeV
Signal
Background
TILEB2OverTILE

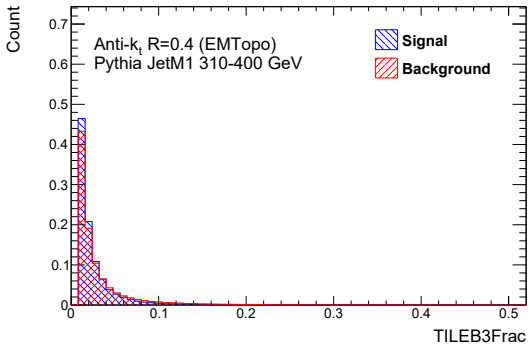
Count
Anti-k$_t$ R=0.4 (EMTopo)
Pythia JetM1 310-400 GeV
Signal
Background
TILEB3Frac

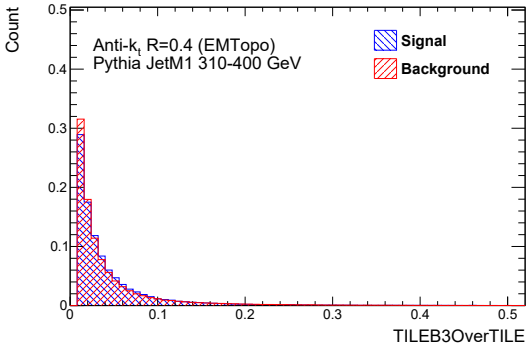
Count
Anti-k$_t$ R=0.4 (EMTopo)
Pythia JetM1 310-400 GeV
Signal
Background
TILEB3OverTILE

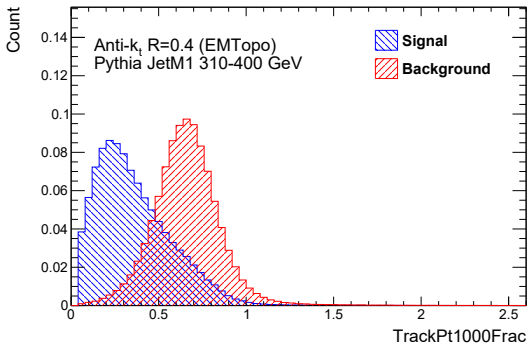
Count
Anti-k$_t$ R=0.4 (EMTopo)
Pythia JetM1 310-400 GeV
Signal
Background
TrackPt1000Frac

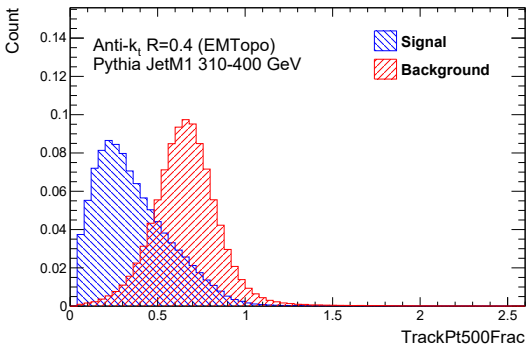
Count
Anti-k$_t$ R=0.4 (EMTopo)
Pythia JetM1 310-400 GeV
Signal
Background
TrackPt500Frac

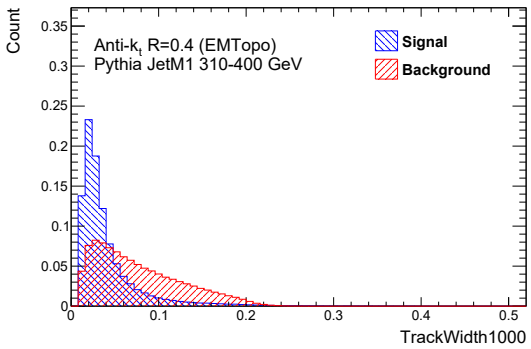
Count
Anti-k$_t$ R=0.4 (EMTopo)
Pythia JetM1 310-400 GeV
Signal
Background
TrackWidth1000

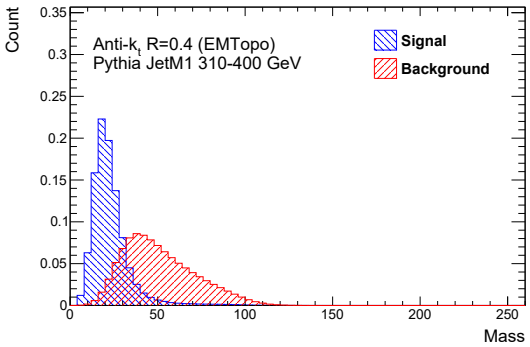
Count
Anti-k$_t$ R=0.4 (EMTopo)
Pythia JetM1 310-400 GeV
Signal
Background
Mass

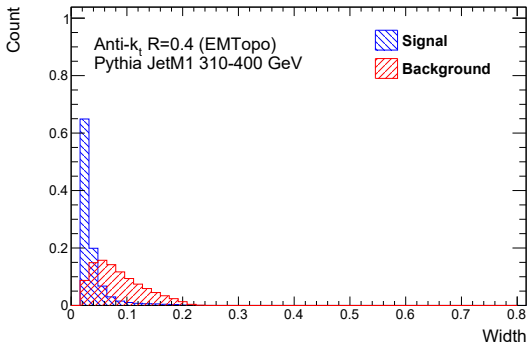
Count
Anti-k$_t$ R=0.4 (EMTopo)
Pythia JetM1 310-400 GeV
Signal
Background
Width

C.11 400-500 GeV

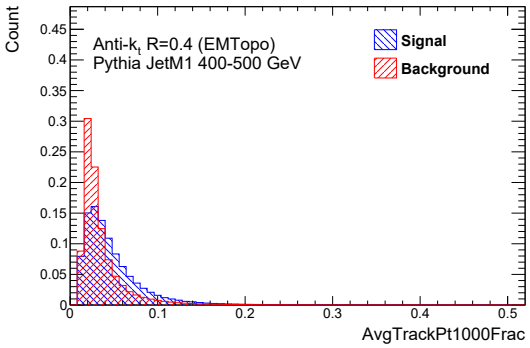

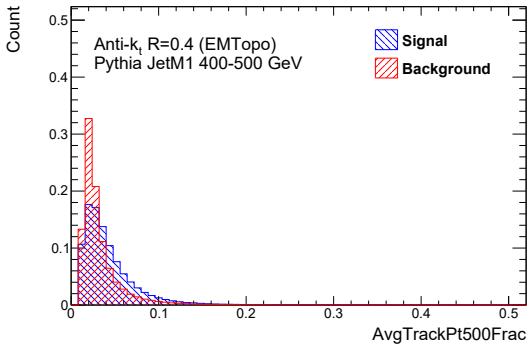

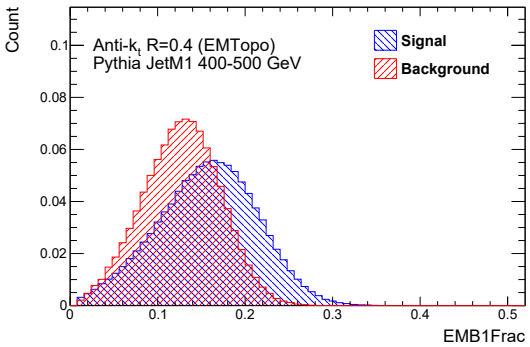

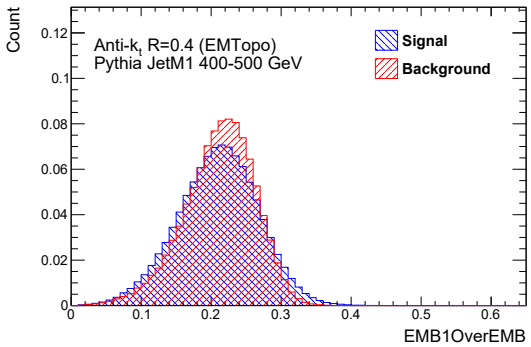

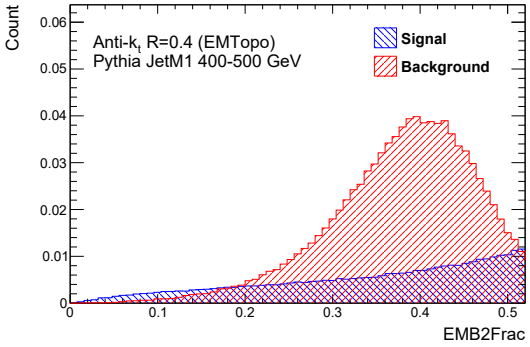

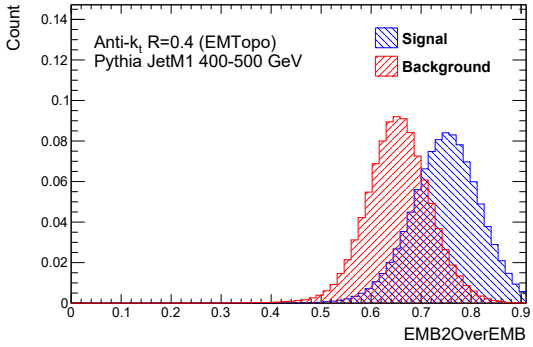

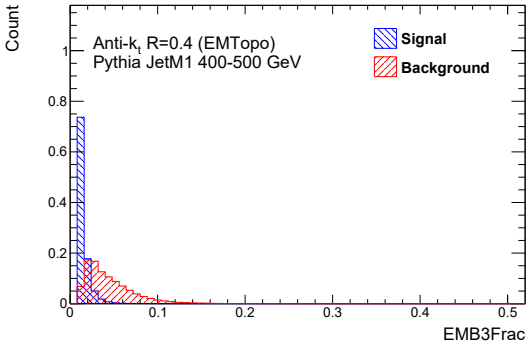

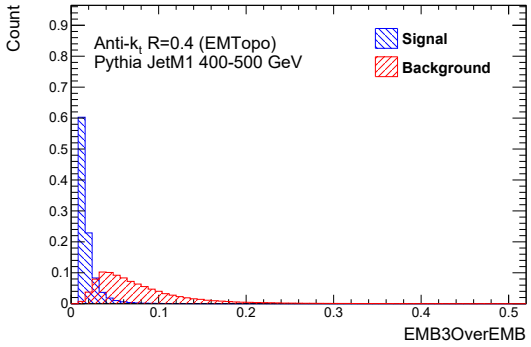

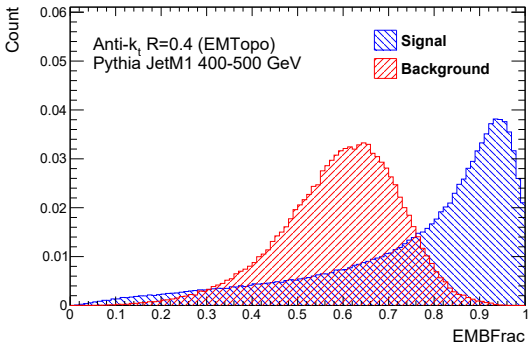
Count
Anti-k$_t$ R=0.4 (EMTopo)
Pythia JetM1 400-500 GeV
Signal
Background
EMBFrac

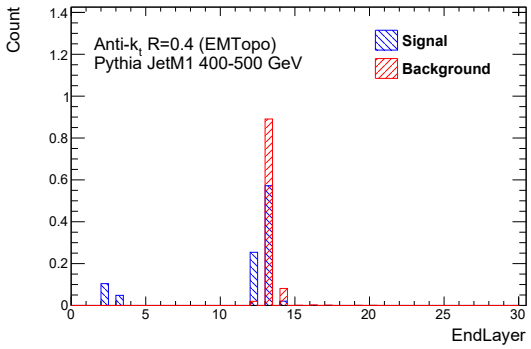
Count
Anti-k$_t$ R=0.4 (EMTopo)
Pythia JetM1 400-500 GeV
Signal
Background
EndLayer

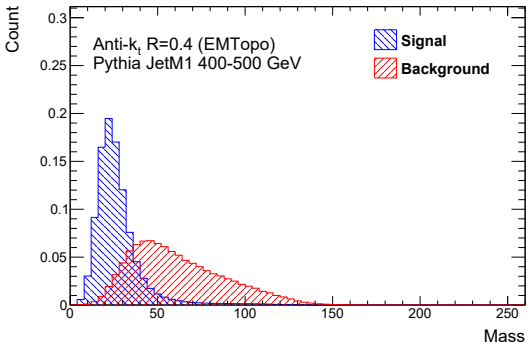
Count
Anti-k$_t$ R=0.4 (EMTopo)
Pythia JetM1 400-500 GeV
Signal
Background
Mass

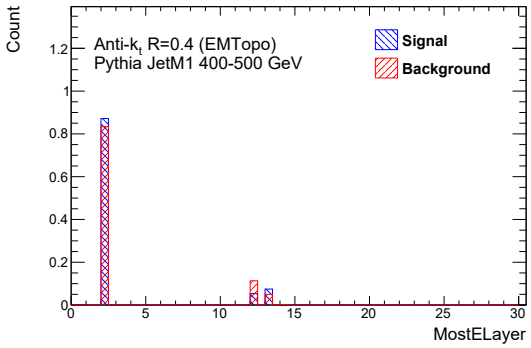
Count
Anti-k$_t$ R=0.4 (EMTopo)
Pythia JetM1 400-500 GeV
Signal
Background
MostELayer

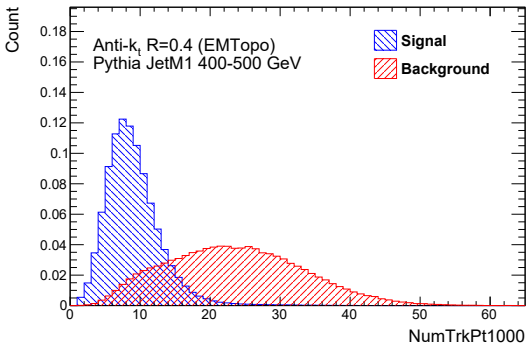
Count
Anti-k$_t$ R=0.4 (EMTopo)
Pythia JetM1 400-500 GeV
Signal
Background
NumTrkPt1000

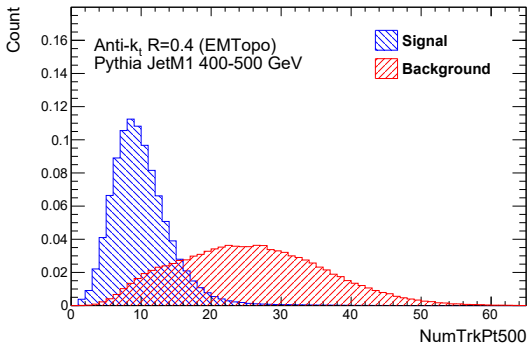
Count
Anti-k$_t$ R=0.4 (EMTopo)
Pythia JetM1 400-500 GeV
Signal
Background
NumTrkPt500

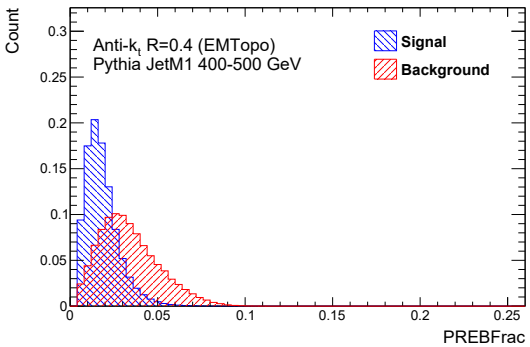
Count
Anti-k$_t$ R=0.4 (EMTopo)
Pythia JetM1 400-500 GeV
Signal
Background
PREBFrac

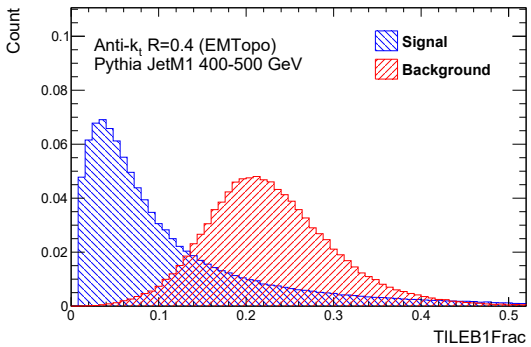
Count
Anti-k$_t$ R=0.4 (EMTopo)
Pythia JetM1 400-500 GeV
Signal
Background
TILEB1Frac

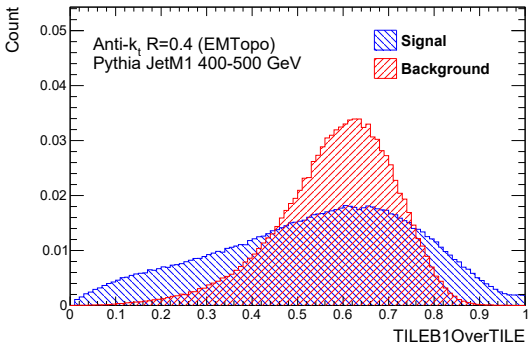
Count
Anti-k$_t$ R=0.4 (EMTopo)
Pythia JetM1 400-500 GeV
Signal
Background
TILEB1OverTILE

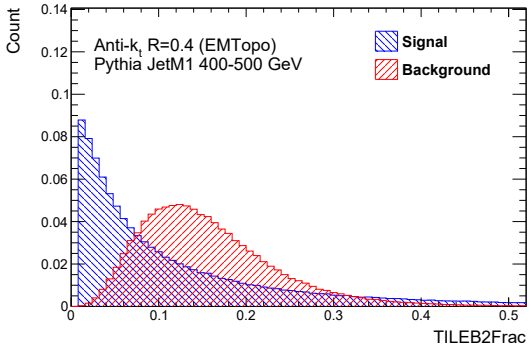
Count
Anti-k$_t$ R=0.4 (EMTopo)
Pythia JetM1 400-500 GeV
Signal
Background
TILEB2Frac

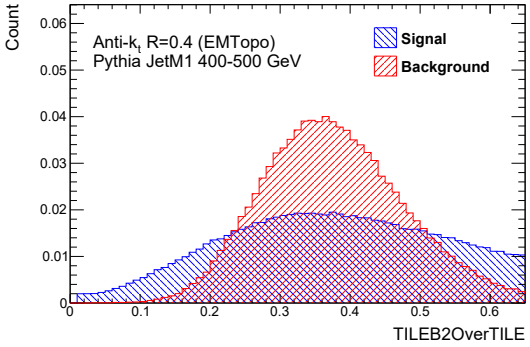
Count
Anti-k$_t$ R=0.4 (EMTopo)
Pythia JetM1 400-500 GeV
Signal
Background
TILEB2OverTILE

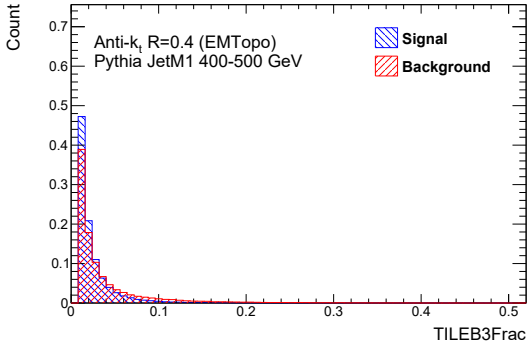
Count
Anti-k$_t$ R=0.4 (EMTopo)
Pythia JetM1 400-500 GeV
Signal
Background
TILEB3Frac

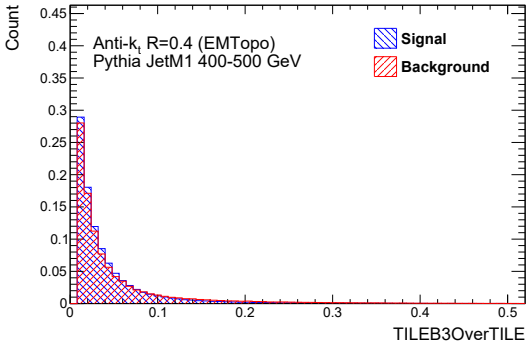
Count
Anti-k$_t$ R=0.4 (EMTopo)
Pythia JetM1 400-500 GeV
Signal
Background
TILEB3OverTILE

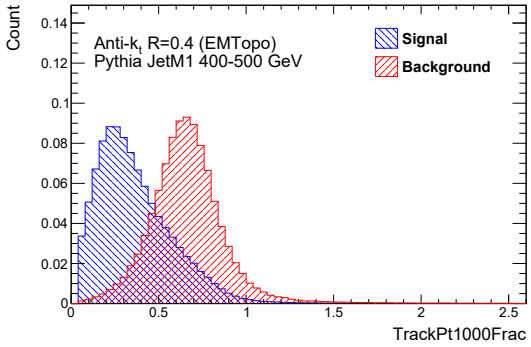
Count
Anti-k$_t$ R=0.4 (EMTopo)
Pythia JetM1 400-500 GeV
Signal
Background
TrackPt1000Frac

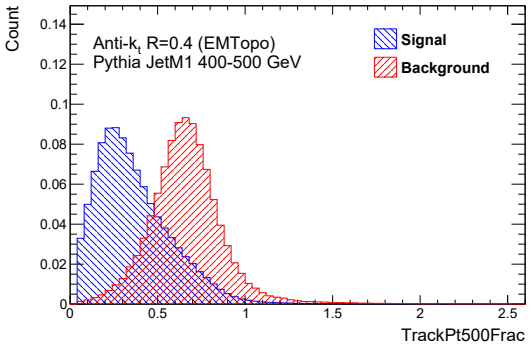
Count
Anti-k$_t$ R=0.4 (EMTopo)
Pythia JetM1 400-500 GeV
Signal
Background
TrackPt500Frac

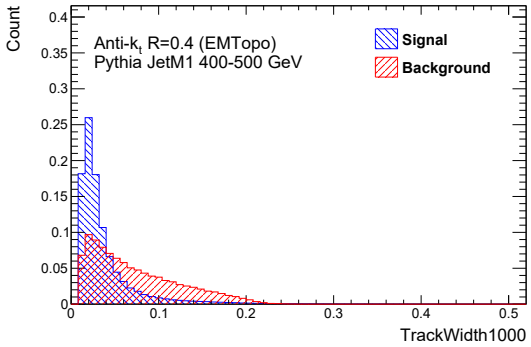
Count
Anti-k$_t$ R=0.4 (EMTopo)
Pythia JetM1 400-500 GeV
Signal
Background
TrackWidth1000

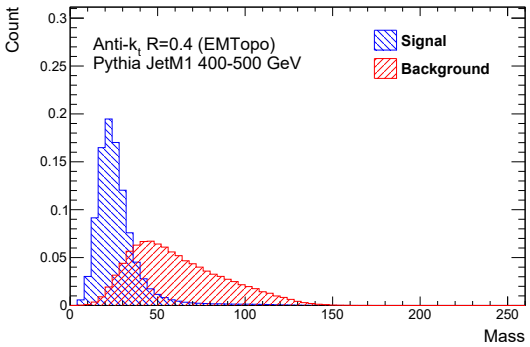
Count
Anti-k$_t$ R=0.4 (EMTopo)
Pythia JetM1 400-500 GeV
Signal
Background
Mass

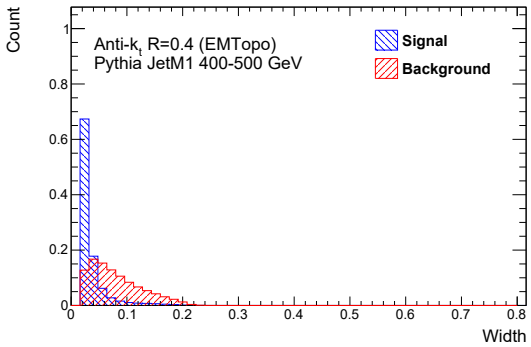
Count
Anti-k$_t$ R=0.4 (EMTopo)
Pythia JetM1 400-500 GeV
Signal
Background
Width

C.12 500-600 GeV

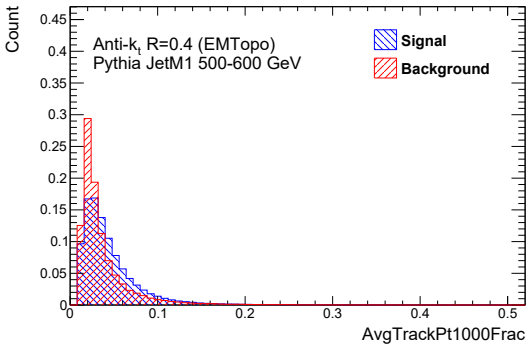

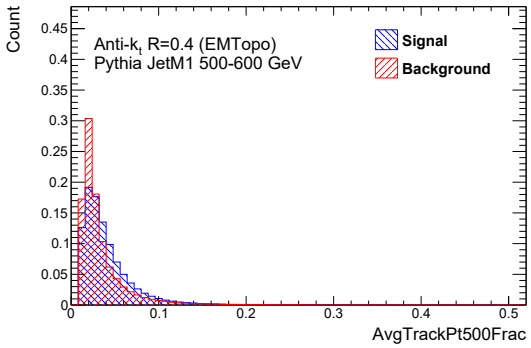

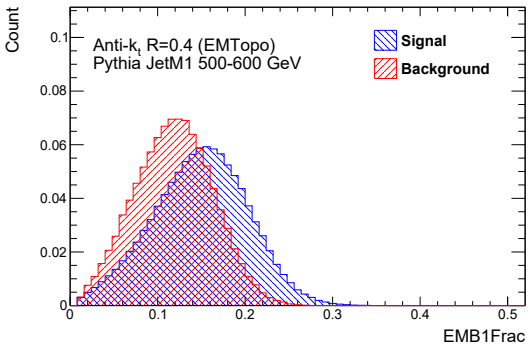

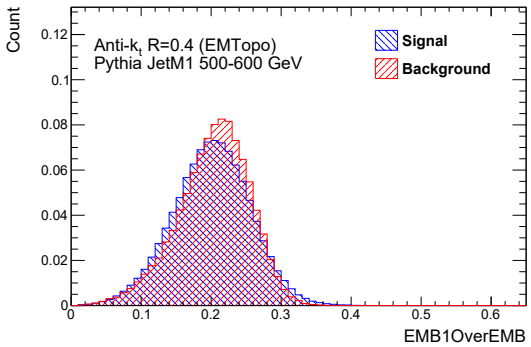

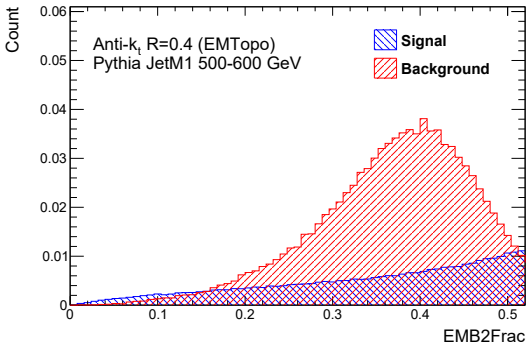

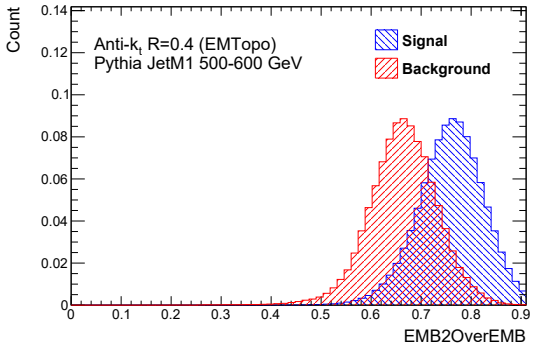

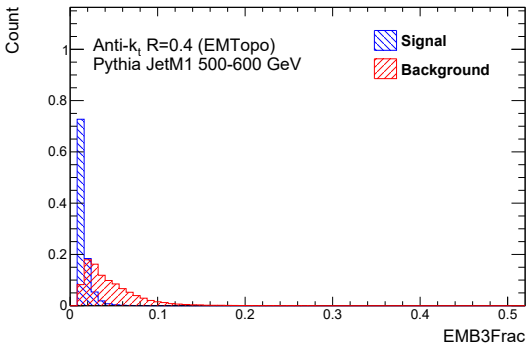

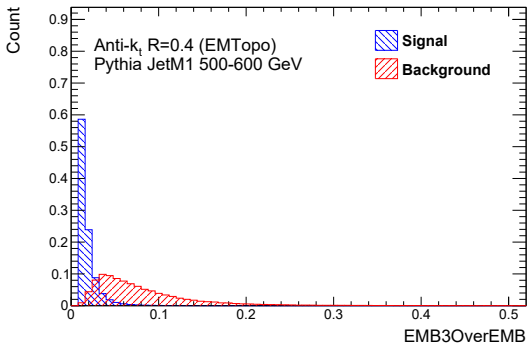

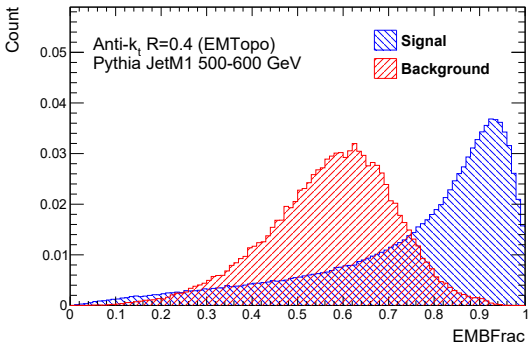
Count
Anti-k$_t$ R=0.4 (EMTopo)
Pythia JetM1 500-600 GeV
Signal
Background
EMBFrac

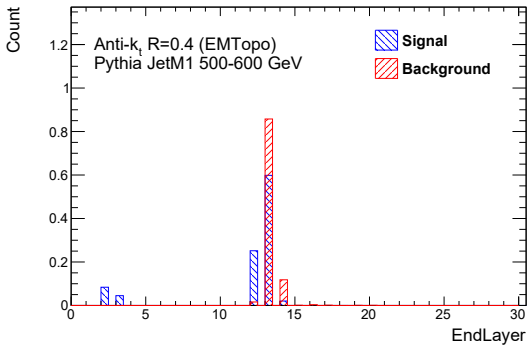
Count
Anti-k$_t$ R=0.4 (EMTopo)
Pythia JetM1 500-600 GeV
Signal
Background
EndLayer

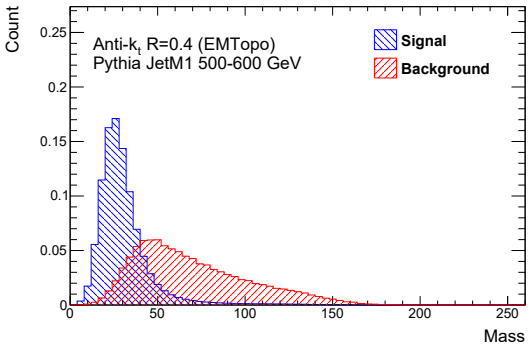
Count
Anti-k$_t$ R=0.4 (EMTopo)
Pythia JetM1 500-600 GeV
Signal
Background
Mass

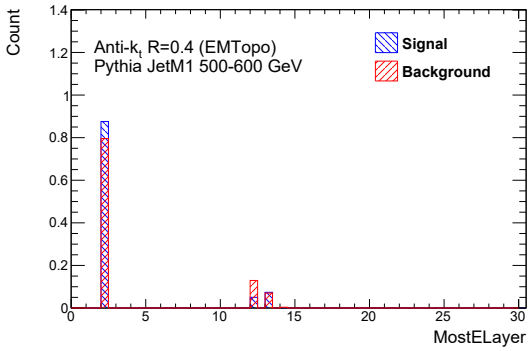
Count
Anti-k$_t$ R=0.4 (EMTopo)
Pythia JetM1 500-600 GeV
Signal
Background
MostELayer

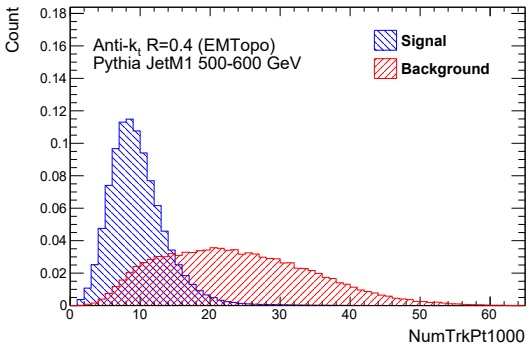
Count
Anti-k$_t$ R=0.4 (EMTopo)
Pythia JetM1 500-600 GeV
Signal
Background
NumTrkPt1000

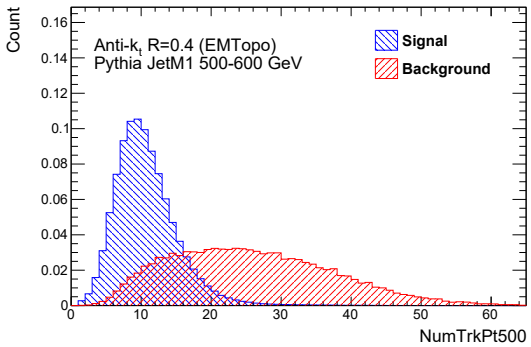
Count
Anti-k$_t$ R=0.4 (EMTopo)
Pythia JetM1 500-600 GeV
Signal
Background
NumTrkPt500

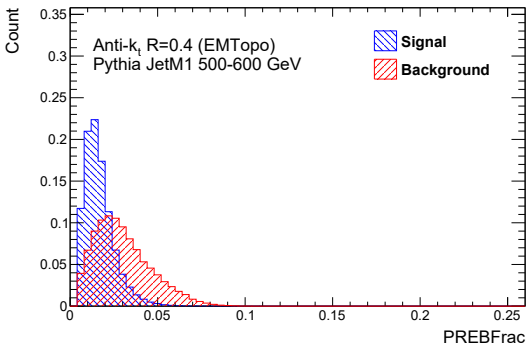
Count
Anti-k$_t$ R=0.4 (EMTopo)
Pythia JetM1 500-600 GeV
Signal
Background
PREBFrac

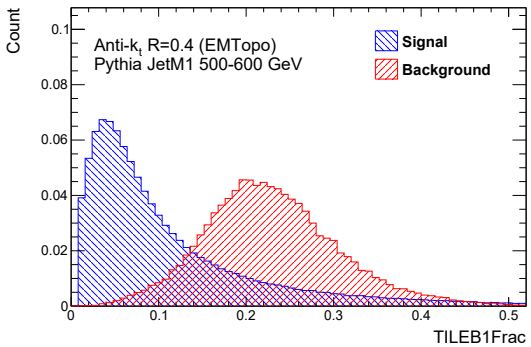
Count
Anti-k$_t$ R=0.4 (EMTopo)
Pythia JetM1 500-600 GeV
Signal
Background
TILEB1Frac

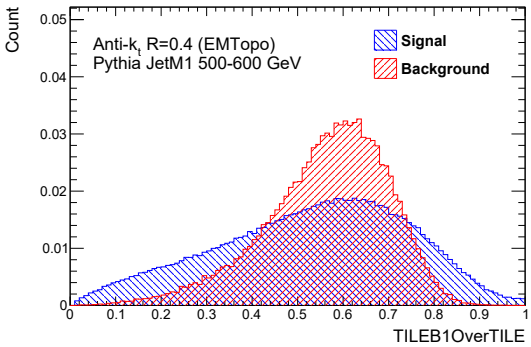
Count
Anti-k$_t$ R=0.4 (EMTopo)
Pythia JetM1 500-600 GeV
Signal
Background
TILEB1OverTILE

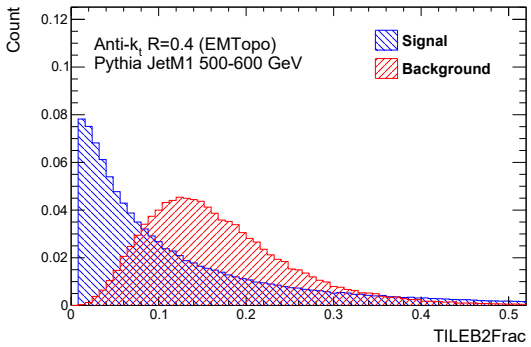
Count
Anti-k$_t$ R=0.4 (EMTopo)
Pythia JetM1 500-600 GeV
Signal
Background
TILEB2Frac

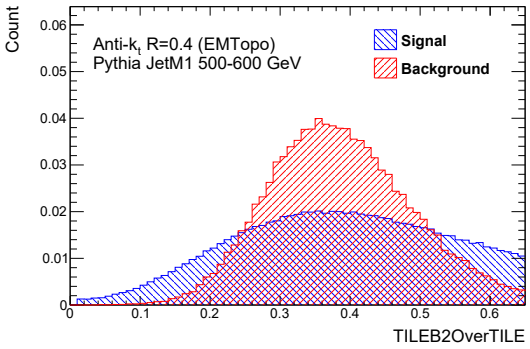
Count
Anti-k$_t$ R=0.4 (EMTopo)
Pythia JetM1 500-600 GeV
Signal
Background
TILEB2OverTILE

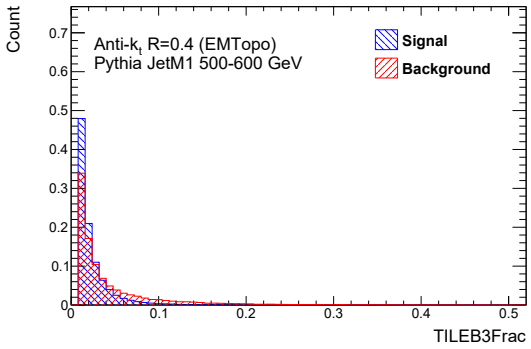
Count
Anti-k$_t$ R=0.4 (EMTopo)
Pythia JetM1 500-600 GeV
Signal
Background
TILEB3Frac

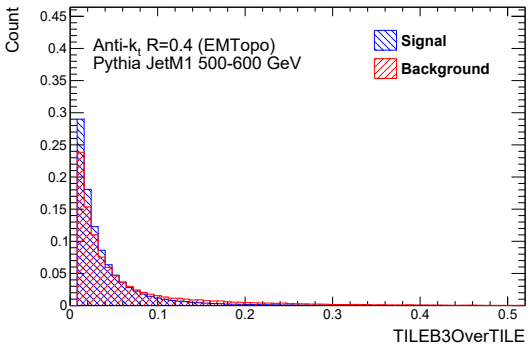
Count
Anti-k$_t$ R=0.4 (EMTopo)
Pythia JetM1 500-600 GeV
Signal
Background
TILEB3OverTILE

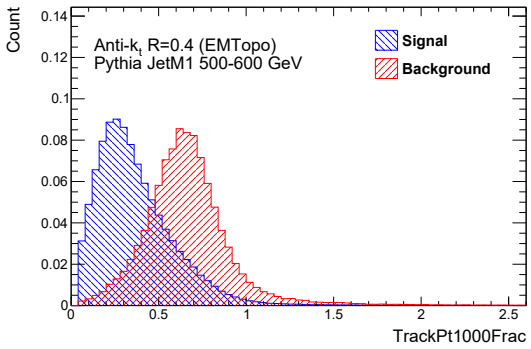
Count
Anti-k$_t$ R=0.4 (EMTopo)
Pythia JetM1 500-600 GeV
Signal
Background
TrackPt1000Frac

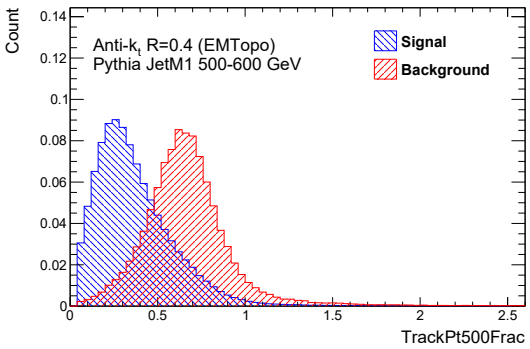
Count
Anti-k$_t$ R=0.4 (EMTopo)
Pythia JetM1 500-600 GeV
Signal
Background
TrackPt500Frac

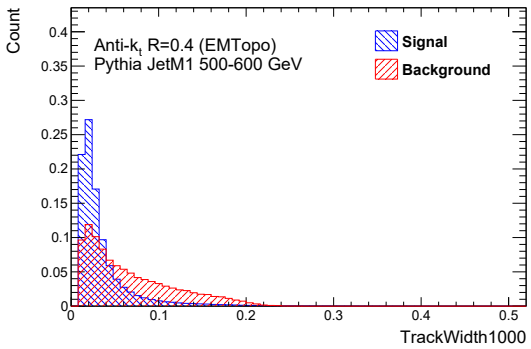
Count
Anti-k$_t$ R=0.4 (EMTopo)
Pythia JetM1 500-600 GeV
Signal
Background
TrackWidth1000

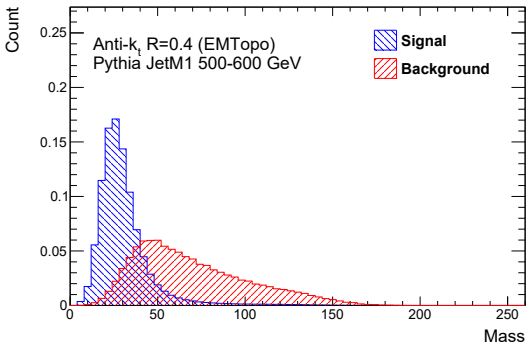
Count
Anti-k$_t$ R=0.4 (EMTopo)
Pythia JetM1 500-600 GeV
Signal
Background
Mass

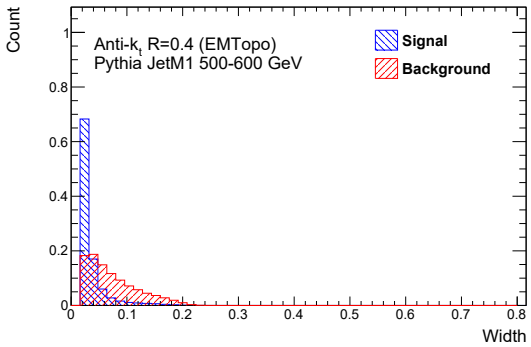
Count
Anti-k$_t$ R=0.4 (EMTopo)
Pythia JetM1 500-600 GeV
Signal
Background
Width

C.13 600-800 GeV

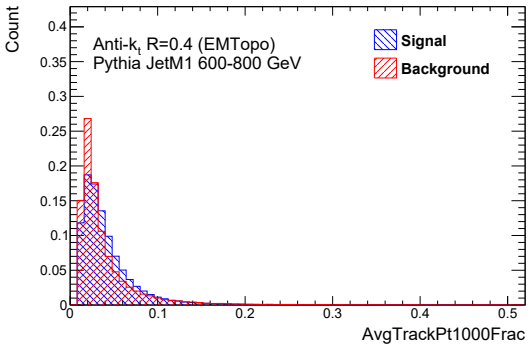

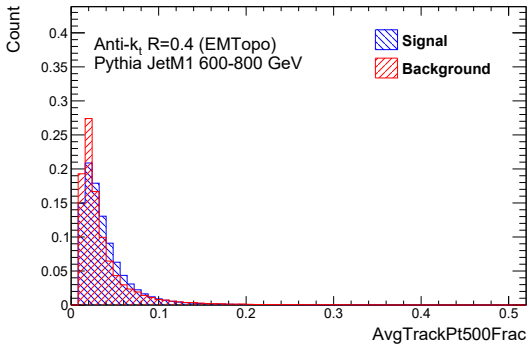

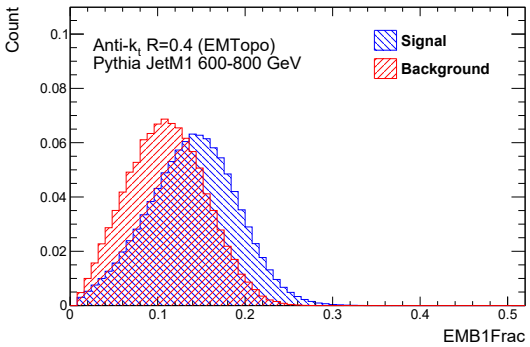

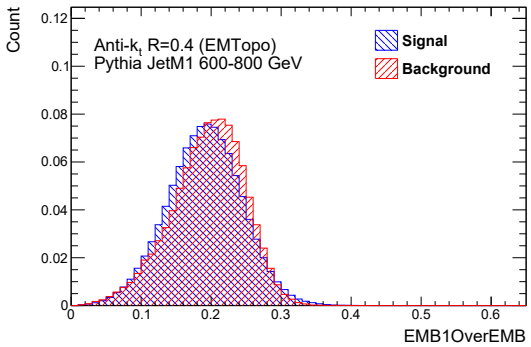

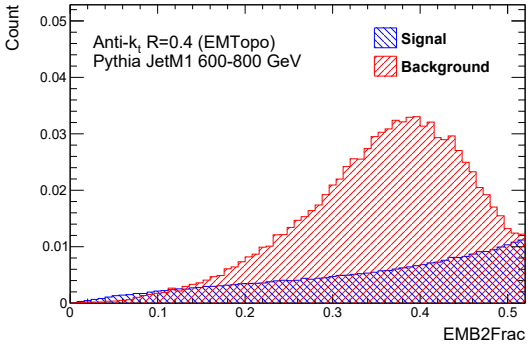

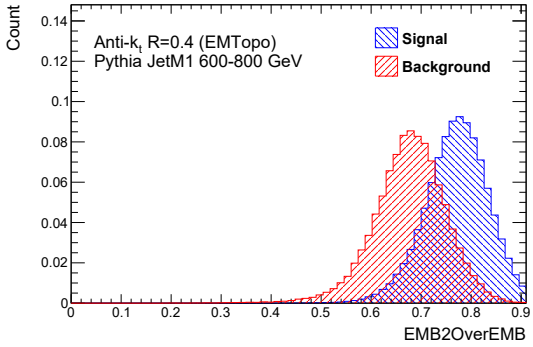

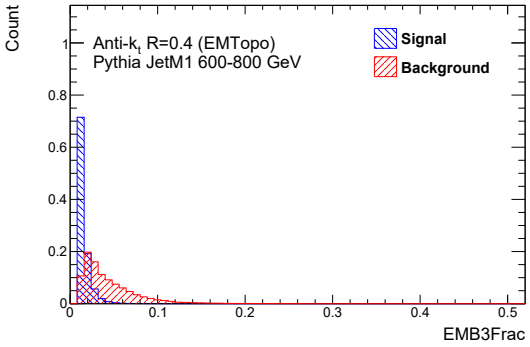

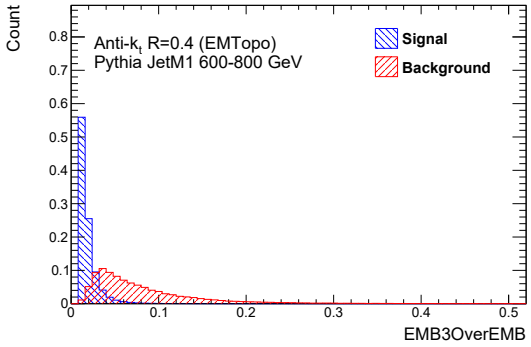

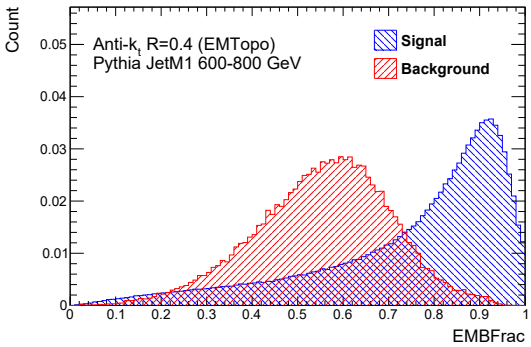
Count
Anti-k$_t$ R=0.4 (EMTopo)
Pythia JetM1 600-800 GeV
Signal
Background
EMBFrac

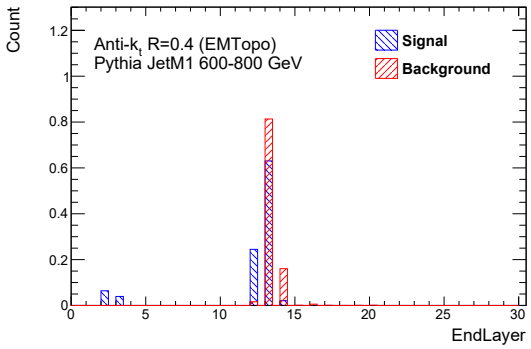
Count
Anti-k$_t$ R=0.4 (EMTopo)
Pythia JetM1 600-800 GeV
Signal
Background
EndLayer

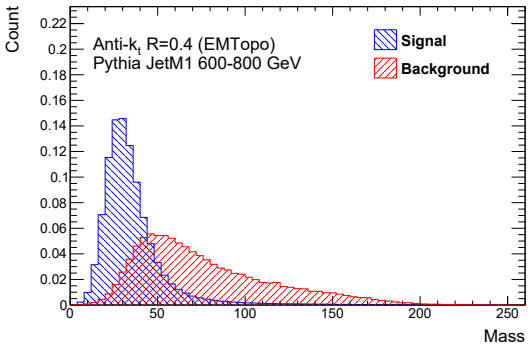
Count
Anti-k$_t$ R=0.4 (EMTopo)
Pythia JetM1 600-800 GeV
Signal
Background
Mass

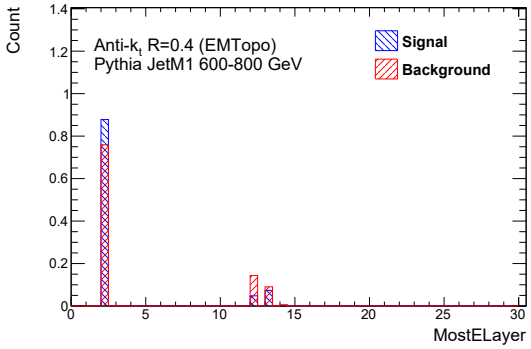
Count
Anti-k$_t$ R=0.4 (EMTopo)
Pythia JetM1 600-800 GeV
Signal
Background
MostELayer

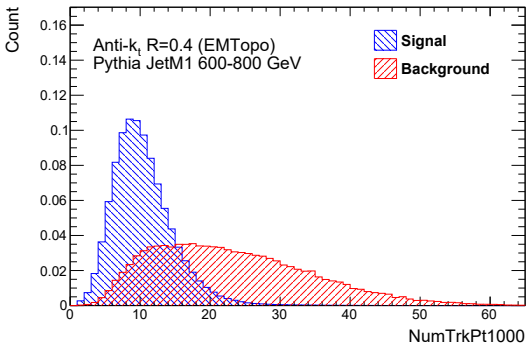
Count
Anti-k$_t$ R=0.4 (EMTopo)
Pythia JetM1 600-800 GeV
Signal
Background
NumTrkPt1000

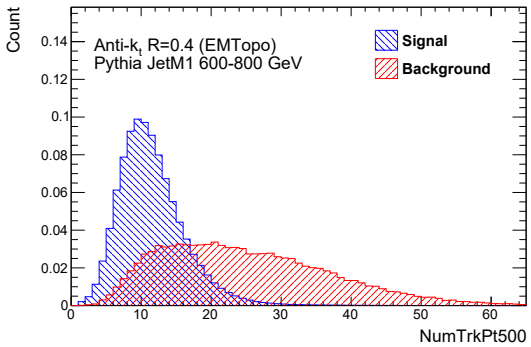
Count
Anti-k$_t$ R=0.4 (EMTopo)
Pythia JetM1 600-800 GeV
Signal
Background
NumTrkPt500

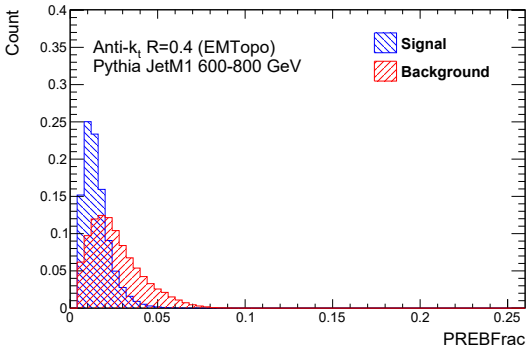
Count
Anti-k$_t$ R=0.4 (EMTopo)
Pythia JetM1 600-800 GeV
Signal
Background
PREBFrac

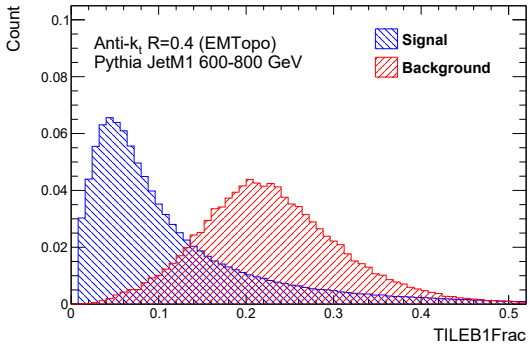
Count
Anti-k$_t$ R=0.4 (EMTopo)
Pythia JetM1 600-800 GeV
Signal
Background
TILEB1Frac

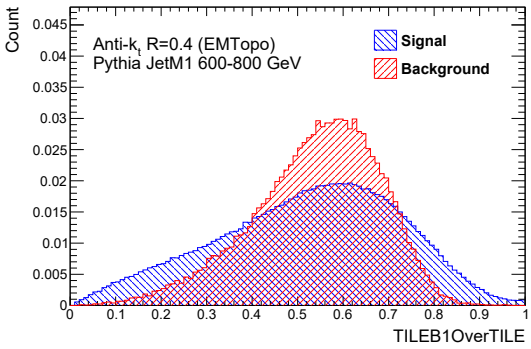
Count
Anti-k$_t$ R=0.4 (EMTopo)
Pythia JetM1 600-800 GeV
Signal
Background
TILEB1OverTILE

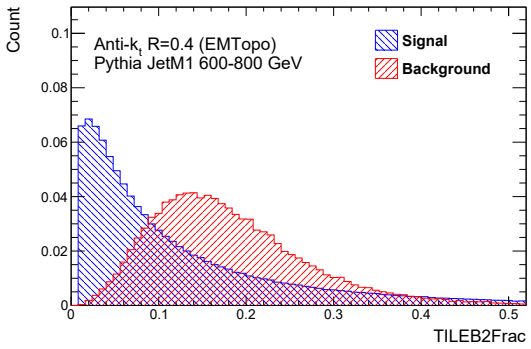
Count
Anti-k$_t$ R=0.4 (EMTopo)
Pythia JetM1 600-800 GeV
Signal
Background
TILEB2Frac

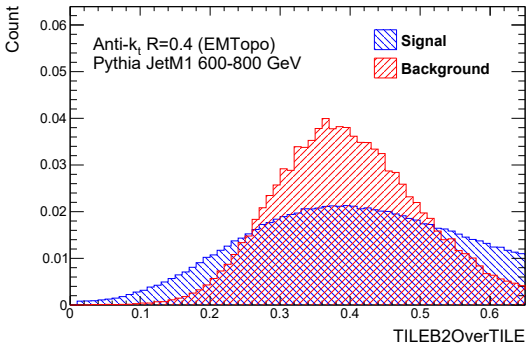
Count
Anti-k$_t$ R=0.4 (EMTopo)
Pythia JetM1 600-800 GeV
Signal
Background
TILEB2OverTILE

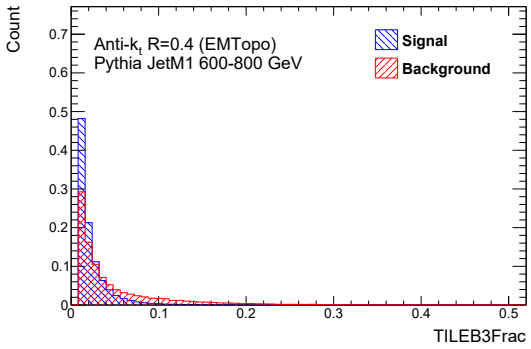
Count
Anti-k$_t$ R=0.4 (EMTopo)
Pythia JetM1 600-800 GeV
Signal
Background
TILEB3Frac

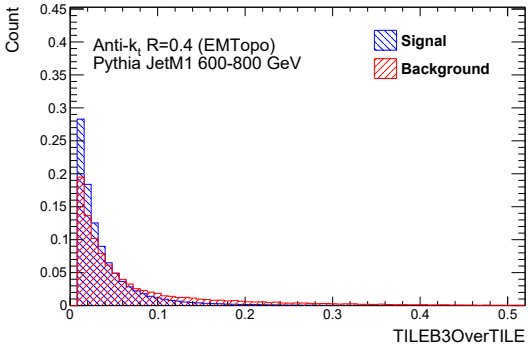
Count
Anti-k$_t$ R=0.4 (EMTopo)
Pythia JetM1 600-800 GeV
Signal
Background
TILEB3OverTILE

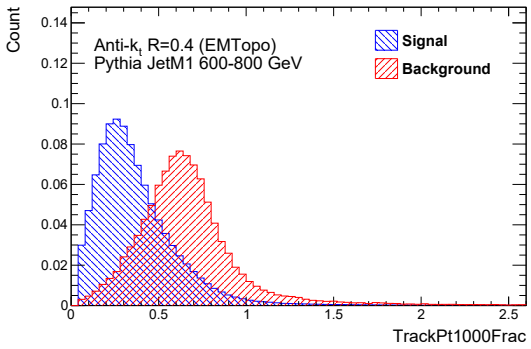
Count
Anti-k$_t$ R=0.4 (EMTopo)
Pythia JetM1 600-800 GeV
Signal
Background
TrackPt1000Frac

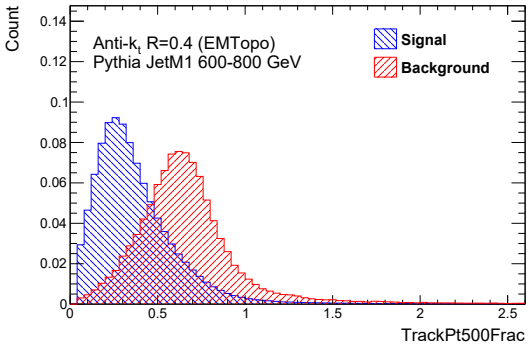
Count
Anti-k$_t$ R=0.4 (EMTopo)
Pythia JetM1 600-800 GeV
Signal
Background
TrackPt500Frac

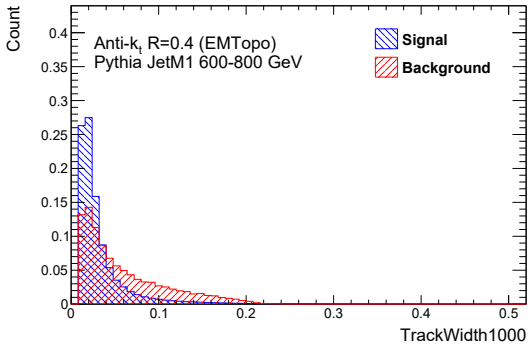
Count
Anti-k$_t$ R=0.4 (EMTopo)
Pythia JetM1 600-800 GeV
Signal
Background
TrackWidth1000

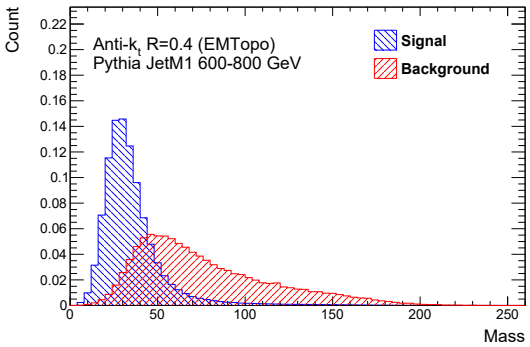
Count
Anti-k$_t$ R=0.4 (EMTopo)
Pythia JetM1 600-800 GeV
Signal
Background
Mass

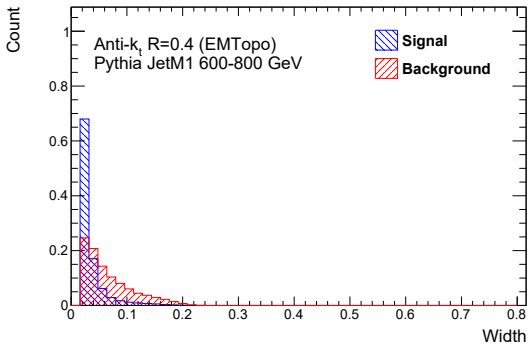
Count
Anti-k$_t$ R=0.4 (EMTopo)
Pythia JetM1 600-800 GeV
Signal
Background
Width

C.14 800-1100 GeV

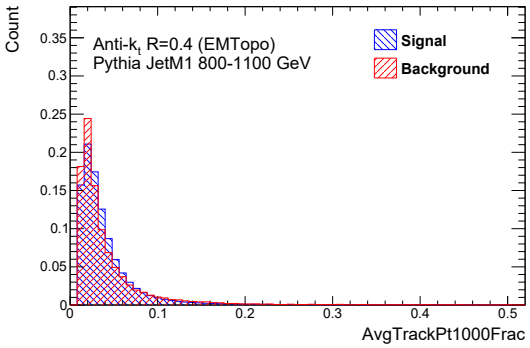

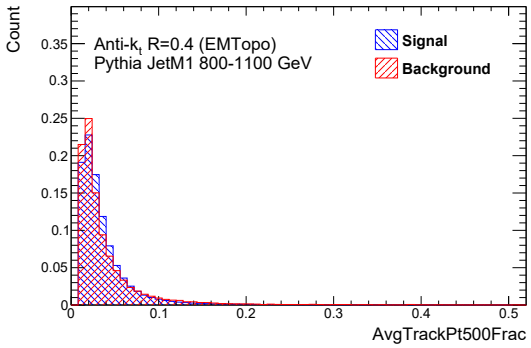

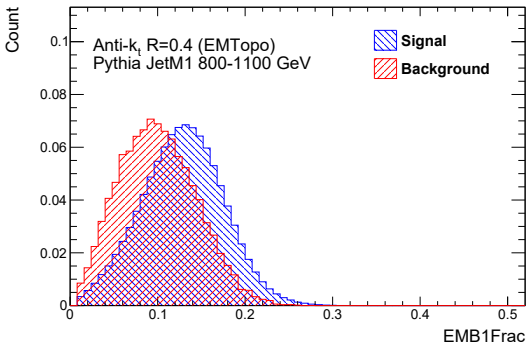

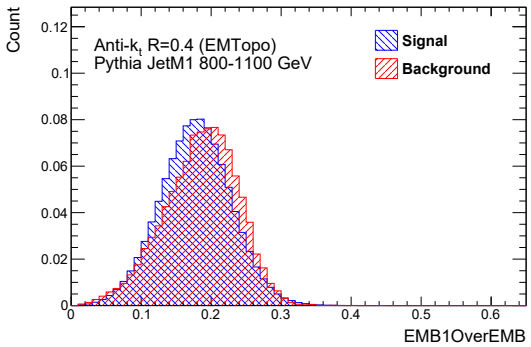

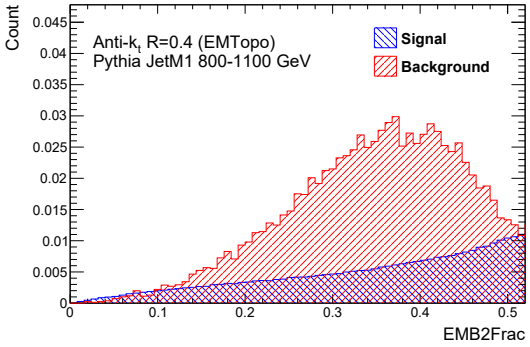

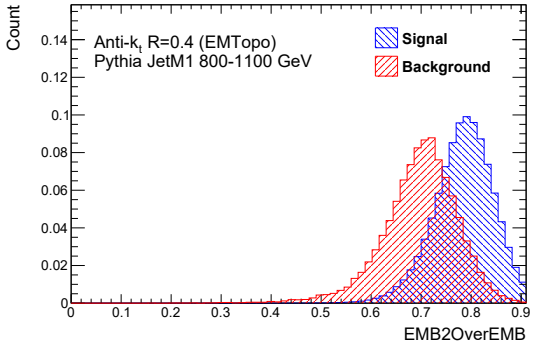

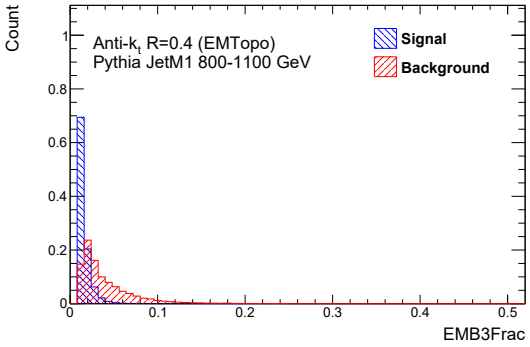

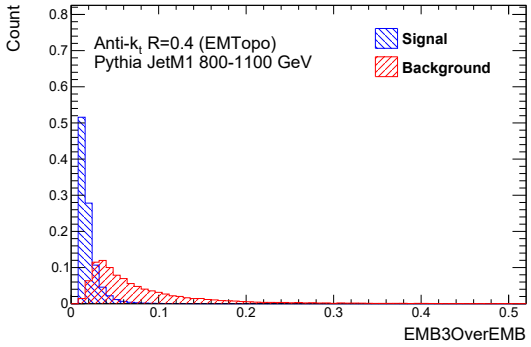

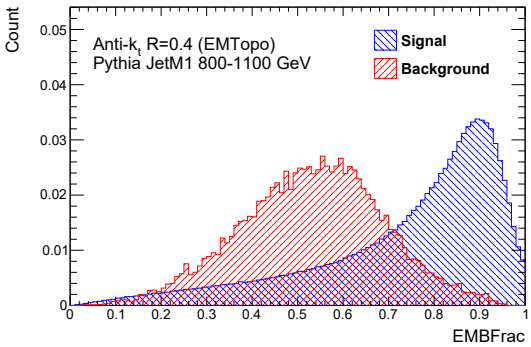
Count
Anti-k$_t$ R=0.4 (EMTopo)
Pythia JetM1 800-1100 GeV
Signal
Background
EMBFrac

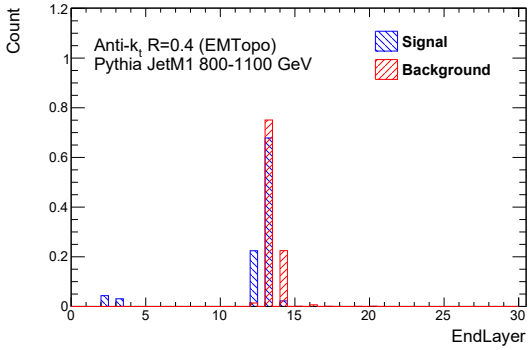
Count
Anti-k$_t$ R=0.4 (EMTopo)
Pythia JetM1 800-1100 GeV
Signal
Background
EndLayer

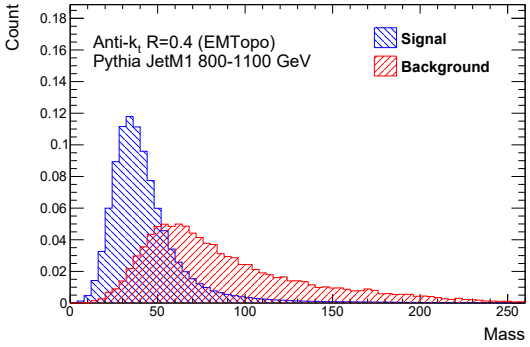
Count
Anti-k$_t$ R=0.4 (EMTopo)
Pythia JetM1 800-1100 GeV
Signal
Background
Mass

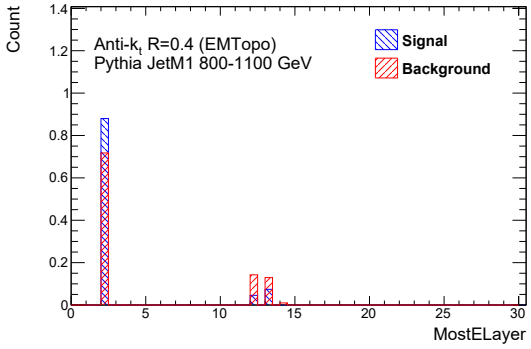
Count
Anti-k$_t$ R=0.4 (EMTopo)
Pythia JetM1 800-1100 GeV
Signal
Background
MostELayer

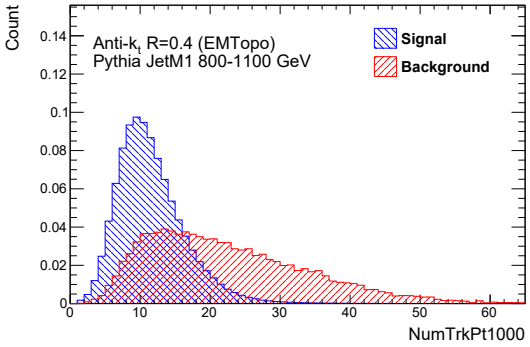
Count
Anti-k$_t$ R=0.4 (EMTopo)
Pythia JetM1 800-1100 GeV
Signal
Background
NumTrkPt1000

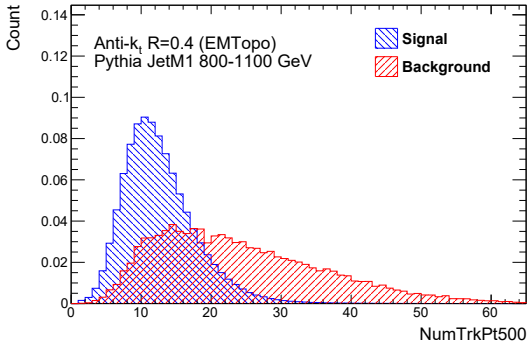
Count
Anti-k$_t$ R=0.4 (EMTopo)
Pythia JetM1 800-1100 GeV
Signal
Background
NumTrkPt500

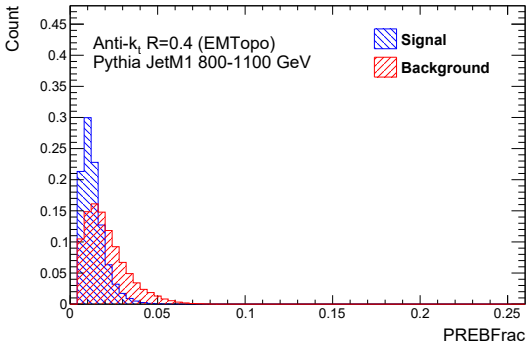
Count
Anti-k$_t$ R=0.4 (EMTopo)
Pythia JetM1 800-1100 GeV
Signal
Background
PREBFrac

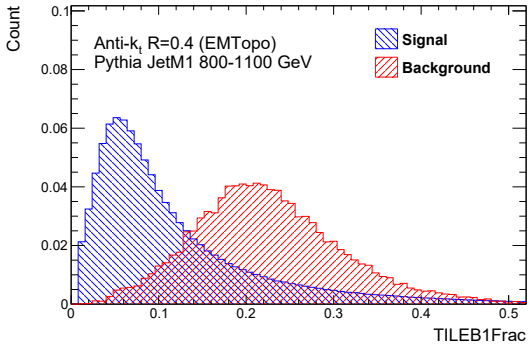
Count
Anti-k$_t$ R=0.4 (EMTopo)
Pythia JetM1 800-1100 GeV
Signal
Background
TILEB1Frac

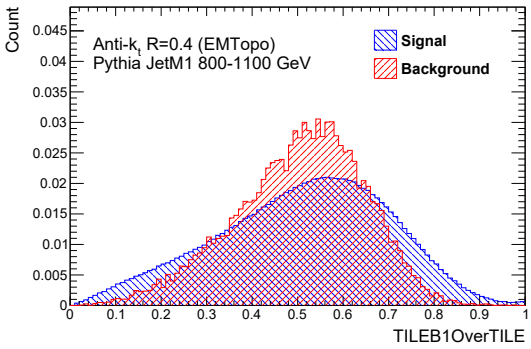
Count
Anti-k$_t$ R=0.4 (EMTopo)
Pythia JetM1 800-1100 GeV
Signal
Background
TILEB1OverTILE

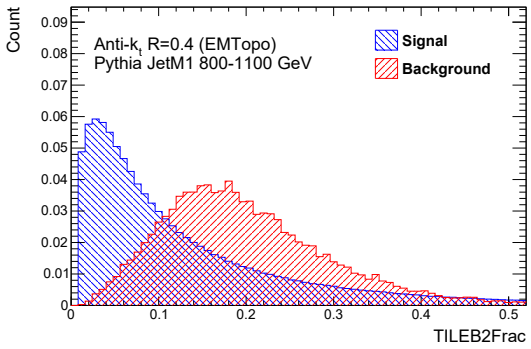
Count
Anti-k$_t$ R=0.4 (EMTopo)
Pythia JetM1 800-1100 GeV
Signal
Background
TILEB2Frac

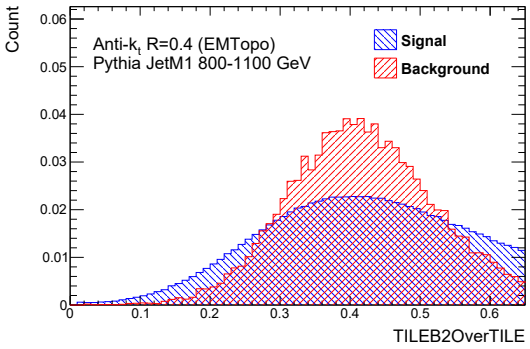
Count
Anti-k$_t$ R=0.4 (EMTopo)
Pythia JetM1 800-1100 GeV
Signal
Background
TILEB2OverTILE

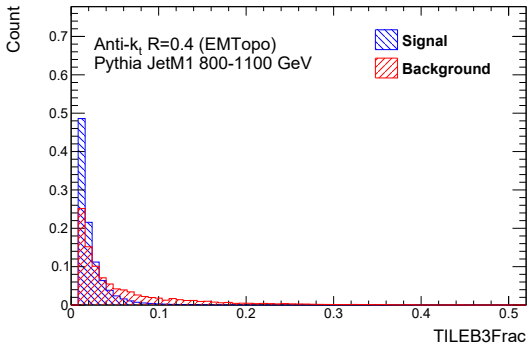
Count
Anti-k$_t$ R=0.4 (EMTopo)
Pythia JetM1 800-1100 GeV
Signal
Background
TILEB3Frac

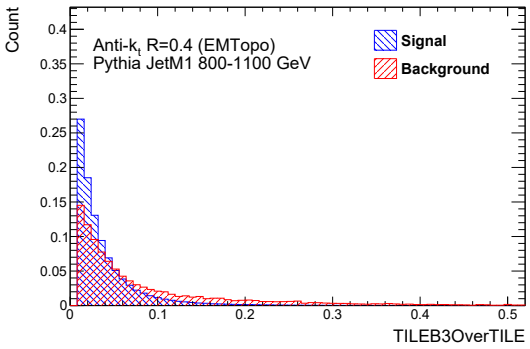
Count
Anti-k$_t$ R=0.4 (EMTopo)
Pythia JetM1 800-1100 GeV
Signal
Background
TILEB3OverTILE

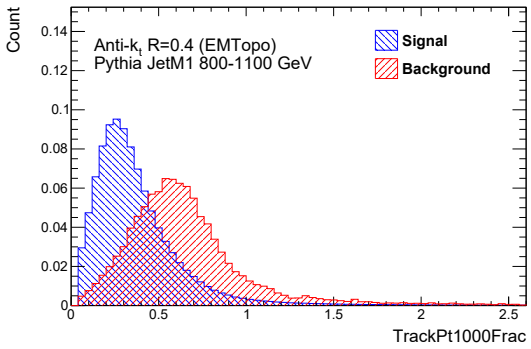
Count
Anti-k$_t$ R=0.4 (EMTopo)
Pythia JetM1 800-1100 GeV
Signal
Background
TrackPt1000Frac

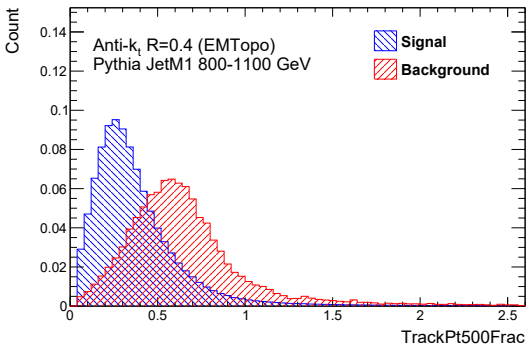
Count
Anti-k$_t$ R=0.4 (EMTopo)
Pythia JetM1 800-1100 GeV
Signal
Background
TrackPt500Frac

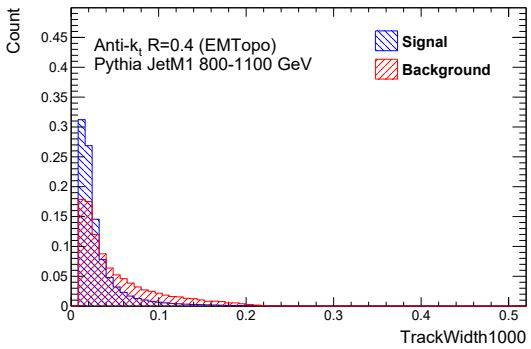
Count
Anti-k$_t$ R=0.4 (EMTopo)
Pythia JetM1 800-1100 GeV
Signal
Background
TrackWidth1000

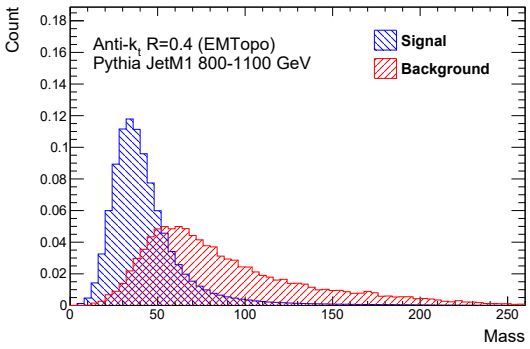
Count
Anti-k$_t$ R=0.4 (EMTopo)
Pythia JetM1 800-1100 GeV
Signal
Background
Mass

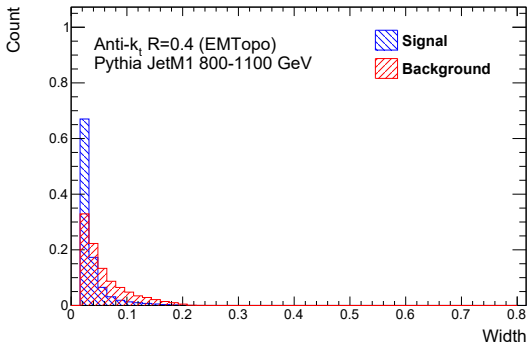
Count
Anti-k$_t$ R=0.4 (EMTopo)
Pythia JetM1 800-1100 GeV
Signal
Background
Width

Appendix D

Jet Property Correlations

This appendix shows the correlations of different jet properties in each momentum bin.

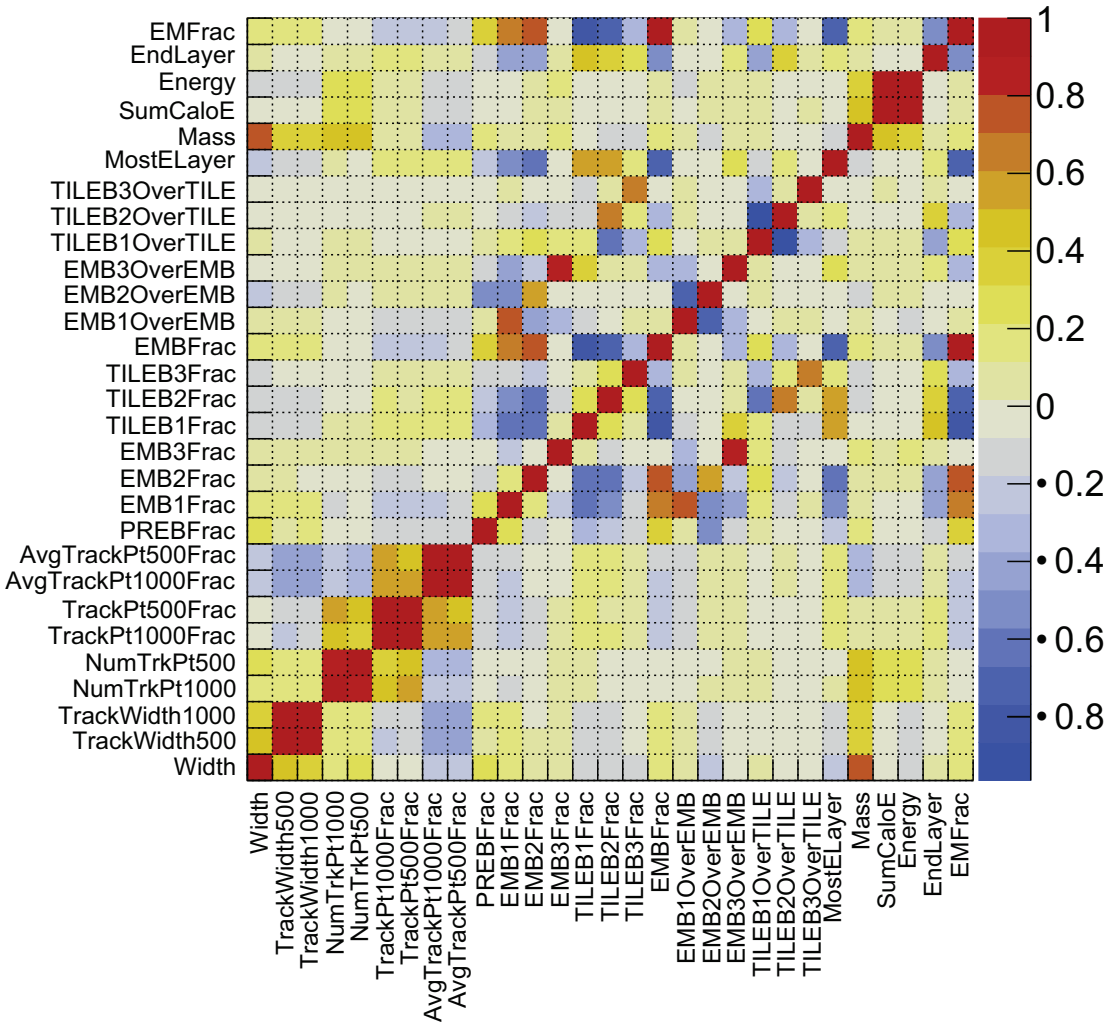
Jet variable Correlations, 25_45GeV
EMFrac
EndLayer
Energy
SumCaloE
Mass
MostELayer
TILEB3OverTILE
TILEB2OverTILE
TILEB1OverTILE
EMB3OverEMB
EMB2OverEMB
EMB1OverEMB
EMBFrac
TILEB3Frac
TILEB2Frac
TILEB1Frac
EMB3Frac
EMB2Frac
EMB1Frac
PREBFrac
AvgTrackPt500Frac
AvgTrackPt1000Frac
TrackPt500Frac
TrackPt1000Frac
NumTrkPt500
NumTrkPt1000
TrackWidth1000
TrackWidth500
Width
1
0.8
0.6
0.4
0.2
0
• 0.2
• 0.4
• 0.6
• 0.8
Width
TrackWidth500
TrackWidth1000
NumTrkPt1000
NumTrkPt500
TrackPt1000Frac
TrackPt500Frac
AvgTrackPt1000Frac
AvgTrackPt500Frac
PREBFrac
EMB1Frac
EMB2Frac
EMB3Frac
TILEB1Frac
TILEB2Frac
TILEB3Frac
EMBFrac
EMB1OverEMB
EMB2OverEMB
EMB3OverEMB
TILEB1OverTILE
TILEB2OverTILE
TILEB3OverTILE
MostELayer
Mass
SumCaloE
Energy
EndLayer
EMFrac

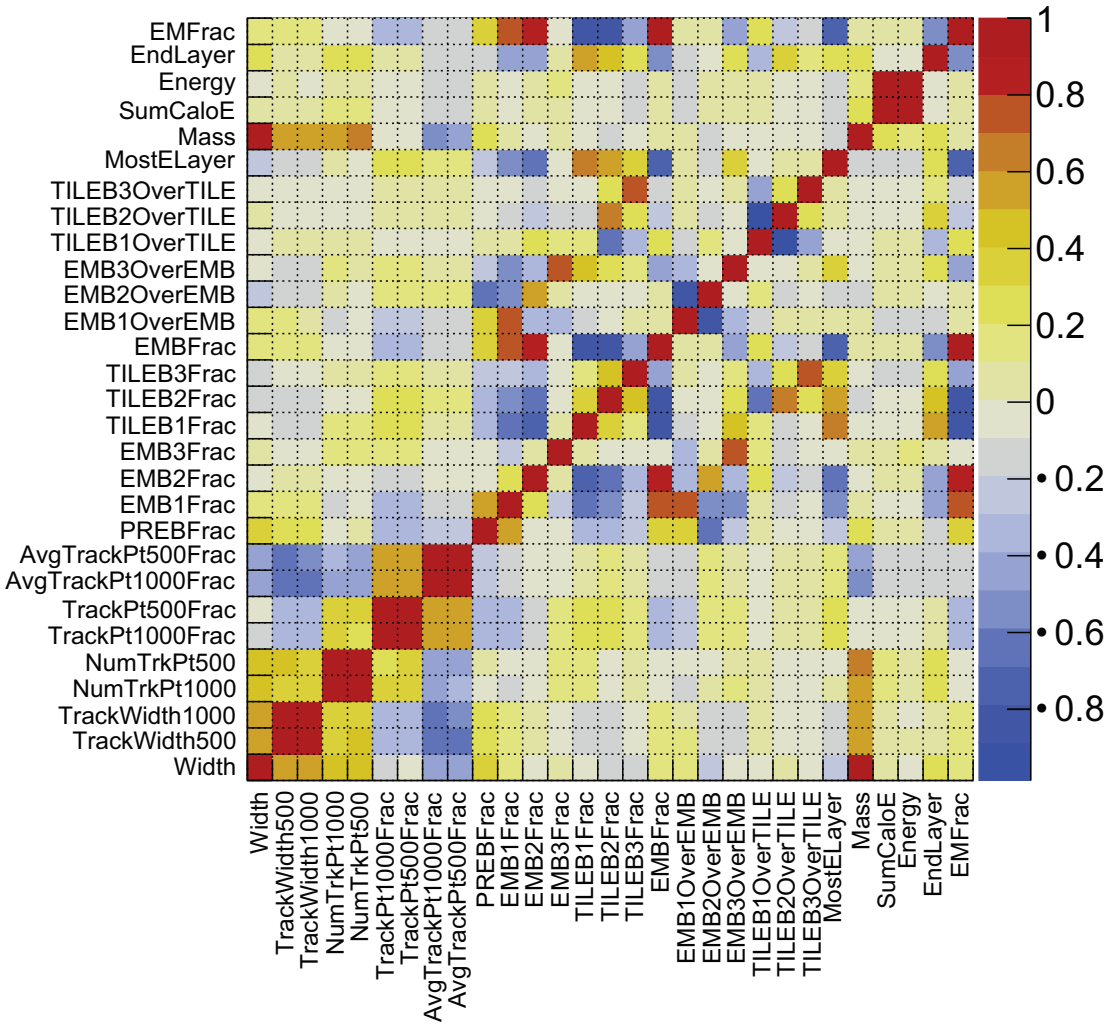
Jet variable Correlations, 45_65GeV
EMFrac
EndLayer
Energy
SumCaloE
Mass
MostELayer
TILEB3OverTILE
TILEB2OverTILE
TILEB1OverTILE
EMB3OverEMB
EMB2OverEMB
EMB1OverEMB
EMBFrac
TILEB3Frac
TILEB2Frac
TILEB1Frac
EMB3Frac
EMB2Frac
EMB1Frac
PREBFrac
AvgTrackPt500Frac
AvgTrackPt1000Frac
TrackPt500Frac
TrackPt1000Frac
NumTrkPt500
NumTrkPt1000
TrackWidth1000
TrackWidth500
Width
1
0.8
0.6
0.4
0.2
0
• 0.2
• 0.4
• 0.6
• 0.8
Width
TrackWidth500
TrackWidth1000
NumTrkPt1000
NumTrkPt500
TrackPt1000Frac
TrackPt500Frac
AvgTrackPt1000Frac
AvgTrackPt500Frac
PREBFrac
EMB1Frac
EMB2Frac
EMB3Frac
TILEB1Frac
TILEB2Frac
TILEB3Frac
EMBFrac
EMB1OverEMB
EMB2OverEMB
EMB3OverEMB
TILEB1OverTILE
TILEB2OverTILE
TILEB3OverTILE
MostELayer
Mass
SumCaloE
Energy
EndLayer
EMFrac

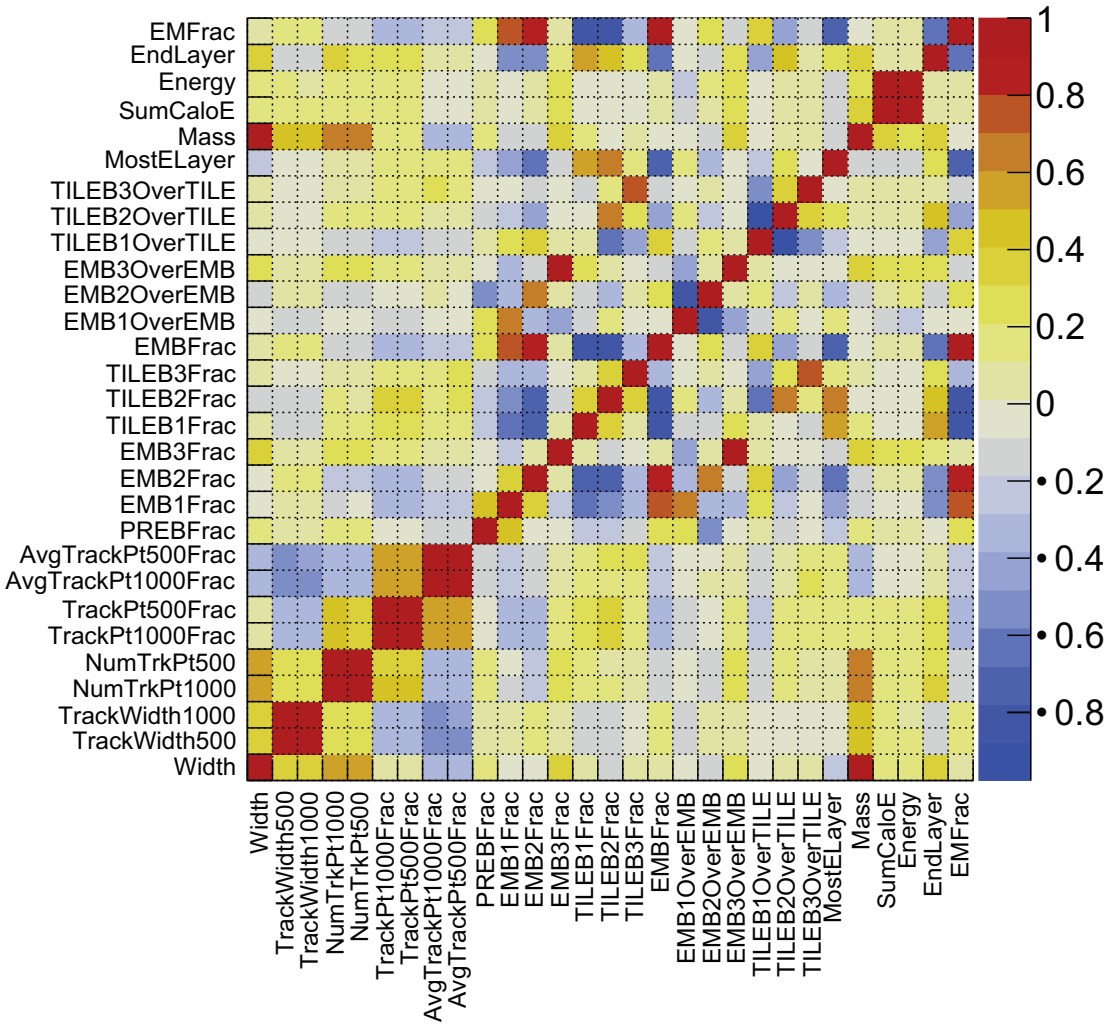
Jet variable Correlations, 65_85GeV
EMFrac
EndLayer
Energy
SumCaloE
Mass
MostELayer
TILEB3OverTILE
TILEB2OverTILE
TILEB1OverTILE
EMB3OverEMB
EMB2OverEMB
EMB1OverEMB
EMBFrac
TILEB3Frac
TILEB2Frac
TILEB1Frac
EMB3Frac
EMB2Frac
EMB1Frac
PREBFrac
AvgTrackPt500Frac
AvgTrackPt1000Frac
TrackPt500Frac
TrackPt1000Frac
NumTrkPt500
NumTrkPt1000
TrackWidth1000
TrackWidth500
Width
1
0.8
0.6
0.4
0.2
0
• 0.2
• 0.4
• 0.6
• 0.8

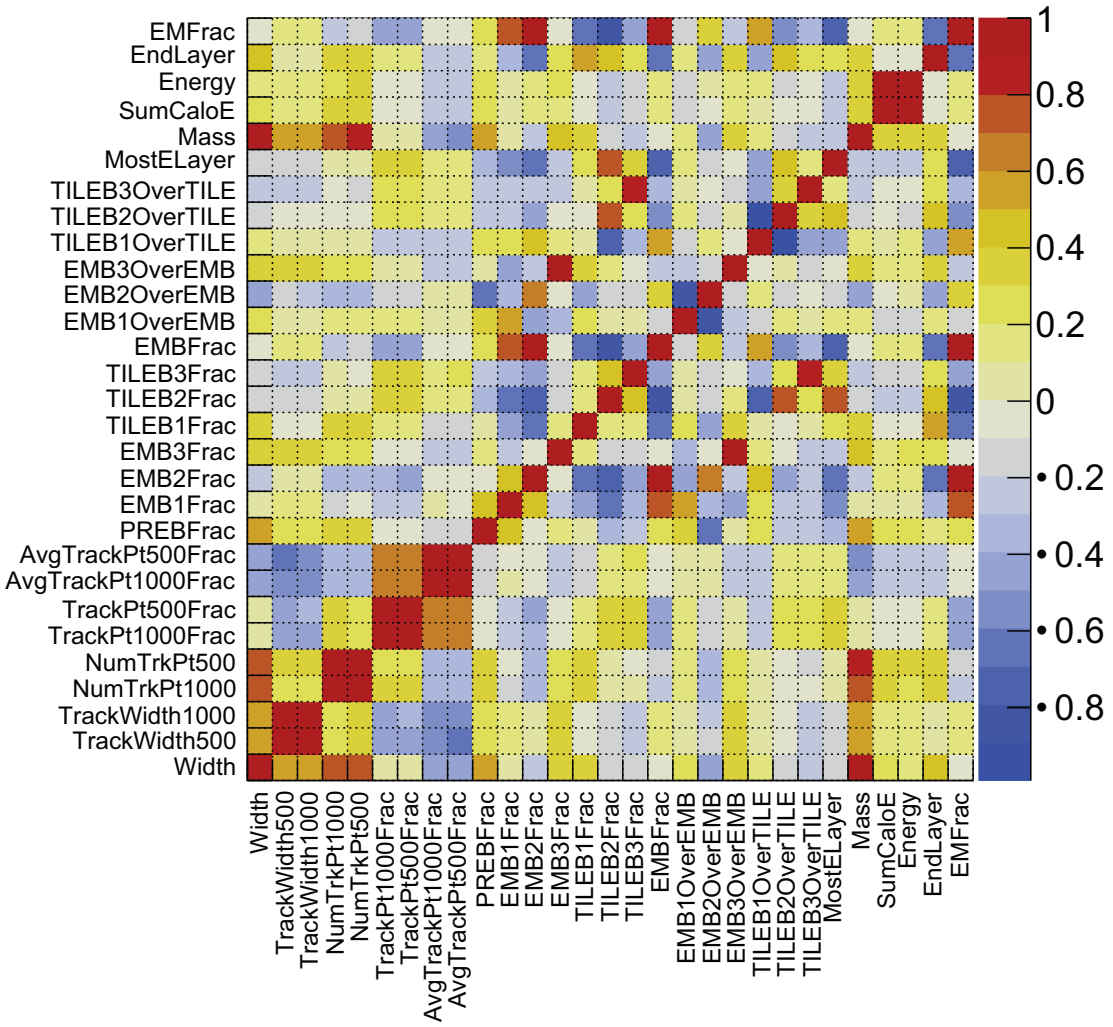
Jet variable Correlations, 85_105GeV
EMFrac
EndLayer
Energy
SumCaloE
Mass
MostELayer
TILEB3OverTILE
TILEB2OverTILE
TILEB1OverTILE
EMB3OverEMB
EMB2OverEMB
EMB1OverEMB
EMBFrac
TILEB3Frac
TILEB2Frac
TILEB1Frac
EMB3Frac
EMB2Frac
EMB1Frac
PREBFrac
AvgTrackPt500Frac
AvgTrackPt1000Frac
TrackPt500Frac
TrackPt1000Frac
NumTrkPt500
NumTrkPt1000
TrackWidth1000
TrackWidth500
Width
1
0.8
0.6
0.4
0.2
0
• 0.2
• 0.4
• 0.6
• 0.8

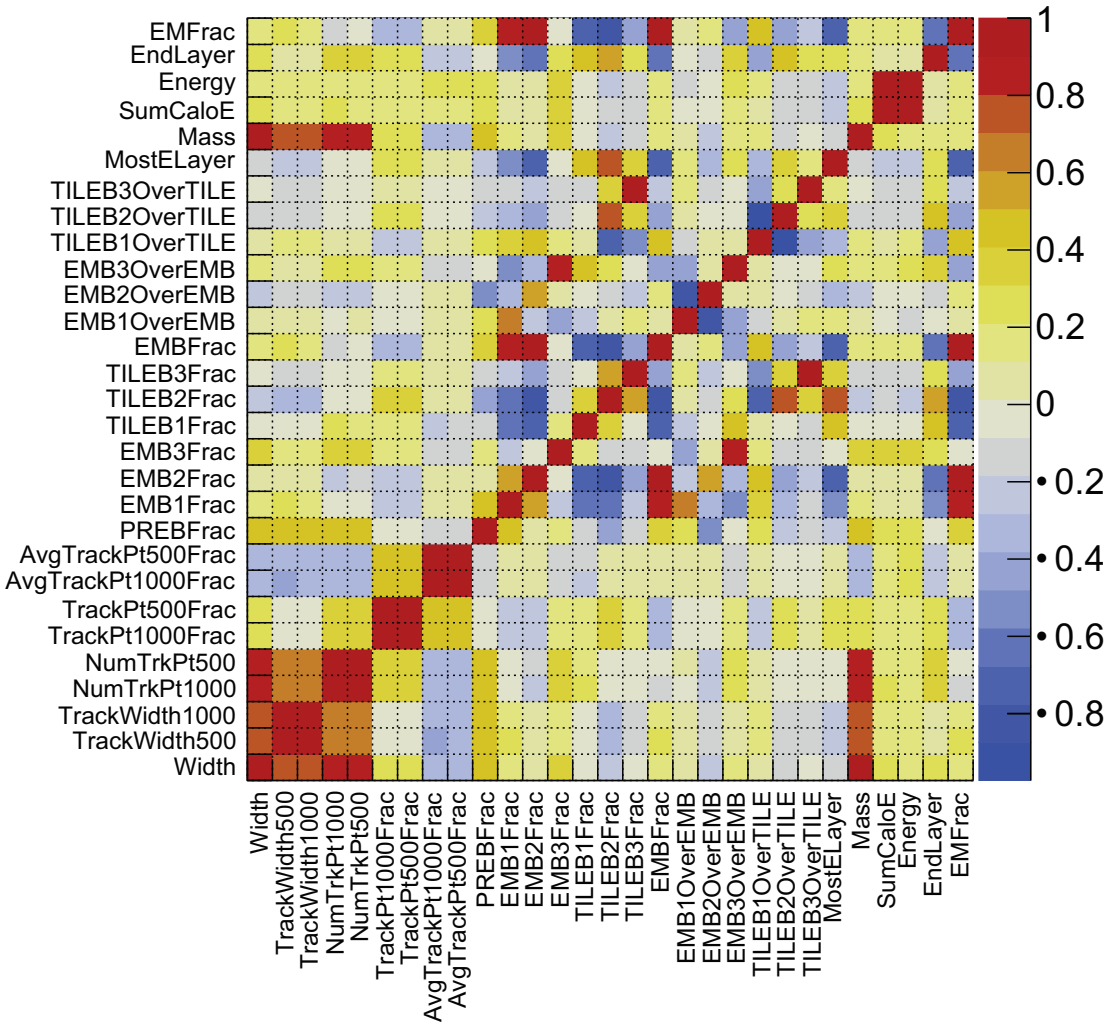
Jet variable Correlations, 105_125GeV
EMFrac
EndLayer
Energy
SumCaloE
Mass
MostELayer
TILEB3OverTILE
TILEB2OverTILE
TILEB1OverTILE
EMB3OverEMB
EMB2OverEMB
EMB1OverEMB
EMBFrac
TILEB3Frac
TILEB2Frac
TILEB1Frac
EMB3Frac
EMB2Frac
EMB1Frac
PREBFrac
AvgTrackPt500Frac
AvgTrackPt1000Frac
TrackPt500Frac
TrackPt1000Frac
NumTrkPt500
NumTrkPt1000
TrackWidth1000
TrackWidth500
Width
1
0.8
0.6
0.4
0.2
0
• 0.2
• 0.4
• 0.6
• 0.8

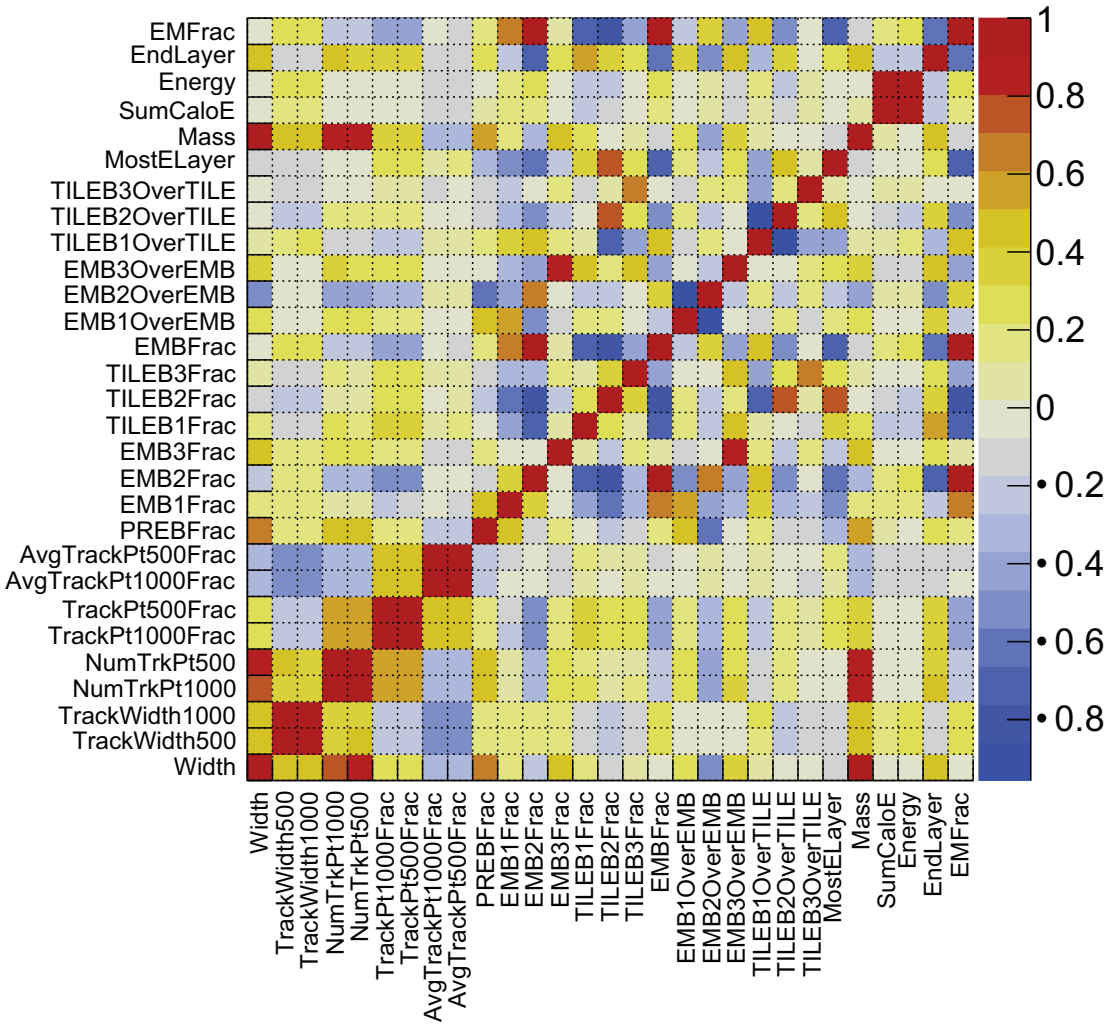
Jet variable Correlations, 125_160GeV
EMFrac
EndLayer
Energy
SumCaloE
Mass
MostELayer
TILEB3OverTILE
TILEB2OverTILE
TILEB1OverTILE
EMB3OverEMB
EMB2OverEMB
EMB1OverEMB
EMBFrac
TILEB3Frac
TILEB2Frac
TILEB1Frac
EMB3Frac
EMB2Frac
EMB1Frac
PREBFrac
AvgTrackPt500Frac
AvgTrackPt1000Frac
TrackPt500Frac
TrackPt1000Frac
NumTrkPt500
NumTrkPt1000
TrackWidth1000
TrackWidth500
Width
1
0.8
0.6
0.4
0.2
0
• 0.2
• 0.4
• 0.6
• 0.8
Width
TrackWidth500
TrackWidth1000
NumTrkPt1000
NumTrkPt500
TrackPt1000Frac
TrackPt500Frac
AvgTrackPt1000Frac
AvgTrackPt500Frac
PREBFrac
EMB1Frac
EMB2Frac
EMB3Frac
TILEB1Frac
TILEB2Frac
TILEB3Frac
EMBFrac
EMB1OverEMB
EMB2OverEMB
EMB3OverEMB
TILEB1OverTILE
TILEB2OverTILE
TILEB3OverTILE
MostELayer
Mass
SumCaloE
Energy
EndLayer
EMFrac

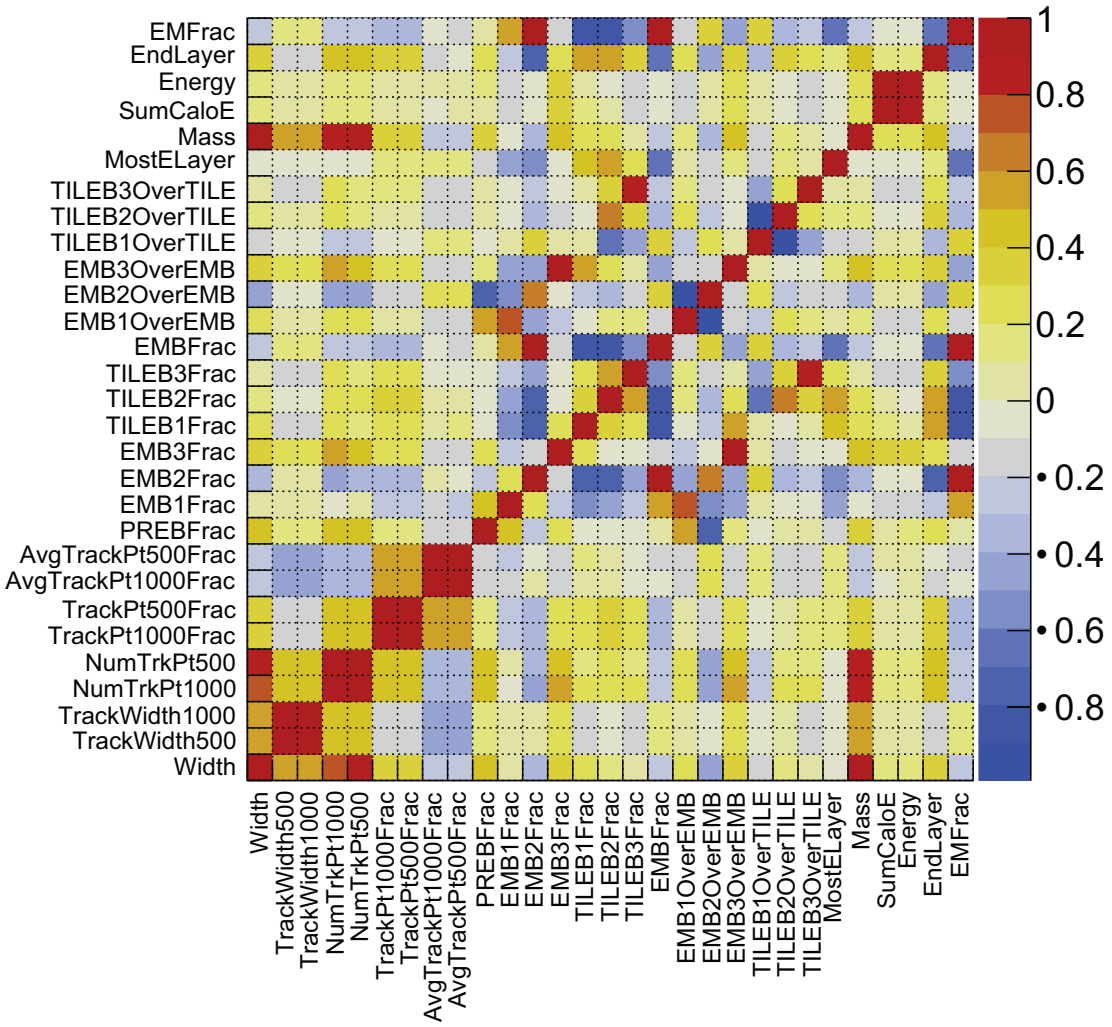
Jet variable Correlations, 160_210GeV
EMFrac
EndLayer
Energy
SumCaloE
Mass
MostELayer
TILEB3OverTILE
TILEB2OverTILE
TILEB1OverTILE
EMB3OverEMB
EMB2OverEMB
EMB1OverEMB
EMBFrac
TILEB3Frac
TILEB2Frac
TILEB1Frac
EMB3Frac
EMB2Frac
EMB1Frac
PREBFrac
AvgTrackPt500Frac
AvgTrackPt1000Frac
TrackPt500Frac
TrackPt1000Frac
NumTrkPt500
NumTrkPt1000
TrackWidth1000
TrackWidth500
Width
1
0.8
0.6
0.4
0.2
0
• 0.2
• 0.4
• 0.6
• 0.8
Width
TrackWidth500
TrackWidth1000
NumTrkPt1000
NumTrkPt500
TrackPt1000Frac
TrackPt500Frac
AvgTrackPt1000Frac
AvgTrackPt500Frac
PREBFrac
EMB1Frac
EMB2Frac
EMB3Frac
TILEB1Frac
TILEB2Frac
TILEB3Frac
EMBFrac
EMB1OverEMB
EMB2OverEMB
EMB3OverEMB
TILEB1OverTILE
TILEB2OverTILE
TILEB3OverTILE
MostELayer
Mass
SumCaloE
Energy
EndLayer
EMFrac

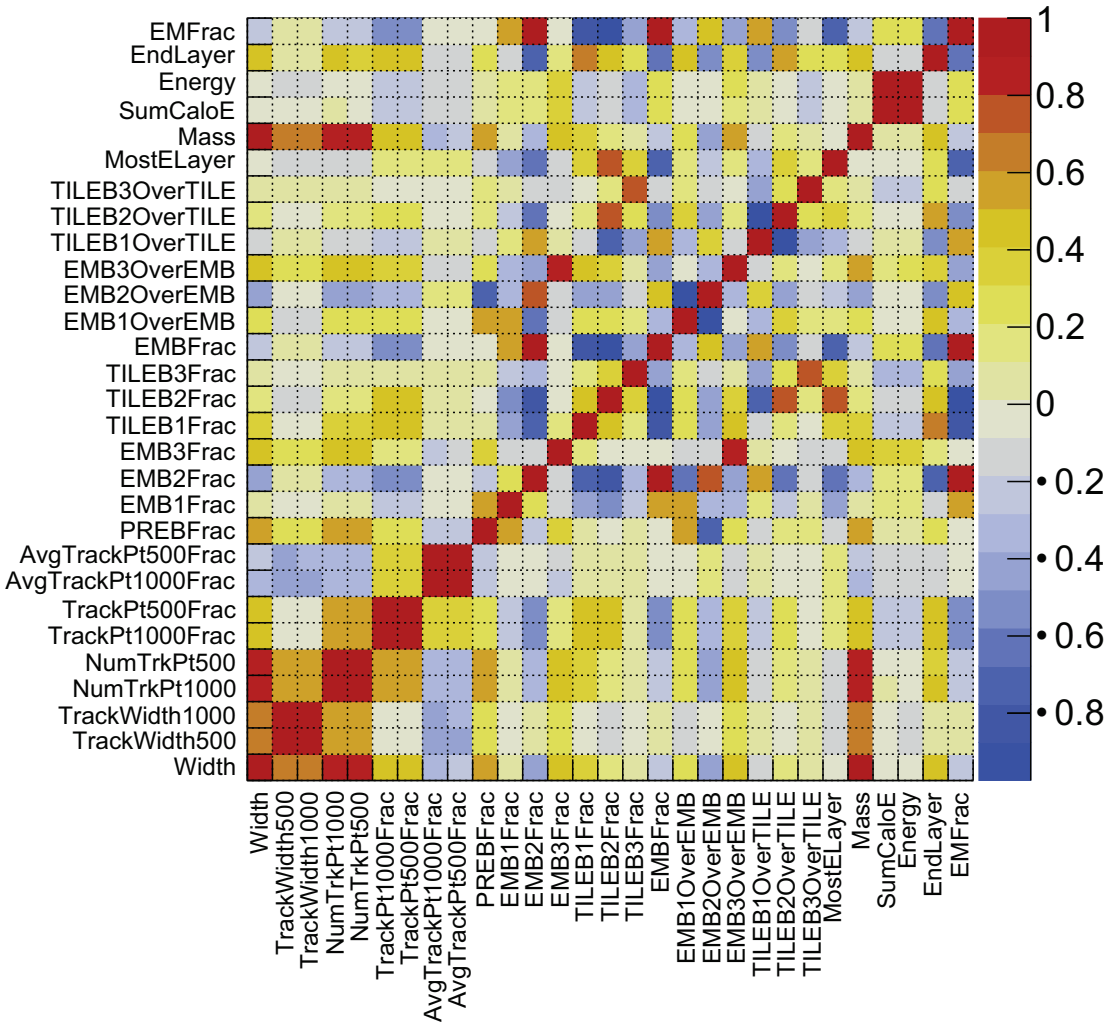
Jet variable Correlations, 210_260GeV
EMFrac
EndLayer
Energy
SumCaloE
Mass
MostELayer
TILEB3OverTILE
TILEB2OverTILE
TILEB1OverTILE
EMB3OverEMB
EMB2OverEMB
EMB1OverEMB
EMBFrac
TILEB3Frac
TILEB2Frac
TILEB1Frac
EMB3Frac
EMB2Frac
EMB1Frac
PREBFrac
AvgTrackPt500Frac
AvgTrackPt1000Frac
TrackPt500Frac
TrackPt1000Frac
NumTrkPt500
NumTrkPt1000
TrackWidth1000
TrackWidth500
Width
1
0.8
0.6
0.4
0.2
0
• 0.2
• 0.4
• 0.6
• 0.8
Width
TrackWidth500
TrackWidth1000
NumTrkPt1000
NumTrkPt500
TrackPt1000Frac
TrackPt500Frac
AvgTrackPt1000Frac
AvgTrackPt500Frac
PREBFrac
EMB1Frac
EMB2Frac
EMB3Frac
TILEB1Frac
TILEB2Frac
TILEB3Frac
EMBFrac
EMB1OverEMB
EMB2OverEMB
EMB3OverEMB
TILEB1OverTILE
TILEB2OverTILE
TILEB3OverTILE
MostELayer
Mass
SumCaloE
Energy
EndLayer
EMFrac

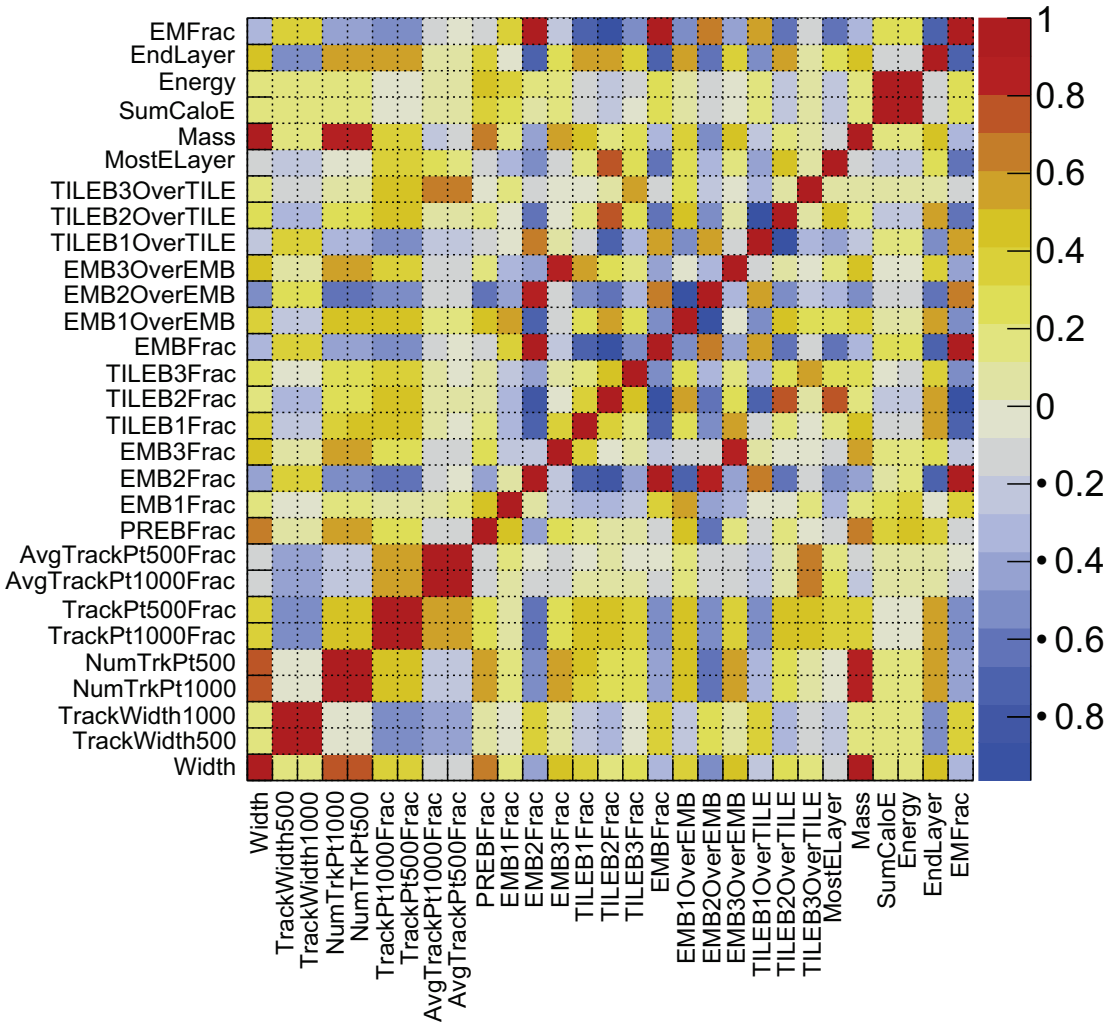
Jet variable Correlations, 260_310GeV
EMFrac
EndLayer
Energy
SumCaloE
Mass
MostELayer
TILEB3OverTILE
TILEB2OverTILE
TILEB1OverTILE
EMB3OverEMB
EMB2OverEMB
EMB1OverEMB
EMBFrac
TILEB3Frac
TILEB2Frac
TILEB1Frac
EMB3Frac
EMB2Frac
EMB1Frac
PREBFrac
AvgTrackPt500Frac
AvgTrackPt1000Frac
TrackPt500Frac
TrackPt1000Frac
NumTrkPt500
NumTrkPt1000
TrackWidth1000
TrackWidth500
Width
1
0.8
0.6
0.4
0.2
0
• 0.2
• 0.4
• 0.6
• 0.8

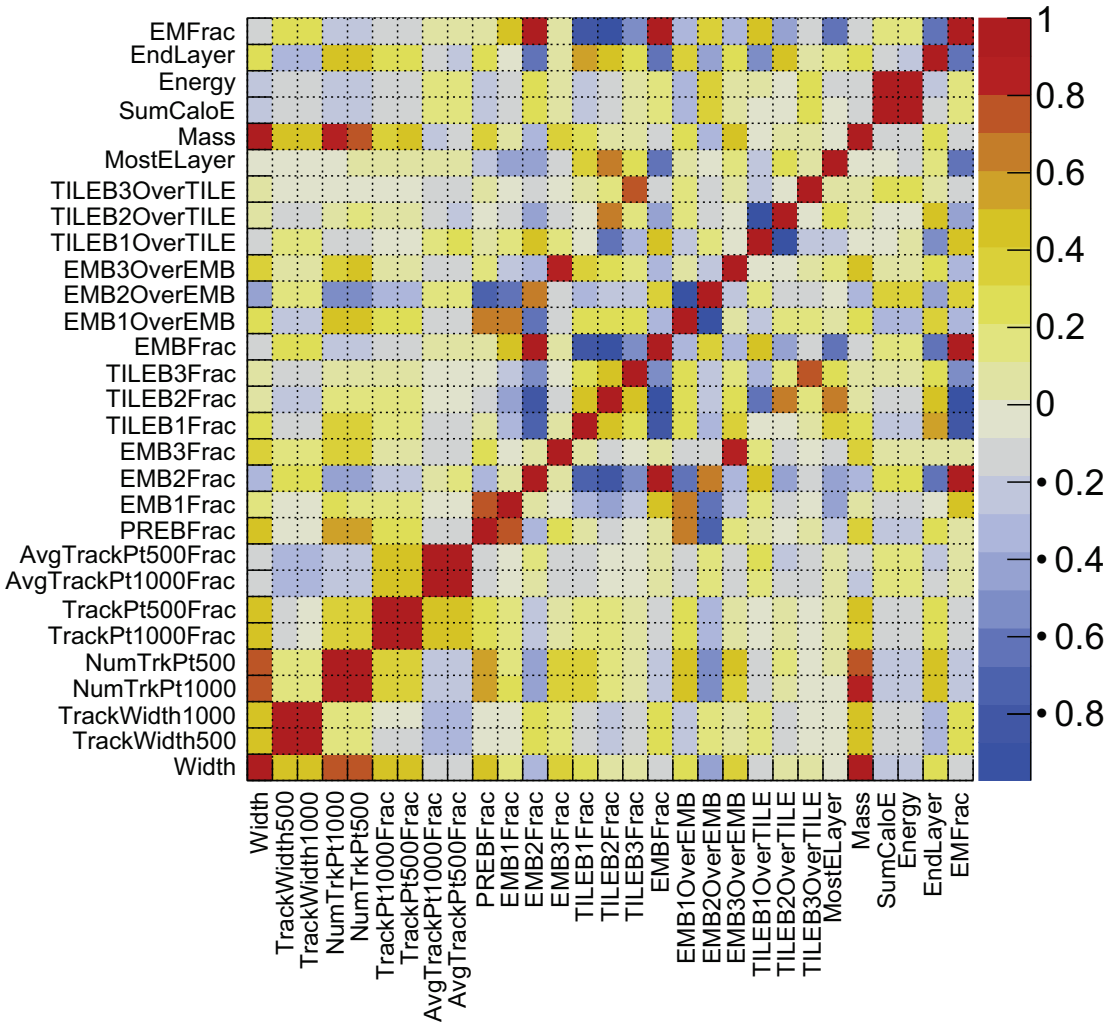
Jet variable Correlations, 310_400GeV
EMFrac
EndLayer
Energy
SumCaloE
Mass
MostELayer
TILEB3OverTILE
TILEB2OverTILE
TILEB1OverTILE
EMB3OverEMB
EMB2OverEMB
EMB1OverEMB
EMBFrac
TILEB3Frac
TILEB2Frac
TILEB1Frac
EMB3Frac
EMB2Frac
EMB1Frac
PREBFrac
AvgTrackPt500Frac
AvgTrackPt1000Frac
TrackPt500Frac
TrackPt1000Frac
NumTrkPt500
NumTrkPt1000
TrackWidth1000
TrackWidth500
Width
1
0.8
0.6
0.4
0.2
0
• 0.2
• 0.4
• 0.6
• 0.8

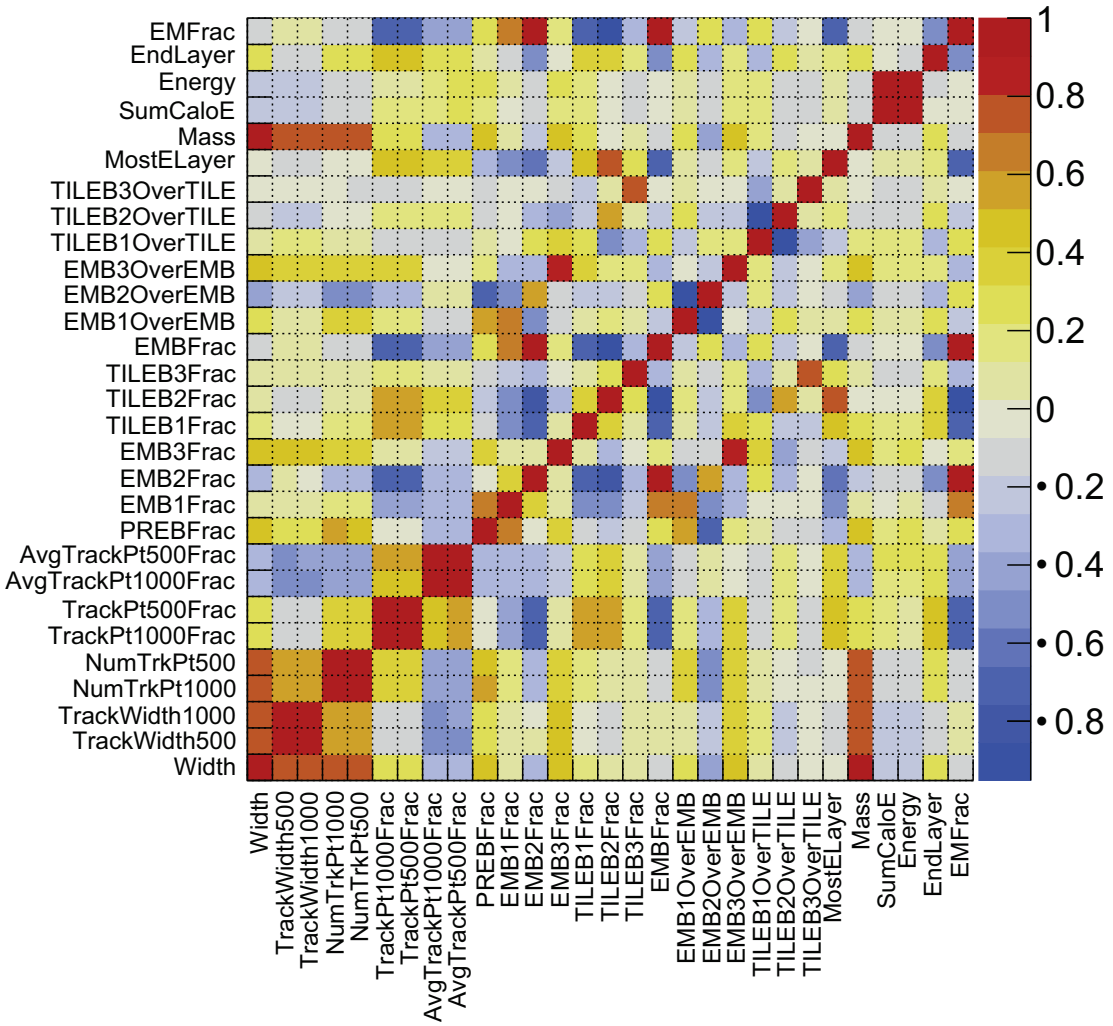
Jet variable Correlations, 400_500GeV
EMFrac
EndLayer
Energy
SumCaloE
Mass
MostELayer
TILEB3OverTILE
TILEB2OverTILE
TILEB1OverTILE
EMB3OverEMB
EMB2OverEMB
EMB1OverEMB
EMBFrac
TILEB3Frac
TILEB2Frac
TILEB1Frac
EMB3Frac
EMB2Frac
EMB1Frac
PREBFrac
AvgTrackPt500Frac
AvgTrackPt1000Frac
TrackPt500Frac
TrackPt1000Frac
NumTrkPt500
NumTrkPt1000
TrackWidth1000
TrackWidth500
Width
1
0.8
0.6
0.4
0.2
0
• 0.2
• 0.4
• 0.6
• 0.8
Width
TrackWidth500
TrackWidth1000
NumTrkPt1000
NumTrkPt500
TrackPt1000Frac
TrackPt500Frac
AvgTrackPt1000Frac
AvgTrackPt500Frac
PREBFrac
EMB1Frac
EMB2Frac
EMB3Frac
TILEB1Frac
TILEB2Frac
TILEB3Frac
EMBFrac
EMB1OverEMB
EMB2OverEMB
EMB3OverEMB
TILEB1OverTILE
TILEB2OverTILE
TILEB3OverTILE
MostELayer
Mass
SumCaloE
Energy
EndLayer
EMFrac

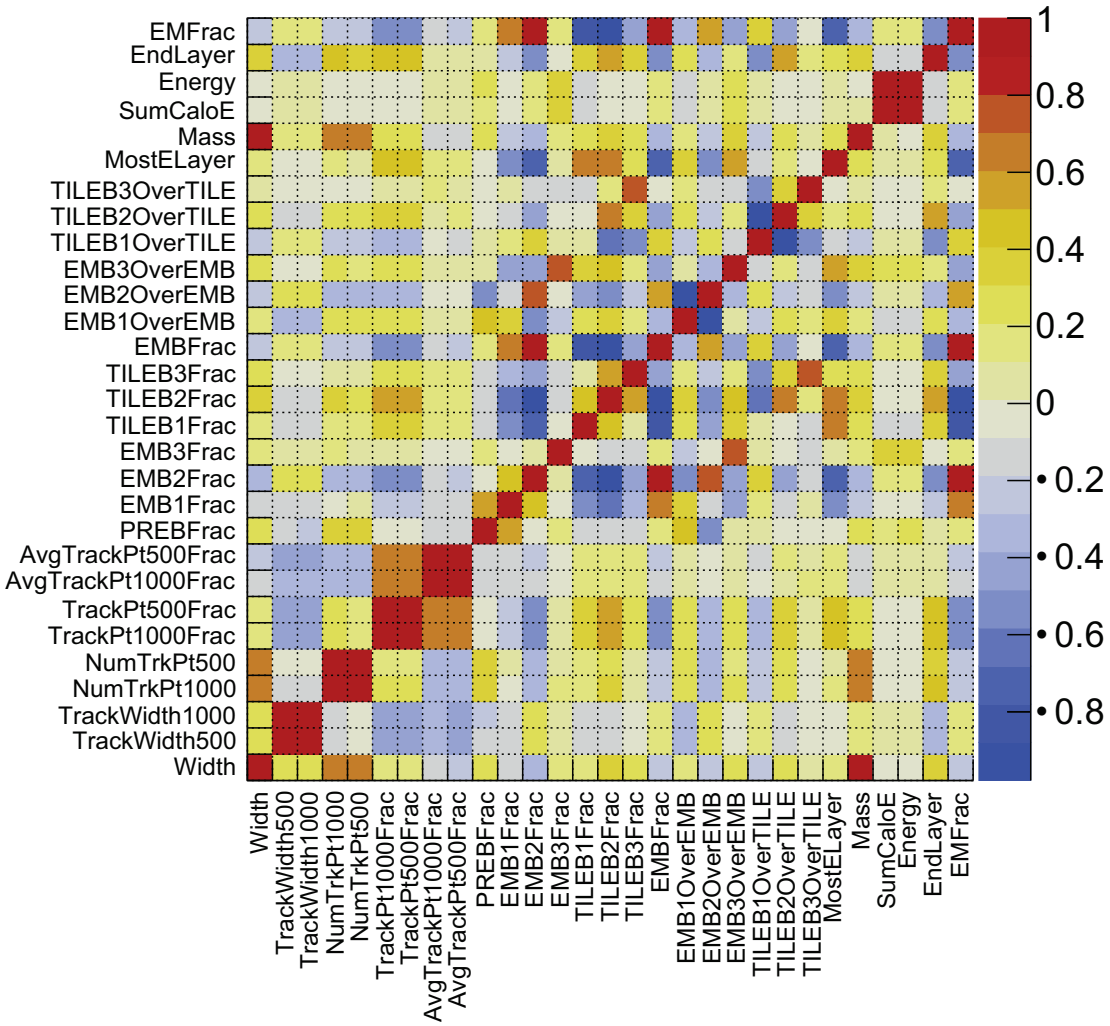
Jet variable Correlations, 500_600GeV
EMFrac
EndLayer
Energy
SumCaloE
Mass
MostELayer
TILEB3OverTILE
TILEB2OverTILE
TILEB1OverTILE
EMB3OverEMB
EMB2OverEMB
EMB1OverEMB
EMBFrac
TILEB3Frac
TILEB2Frac
TILEB1Frac
EMB3Frac
EMB2Frac
EMB1Frac
PREBFrac
AvgTrackPt500Frac
AvgTrackPt1000Frac
TrackPt500Frac
TrackPt1000Frac
NumTrkPt500
NumTrkPt1000
TrackWidth1000
TrackWidth500
Width
1
0.8
0.6
0.4
0.2
0
• 0.2
• 0.4
• 0.6
• 0.8
Width
TrackWidth500
TrackWidth1000
NumTrkPt1000
NumTrkPt500
TrackPt1000Frac
TrackPt500Frac
AvgTrackPt1000Frac
AvgTrackPt500Frac
PREBFrac
EMB1Frac
EMB2Frac
EMB3Frac
TILEB1Frac
TILEB2Frac
TILEB3Frac
EMBFrac
EMB1OverEMB
EMB2OverEMB
EMB3OverEMB
TILEB1OverTILE
TILEB2OverTILE
TILEB3OverTILE
MostELayer
Mass
SumCaloE
Energy
EndLayer
EMFrac

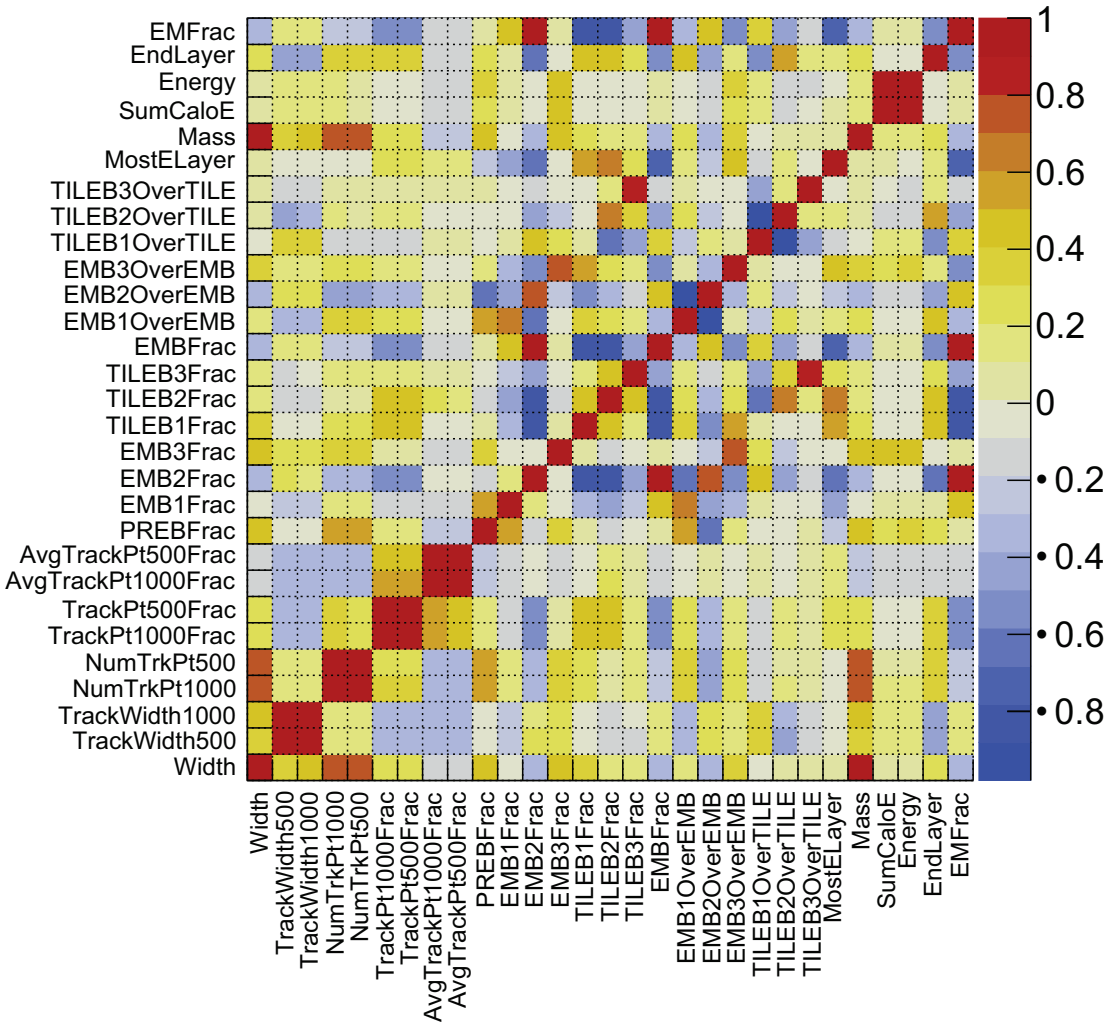
Jet variable Correlations, 600_800GeV
EMFrac
EndLayer
Energy
SumCaloE
Mass
MostELayer
TILEB3OverTILE
TILEB2OverTILE
TILEB1OverTILE
EMB3OverEMB
EMB2OverEMB
EMB1OverEMB
EMBFrac
TILEB3Frac
TILEB2Frac
TILEB1Frac
EMB3Frac
EMB2Frac
EMB1Frac
PREBFrac
AvgTrackPt500Frac
AvgTrackPt1000Frac
TrackPt500Frac
TrackPt1000Frac
NumTrkPt500
NumTrkPt1000
TrackWidth1000
TrackWidth500
Width
1
0.8
0.6
0.4
0.2
0
• 0.2
• 0.4
• 0.6
• 0.8
Width
TrackWidth500
TrackWidth1000
NumTrkPt1000
NumTrkPt500
TrackPt1000Frac
TrackPt500Frac
AvgTrackPt1000Frac
AvgTrackPt500Frac
PREBFrac
EMB1Frac
EMB2Frac
EMB3Frac
TILEB1Frac
TILEB2Frac
TILEB3Frac
EMBFrac
EMB1OverEMB
EMB2OverEMB
EMB3OverEMB
TILEB1OverTILE
TILEB2OverTILE
TILEB3OverTILE
MostELayer
Mass
SumCaloE
Energy
EndLayer
EMFrac

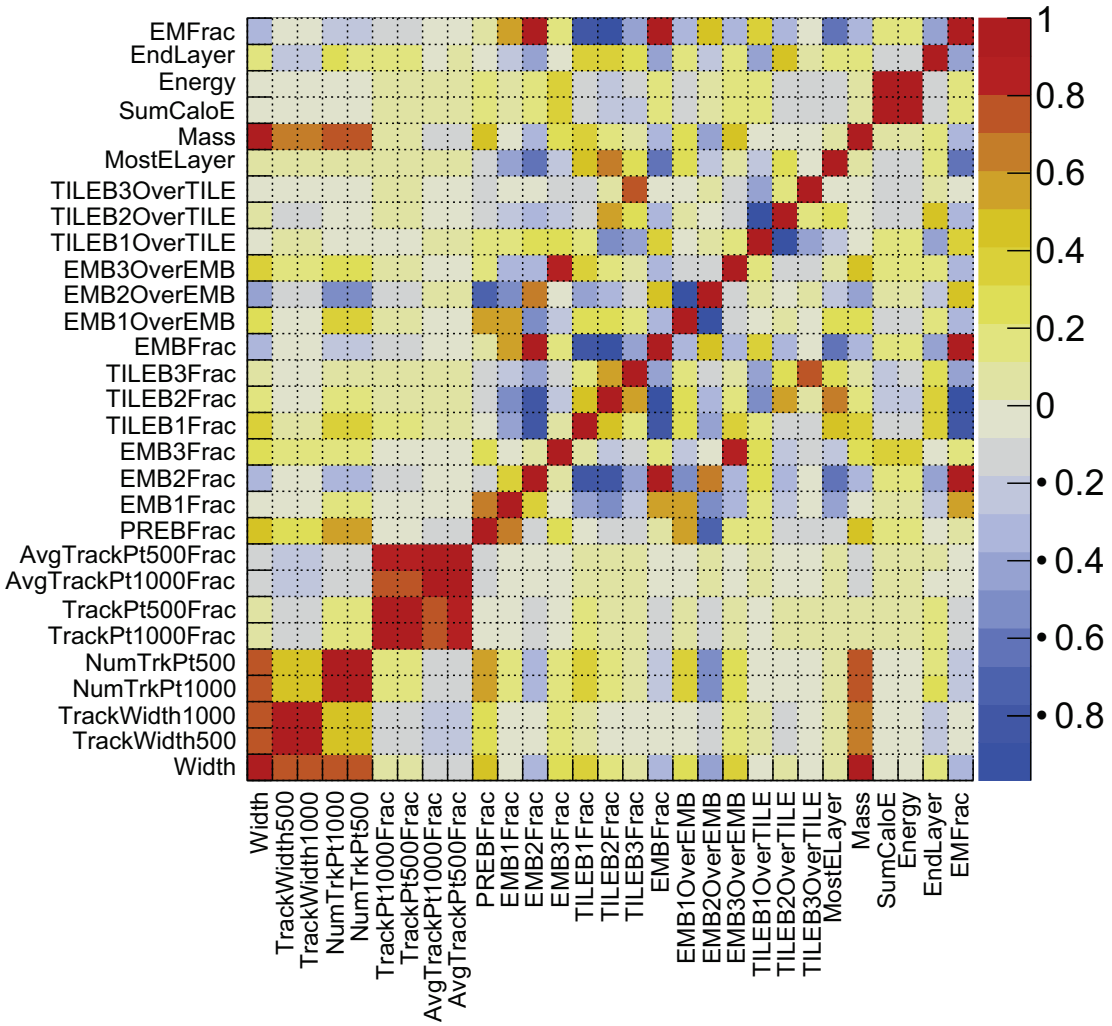
Jet variable Correlations, 800_1100GeV
EMFrac
EndLayer
Energy
SumCaloE
Mass
MostELayer
TILEB3OverTILE
TILEB2OverTILE
TILEB1OverTILE
EMB3OverEMB
EMB2OverEMB
EMB1OverEMB
EMBFrac
TILEB3Frac
TILEB2Frac
TILEB1Frac
EMB3Frac
EMB2Frac
EMB1Frac
PREBFrac
AvgTrackPt500Frac
AvgTrackPt1000Frac
TrackPt500Frac
TrackPt1000Frac
NumTrkPt500
NumTrkPt1000
TrackWidth1000
TrackWidth500
Width
1
0.8
0.6
0.4
0.2
0
• 0.2
• 0.4
• 0.6
• 0.8
Width
TrackWidth500
TrackWidth1000
NumTrkPt1000
NumTrkPt500
TrackPt1000Frac
TrackPt500Frac
AvgTrackPt1000Frac
AvgTrackPt500Frac
PREBFrac
EMB1Frac
EMB2Frac
EMB3Frac
TILEB1Frac
TILEB2Frac
TILEB3Frac
EMBFrac
EMB1OverEMB
EMB2OverEMB
EMB3OverEMB
TILEB1OverTILE
TILEB2OverTILE
TILEB3OverTILE
MostELayer
Mass
SumCaloE
Energy
EndLayer
EMFrac

Appendix E

Response Vs. Likelihood Heatmaps

The heatmaps in this appendix show the relationship between jet response and the likelihood function. Correction factors (α) were extracted from these plots.

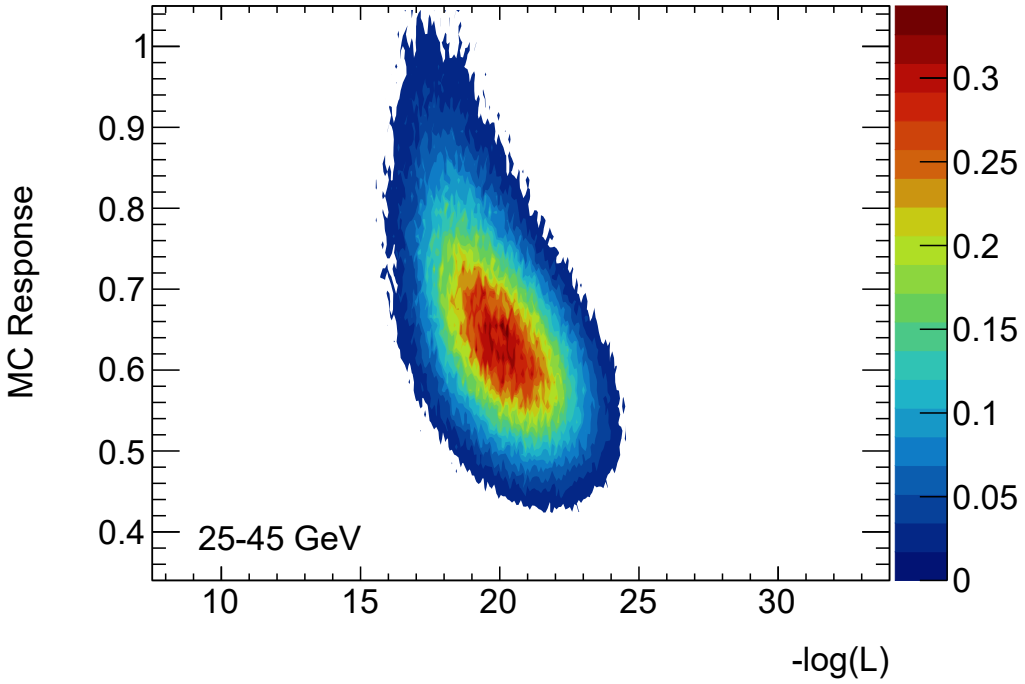

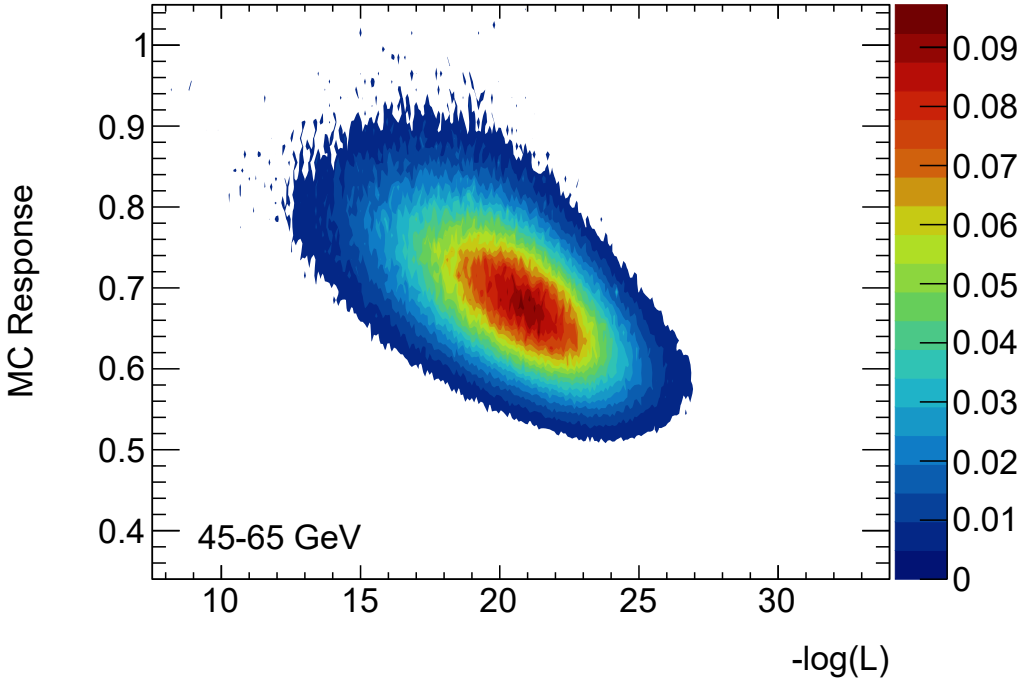
MC Response
1
0.9
0.8
0.7
0.6
0.5
0.4
45-65 GeV
10
15
20
25
30
-log(L)
0.09
0.08
0.07
0.06
0.05
0.04
0.03
0.02
0.01
0

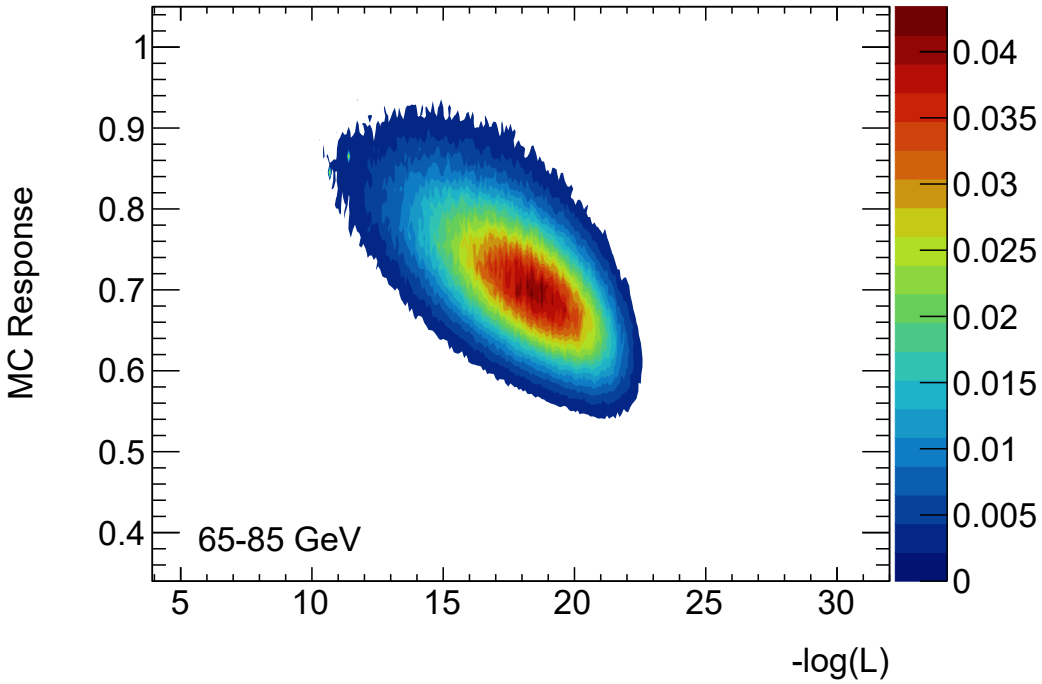
MC Response
1
0.9
0.8
0.7
0.6
0.5
0.4
65-85 GeV
5
10
15
20
25
30
-log(L)
0.04
0.035
0.03
0.025
0.02
0.015
0.01
0.005
0

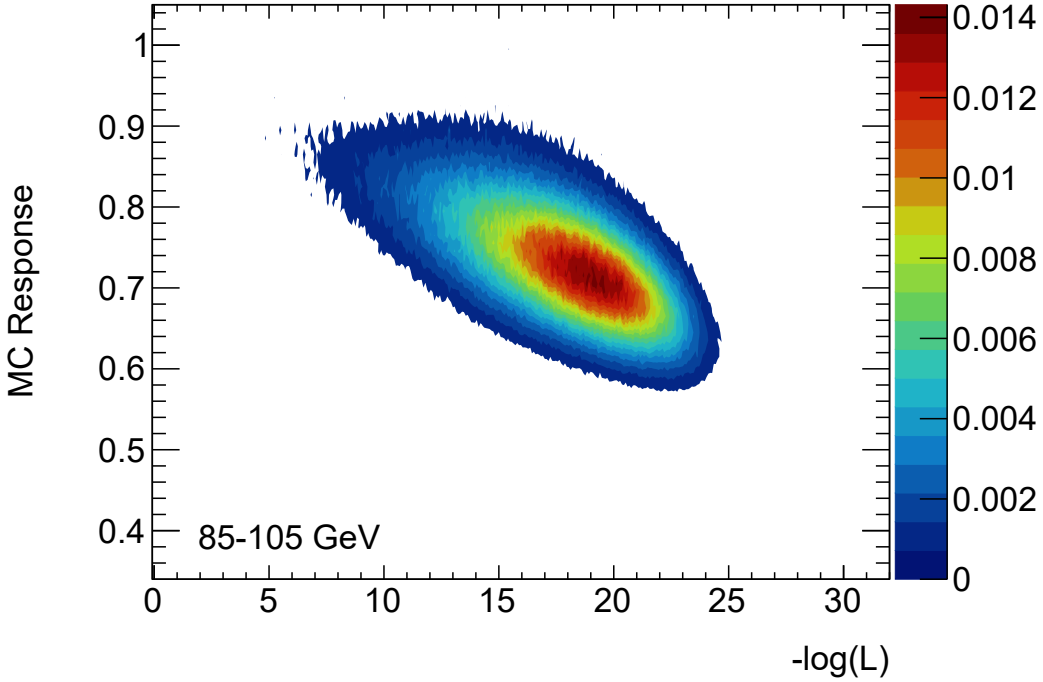
MC Response
1
0.9
0.8
0.7
0.6
0.5
0.4
85-105 GeV
0
5
10
15
20
25
30
-log(L)
0.014
0.012
0.01
0.008
0.006
0.004
0.002
0

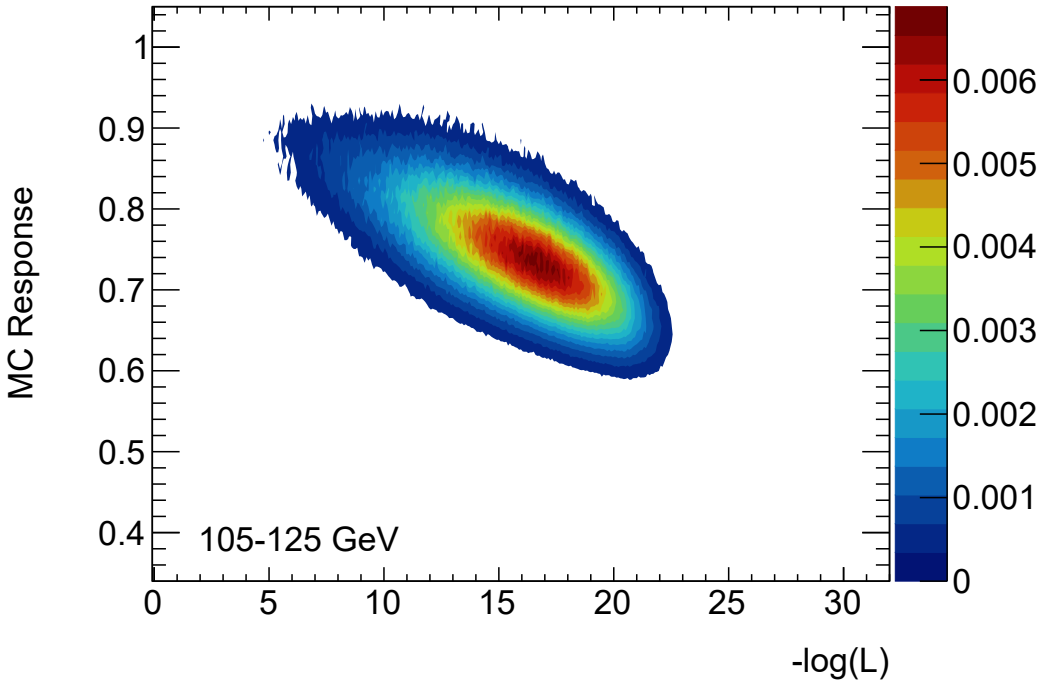
MC Response
1
0.9
0.8
0.7
0.6
0.5
0.4
105-125 GeV
0
5
10
15
20
25
30
-log(L)
0.006
0.005
0.004
0.003
0.002
0.001
0

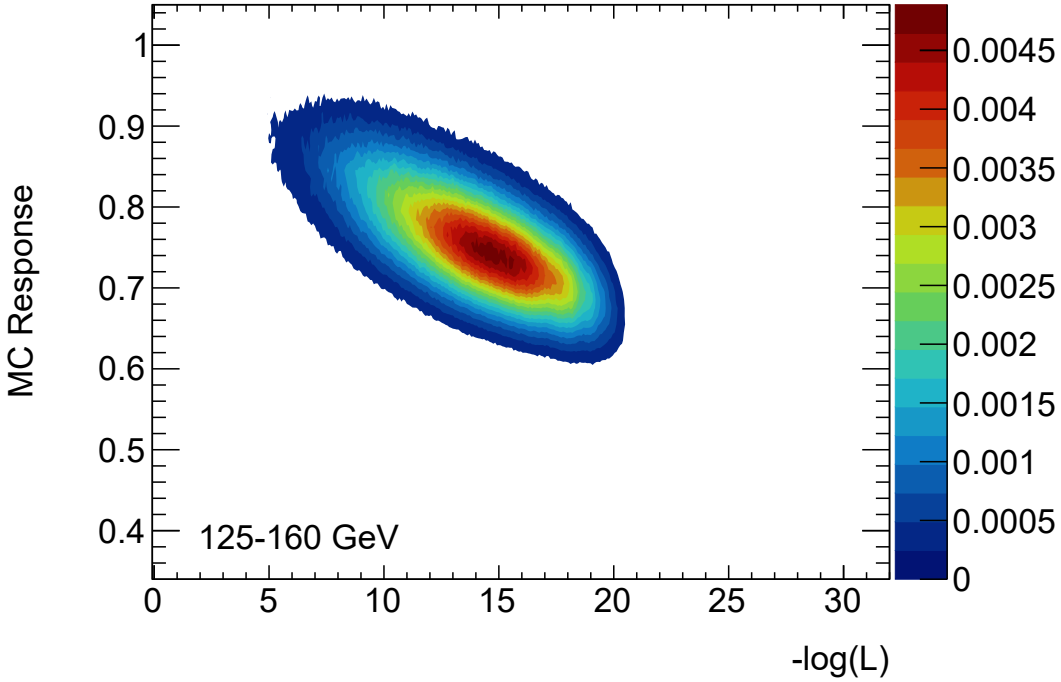
MC Response
1
0.9
0.8
0.7
0.6
0.5
0.4
125-160 GeV
0
5
10
15
20
25
30
-log(L)
0.0045
0.004
0.0035
0.003
0.0025
0.002
0.0015
0.001
0.0005
0

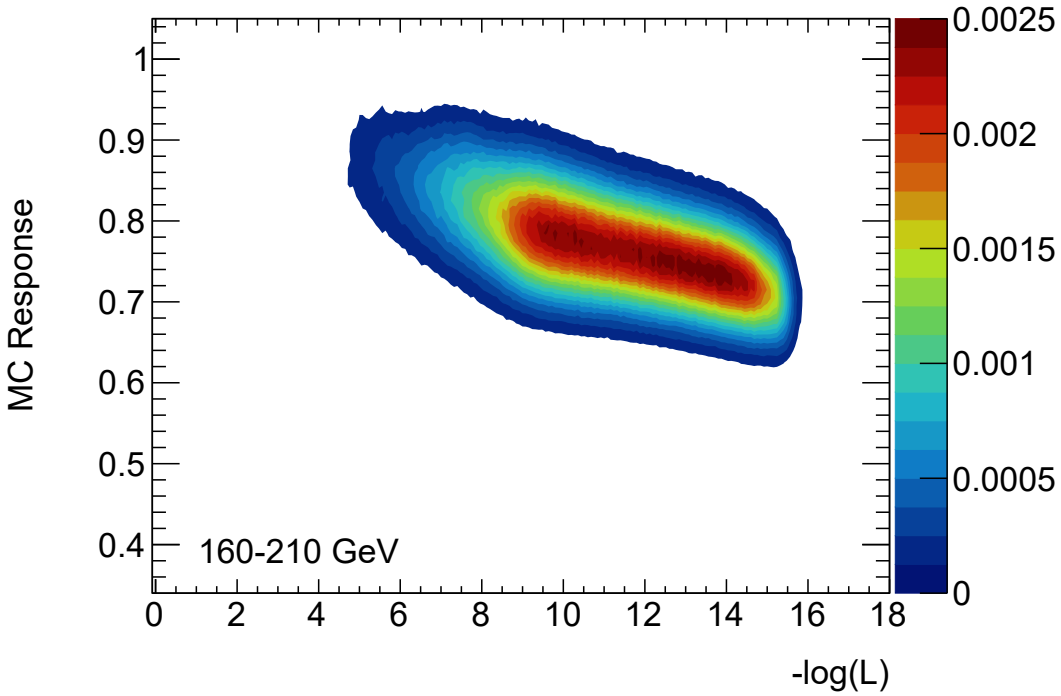
MC Response
1
0.9
0.8
0.7
0.6
0.5
0.4
160-210 GeV
0
2
4
6
8
10
12
14
16
18
-log(L)
0.0025
0.002
0.0015
0.001
0.0005
0

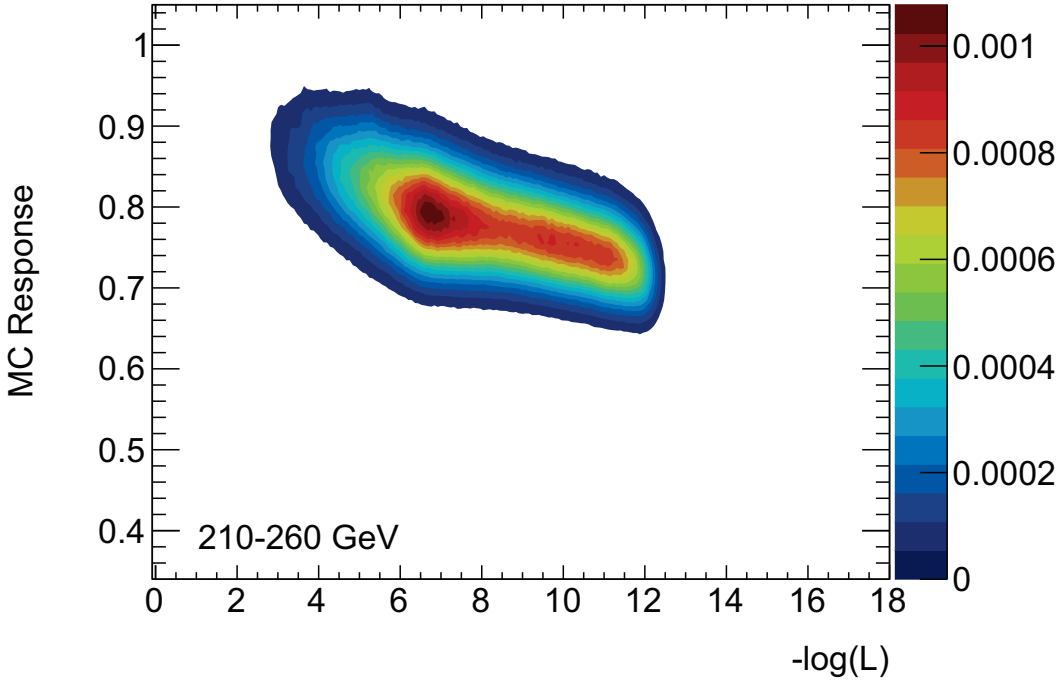
MC Response
1
0.9
0.8
0.7
0.6
0.5
0.4
210-260 GeV
0
2
4
6
8
10
12
14
16
18
-log(L)
0.001
0.0008
0.0006
0.0004
0.0002
0

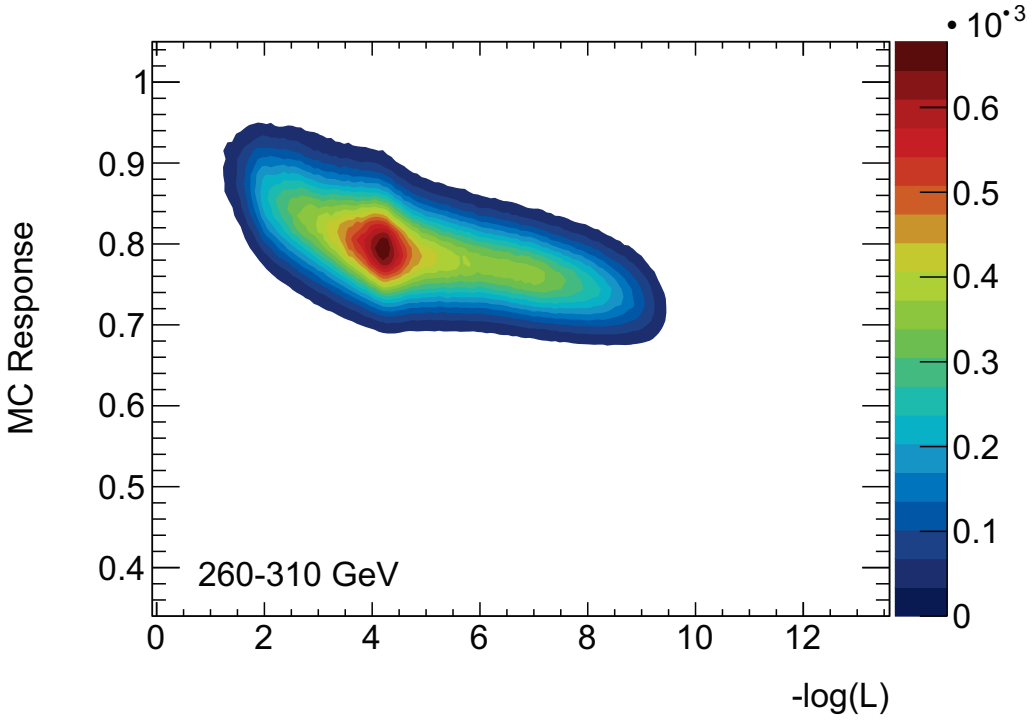
MC Response
1
0.9
0.8
0.7
0.6
0.5
0.4
260-310 GeV
0
2
4
6
8
10
12
-log(L)
• 10•3
0.6
0.5
0.4
0.3
0.2
0.1
0

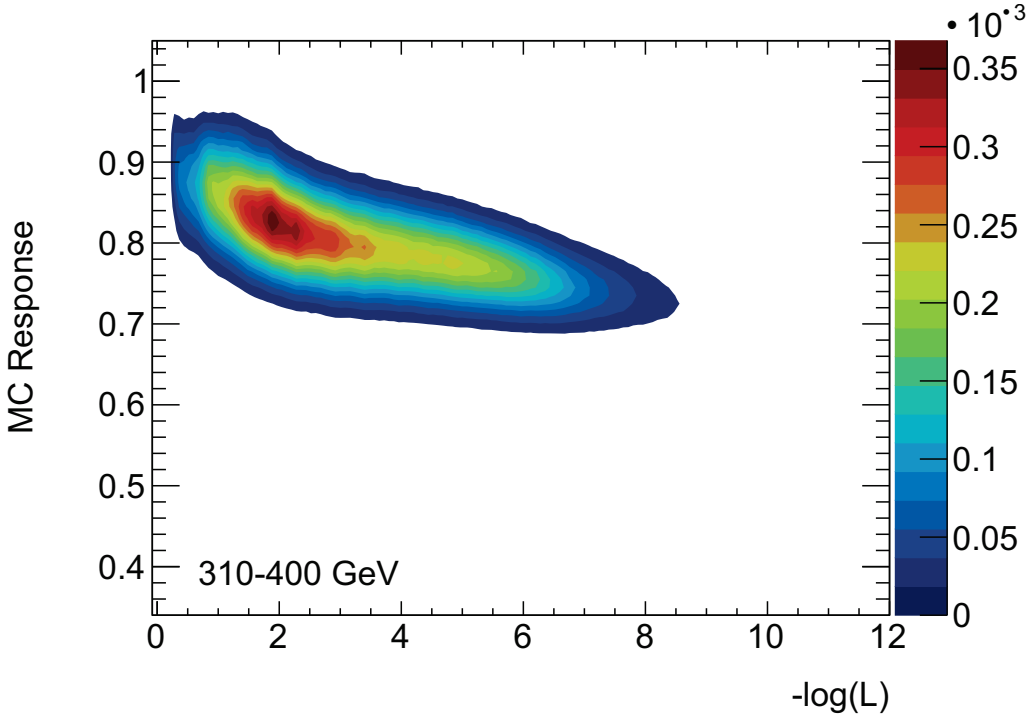
MC Response
-log(L)
310-400 GeV
• 10^-3
0.35
0.3
0.25
0.2
0.15
0.1
0.05
0

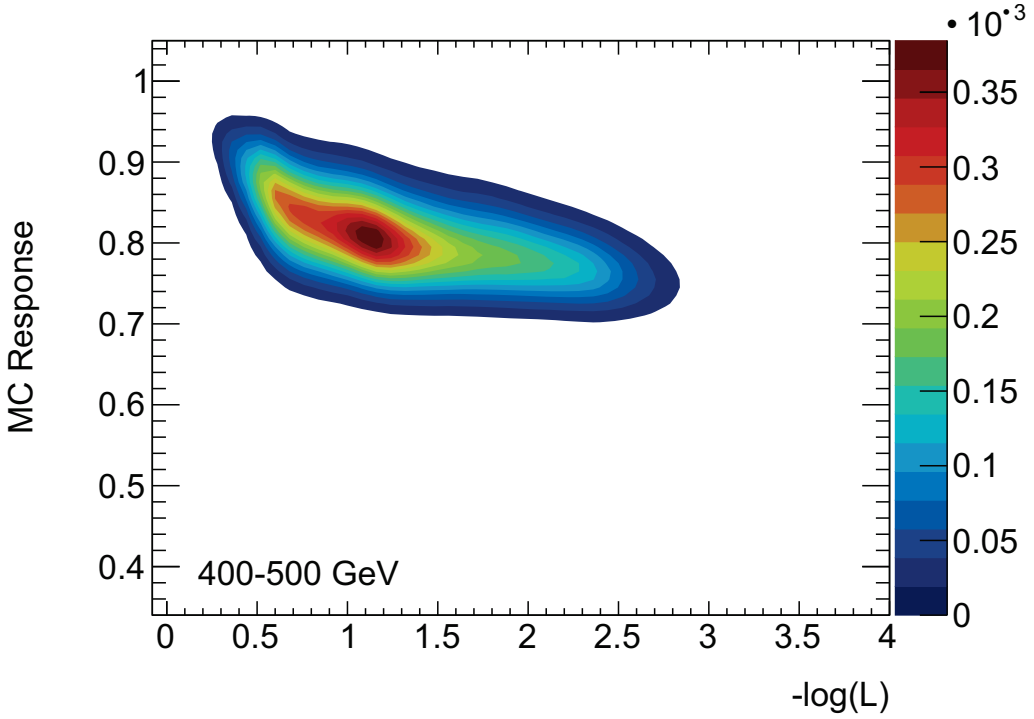
MC Response
-log(L)
400-500 GeV
• 10^-3
0.35
0.3
0.25
0.2
0.15
0.1
0.05
0

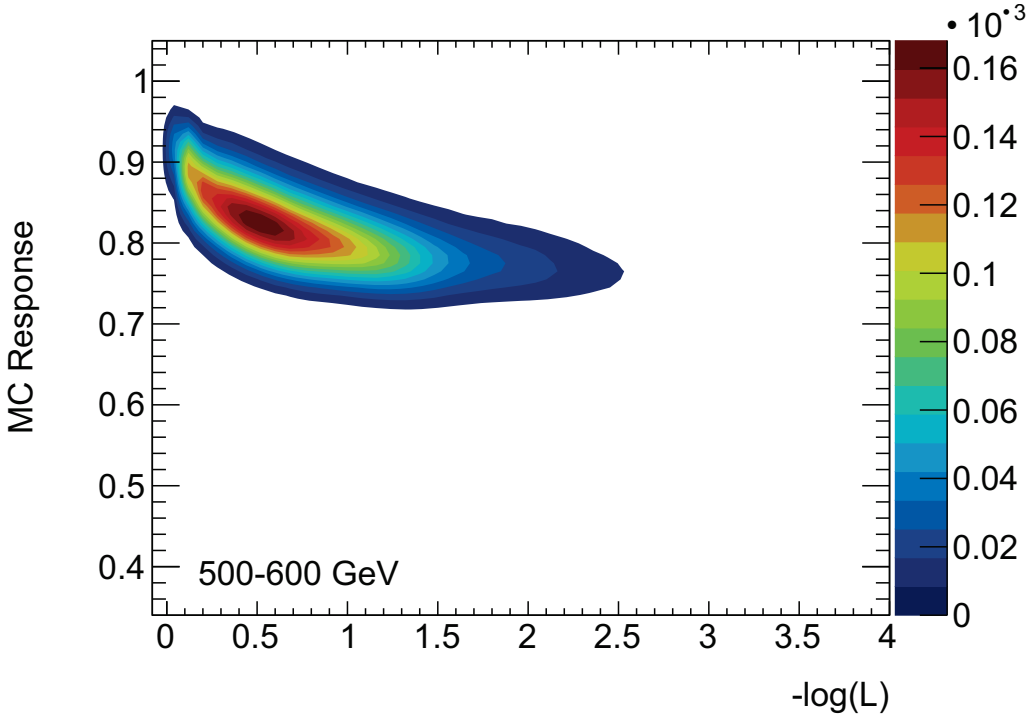
MC Response
-log(L)
500-600 GeV
• 10^-3
0.16
0.14
0.12
0.1
0.08
0.06
0.04
0.02
0

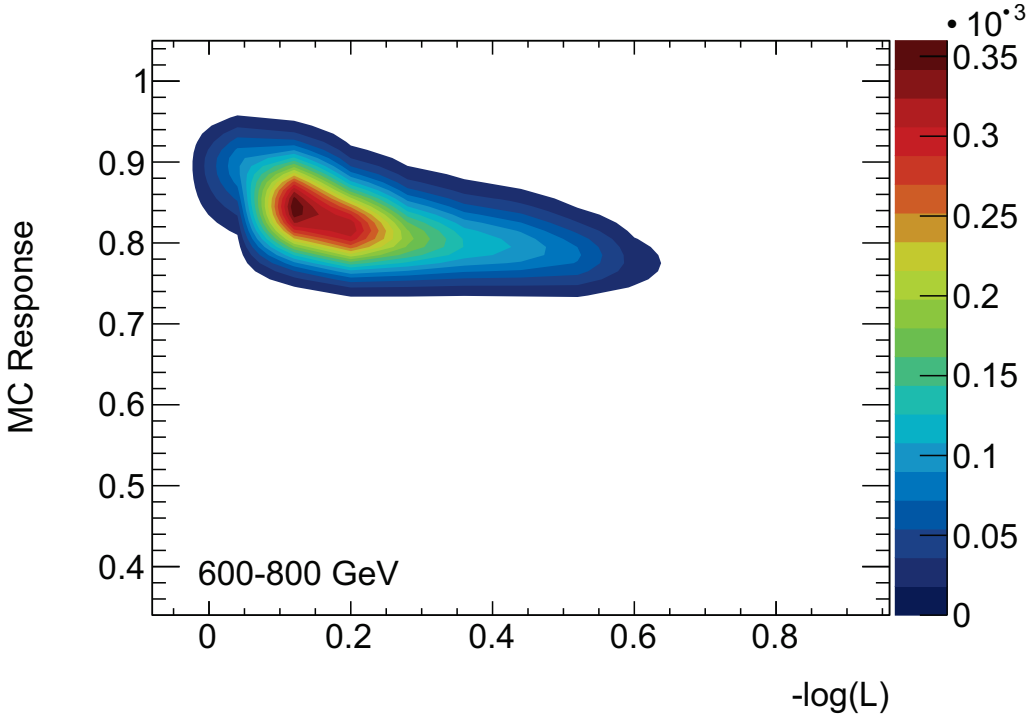
MC Response
-log(L)
600-800 GeV
• 10^-3
0.35
0.3
0.25
0.2
0.15
0.1
0.05
0

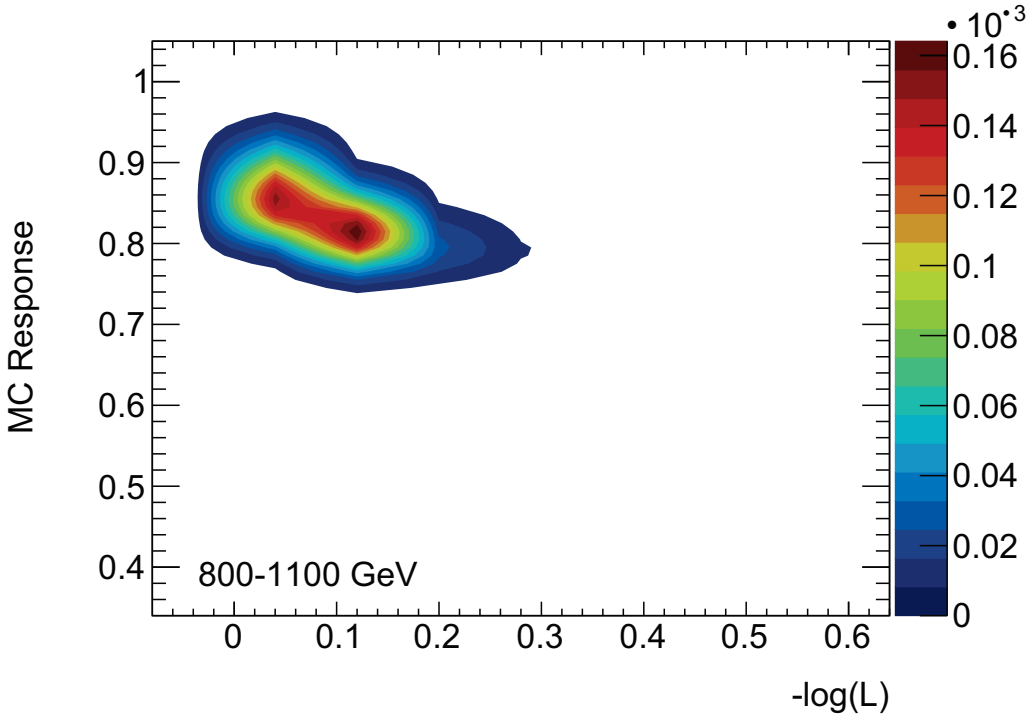
• 10^-3
0.16
0.14
0.12
0.1
0.08
0.06
0.04
0.02
0
MC Response
1
0.9
0.8
0.7
0.6
0.5
0.4
800-1100 GeV
0
0.1
0.2
0.3
0.4
0.5
0.6
-log(L)

Appendix F

Variable Lists

Here are presented the nominal variable lists used in creating the correction factors. Note that while the momentum range 1100-1500 GeV is included here, it was not used in the study.

25-45 GeV	45-65 GeV	65-85 GeV
NumTrkPt1000	NumTrkPt500	NumTrkPt1000
Width	TrackPt500Frac	EMBFrac
AvgTrackPt1000Frac	EMFrac	EMB3OverEMB
EMB1OverEMB	EMB1OverEMB	AvgTrackPt500Frac
EMBFrac	TILEB2OverTILE	EMB2OverEMB
EMB3OverEMB	EMB3OverEMB	TILEB3Frac

85-105 GeV	105-125 GeV	125-160 GeV
NumTrkPt1000	NumTrkPt1000	NumTrkPt1000
TrackPt500Frac	TrackPt500Frac	TILEB1Frac
TILEB1Frac	TILEB1Frac	EMB3Frac
EMB3OverEMB	EMB3Frac	TILEB2OverTILE
TILEB2Frac	TILEB2OverTILE	AvgTrackPt1000Frac
EMB1OverEMB	EMB2OverEMB	EMB1OverEMB

160-210 GeV	210-260 GeV	260-310 GeV
NumTrkPt1000	NumTrkPt1000	NumTrkPt1000
TILEB1Frac	TILEB1Frac	TILEB1Frac
TILEB2OverTILE	TILEB2OverTILE	TILEB2OverTILE
AvgTrackPt1000Frac	AvgTrackPt1000Frac	TrackWidth1000
EMB1OverEMB	EMB1OverEMB	EMB1Frac
TILEB3Frac	TILEB3Frac	TILEB3Frac

310-400 GeV	400-500 GeV	500-600 GeV
NumTrkPt1000	Mass	Mass
TILEB1Frac	TrackPt500Frac	TrackPt500Frac
EMB3Frac	TILEB2OverTILE	EMB3OverEMB
TILEB2OverTILE	TILEB3Frac	TILEB1Frac
TrackWidth1000	EMB1Frac	TILEB2OverTILE
AvgTrackPt1000Frac	EMB2OverEMB	EMB2OverEMB

600-800 GeV	800-1100 GeV	1100-1500 GeV
Mass	Mass	Mass
TrackPt500Frac	TrackPt500Frac	TrackPt500Frac
EMB2OverEMB	TILEB1Frac	EMB3OverEMB
TILEB2OverTILE	EMB3Frac	TILEB1Frac
TILEB3Frac	TILEB2OverTILE	TILEB2Frac
TrackWidth500	TILEB3Frac	EMB2OverEMB